PHOTONIC INTEGRATION AND PHOTONICS-ELECTRONICS CONVERGENCE ON SILICON PLATFORM

EDITED BY: Koji Yamada, Jifeng Liu, Toshihiko Baba, Laurent Vivien and Dan-Xia Xu

PUBLISHED IN: Frontiers in Materials and Frontiers in Physics

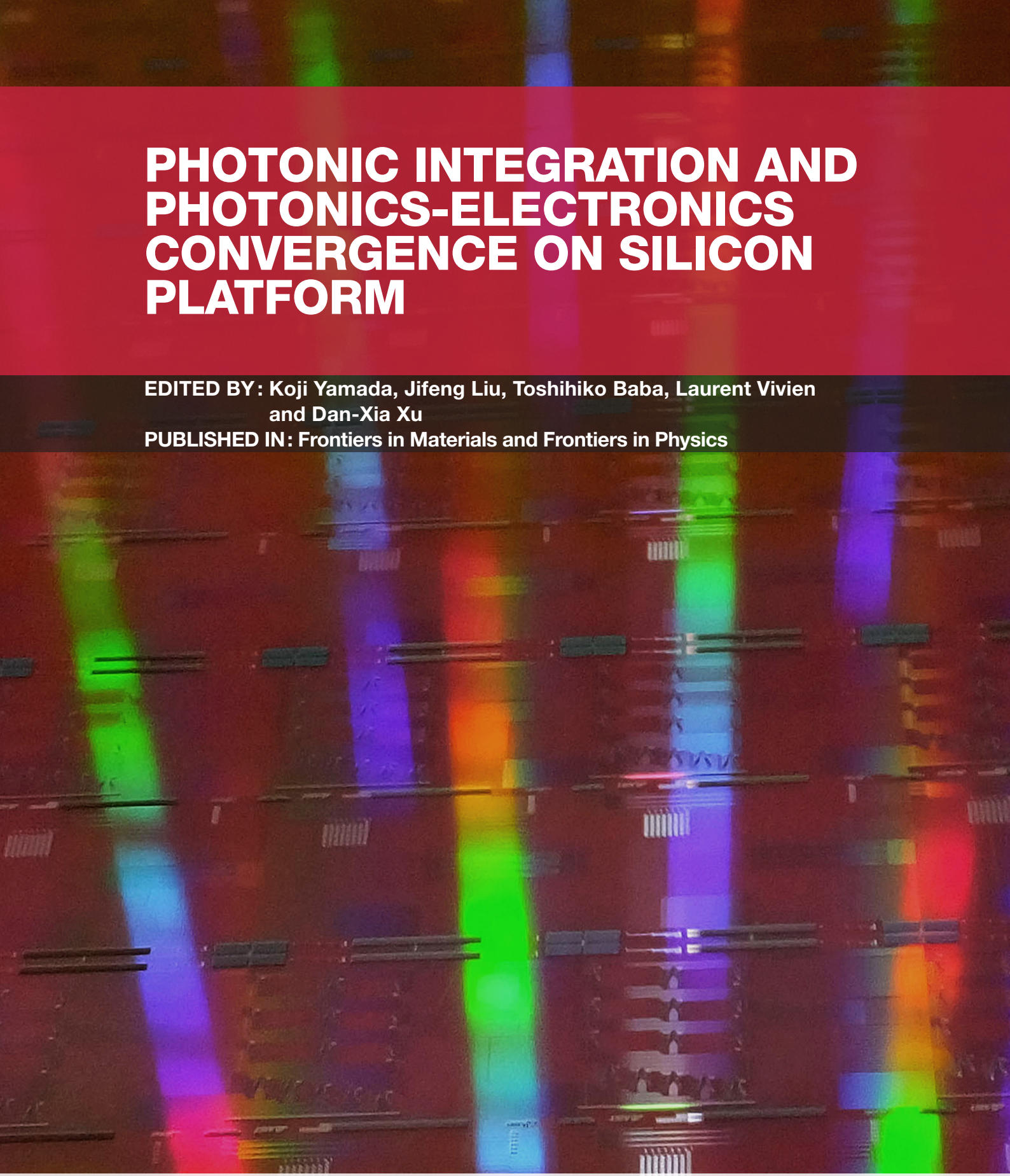

frontiers Research Topics

frontiers

ISSN 1664-8714
ISBN 978-2-88919-693-7
DOI 10.3389/978-2-88919-693-7

About Frontiers

Frontiers is more than just an open-access publisher of scholarly articles: it is a pioneering approach to the world of academia, radically improving the way scholarly research is managed. The grand vision of Frontiers is a world where all people have an equal opportunity to seek, share and generate knowledge. Frontiers provides immediate and permanent online open access to all its publications, but this alone is not enough to realize our grand goals.

Frontiers Journal Series

The Frontiers Journal Series is a multi-tier and interdisciplinary set of open-access, online journals, promising a paradigm shift from the current review, selection and dissemination processes in academic publishing. All Frontiers journals are driven by researchers for researchers; therefore, they constitute a service to the scholarly community. At the same time, the Frontiers Journal Series operates on a revolutionary invention, the tiered publishing system, initially addressing specific communities of scholars, and gradually climbing up to broader public understanding, thus serving the interests of the lay society, too.

Dedication to quality

Each Frontiers article is a landmark of the highest quality, thanks to genuinely collaborative interactions between authors and review editors, who include some of the world's best academicians. Research must be certified by peers before entering a stream of knowledge that may eventually reach the public - and shape society; therefore, Frontiers only applies the most rigorous and unbiased reviews.
Frontiers revolutionizes research publishing by freely delivering the most outstanding research, evaluated with no bias from both the academic and social point of view.
By applying the most advanced information technologies, Frontiers is catapulting scholarly publishing into a new generation.

What are Frontiers Research Topics?

Frontiers Research Topics are very popular trademarks of the Frontiers Journals Series: they are collections of at least ten articles, all centered on a particular subject. With their unique mix of varied contributions from Original Research to Review Articles, Frontiers Research Topics unify the most influential researchers, the latest key findings and historical advances in a hot research area! Find out more on how to host your own Frontiers Research Topic or contribute to one as an author by contacting the Frontiers Editorial Office: **researchtopics@frontiersin.org**

PHOTONIC INTEGRATION AND PHOTONICS-ELECTRONICS CONVERGENCE ON SILICON PLATFORM

Topic Editors:
Koji Yamada, National Institute of Advanced Industrial Science and Technology, Japan
Jifeng Liu, Thayer School of Engineering, USA
Toshihiko Baba, Yokohama National University, Japan
Laurent Vivien, Institute of Fundamental Electronics, France
Dan-Xia Xu, National Research Council, Canada

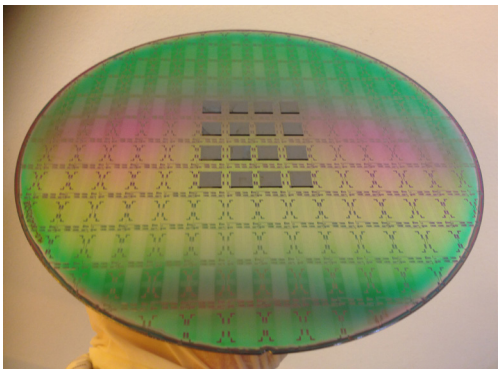

Multifunctional integration on a silicon photonic platform. Photograph by Dr. Patrick Lo Guo-Qiang.

Taken from: Luo X, Cao Y, Song J, Hu X, Cheng Y, Li C, Liu C, Liow T-Y, Yu M, Wang H, Wang QJ and Lo PG-Q (2015) High-throughput multiple dies-to-wafer bonding technology and III/V-on-Si hybrid lasers for heterogeneous integration of optoelectronic integrated circuits. Front. Mater. 2:28. doi: 10.3389/fmats.2015.00028

Silicon photonics technology, which has the DNA of silicon electronics technology, promises to provide a compact photonic integration platform with high integration density, mass-producibility, and excellent cost performance. This technology has been used to develop and to integrate various photonic functions on silicon substrate. Moreover, photonics-electronics convergence based on silicon substrate is now being pursued. Thanks to these features, silicon photonics will have the potential to be a superior technology used in the construction of energy-efficient cost-effective apparatuses for various applications, such as communications, information processing, and sensing.

Considering the material characteristics of silicon and difficulties in microfabrication technology, however, silicon by itself is not necessarily an ideal material. For example, silicon is not suitable for light emitting devices because it is an indirect transition material. The resolution and dynamic range of silicon-based interference devices, such as wavelength filters, are significantly limited by fabrication errors in microfabrication processes.

For further performance improvement, therefore, various assisting materials, such as indium-phosphide, silicon-nitride, germanium-tin, are now being imported into silicon photonics by using various heterogeneous integration technologies, such as low-temperature film deposition and wafer/die bonding. These assisting materials and heterogeneous integration technologies would also expand the application field of silicon photonics technology. Fortunately, silicon photonics technology has superior flexibility and robustness for heterogeneous integration. Moreover, along with photonic functions, silicon photonics technology has an ability of integration of electronic functions. In other words, we are on the verge of obtaining an ultimate technology that can integrate all photonic and electronic functions on a single Si chip.

This e-Book aims at covering recent developments of the silicon photonic platform and novel functionalities with heterogeneous material integrations on this platform.

Citation: Yamada, K., Liu, J., Baba, T., Vivien, L., Xu, D.-X., eds. (2015). Photonic integration and photonics-electronics convergence on silicon platform. Lausanne: Frontiers Media. doi: 10.3389/978-2-88919-693-7

Cover image: Large-scale photonic integration on silicon wafer.
Photograph by Koji Yamada

Table of Contents

frontiers in Materials

EDITORIAL
published: 14 October 2015
doi: 10.3389/fmats.2015.00065

Editorial: Photonic integration and photonics–electronics convergence on silicon platform

*Koji Yamada**

National Institute of Advanced Industrial Science and Technology, Tsukuba, Japan

Keywords: silicon photonics, photonic integration, additional waveguide system, III–V semiconductors, germanium-based emitter, wafer bonding, telecommunications applications, bio-chemical applications

Silicon-based photonics technology, which is based on the same paradigm of silicon (Si) electronics technology, promises to provide us with a compact photonic integration platform with high integration density, mass manufacturing, and excellent cost performance. This technology has been used to develop various photonic devices based on silicon, such as waveguides, filters, and modulators. In addition, germanium (Ge) photodetectors have been built on a silicon-based photonic platform. These photonic devices have already been monolithically integrated on silicon chips. Moreover, photonics–electronics convergence based on silicon photonics is now being pursued. These emerging compact photonics–electronics convergent modules have the potential to be used in the fabrication of energy-efficient cost-effective systems for various applications, such as communications, information processing, and sensing.

The last decade first saw the development of Si-based photonic technologies for communication applications, and commercial products are now available for short-range data communications. For medium-/long-range telecommunication applications, in which stringent technical standards are applied to guarantee long-distance data transmission, intensive R&D is now providing us with technologies for high-performance Si-based photonic modules with complex device integrations (Doerr, 2015). In such high-performance applications, various assisting technologies should be implemented on the silicon photonic platform. For example, the resolution and dynamic range of silicon-based interference devices, such as wavelength filters, are considerably limited by fabrication errors in microfabrication processes. To overcome such limitations, additional waveguide systems, based on silicon nitride and silicon-rich silica, have been implemented (Yamada et al., 2014; Doerr, 2015).

Additional waveguide systems can also provide novel functionalities for further performance improvements. For example, the thermo-optic response of photonic devices can be controlled by combining silicon nitride and silicon waveguides, which could guarantee temperature-insensitive operation of data transmission systems (Hiraki et al., 2015). Thermo-optic responses can also be widely controlled by using titania as a cladding material in a Si waveguide (Lee, 2015). Moreover, an additional waveguide system can expand the application field of the Si photonic platform. For instance, silicon nitride waveguides, which are transparent to visible light, can be used to construct compact bio-sensing systems on a small Si chip (Wang et al., 2015).

Light-source integration, which is the most important open issue for the Si photonic platform, requires the help of other materials. For this purpose, III–V semiconductor materials have been bonded on silicon by using various hybrid integration techniques, such as direct die-to-wafer bonding (Fang et al., 2006; Luo et al., 2015). For monolithic integration, Ge-based light sources are now being studied intensively. The most important technology for Ge-based light sources is band-gap engineering, which aims to achieve a direct transition in Ge, which is originally an indirect-transition material. The recent status of Ge-based light sources on Si is reviewed in this special issue (Saito et al., 2014; Geiger et al., 2015). Mechanical stress and heavily doped n-type carriers

OPEN ACCESS

Edited and reviewed by:
Lorenzo Pavesi, University of Trento, Italy

***Correspondence:**
Koji Yamada
yamada.koji@aist.go.jp

Specialty section:
This article was submitted to Optics and Photonics, a section of the journal Frontiers in Materials

Received: *24 September 2015*
Accepted: *29 September 2015*
Published: *14 October 2015*

Citation:
Yamada K (2015) Editorial: Photonic integration and photonics–electronics convergence on silicon platform. Front. Mater. 2:65. doi: 10.3389/fmats.2015.00065

would significantly contribute to making Ge a direct-transition material. GeSn alloy is also a very attractive material for light sources on a Si platform because Sn, which can easily be dissolved in Ge, offers an important degree of freedom in band-gap engineering (Mosleh et al., 2015). Another approach now being investigated for monolithic integration of light sources is Si-based electro-luminescence at room temperature, although its physical origin has not fully understood (Li et al., 2015).

The Si-based photonic platform requires various assisting materials for accomplishing practical photonic functions. Fortunately, it has superior flexibility and robustness for integrating these materials. Along with photonic functions, the Si-based photonic platform can integrate electronic functions monolithically. In other words, we are on the verge of obtaining an ultimate technology that can integrate all photonic and electronic functions on a single Si chip.

ACKNOWLEDGMENTS

I would like to acknowledge all the authors, reviewers, editors, and publishers, who have supported this Research Topic.

REFERENCES

Doerr, C. R. (2015). Silicon photonic integration in telecommunications. *Front. Phys.* 3:37. doi:10.3389/fphy.2015.00037

Fang, A. W., Park, H., Cohen, O., Jones, R., Paniccia, M. J., and Bowers, J. E. (2006). Electrically pumpled hybrid AlGaInAs-silicon evanescent laser. *Opt. Express* 14, 9203–9216. doi:10.1364/OE.14.009203

Geiger, R., Zabel, T., and Sigg, H. (2015). Group IV direct band gap photonics: methods, challenges, and opportunities. *Front. Mater.* 2:52. doi:10.3389/fmats.2015.00052

Hiraki, T., Fukuda, H., Yamada, K., and Yamamoto, T. (2015). Small sensitivity to temperature variations of Si-photonic Mach-Zhender interferometer using Si and SiN waveguides. *Front. Mater.* 2:26. doi:10.3389/fmats.2015.00026

Lee, J.-M. (2015). Ultrahigh temperature-sensitive silicon MZI with titania cladding. *Front. Mater.* 2:36. doi:10.3389/fmats.2015.00036

Li, S., Gao, Y., Fan, R., Li, D., and Yang, D. (2015). Room-temperature near-infrared electroluminescence from boron-diffused silicon pn-junction diodes. *Front. Mater.* 2:8. doi:10.3389/fmats.2015.00008

Luo, X., Cao, Y., Song, J., Hu, X., Cheng, Y., Li, C., et al. (2015). High-throughput multiple dies-to-wafer bonding technology and III/V-on-Si hybrid lasers for heterogeneous integration of optoelectronic integrated circuits. *Front. Mater.* 2:28. doi:10.3389/fmats.2015.00028

Mosleh, A., Alher, M. A., Cousar, L. C., Du, W., Ghetmiri, S. A., Pham, T., et al. (2015). Direct growth of $Ge_{1-x}Sn_x$ films on Si using a cold-wall ultra-high vacuum chemical-vapor-deposition system. *Front. Mater.* 2:30. doi:10.3389/fmats.2015.00030

Saito, S., Gardes, F. Y., Al-Attili, A. Z., Tani, K., Oda, K., Suwa, Y., et al. (2014). Group IV light sources to enable the convergence of photonics and electronics. *Front. Mater.* 1:15. doi:10.3389/fmats.2014.00015

Wang, J., Yao, Z., and Poon, A. W. (2015). Silicon-nitride-based integrated optofluidic biochemical sensors using a coupled-resonator optical waveguide. *Front. Mater.* 2:34. doi:10.3389/fmats.2015.00034

Yamada, K., Tsuchizawa, T., Nishi, H., Kou, R., Hiraki, T., Takeda, K., et al. (2014). High-performance silicon photonics technology for telecommunications applications. *Sci. Technol. Adv. Mater.* 15, 024603. doi:10.1088/1468-6996/15/2/024603

Conflict of Interest Statement: The author declares that the research was conducted in the absence of any commercial or financial relationships that could be construed as a potential conflict of interest.

frontiers in Physics

REVIEW
published: 05 August 2015
doi: 10.3389/fphy.2015.00037

Silicon photonic integration in telecommunications

Christopher R. Doerr *

Acacia Communications, Hazlet, NJ, USA

Silicon photonics is the guiding of light in a planar arrangement of silicon-based materials to perform various functions. We focus here on the use of silicon photonics to create transmitters and receivers for fiber-optic telecommunications. As the need to squeeze more transmission into a given bandwidth, a given footprint, at a given cost increases, silicon photonics makes more and more economic sense.

Keywords: integrated optics, silicon photonics, optical fiber, optical communications, coherent, gratings, waveguides

OPEN ACCESS

Edited by:
Qiaoliang Bao,
Soochow University, China

Reviewed by:
Lukas Novotny,
ETH Zurich, Switzerland
Satoshi Iwamoto,
The University of Tokyo, Japan
Xiangping Li,
Swinburne University of Technology, Australia

***Correspondence:**
Christopher R. Doerr,
Acacia Communications, 1301 Route 36, Hazlet, NJ 07730 USA
chris.doerr@acacia-inc.com

Specialty section:
This article was submitted to Optics and Photonics, a section of the journal Frontiers in Physics

Received: *11 February 2015*
Paper pending published: *23 March 2015*
Accepted: *13 May 2015*
Published: *05 August 2015*

Citation:
Doerr CR (2015) Silicon photonic integration in telecommunications. Front. Phys. 3:37. doi: 10.3389/fphy.2015.00037

1. Introduction

Until circa 2002, fiber-optic communication for metropolitan distances (80—600 km) and long-haul distances (600–15,000 km) employed mostly simple on-off keying (OOK) transmission. On-off keying is simply turning on and off the light to transmit "1" s and "0" s. Higher performance, i.e., a lower bit-error rate (BER) for the same received optical power and/or for the same optical signal-to-noise ratio (OSNR), can be obtained by using phase-modulated formats, such as binary phase-shift keying (BPSK) or quadrature phase-shift keying (QPSK). They maximize the distance between constellation points for the same average signal power. In these "advanced" modulation formats [1], the term "symbol" is used to represent each data portion in time, because each symbol can carry multiple bits of information. Early BSPK and QPSK were detected by differential detection, i.e., by interfering one symbol with the previous symbol in an interferometer in the receiver.

However, bandwidth needs have been constantly growing exponentially. It is expensive to install new optical fibers, ∼ $30 k per mile [2], so carriers and data-center operators needed to send more bits per second in the same fiber in the same optical bandwidth. One key way is to use both optical polarizations, because this doubles the available bandwidth. Although signal orthogonality is maintained, their polarizations are essentially randomly changed during propagation through fiber. To unscramble them requires significant signal processing. Optical coherent detection allows this to be done by digital electronics.

Optical coherent detection was a hot topic in the 1980s, because it is a form of optical amplification. However, the invention of the erbium-doped fiber amplifier (EDFA) eliminated that advantage and coherent interest died away. Another advantage of coherent detection is the ability to receive the full optical field, both the real and imaginary parts of both polarizations. With improvements in complementary metal-oxide-semiconductor (CMOS) electronics, digital signal processing (DSP) became available circa 2002 to handle coherent detection even up to 100-Gb/s, causing a revival of coherent detection. In the past, coherent detection was simply single quadrature and single polarization. Now it is dual quadrature and dual polarization.

100-Gb/s coherent systems have proven to be extremely compelling. They allow an upgrade of a 10-Gb/s channel to a 100-Gb/s channel with actually improved reach. Industry analyses show the number of metro and long-haul 100-Gb/s coherent transceivers sold per year to be on a steep upwards ramp as 10-Gb/s OOK transceivers are replaced by 100-Gb/s coherent transceivers.

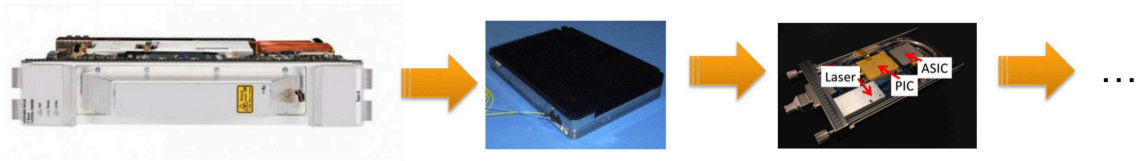

FIGURE 1 | 100-Gb/s coherent transceiver form-factor evolution. It went from a full line card, to a multi-source agreement (MSA) module, to a 100-Gb/s form-factor pluggable (CFP) module. The D in D-CFP means that it is a digital module and the DSP is included inside, as opposed to a module that contains only the optics.

However, the price of 100-Gb/s coherent transceivers is expected to drop significantly. This is because users want to pay the same price per connection even though the bit rate keeps increasing. However, not only must the price drop, but the footprint and power consumption as well. As seen in **Figure 1**, 100-Gb/s modules have gone from full line cards to 5×7 in^2 screwed-on modules to 3.2×5.7 in^2 pluggable modules today. Today's 100-Gb/s pluggable form factor is called a CFP. Tomorrow's will be a CFP2, which is half the size, and eventually a CFP4, which is a quarter the size. Power consumptions have gone from more than 100 W on a line card, to 70 W for the screwed-on module, to 28 W for the CFP. The next step, the CFP2, allows only 12W.

There are two main components in a coherent transceiver—the DSP chip and the optics. Today's coherent CFP contains both. There is a, possibly temporary, trend to take the DSP out of the module and put it on the line card. Such modules are called "analog" modules, rather than digital. With today's technology, it is not possible to have both the optics and DSP be under 12 W, the maximum power in a CFP2. However, in 1–2 years, technology will likely be ready for a "digital" CFP2.

To meet these requirements of lower price, lower power and smaller footprint, one must make advancements in technology. For the DSP, one can take advantage of the steady reduction in transistor size in industry, which reduces power and footprint. Node size and introduction year are shown in **Table 1** [3]. Today's coherent DSPs use 20–28 nm. Tomorrow's will use 14 nm.

For the optics, one must use photonic integration, the focus of this article. Most of today's coherent transceivers are built using separate $LiNbO_3$/planar lightwave circuit (PLC) modulators and InP/PLC receivers, as shown in **Figure 2**. More and more, smaller InP modulators and InP receivers are being used. In today's coherent CFP, there is a single silicon photonic (SiPh) integrated circuit (PIC) containing both the transmitter and receiver [4]. Not shown is a separate tunable laser.

Finally, a dominant cost for the DSP and optics is the packaging; one can further reduce cost, power, and footprint by co-packaging the DSP and optics. Such transceivers are expected in 2–3 years.

Figure 3 shows many of the elements that may be integrated in a PIC. The blue are passive, the red are active (have an intended dynamic interaction between light and matter), and the green are electronic components. PICs have been around more than 20 years. The main advantages of photonic integration are a small footprint, due to strongly confining waveguides and lens-free connections between parts; low power, due to an obviation of 50-Ω RF lines; higher bandwidth RF connections; and low price, due to fewer touch points, no mechanical adjustments, less test equipment, and less material. The main disadvantages of PICs are typically a higher insertion loss and the inability to optimize components independently.

TABLE 1 | Node size and first year of commercial introduction for CMOS electronics.

Node size	Year
10 μm	1971
6 μm	1974
3 μm	1977
1.5 μm	1982
1 μm	1985
800 nm	1989
600 nm	1994
350 nm	1995
250 nm	1997
180 nm	1999
130 nm	2001
90 nm	2004
65 nm	2006
45 nm	2008
32 nm	2010
22 nm	2012
14 nm	2014
10 nm	2016
7 nm	2018
5 nm	2020

2. PIC Material Systems

Figure 4 shows the most popular PIC material systems. From left to right there are silica-on-silicon PICs, also called PLCs; silicon-on-insulator PICs, also called silicon photonics; lithium niobite ($LiNbO_3$); and III–V PICs, such as InP and GaAs. This article focuses on silicon photonics. In silicon photonics, the light is mostly guided in silicon, which has an indirect bandgap of 1.12

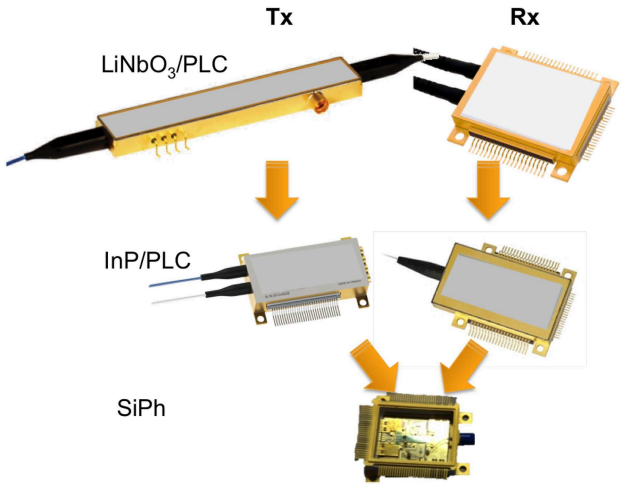

FIGURE 2 | 100-Gb/s coherent optics evolution, going from $LiNbO_3$ modulators and planar lightwave circuit (PLC)-based receivers to InP-based modulators and receivers to silicon photonic modulators and receivers.

eV (1.1 μm). The silicon is a pure crystal grown in a boule and then sliced into wafers, today typically 300 mm in diameter, as shown in **Figure 5**. The surfaces are oxidized to form SiO_2 layers. One wafer is bombarded with hydrogen atoms to a specified depth. Then the two wafers are placed together in a vacuum, and the oxide layers bond to each other. The assembly is cracked at the hydrogen implantation line. Then the silicon layer where the crack was is polished, and one is left with a thin layer of crystalline silicon on a layer of oxide on a full silicon "handle" wafer. The waveguides are formed from this thin crystalline layer. While these silicon-on-insulator (SOI) wafers are what makes low-loss silicon photonic waveguides possible, they are actually used mostly for low-power CMOS circuits, because of the low leakage currents they offer.

There is a wide family of possible silicon-based optical waveguides, shown in **Figure 6**. They range from micro-scale Ge-doped SiO_2 waveguides to nano-scale Si wire waveguides. By adding Ge, one can make photodetectors and electro-absorption modulators. Potentially even optical amplifiers. By doping the silicon one can make optical modulators. From left to right at the bottom are silicon wire waveguides, silicon nitride waveguides,

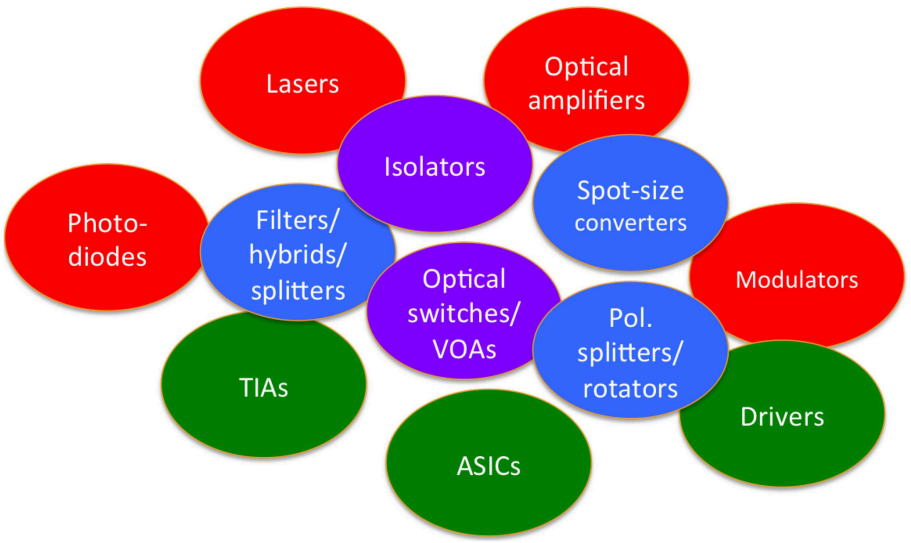

FIGURE 3 | Some of the possible PIC integration elements.

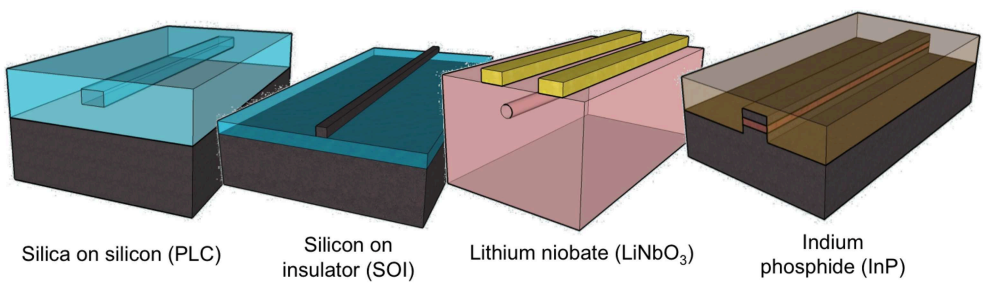

FIGURE 4 | Popular PIC material systems. The second from the left is a silicon wire waveguide and is the focus of this article.

silicon oxynitride waveguides, thick silicon rib waveguides, thin silicon nitride waveguides, and doped silica waveguides. From left to right at the top are a depletion modulator, a Ge photodetector, and a Ge optical amplifier.

3. Si Photonic Passive Elements

There are several key silicon photonic passive elements. One is the surface-emitting grating coupler, as shown in **Figure 7A** [5, 6]. It consists of a strong grating in the waveguide with a pitch approximately equal to the wavelength in the waveguide. This causes light to emit or be received vertical to the surface, which is well-suited for wafer level measurements and/or coupling to an optical fiber. The grating coupler is somewhat unique to silicon photonics because it requires a high vertical index contrast. For example, if one tried to do a grating coupler in traditional InP waveguides, the light would simply leak away into the substrate rather than be emitted vertically, because the average index of the grating waveguide would be below that of the substrate. To make it work in InP, one must undercut the material under the grating, suspending it, as shown in **Figure 7B** [7].

Another key element is a spot-size converter, which converts the $\sim 0.5 \times 1\ \mu m^2$ mode of a Si wire waveguide to the $\sim 10 \times 10\ \mu m^2$ mode of an optical fiber. A typical method is to use an inverse taper, in which the waveguide is narrowed down to a small tip, causing the optical mode to expand very large [8]. The mode can be captured by a suspended glass waveguide, such as in **Figure 8** [9]. Coupling losses less than 1.5 dB are readily achievable with such spot-size converters.

Another key passive element is a polarization splitter. Some polarization splitter examples are shown in **Figure 9**. The first is a Mach-Zender interferometer with a different birefringence in each arm [10]. The second is a simple directional coupler [11]. The shape birefringence is so high in typical silicon wire waveguides, that the transverse-magnetic (TM) polarization can couple fully while the transverse-electric (TE) polarization has barely begun to couple. The third is a grating coupler in which the fiber is placed at an angle such that TE couples in one direction

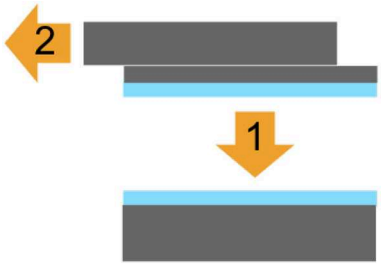

FIGURE 5 | How a silicon-on-insulator (SOI) wafer is made. Each wafer is made from two silicon wafers. The wafers are oxidized, bonded, and one is cut and polished to a thin layer.

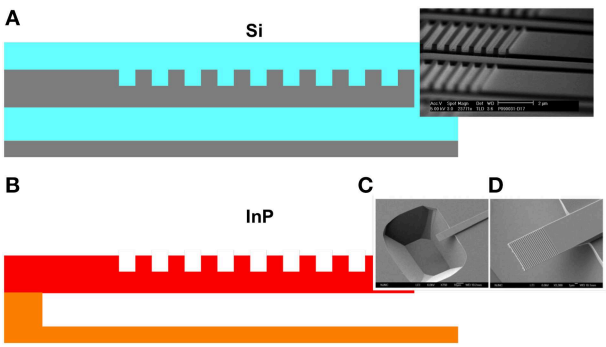

FIGURE 7 | Surface-emitting 1-D grating couplers in silicon (A) and InP (B). In **(A)**, the gray and light blue represent silicon and silicon dioxide, respectively. In **(B)**, the red and orange represent InGaAsP and InP, respectively. **(C,D)** SEM pictures of the InP suspended cantilever grating coupler.

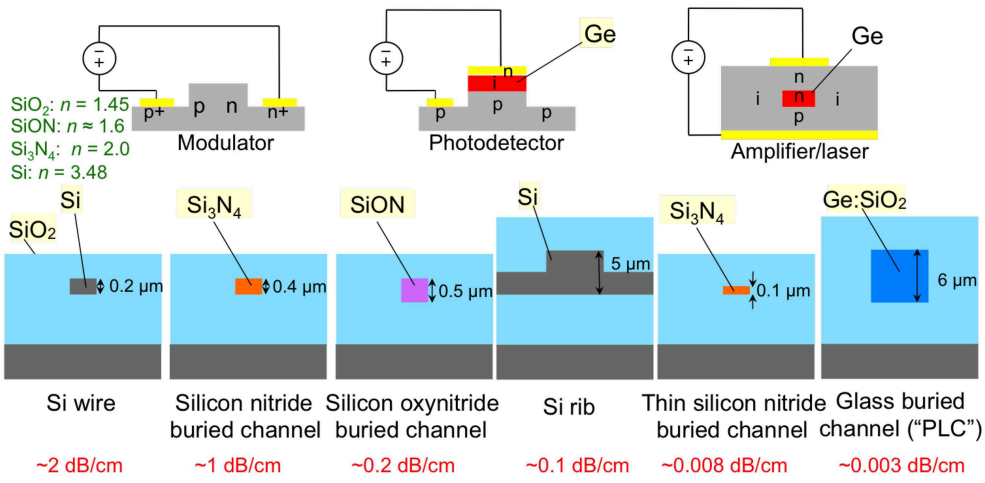

FIGURE 6 | Cross sections of the family of Si-based optical waveguides. Also shown are typical propagation losses and refractive indices.

and TM the other [12]. The fourth is a 2D grating coupler [13]. The fiber mode with its electric field perpendicular to the waveguide propagation direction will couple to that waveguide. The fiber can be either tilted and couple to two waveguides or be normal to the surface and couple to four waveguides. The 2D grating coupler has the added advantage of acting as a polarization rotator, in that all the light on the chip has the same polarization yet was two orthogonal polarizations in the fiber.

4. Si Photonic Active Elements

As mentioned above, a photonic active element has an intentional dynamic interaction between light and matter. A typical photonic active element is an optical modulator. All the Si optical modulators today are based on the plasma free carrier effect. The complex refractive index of the silicon changes by changing the number of free electrons and holes, either by doping, electrical means, or optical means, as shown in Equations (1, 2), obtained by fitting to data in Soref and Bennett at 1550-nm wavelength [14]. The holes have a larger ratio of real to imaginary index change, i.e., more phase change for a given loss change, and thus are usually favored for making the phase modulators in Mach-Zehnder and ring modulators.

$$\Delta n_r = -8.8 \times 10^{-22} N_e - 8.5 \times 10^{-18} N_h^{0.8} \quad (1)$$

$$n_i = 1.0 \times 10^{-22} N_e + 7.4 \times 10^{-23} N_h \quad (2)$$

Various Si modulator types are shown in **Figure 10A**. In the carrier injection modulator, the light is in intrinsic silicon inside a very wide p-i-n junction, and electrons and holes are injected. Such a modulator is slow, however, typically 500-MHz bandwidth, because it takes a long time for the free electrons and holes to recombine after injection. Thus, such structures are usually used as variable optical attenuators (VOAs) rather than modulators [15, 16]. In the carrier depletion modulator, the light is partly in a narrow p-n junction, and the depletion width of the p-n junction is varied by an applied electric field. Such a modulator can operate at over 50 Gb/s [17], but has a high background insertion loss. A typical $V_\pi L$ is 2 V-cm. The metal-oxide-semiconductor (MOS) (really semiconductor-oxide-semiconductor) modulator contains a thin oxide layer in the p-n junction [18]. It allows for some carrier accumulation as well as carrier depletion, allowing for a smaller $V_\pi L$ of ~0.2 V-cm, but with the drawbacks of higher optical loss and higher capacitance per unit length. There are also SiGe electroabsorption modulators [19] that rely on band-edge movement in SiGe. There are also graphene modulators that rely on switching the graphene between an absorbing metal and a transparent insulator [20].

Various Si-based photodetectors are shown in **Figure 10B**. The absorption material is Ge. Ge absorbs light with wavelengths up to about 1.6 μm. Shown on the left is a p-i-n configuration

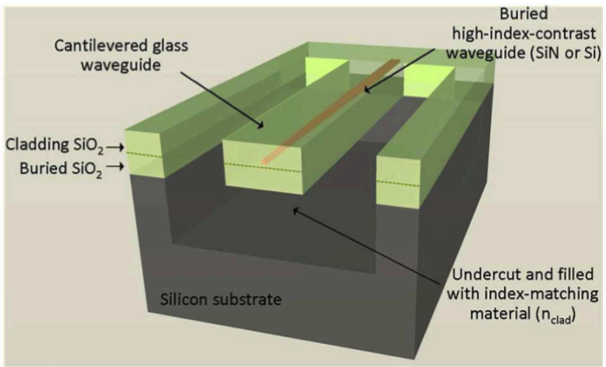

FIGURE 8 | Spot-size converter for silicon wire waveguides. The silicon is inverse tapered inside a suspended glass waveguide. The silicon substrate has been etched away under the suspended glass waveguide.

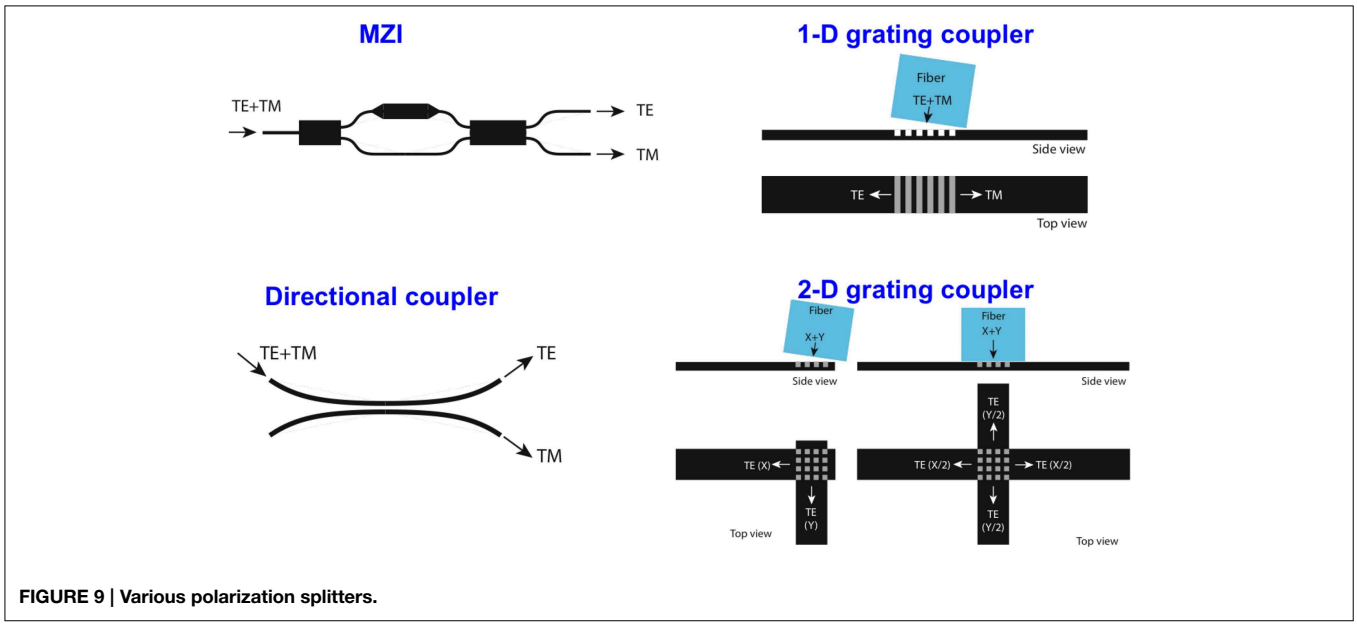

FIGURE 9 | Various polarization splitters.

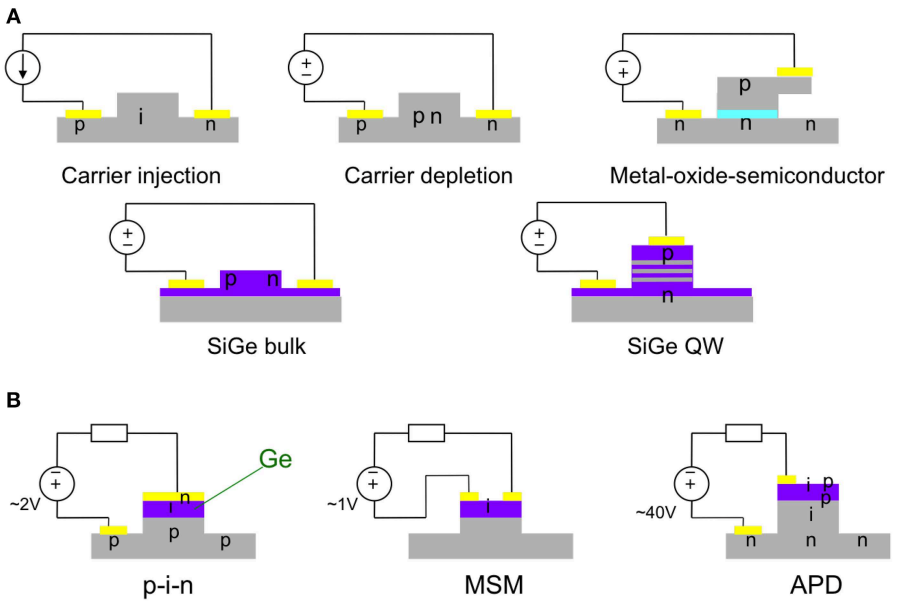

FIGURE 10 | (A) Cross sections of various silicon-based optical modulator designs and **(B)** photodetector designs.

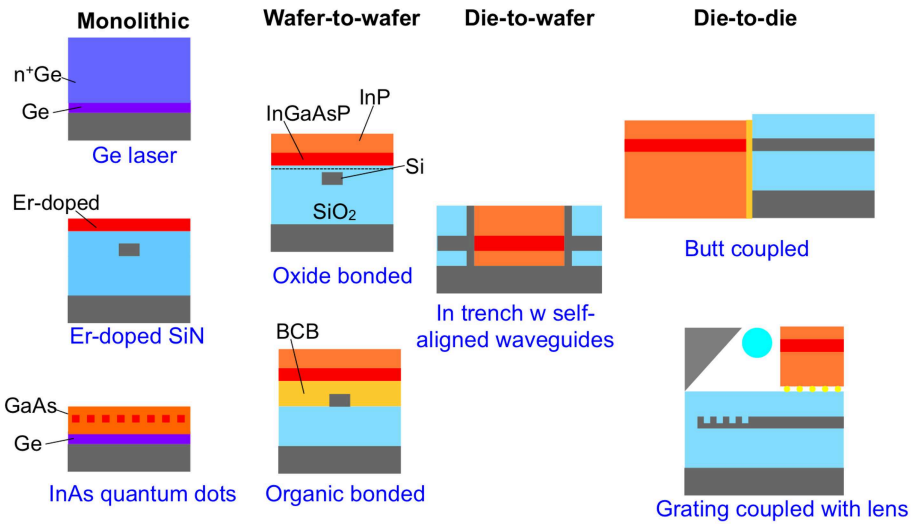

FIGURE 11 | Configurations for integrating optical gain into silicon photonics. Fabrication insertion point becoming later in the process as one moves from left to right.

[21], the most successful commercially today. It consists of p-doped silicon on which Ge is grown. Ge and Si have a 4% lattice mismatch, so to minimize dislocations, a thin layer of SiGe is grown first. The top of the Ge is n doped. Shown in the middle is a metal-semiconductor-metal (MSM) photodiode [22] and at the right avalanche photodiodes (APDs) [23]. The APD avalanche region is in Si, which has a lower noise than avalanche regions in III–V materials.

There is still no clear-winning solution for integrating optical gain with silicon photonics. Some of the various option are shown in **Figure 11**, organized by assembly level. On the far left is monolithic integration, including using epitaxially grown Ge as an optical gain material [24], Er-doped glass waveguides, such as Al_2O_3, (which require optical pumping) [25], and epitaxially grown GaAs quantum dots [26]. The next column is wafer-to-wafer assembly, including oxide bonding [27] and organic bonding [28] of III–V gain regions. The next column is die-to-wafer assembly, including inserting III–V die into cavities in the Si wafer and then patterning the waveguides [29]. The advantages of all the left three columns is that the full device can be tested on the wafer level, before it is diced out. The far right column is die-to-die assembly, including butt coupling of a Si die and a

III–V die and coupling with a lens and a grating coupler [30]. Commercial deployment is tending to move from the right to left of this figure.

An element that is partway between an active and passive element is an optical isolator. Optical isolators are required to stop back reflections from causing noise and oscillations in lasers and optical amplifiers. An isolator requires a non-reciprocal element [31]. In silicon photonics, two main types of isolators have been reported: magneto-optic and modulation-based. In magneto-optic isolators, garnets are placed on the side or top of the waveguide [32, 33]. In a modulation-based isolator, the optical field is modulated with either a traveling wave or a time delay between multiple modulators [34]. **Figure 12** shows a modulation-based isolator design based on a parallel arrangement of phase modulators in series [35]. Each modulator is driven by a sine wave. In the forward direction, the second modulator in each arm undoes the modulation of the first modulator; but in the backward direction, the two modulators add constructively. Thus, there is no effect at all on the signal in the forward direction but in the backward direction it is strongly phase modulated. If the phase modulation amplitude is just right, then a continuous-wave signal passing backwards is completely attenuated at its original frequency. This gives narrow-band isolation. By having multiple such narrow-band isolators in parallel, driven by the same frequency but appropriate different RF drive phases in each arm, one can achieve broadband isolation. A two-arm version was demonstrated in silicon photonics, achieving ~3 dB of isolation. The modulation was done by carrier injection in the silicon waveguide. The isolation can be improved by reducing the residual amplitude modulation in the phase modulators, by increasing the speed of the modulators, and/or by increasing the number of arms in the interferometer.

5. PIC Material System Comparison

Table 2 shows a comparison between InP and Si. InP is a much more expensive material than Si because of the rarity of In. Si circuits tend to have a higher yield than InP circuits because there is much less epitaxy involved in Si circuits. In Si circuits, usually the only epitaxy is Ge, used in the photodetectors, whereas in InP all of the waveguides, even the passive ones, must be grown by epitaxy. Epitaxy tends to have a higher defect density than crystal growth from a boule. InP waveguides have high index contrast only laterally, whereas Si waveguides have high index contrast laterally and vertically. This allows much smaller bend radii and other more compact structures in Si. InGaAsP has a direct bandgap, whereas Si and Ge do not. Thus, the InP material system has a much more efficient laser. The native oxide of the InP system is much less robust than the native oxide of Si, which is SiO_2. Silicon is a stronger material than InP, allowing for much larger wafers, 75 mm compared to 300 mm (going to 450 mm soon). InP modulators usually depend on the quantum-confined Stark effect, which is temperature sensitive because of the band edge movement with temperature. Silicon modulators have very minimal temperature dependence.

Silicon photonics is usually considered only for low-cost, short-reach, high-volume (>1M/year) products. This is because it is assumed that a large number of wafer starts is required to pay for mask and development costs and that silicon photonics has a significant performance penalty for metro and long-haul products. However, the real situation is actually the opposite. This is because in low-cost, short-reach, high-volume applications, there is tremendous competition from vertical cavity surface-emitting lasers (VCSELs) and directly modulated lasers (DMLs), and silicon photonics' weakness of not having an easy way to integrate lasers is a significant disadvantage. On the other hand, in metro and long-haul applications, it is better to keep the laser separate anyway as it is preferable to integrate the silicon photonics and DSP together, which is a hot environment. Also, coherent detection can make up for many

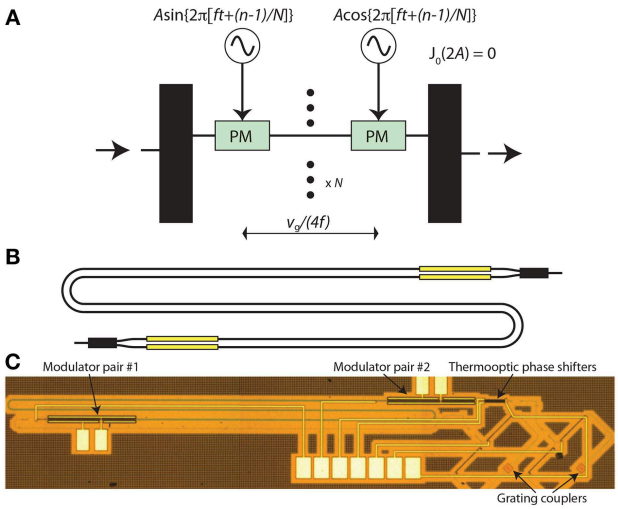

FIGURE 12 | (A) configuration of an optical isolator that uses a tandem arrangement of phase shifters. There are *N* arms in the interferometer. The more the arms, the higher the broadband isolation. **(B,C)** 2-arm version built in silicon photonics.

TABLE 2 | Pros and cons of InP and Si for photonic integrated circuits.

InP	Si
Expensive material	Cheap material
• In is scarce	• 27% mass Earth's crust is Si
Medium yield	High yield
• W.g. material from epitaxy	• W.g. material from original boule
Small footprint	Extremely small footprint
• High index contrast in 1D	• High index contrast in 2D
Native laser	No native laser
Poor native oxide	Excellent native oxide
Low dark current	Medium dark current
Small wafers (75 mm typ.)	Large wafers (300 mm typ.)
• 75 mm typical	• 300 mm typical
• Brittle material	• Strong material
Modulator temperature sensitive	Modulator temperature insensitive
• Band edge moves with temperature	• Carrier density not v. temp. dep.

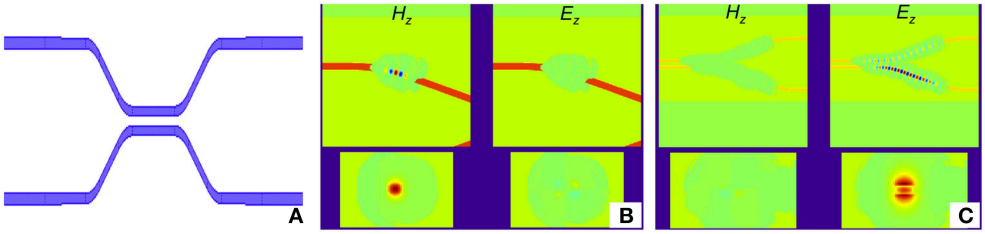

FIGURE 13 | Simulation results from 3D sparse FDTD. (A) is the top view of the structure being simulated, which is a directional coupler. **(B)** Shows a screen shot from a simulation using a quasi-TE launch. The top two figures show the top views of the quasi-TE and quasi-TM signals, and the lower two figures show the corresponding cross-section views. **(C)** Shows a screen shot from a simulation using a quasi-TM launch.

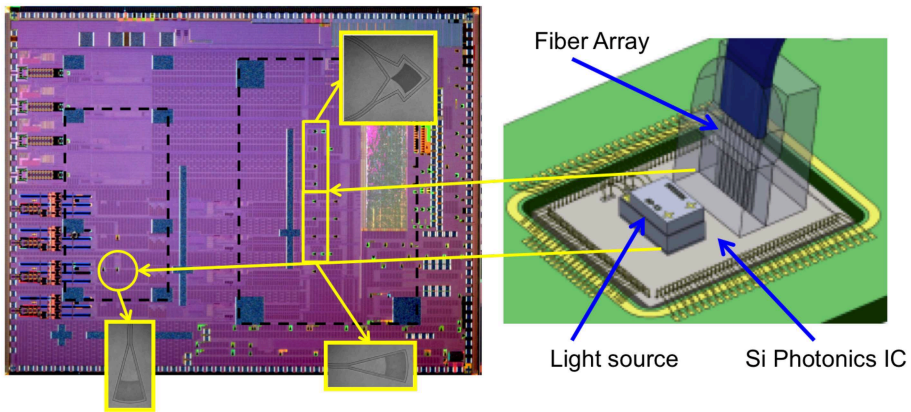

FIGURE 14 | Silicon photonics 8-PSM transceiver. Courtesy of Luxtera.

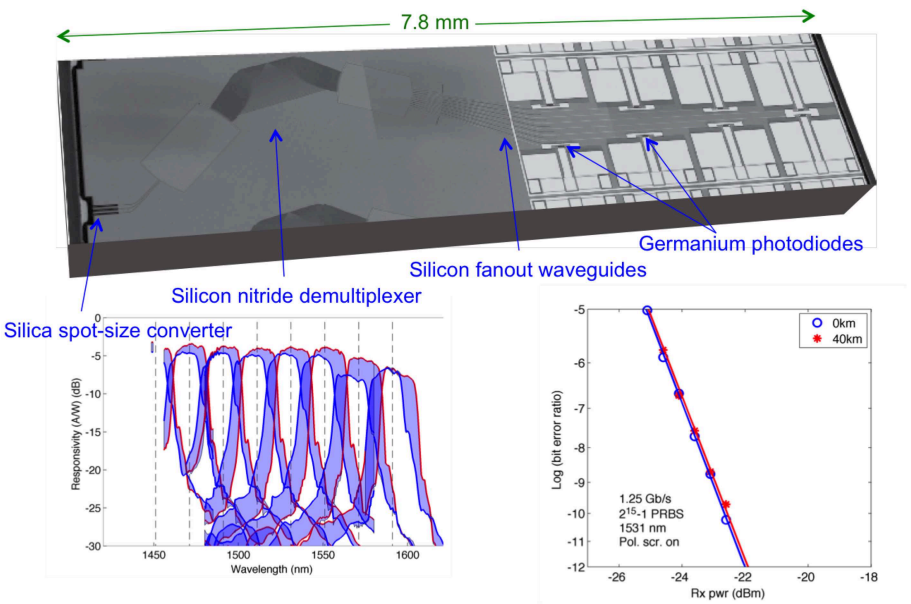

FIGURE 15 | Silicon photonics 8-WDM receiver. The upper figure shows a photograph of the chip, the lower left figure shows the measured responsivities to the 8 detectors vs. wavelength, and the lower right figure shows the measured bit-error rate at 1.25 Gb/s for one of the channels using a polarization scrambler.

of silicon photonics' imperfections, such as the dark current is much smaller than the local oscillator photocurrent. Also, the argument that one needs a large number of wafer starts to pay for mask and development costs is fallacious, because silicon photonics is done in a very large node size compared to state-of-the-art CMOS, and thus the masks and runs are relatively inexpensive.

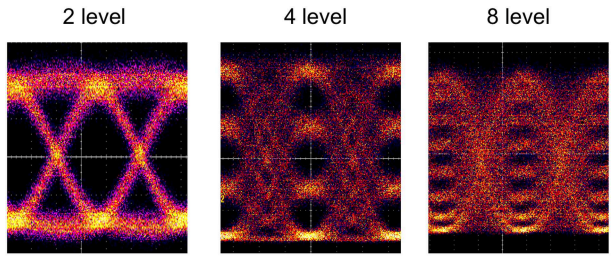

FIGURE 16 | Measured PAM-2, -4, and -8 optical eye diagrams at 28 Gbaud using a silicon photonics modulator.

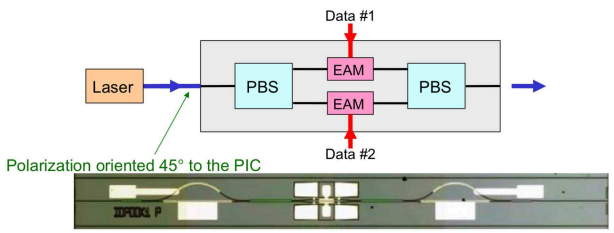

FIGURE 17 | 80-Gb/s dual-polarization transmitter in InP. It consists of two electro-absorption InGaAsP modulators, a polarization splitter, and a polarization combiner. The incoming laser has its polarization oriented at 45°.

6. PIC Design

PICs are usually laid out in using mathematical scripts. This is because usually in PICs, path lengths matter, when in interferometers or because of skew. The PIC is made by patterning multiple layers, typically 10 to 30, on a wafer. These layers consist of many polygon shapes, typically in a GDSII format. Before sending the files to the photomask shop, there is a strong desire to be able to simulate the PIC to verify the design. There are multiple levels of simulation. The lowest level is 3D electromagnetic (EM) simulation, in which simulation is done at the sub-wavelength level. Interaction with atoms in the materials is done on the macroscopic scale. Typical methods are the 3D finite-difference time domain (3D FDTD) [36] and eigenmode expansion (EME) methods [37]. These methods are the most accurate but simulation times for an entire PIC are prohibitive. The next level is 2.5D EM simulation, such as the finite-difference beam propagation method (FD-BPM). These methods are significantly faster, with a tradeoff of accuracy. Also, BPMs can handle only paraxial propagation, e.g., they cannot be used to simulate a resonator. The next level is 2D EM simulation, such as 2D FDTD and 2D BPM. Again, these are faster, but limited. These cannot simulate e.g., a polarization rotator. The next level up is transmission and/or scattering matrix simulation. Each main component is reduced to an element with inputs and outputs, and connecting waveguides are reduced to phase shift and attenuation elements. These simulations are extremely fast. A transmission matrix is

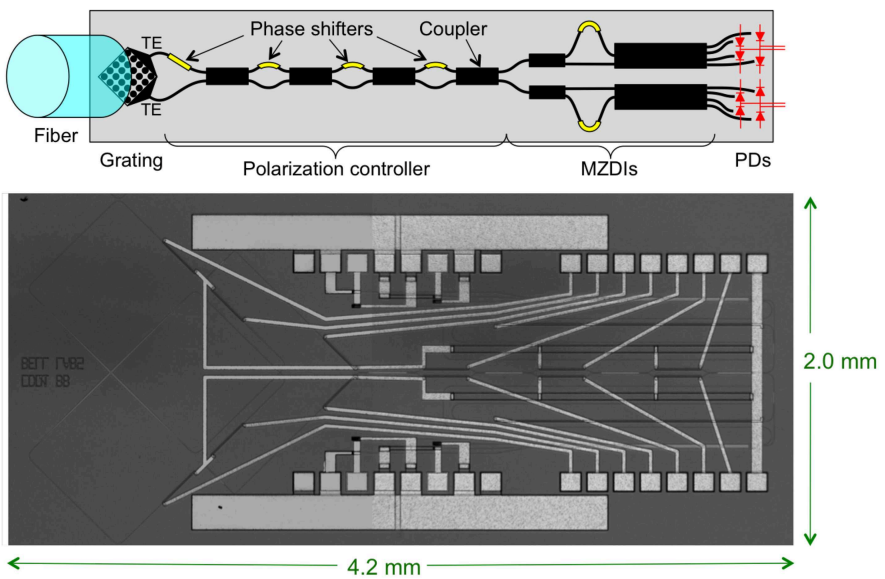

FIGURE 18 | DP-DQPSK receiver in silicon photonics. Uses optical polarization tracking. The upper figure shows a schematic, and the lower figure a device photograph. The incoming signal is separated into two polarizations by a 2D grating coupler, a series of couplers and phase shifters demultiplex the two signals, which had been mixed during fiber transmission, and two Mach-Zehnder delay interferometers demodulate the signals.

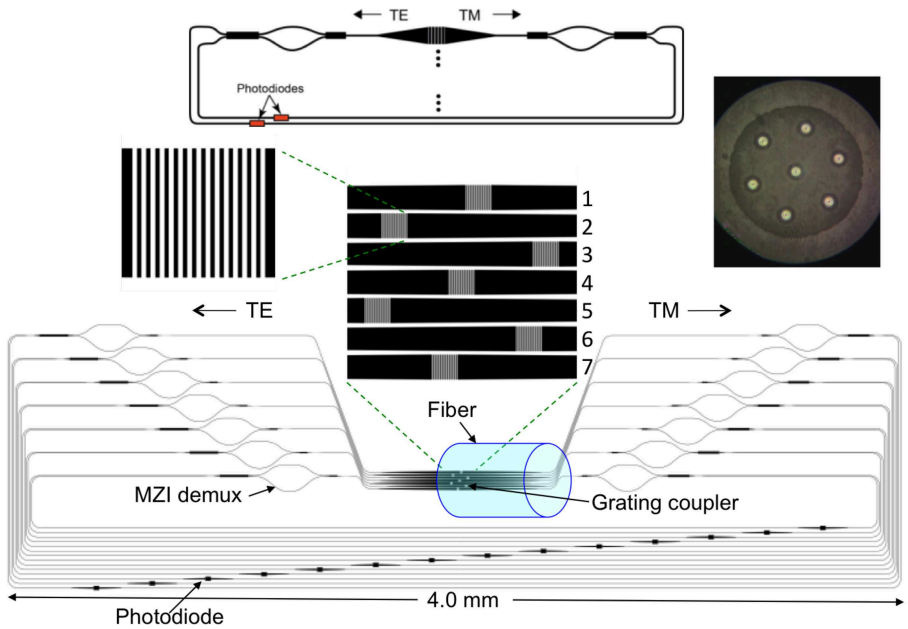

FIGURE 19 | 7-core-fiber silicon photonics receiver. The upper right figure shows a photograph of the fiber cross section, showing the seven cores. The top shows the schematic for each channel in the silicon photonic circuit shown in the bottom figure. The incoming fiber is tilted at the proper angle to the 1D grating couplers such that TE polarization couples to the left and TM polarization couples to the right.

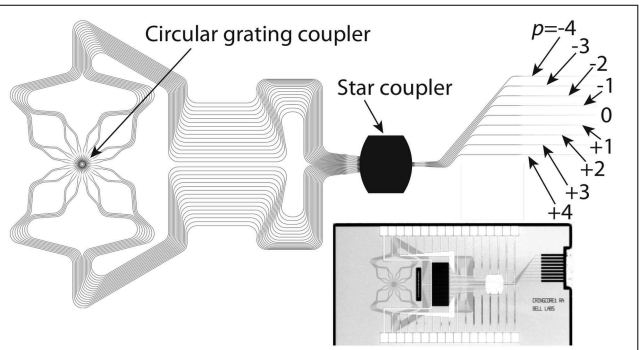

FIGURE 20 | PIC for coupling to the multimodes of a ring-core fiber by using a circular grating coupler connected to a star coupler. The upper figure shows a schematic of the silicon photonic circuit photograph shown at the bottom. The circuit contains a circular grating coupler connected to an array of waveguides of equal length.

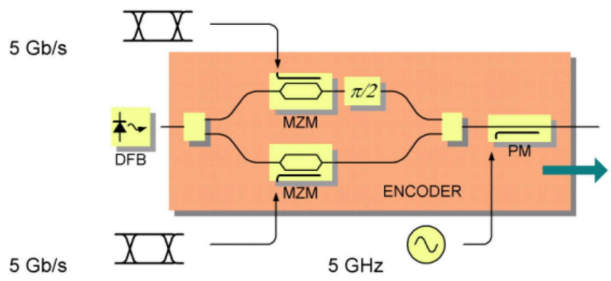

FIGURE 21 | First reported vector modulator. It was in GaAs.

multiplied by the incoming signals to find the outgoing signals. A scattering matrix (whose elements are called s-parameters) is multiplied by the incoming and outgoing signals on one side of the element to find the incoming and outgoing signals on the other side of the element. Basically, scattering matrices include reflections within the element. Scattering matrices are typically twice as large in each dimension as transmission matrices.

However, relying on EM simulation of some elements and scattering/transmission matrices to simulate the entire PIC does not guarantee that the design is error-free before tape out. For example, a miscalculated path length, a multimode waveguide without sufficient high-order mode rejection, or two waveguides that pass too close to each other and have undesired coupling are unlikely to be caught.

A technique called sparse FDTD allows one to do 3D and 2D FDTD simulation directly on the entire PIC design to verify the design [38]. While it is unlikely any EM simulation tool can simulate a very large PIC, sparse FDTD can simulate quite large portions. In conventional 3D FDTD, one starts with all six components of the EM fields in a specified quantized volume. Time is advanced a step, and the new field components are calculated in the volume, and so on. So many calculations every step takes a very long time. In sparse 3D FDTD, rather than do calculations for every point in the volume every step, a list of field components is maintained, theoretically in an arbitrarily large volume, is maintained and calculations are done on these. At each time step points neighboring the field components are

added, and field components with power below a certain level are discarded. For certain structures this calculation can be orders of magnitude faster than conventional 3D FDTD. However, sparse FDTD performs poorly with dispersive structures, because then the optical field spreads out too much, making the list too long. Example screen shots from 3D FDTD simulation of a PBS like that shown in **Figure 9B** are shown in **Figure 13** [39].

7. Short Reach PICs

Short reach communications typically means less than 2 km, but can sometimes include up to 40 km. Short reach is usually for intra-data center, connecting racks, or client-side optics. There is an emerging need for very short reach communications in which boards are connected optically within a rack. Such optics are no longer considered "transceivers" and for the sake of focus are left out of this article.

Because of the fast growth and turn-over in data centers there is usually insufficient time for standards to develop. This allows for a wide diversity of solutions. These various solutions do not interoperate, but the users do not care so much, as long as prices are low.

Today, most of the short reach links are based on vertical-cavity surface-emitting lasers (VCSELs) over multimode fiber, i.e., do not involve PICs at all. VCSELs are very inexpensive and easy to couple to multimode fiber. It is nearly impossible for PICs to compete against VCSELs on price. However, the bandwidth-distance product for a VCSEL over multimode fiber is ∼ 2 GHz-km. At 25 Gb/s, this limits distances to ∼100 m. Also, multimode fiber (MMF) costs more than standard single-mode fiber (SSMF), because many more km of SSMF have been produced than MMF. Thus, when new data centers are built, it can be advantageous to outfit them with SSMF. Single-mode VCSELs are difficult to make today, so this is a good opportunity for PICs. However, VCSEL technology is constantly improving, providing a constant challenge to PICs in short-reach applications.

A successful PIC short-reach commercial solution today is based on parallel single-mode fibers (PSM). **Figure 14** shows an

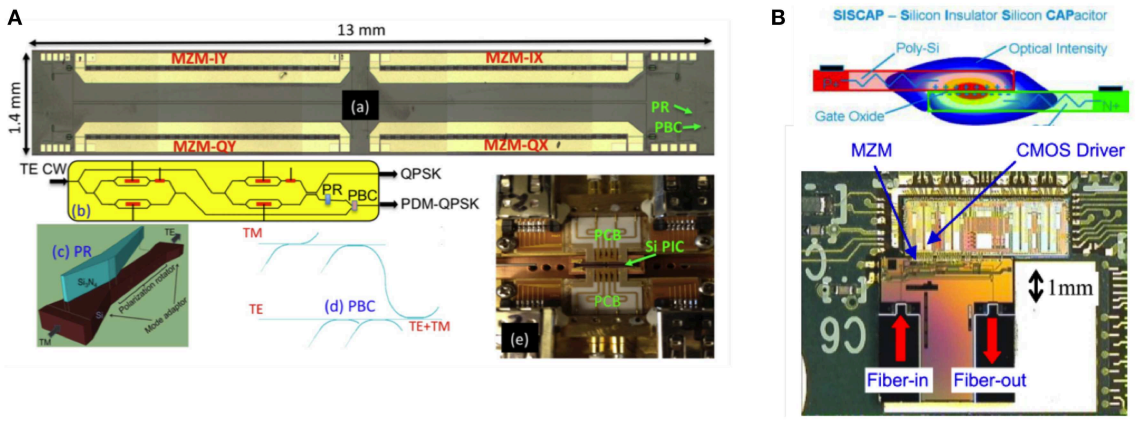

FIGURE 22 | Early reported silicon photonic vector modulators.

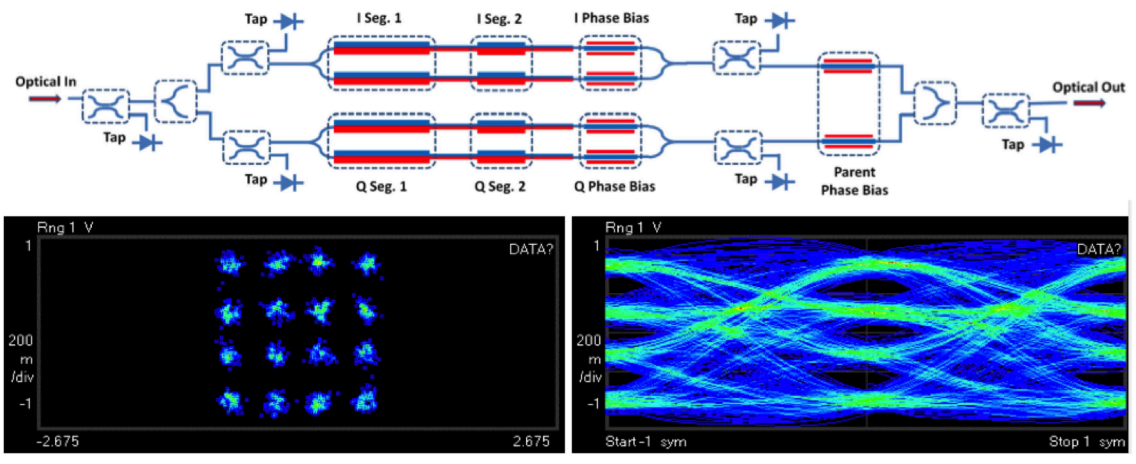

FIGURE 23 | 2-bit optical DAC in silicon photonics.

8-fiber PSM solution (4 fibers out and 4 fibers in) based on silicon photonics from Luxtera [40]. The chip contains a 1.4-μm laser in a small hermetic assembly on top of the PIC. This wavelength was chosen as optimum for the grating couplers that couple the laser light into the PIC. This laser is split four ways to four 10-Gb/s on-off-keying (OOK) distributed-driven Mach-Zehnder-interferometer modulators (MZMs). The CMOS drive electronics are monolithically integrated with the photonics. Distributed driven means that the modulator is broken into N sections in series, each with a separate driver timed appropriately. This saves power consumption over a traveling-wave modulator, because a traveling-wave modulator has a termination resistor into which power must be dumped.

Another successful PIC short-reach solution is based on wavelength-division multiplexing (WDM). Typically four wavelengths, each modulated with OOK at 25 Gb/s, are multiplexed in the transmitter and demultiplexed at the receiver. The advantage over PSM is requiring only two fibers instead of eight, and the disadvantage is requiring four lasers instead of one. WDM makes more sense as the cost of transceivers drops compared to the cost of fiber and installing it, especially ribbon fibers. **Figure 15** shows an 8-channel CWDM receiver in silicon photonics [41]. It uses a silicon nitride spot-size converter and arrayed waveguide grating (AWG), which is polarization independent via variation of waveguide widths, silicon output multimode waveguides, and Ge photodetectors.

Yet another solution is to use multi-level modulation, called pulse amplitude modulation (PAM). **Figure 16** shows PAM4 and PAM8 eye diagrams at 28 Gb/s generated by a silicon photonics MZM.

One can also use polarization-division multiplexing (PDM), also called dual-polarization (DP) transmission. In this case, different signals are in each polarization. **Figure 17** shows a dual-polarization 80-Gb/s modulator in InP [42]. Such a design

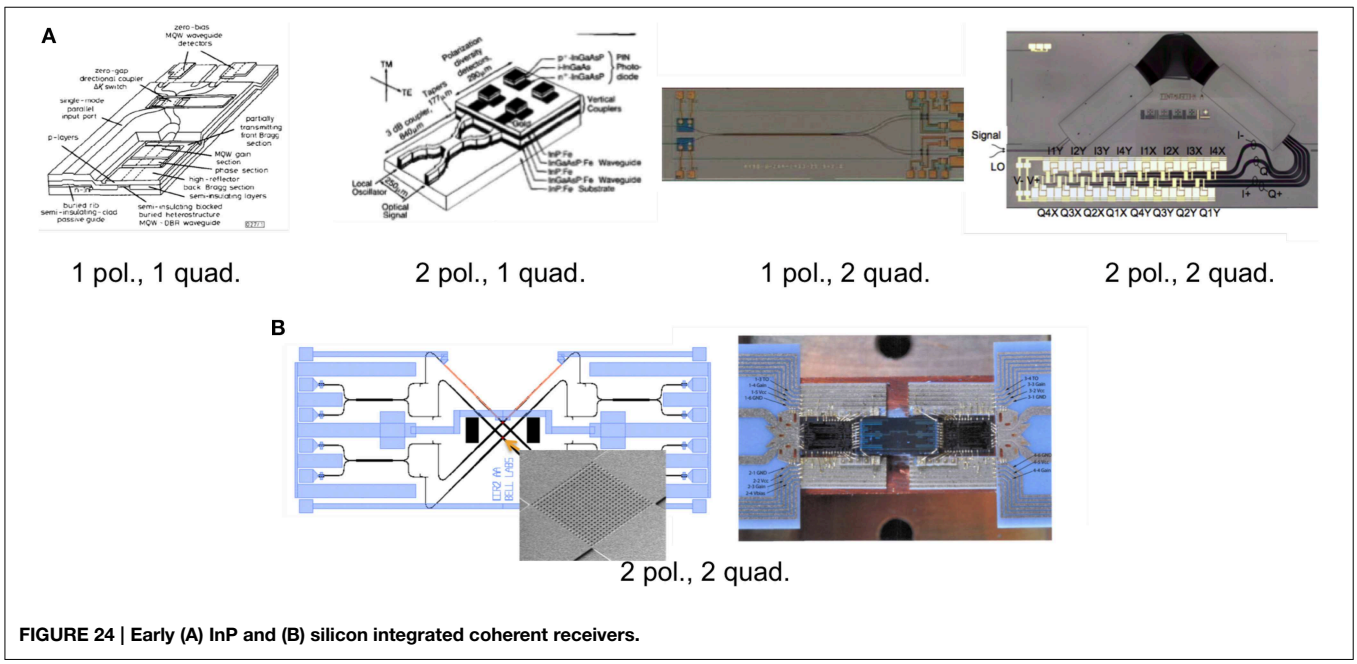

FIGURE 24 | Early (A) InP and (B) silicon integrated coherent receivers.

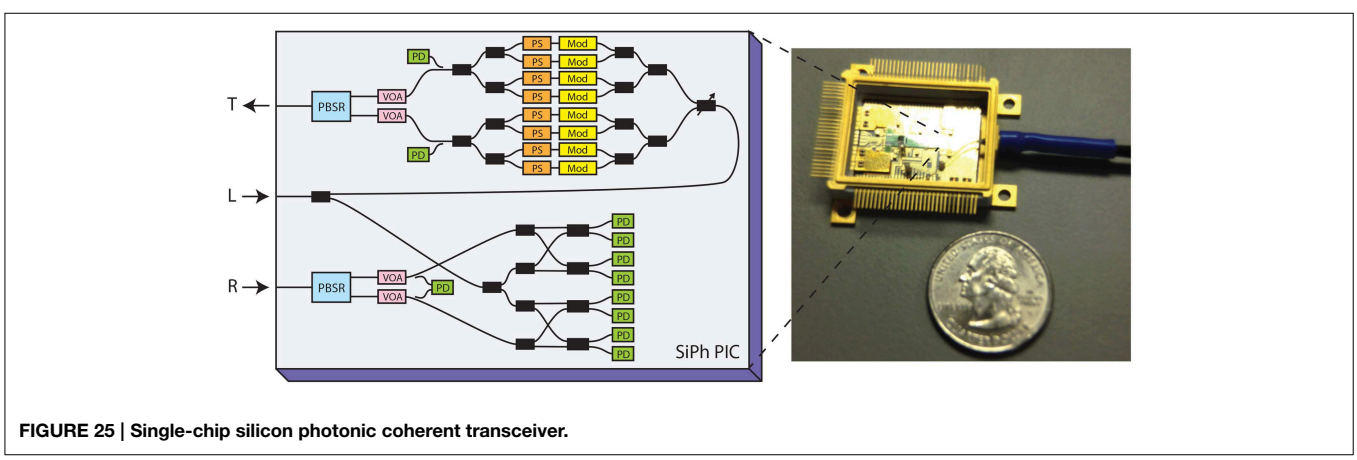

FIGURE 25 | Single-chip silicon photonic coherent transceiver.

could be readily made in silicon photonics. In the fiber, the two signals will stay predominantly orthogonally polarized, but the polarization will vary unpredictably with time. At the receiver, if one does not use coherent detection, one needs to optically demultiplex the two polarizations. **Figure 18** shows a device in silicon photonics that can optically demultiplex polarization [43, 44]. It does this by receiving two orthogonal polarizations from the fiber, these polarizations not necessarily that of the signals, and then interferes the two with a controllable phase and coupling ratio to demultiplex them. To do this in an endless fashion, i.e., without ever needing phase-shifter resets back to zero, one needs multiple interferometer stages.

In the far future one may find the data center interconnections so crowded that one must reduce the number of fiber strands and instead put multiple cores and/or modes in a single fiber. **Figure 19** shows a PIC for receiving from a 7-core fiber, using polarization diversity [45]. It includes optical filters for WDM. **Figure 20** shows a PIC for receiving from a multi-mode ring-core fiber [46]. A multi-mode ring core fiber is advantageous because the modes can be accessed without waveguide crossings and conveniently demultiplexed by a star coupler.

8. Metro and Long-reach PICs

Unlike short-reach links, which we saw have many choices of transmission type, metro and long-reach links demand intradyne coherent transmission. This is because long fiber routes are expensive to install/obtain, and thus the user wants to push as much information over each fiber as possible. Coherent receivers make it possible to receive WDM, PDM, and high-order constellations with high-performance, because the complete optical field is received and acted on by a DSP. In intradyne coherent communications, the transmitted signal comes from a dual-polarization vector modulator, and the received signal is interfered with a continuous-wave (CW) laser signal whose frequency is close to the carrier of the signal (within ∼2–3 GHz), but does not need to be exact.

The first reported vector modulator was a GaAs PIC, shown in **Figure 21** [47]. It consists of two MZMs in a larger interferometer. **Figure 22** show some early vector modulators in silicon photonics. The modulator in **Figure 22A** contains two vector modulators, one for each polarization, along with the polarization splitting optics [48]. The single-polarization modulator in **Figure 22B** uses a thin-oxide layer in the p-n junction to obtain a low $V_\pi L$ product and is driven directly by CMOS inverters [49]. By using multiple segments in the modulator, one can create an optical digital-to-analog converter (DAC). The segment lengths are in a geometric sequence. **Figure 23** shows a demonstration that achieved 16-QAM modulation at 13 Gbaud using a silicon photonic optical DAC [50].

The first reported coherent receivers were in InP, as shown in **Figure 24A** [51–55]. **Figure 24B** shows an early

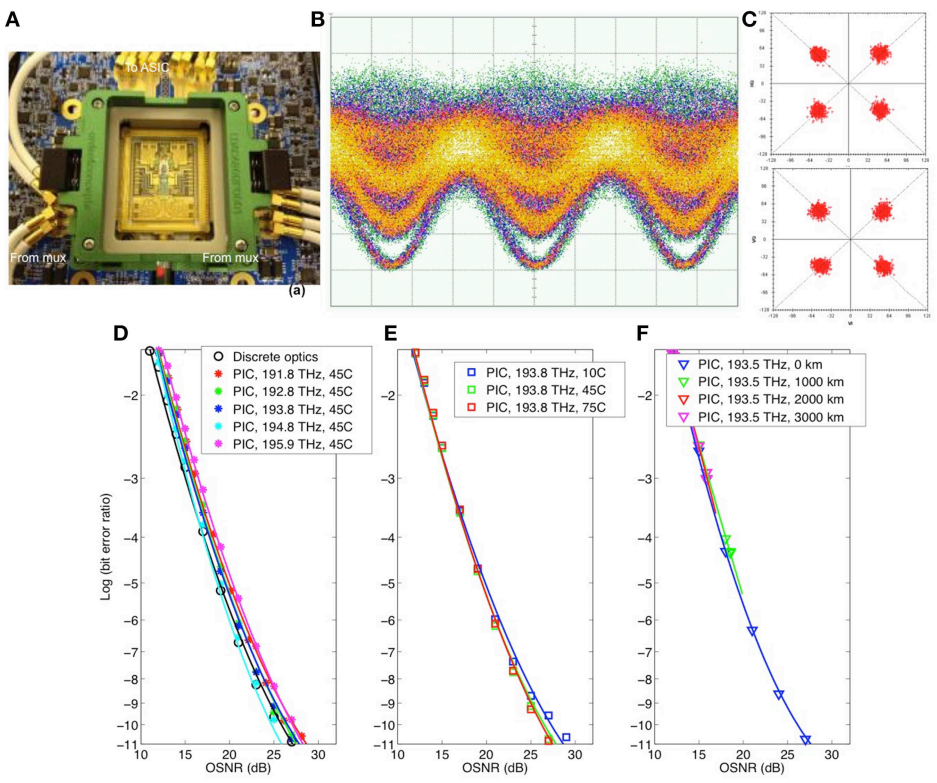

FIGURE 26 | (A) Measurement setup, **(B)** measured 30-Gbaud eye diagram for DP-QPSK, **(C)** real-time-processed constellations at 120 Gb/s, and **(D–F)** bit-error rate vs. OSNR for various cases for the silicon photonics single-chip coherent transceiver in an optical loop back configuration.

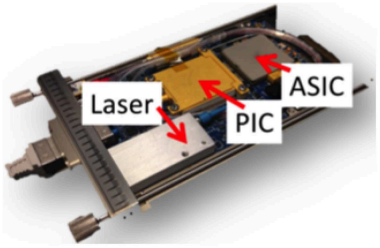

FIGURE 27 | 100-Gb/s coherent CFP module using silicon photonics.

dual-polarization, dual-quadrature receiver in silicon photonics [56]. It uses a 2-D grating coupler as a fiber coupler, polarization splitter, and polarization rotator.

Figure 25 shows a recent silicon photonic PIC that contains the full vector modulator and full coherent receiver on a single chip [4]. This is lower cost and smaller footprint than separate transmitter and receiver chips. There are three fibers connected to the module: laser input, which is split between transmitter and receiver; transmitter output; and receiver input. The fibers are connected in a 3-fiber array, reducing cost and assembly time. It is co-packaged in a hermetic gold box with four drivers and four transimpedance amplifiers. It does not require any temperature control, allowing the total power consumption to be less than 5 W, −5 to 80°C. A silicon photonics modulator does have some imperfections compared to Pockels-effect modulators, like GaAs and $LiNbO_3$. It has residual amplitude modulation, diode nonlinearity, capacitance change with voltage, and bandwidth limitations. A simulation including these effects shows that the imperfection performance penalty is only 0.1 dB compared to an ideal modulator.

Each PIC was tested in a socket in an optical loop-back configuration using a 100-Gb/s DSP for real-time measurements, as shown in **Figure 26A**. Optical loop-back insures that any potential crosstalk between the transmitter and receiver would show up as degradation. **Figure 26B** shows a measured 30-Gbaud DP-QPSK eye diagram. There are five levels in such a signal. **Figure 26C** shows measured real-time-processed 120-Gb/s DP-QPSK constellations. Measured BER vs. OSNR curves at multiple wavelengths across the C-band are shown in **Figure 26D** shown for comparison is the performance of discrete optics. The performance of the silicon PIC is nearly the same as the discrete optics. **Figure 26E** shows the performance at various temperatures, showing that the silicon photonics can indeed work without temperature control. **Figure 26F** shows the performance up to 3000 km without significant penalty. This shows that the chirp of the silicon photonics modulator is low.

Figure 27 shows this PIC in a 100-Gb/s CFP module. As one can see, the module is tightly packed and would be very difficult to make with discrete optics.

This single-chip coherent transceiver contains all the optics needed for a coherent transmitter except the tunable laser. As mentioned earlier, it is probably better to keep the laser separate anyways because this chip can be co-packaged with the DSP, which runs very hot.

9. Conclusion

The touted advantage of silicon photonics is the die are lower cost than any other solution. While this may be true, it is of limited help in short-reach applications, where the lack of an integrated laser puts silicon photonics at a significant disadvantage compared to the incumbents, such as VCSELs and DMLs. Instead, the less-touted advantages of silicon photonics: high yield, low modulator temperature sensitivity, high chip strength, and ability to do polarization handling; make it ideal for metro and long-haul applications. Spending its adolescence in metro and long-haul, silicon photonics will have time to develop mature laser integration methods, more routine foundry services, and sophisticated packaging solutions so it can later take on the short-reach incumbents. By that time, coherent transmission may be cost- and power-effective enough to work in very short links, bringing its advantages of high sensitivity, high spectral efficiency, high-order modulation, and wavelength selection.

Acknowledgments

The author is indebted to Long Chen, Diedrik Vermeulen, Torben Nielsen, Scott Stulz, Saeid Azemati, Greg McBrien, Benny Mikkelsen, Christian Rasmussen, Mehrdad Givehchi, Seo Yeon Park, Jonas Geyer, Xiao-Ming Xu, and many others.

References

1. Winzer P. Advanced optical modulation formats. *Proc IEEE* (2006) **94**:952–85. doi: 10.1109/jproc.2006.873438
2. Wellbrock G. Where do we go from here? In: *OIDA Workshop on State of the Art Integrated Photonics.* Washington, DC (2014).
3. Wikipedia. *Semiconductor Device Fabrication* (2008).
4. Doerr CR, Chen L, Vermeulen D, Nielsen T, Azemati S, Stulz S, et al. Single-chip silicon photonics 100-Gb/s coherent transceiver. In: *Optical Fiber Communication Conference: Postdeadline Papers.* San Jose, CA (2014).
5. Taillaert D, Van Laere F, Ayre M, Bogaerts W, Van Thourhout D, Bienstman P, et al. Grating couplers for coupling between optical fibers and nanophotonic waveguides. *Jpn J Appl Phys.* (2006) **45**:6071–7. doi: 10.1143/JJAP.45.6071
6. Mekis A, Gloeckner S, Masini G, Narasimha A, Pinguet T. A grating-coupler-enabled CMOS photonics plaform. *J Sel Topics Quant Electron* (2011) **17**:597–608.
7. Chen L, Zhang L, Doerr CR, Dupuis N, Weimann NG, Kopf RF. Efficient membrane grating couplers on InP. *IEEE Photon Tech Lett.* (2010) **22**:890–2. doi: 10.1109/LPT.2010.2047391
8. Shoji T, Tsuchizawa T, Watanabe T, Yamada K, Morita H. Low loss mode size converter from 0.3 um square Si wire waveguides to singlemode fibres. *Electron Lett.* (2002) **38**:1669. doi: 10.1049/el:20021185
9. Chen L, Doerr CR, Chen YK, Liow TY. Low-loss and broadband cantilever couplers between standard cleaved fibers and high-index-contrast SiN or Si waveguides. *IEEE Photon Tech Lett.* (2010) **22**:1744–6. doi: 10.1109/LPT.2010.2085040

10. Yamazaki H, Yamada T, Goh T, Kaneko A, Sano A. Integrated 100-Gb/s PDM-QPSK modulator using a hybrid assembly technique with silica-based PLCs and LiNbO3 phase modulators. In: *European Conference and Exposition on Optical Communications* Brussels: IEEE (2008). 1–4. doi: 10.1109/ECOC.2008.4729119
11. Fukuda H, Yamada K, Tsuchizawa T, Watanabe T, Shinojima H, Itabashi SI. Silicon photonic circuit with polarization diversity. *Opt Express* (2008) **16**:4872–80. doi: 10.1364/OE.16.004872
12. Tang Y, Dai D, He S. Proposal for a grating waveguide serving as both a polarization splitter and an efficient coupler for silicon-on-insulator nanophotonic circuits. *IEEE Photonics Technol Lett.* (2009) **21**:242–4. doi: 10.1109/LPT.2008.2010528
13. Taillert D, Chong H, Borel PI, Frandsen LH, Rue RMDL, Baets R. A compact two-dimensional grating coupler used as a polarization splitter. *IEEE Photonics Technol Lett.* (2003) **15**:1249–51. doi: 10.1109/LPT.2003.816671
14. Soref R, Bennett B. Electrooptical effects in silicon. *IEEE J Quantum Electron.* (1987) **23**:123–9. doi: 10.1109/JQE.1987.1073206
15. Zheng D, Smith B. Improved efficiency Si-photonic attenuator. *Opt Express* (2008) **16**:16754–65. doi: 10.1364/OE.16.016754
16. Dong P, Chen L. Monolithically integrated VOA-MUX with power monitors based on submicron silicon photonics platform. *Opt Fiber Commun* Los Angeles, CA: IEEE (2012) 9–11. doi: 10.1364/ofc.2012.otu2i.5
17. Thomson DJ, Gardes FY, Fedeli JM, Zlatanovic S, Hu Y, Ping B, et al. 50-Gb/s silicon optical modulator. *IEEE Photonics Technol Lett.* (2012) **24**:234–6. doi: 10.1109/LPT.2011.2177081
18. Liu A, Jones R, Liao L, Samara-Rubio D, Rubin D. A high-speed silicon optical modulator based on a metal âĂŞ oxide âĂŞ semiconductor capacitor. *Nature* (2004) **427**:615–8. doi: 10.1038/nature02310
19. Liu J, Beals M, Pomerene A, Bernardis S, Sun R, Cheng J, et al. Waveguide-integrated, ultralow-energy GeSi electro-absorption modulators. *Nat Photonics* (2008) **2**:433–7. doi: 10.1038/nphoton.2008.99
20. Liu M, Yin X, Ulin-Avila E, Geng B, Zentgraf T, Ju L, et al. A graphene-based broadband optical modulator. *Nature* (2011) **474**:64–7. doi: 10.1038/nature10067
21. Ahn D, Hong Cy, Liu J, Giziewicz W, Beals M, Kimerling LC, et al. High performance, waveguide integrated Ge photodetectors. *Opt Express* (2007) **15**:3916–21. doi: 10.1364/OE.15.003916
22. Assefa S, Xia F, Bedell S, Zhang Y. CMOS-integrated 40GHz germanium waveguide photodetector for on-chip optical interconnects. In: *Optical Fiber Communication Conference* (2009). p. 10–2. Available online at: http://www.opticsinfobase.org/abstract.cfm?id=177916
23. Kang Y, Liu H, Morse M, Paniccia M. Monolithic germanium / silicon avalanche photodiodes with 340 GHz gain-bandwidth product. *Nat Photonics* (2008) **3**:59–63. doi: 10.1038/nphoton.2008.247
24. Michel J, Camacho-aguilera RE, Cai Y, Patel N, Bessette JT, Dutt BR, et al. An electrically pumped Ge-on-Si laser. In: *Optical Fiber Communication Conference*. Los Angeles, CA: IEEE (2012). p. 5–7.
25. Purnawirman, Sun J, Adam TN, Leake G, Coolbaugh D, Bradley JDB, et al. C-and L-band erbium-doped waveguide lasers with wafer-scale silicon nitride cavities. *Opt Lett.* (2013) **38**:2–5. doi: 10.1364/OL.38.001760
26. Liu AY, Zhang C, Norman J, Snyder A, Lubyshev D, Fastenau JM, et al. High performance continuous wave 1.3 μ m quantum dot lasers on silicon. *Appl Phys Lett.* (2014) **104**:3–7. doi: 10.1063/1.4863223
27. Fang A, Park H, Cohen O, Jones R, Paniccia M. Electrically pumped hybrid AlGaInAs-silicon evanescent laser. *Opt Express* (2006) **14**:9203–10. doi: 10.1364/OE.14.009203
28. Roelkens G, Brouckaert J, Van Thourhout D, Baets R, NoĬĹtzel R, Smit M. Adhesive bonding of InPâĹŢInGaAsP dies to processed silicon-on-insulator wafers using DVS-bis-benzocyclobutene. *J. Electrochem Soc.* (2006) **153**:G1015. doi: 10.1149/1.2352045
29. Marchena E, Creazzo T, Krasulick SB, Yu PKL, Van Orden D, Spann JY, et al. Integrated tunable CMOS laser. In: *Optical Fiber Communication Conference* (2013). Available online at: http://www.opticsinfobase.org/abstract.cfm?URI=oe-21-23-28048
30. Snyder B, Corbett B, O'Brien P. Hybrid integration of the wavelength-tunable laser with a silicon photonic integrated circuit. *J Lightwave Technol.* (2013) **31**:3934–42. doi: 10.1109/JLT.2013.2276740
31. Jalas D, Petrov A, Eich M, Freude W, Fan S, Yu Z, et al. What is and what is not an optical isolator. *Nat Photonics* (2013) **7**:579–82.
32. Levy M, Osgood RMJr, Hegde H, Cadieu FJ, Wolfe R, Fratello VJ. Integrated optical isolators with sputter-deposited thin-film magnets. *IEEE Photonics Technol Lett.* (1996) **8**:903–5. doi: 10.1109/68.502265
33. Shoji Y, Mizumoto T, Yokoi H, Hseih IW, Osgood R. Magneto-optical isolator with silicon waveguides fabricated by direct bonding. *Appl Phys Lett.* (2008) **92**:071117. doi: 10.1063/1.2884855
34. Bhandare S, Ibrahim SK, Sandel D, Zhang H, Wust F, Noe R. Novel nonmagnetic 30-dB traveling-wave single-sideband optical isolator integrated in III/V material. *IEEE J Sel Top Quantum Electron.* (2005) **11**:417–21. doi: 10.1109/JSTQE.2005.845620
35. Doerr CR, Chen L, Vermeulen D. Silicon photonics broadband modulation-based isolator. *Opt Express* (2014) **22**:4493. doi: 10.1364/OE.22.004493
36. Yee KS. Numerical solution of initial boundary value problems involving Maxwell's equations in isotropic media. *Antennas Propagation IEEE Trans* Livermore, CA: IEEE (1966). 302–7. doi: 10.1109/TAP.1966.1138693
37. Bienstman P, Baets R. Optical modelling of photonic crystals and VCSELs using eigenmode expansion and perfectly matched layers. *Opt Quantum Electron.* (2001) **33**:327–41. doi: 10.1023/A:1010882531238
38. Doerr CR. Sparse finite difference time domain method. *IEEE Photonics Technol Lett.* (2013) **25**:2259–62. doi: 10.1109/LPT.2013.2285181
39. Doerr CR. 3D sparse finite-difference time-domain simulation of silicon photonic integrated circuits. In: *Optical Fiber Communication Conference*. Los Angeles, CA (2015).
40. Narasimha A, Analui B, Liang Y, Member S, Sleboda TJ, Abdalla S, et al. A fully integrated 4 x 10-Gb / s DWDM optoelectronic transceiver implemented in a standard 1.3 um CMOS SOI technology. *IEEE J Solid State Circ.* (2007) **42**:2736–44. doi: 10.1109/JSSC.2007.908713
41. Doerr CR, Chen L, Buhl LL, Chen YK. Eight-channel SiO_2/Si_3N_4/Si/Ge CWDM receiver. *IEEE Photonics Technol Lett.* (2011) **23**:1201–03. doi: 10.1109/LPT.2011.2158091
42. Doerr CR, Zhang L. Monolithic 80-Gb / s dual-polarization On-off-keying modulator in InP. *J Lightwave Technol.* (2008) **2**:19–21.
43. Doerr CR, Chen L. Monolithic PDM-DQPSK receiver in silicon. In: *Optical Communication (ECOC), 2010 36th European Conference and Exhibition on* (IEEE) (2010). p. 1–3. Available online at: http://ieeexplore.ieee.org/xpls/abs_all.jsp?arnumber=5621418
44. Doerr CR, Fontaine NK, Buhl LL. PDM DQPSK silicon receiver with integrated monitor and minimum number of controls. *IEEE Photonics Technol Lett.* (2012) **24**:697–9. doi: 10.1109/LPT.2012.2187048
45. Doerr CR, Taunay TF. Silicon photonics core-, wavelength-, and polarization-diversity receiver. *IEEE Photonics Technol Lett.* (2011) **23**:597–9. doi: 10.1109/LPT.2011.2118748
46. Doerr CR, Fontaine N, Hirano M, Sasaki T, Buhl L, Winzer P. Silicon photonic integrated circuit for coupling to a ring-core multimode fiber for space-division multiplexing. In: *European Conference and Exposition on Optical Communications* (2011). Available online at: http://www.opticsinfobase.org/abstract.cfm?URI=ECOC-2011-Th.13.A.3
47. Griffin R, Johnstone R, Walker R, Wadsworth S, Carter A, Wale M. Integrated DQPSK transmitter for dispersion-tolerant and dispersion-managed DWDM transmission. *OFC 2003 Optical Fiber Communications Conference* (2003). p. 7–8. doi: 10.1109/OFC.2003.1248559
48. Dong P, Xie C, Chen L, Buhl LL, Chen YK. 112-Gb/s monolithic PDM-QPSK modulator in silicon. *Opt Express* (2012) **20**:B624–9. doi: 10.1364/OE.20.00B624
49. Milivojevic B, Raabe C, Shastri A, Webster M, Metz P, Sunder S, et al. 112Gb / s DP-QPSK transmission over 2427km SSMF using small-size silicon photonic IQ modulator and low-power CMOS driver. In: *Optical Fiber Communications Conference.* San Jose, CA (2013). p. 5–7.
50. Shastri A, Webster M, Jeans G, Metz P, Sunder S, Chattin B, et al. Experimental demonstration of ultra-low-power single polarization 56 Gb / s QAM-16 generation without DAC using CMOS photonics. In: *European Conference and Exposition on Optical Communications.* Cannes (2014). p. 16–8.
51. Koch T, Koren U, Gnall R, Choa F, Hernandez-Gil F, Burrus C, et al. GaInAs/GaInAsP multiple-quantum-well integrated heterodyne receiver. *Electron Lett.* (1989) **25**:1621. doi: 10.1049/el:19891086

52. Takeuchi H, Kasaya K, Kondo Y, Yasaka H, Oe K, Imamura Y. Monolithic integrated coherent receiver on InP substrate. *IEEE Photonics Technol Lett.* (1989) **1**:398. doi: 10.1109/68.43392
53. Deri RJ, Pennings E, Scherer A, Gozdz A, Caneau C, Andreadakis N, et al. Ultracompact monolithic integration of balanced, polarization diversity photodetectors for coherent lightwave receivers. *IEEE Photonics Technol Lett.* (1992) **4**:1238. doi: 10.1109/68.166954
54. Bach H, Matiss A, Leonhardt CC, Kunkel R, Schmidt D, Schell M, et al. *Monolithic 90° hybrid with balanced PIN photodiodes for 100 Gbit / s PM-QPSK receiver applications*. Optical Fiber Communication Conference (2009). p. 4–6.
55. Doerr CR, Zhang L, Winzer PJ. Monolithic InP multiwavelength coherent receiver using a chirped arrayed waveguide grating. *J Lightwave Technol.* (2011) **29**:536–41. doi: 10.1109/JLT.2010.2097240
56. Doerr CR, Winzer PJ, Chen YK, Chandrasekhar S, Rasras MS, Chen L, et al. Monolithic polarization and phase diversity coherent receiver in silicon. *J Lightwave Technol.* (2010) **28**:520–5. doi: 10.1109/JLT.2009.2028656

Conflict of Interest Statement: The author declares that the research was conducted in the absence of any commercial or financial relationships that could be construed as a potential conflict of interest.

frontiers in
MATERIALS

ORIGINAL RESEARCH ARTICLE
published: 30 March 2015
doi: 10.3389/fmats.2015.00026

Small sensitivity to temperature variations of Si-photonic Mach–Zehnder interferometer using Si and SiN waveguides

***Tatsurou Hiraki*[1,2]*, *Hiroshi Fukuda*[3], *Koji Yamada*[1,2] *and Tsuyoshi Yamamoto*[1]**

[1] *NTT Device Technology Laboratories, NTT Corporation, Kanagawa, Japan*
[2] *NTT Nanophotonics Center, NTT Corporation, Kanagawa, Japan*
[3] *NTT Device Innovation Center, NTT Corporation, Kanagawa, Japan*

Edited by:
Toshihiko Baba, Yokohama National University, Japan

Reviewed by:
Junichi Fujikata, Photonics Electronics Technology Research Association, Japan
Yosuke Terada, Yokohama National University, Japan

***Correspondence:**
Tatsurou Hiraki, Device Technology Laboratories, NTT corporation, 3-1, Morinosato Wakamiya, Atsugi-shi, Kanagawa 243-0198, Japan
e-mail: hiraki.tatsurou@lab.ntt.co.jp

We demonstrated a small sensitivity to temperature variations of delay-line Mach–Zehnder interferometer (DL MZI) on a Si photonics platform. The key technique is to balance a thermo-optic effect in the two arms by using waveguide made of different materials. With silicon and silicon nitride waveguides, the fabricated DL MZI with a free-spectrum range of ~40 GHz showed a wavelength shift of -2.8 pm/K with temperature variations, which is 24 times smaller than that of the conventional Si-waveguide DL MZI. We also demonstrated the decoding of the 40-Gbit/s differential phase-shift keying signals to on-off keying signals with various temperatures. The tolerable temperature variation for the acceptable power penalty was significantly improved due to the small wavelength shifts.

Keywords: silicon photonics, thermo-optic effect, Mach-Zehnder interferometer, waveguide, silicon nitride

INTRODUCTION

Silicon (Si) photonics is one of the most promising technologies for overcoming the limitations on integration in commercially available silica-based planar-lightwave circuits. This is because it provides ultra-compact waveguides and makes the monolithic integration of active and passive devices possible (Lockwood and Pavesi, 2010; Vivien and Pavesi, 2013). Many compact devices, such as arrayed-waveguide gratings, Mach–Zehnder interferometers (MZIs), and ring resonators, have been reported using Si (Fukazawa et al., 2004; Xia et al., 2007) and silicon nitride (SiN) waveguides (Gondarenko et al., 2009; Chen et al., 2011). One of the issues with these devices is performance degradation with temperature variations due to the thermo-optic (TO) coefficient's of Si (~1.86×10^{-4}/K) and SiN ($4 \sim 5 \times 10^{-5}$/K) being higher than that of the silica (~1.0×10^{-5}/K). To overcome this issue, athermal designs of Si-waveguide delay line (DL) MZIs have used different effective-index changes with temperature (dn_{eff}/dT) in the two arms to balance the TO effects in them (Uenuma and Motooka, 2009; Guha et al., 2010; Hai and Liboiron-Ladouceur, 2011). In the previous studies, dn_{eff}/dT was controlled by means of the different optical confinement in the Si cores of narrow and wide Si waveguides. However, the dn_{eff}/dT of the narrow waveguides significantly depended on the core width; therefore, inevitable fabrication errors made it difficult to minimize the TO effect. To prevent the problem, the dn_{eff}/dT should be controlled by changing the TO coefficients of the materials, without using a narrow waveguide. In our previous work, we reported control of the refractive indices and TO coefficients of complementary metal-oxide semiconductor (CMOS) compatible materials by changing the atomic composition of SiOx, SiOxNy, and SiN (Tsuchizawa et al., 2011; Nishi et al., 2012; Hiraki et al., 2013). Using these materials, in this work, we minimized the temperature sensitivity of the DL MZI. In the following sections, we show the details of the design and fabrication of the DL MZI and present experimental results. In addition, as a feasibility demonstration, we show the thermal stability of the decoding of differential phase-shift eying (DPSK) signals to on-off keying (OOK) signals at 40 Gbit/s.

DESIGN AND FABRICATION

Figure 1 shows a schematic of the DL MZI. The temperature sensitivity could be minimized by balancing the TO effect between the two arms, while keeping the differential delay between them. The interference condition is expressed as following equation (Guha et al., 2010)

$$m\lambda = n_{\mathrm{eff},2}L_2 - n_{\mathrm{eff},1}L_1$$

Here, m is an integer for constructive interference or a half-integer destructive interference, $n_{\mathrm{eff},1}$ and $n_{\mathrm{eff},2}$ are the effective indices, and L_1 and L_2 are the physical lengths of arm 1 and 2. Then, the temperature sensitivity of the interference spectrum could be obtained by differentiating above equation with respect to temperature, as expressed by following

$$\frac{d\lambda}{dT} = \left(\frac{dn_{\mathrm{eff},2}}{dT}L_2 - \frac{dn_{\mathrm{eff},1}}{dT}L_1\right) \Big/ \left\{m - \left(\frac{dn_{\mathrm{eff},2}}{d\lambda}L_2 - \frac{dn_{\mathrm{eff},1}}{d\lambda}L_1\right)\right\}$$

Athermal condition is given by the numerator of this equation to be 0. Since we have two design parameters L_1 and L_2, we can make $d\lambda/dT$ to be 0 while keeping the differential delay. The key technique is to control dn_{eff}/dT by changing the core materials of the two arms. In this work, we used Si and SiN waveguides in the

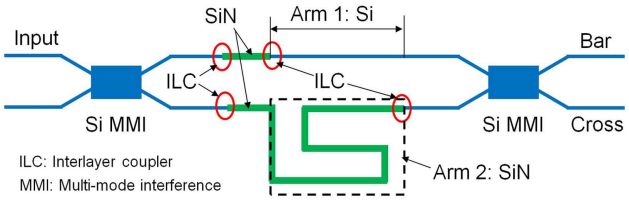

FIGURE 1 | Schematic of Si–SiN-waveguide DL MZI.

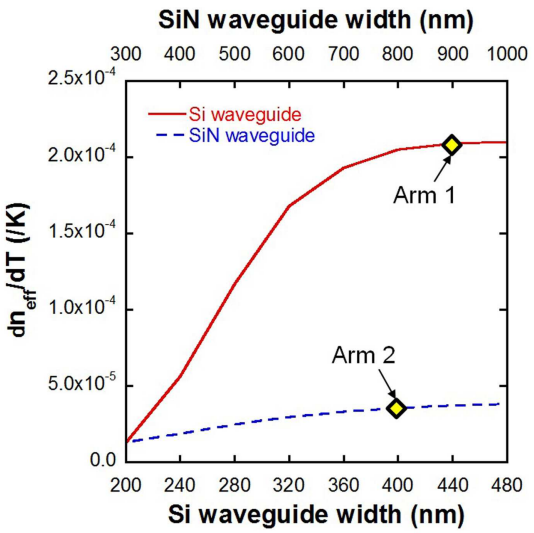

FIGURE 2 | Relationships between dn_{eff}/dT and core width of Si and SiN waveguides.

CMOS compatible materials. In the design, the refractive index and the TO coefficient of the SiN core are 2.0 and 4.0×10^{-5}/K, respectively. The core thicknesses of the waveguides were fixed at 220 and 400 nm, respectively. **Figure 2** shows the calculated results of relationships between dn_{eff}/dT and the core widths of the Si and SiN waveguides. For little change of the dn_{eff}/dT with width variations, we used a 440-nm-wide Si waveguide as arm 1, and an 800-nm-wide SiN-waveguide as arm 2, respectively. We designed the DL MZI with a free spectral range (FSR) of 40 GHz. The FSR is given by the inverse of the differential delay, or 1-bit delay time $\Delta t = (n_{g,2}L_2 - n_{g,1}L_1)/c$, where $n_{g,1}$ and $n_{g,2}$ are group indices of the arm 1 and 2, and c is the speed of light in vacuum. Under this differential delay condition, the $d\lambda/dT$ can be 0 by choosing the L_1 and L_2 as 0.95 mm and 5.77 mm, respectively. It is notable that if we could use the state-of-the-art fabrication process with width variations of 3 nm (Shimura et al., 2014), the $d\lambda/dT$ could be less than 0.1 pm/K, which is over 10 times smaller than that using a 280-nm-wide (narrow) Si-waveguide as arm 2 (Hai and Liboiron-Ladouceur, 2011) with the same width variations.

As other features to construct the DL MZI structure, we used the inverse taper of the Si waveguide for the fiber-chip interface, and 2 × 2 Si-waveguide multimode interference (MMI) couplers.

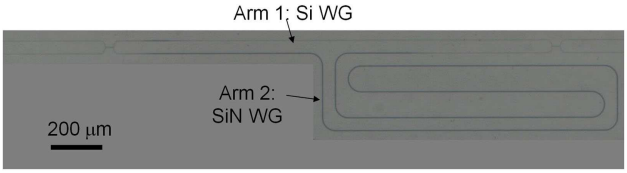

FIGURE 3 | Microscope image of fabricated Si–SiN-waveguide DL MZI.

The taper-tip width and the taper length of the fiber-chip interface were 200 nm and 300 μm, respectively. Since the Si and SiN waveguides were formed in different layers, the interlayer coupler (ILC) between them was designed using adiabatically tapers (Huang et al., 2014). We introduced the ILCs into both arms to cancel out their phase delays. In addition, as reference samples, we designed a conventional Si-waveguide DL MZI and a SiN-waveguide DL MZI without any compensation for thermal sensitivity ($dn_{eff,1}/dT = dn_{eff,2}/dT$). In the conventional DL MZIs, both arms comprised of the same structures, which were the 440-nm-wide Si waveguide and the 800-nm-wide SiN waveguide.

The DL MZI was fabricated on an 8-inch silicon-on-insulator wafer, whose buried-oxide thickness was 3 μm. The Si waveguides were first patterned; then, a clad film was deposited. After that, the clad film was flattened, and SiN-waveguide cores were formed. The interlayer clad thickness between the Si and SiN waveguides was controlled to be 100 nm. Finally, an overclad film was deposited. A microscope image of the fabricated Si–SiN-waveguide DL MZI is shown in **Figure 3**. The total size of the fabricated DL MZI is ~0.56 mm^2/ch, which is comparable to that of the conventional SiN-waveguide DL MZI. It is still larger than that of the Si-waveguide DL MZI; however, it is several-hundred times smaller than one made of the commercially-used silica.

RESULTS AND DISCUSSIONS

We measured transmission spectra of the fabricated DL MZI. We used a tunable laser diode (TLD) as a light source and swept the wavelength of the input light, and measured output light power from the bar port. The input and output fibers were lensed fibers with mode-field diameters of ~3.5 μm, and the polarization of the input light was adjusted to the transverse electric (TE) mode. The chip was set on a temperature-controlled stage by using a heat-dissipation tape. We measured the transmission spectra of the DL MZIs, while varying the chip-stage temperature range from 298–302 K so that the wavelength shift should not exceed the FSR. **Figures 4A–C** show the transmission spectra of the Si–SiN-waveguide DL MZI, the conventional SiN-waveguide DL MZI, and the conventional Si-waveguide DL MZI at 298 and 300 K. The output powers were normalized by the fiber-to-fiber transmission spectra. It is clear that the Si–SiN-waveguide DL MZI highly suppresses the wavelength shift with temperature variations. The measured FSRs and the $d\lambda/dT$ are listed in **Table 1**. The TO effects of the fabricated SiN- and Si waveguides are almost consistent with their designs. The $d\lambda/dT$ of the Si-SiN DL MZI is over six times smaller than that of the conventional

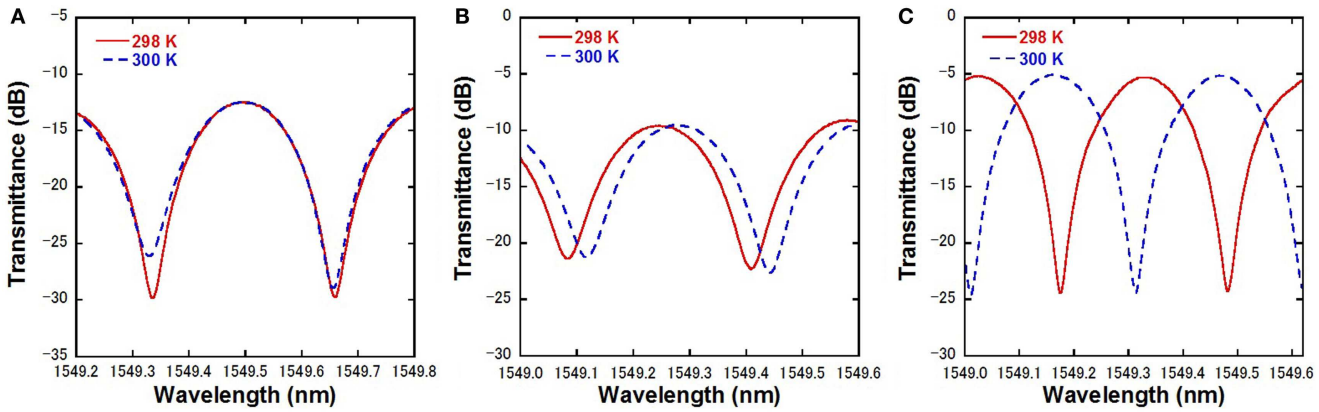

FIGURE 4 | Transmission spectra of (A) Si–SiN-waveguide DL MZI, (B) SiN-waveguide DL MZI, and (C) Si-waveguide DL MZI.

Table 1 | Measured FSRs and dλ/dT.

Sample	Arm 1	Arm 2	FSR (GHz)	dλ/dT (pm/K)
Si–SiN DL MZI	Si	SiN	40.5	−2.8
SiN DL MZI (ref.)	SiN	SiN	40.8	+17.0
Si DL MZI (ref.)	Si	Si	38.3	+68.5

SiN waveguide, and 24 times smaller than that of the conventional Si-waveguide DL MZI. Although the dλ/dT of the Si–SiN DL MZI is larger than the expected value (<0.1 pm/K) because of the large fabrication error over 3 nm, the measured result is still better than those for DLI MZIs with narrow Si waveguides (Uenuma and Motooka, 2009; Guha et al., 2010). The FSR of the Si–SiN DL MZI is 40.5 GHz, which is only about 1% different from the target value. The insertion loss of the Si–SiN-waveguide DL MZI is ~13 dB, which includes the fiber-chip coupling loss of ~2 dB/facet and the interlayer coupling loss of ~0.5 dB/couple. The extinction ratio is ~17 dB, which is mainly determined by an imbalance of propagation loss between two arms of the MZI and an unintentional imbalance of the MMI branch. The propagation loss of SiN and Si waveguides are ~12 dB/cm and ~4 dB/cm, respectively. The unintentional imbalance of the MMI branch is ~1.3 dB. Although the imbalance between two arms is large, the imbalance of the MMI branch improves the extinction ratio. The insertion loss and extinction ratio would be further improved because a well-controlled fabrication environment would reduce the SiN-waveguide loss (Huang et al., 2014). We must mention that the device was designed for only TE mode light. For polarization diversity circuits (Fukuda et al., 2008), a polarization rotator using parallel cores has already been demonstrated using the same Si and SiN layers as in this work (Fukuda and Wada, 2014).

As a feasibility demonstration, we applied the Si–SiN-waveguide DL MZI to decode 40-Gbit/s DPSK signals. **Figure 5** shows the experimental setup. We input the DPSK signals with a non-return-to-zero (NRZ) 40-Gbit/s pseudo-random bit sequence (PRBS) of length 2^{31} - 1. The eye diagram of the input

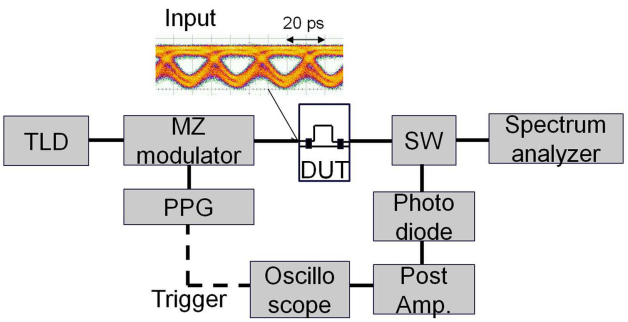

FIGURE 5 | Experimental setup for decoding of 40-Gbit/s DPSK signals.

signals is shown in the inset of **Figure 5**. The polarization state of the input light was adjusted to the TE mode. The output light was coupled by the lensed fiber and then switched to the optical spectrum analyzer or the photodiode. The electrical signals from the photodiode were amplified then fed into the sampling oscilloscope. **Figures 6A,B** show the constructive- and destructive-interference spectra of the bar port at frequency of 193.611 and 193.592 THz, respectively. They were measured at 298 K. The decoded 40-Gbit/s signals were observed as 40-GHz-span dips in the destructive-interference spectra. Their eye diagrams are shown in the insets of **Figures 6A,B**, respectively. Here, the vertical axis is 20 mV/div and the horizontal axis is 10 ps/div. The two output signals carried logically inverted data streams in the DPSK format. The constructive interference carried duobinary, whereas the destructive-interference carries alternate-mark inversion (Gnauck and Winzer, 2005). Using the destructive interference, we demonstrated a thermal tolerance to decode the DPSK format to the OOK format (Winzer and Leuthold, 2001; Lazzeri et al., 2010). **Figures 7A,B** show the eye diagrams of the destructive-interference signals at 299 and 302 K, respectively. The eye diagrams clearly open at 302 K, corresponding to a temperature variation of 4 K from the initial temperature (298 K). From the measured dλ/dT of -2.8 pm/K, the estimated frequency shift by the temperature

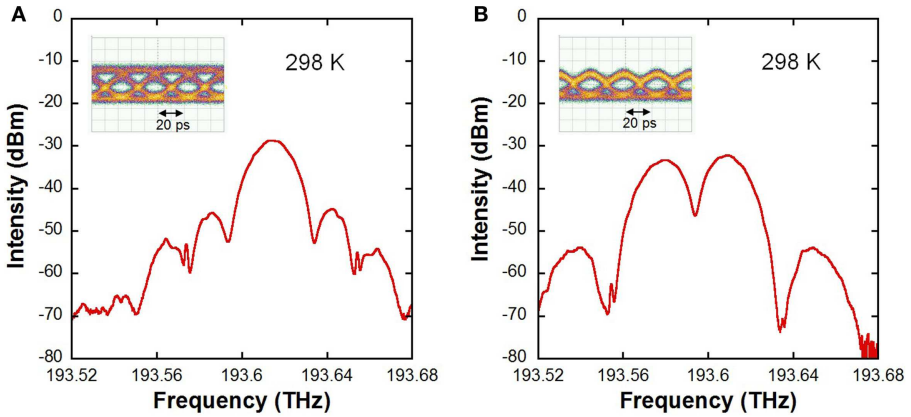

FIGURE 6 | Decoded-signal spectra and eye diagrams (insets) of (A) constructive- and (B) destructive interference at 298 K.

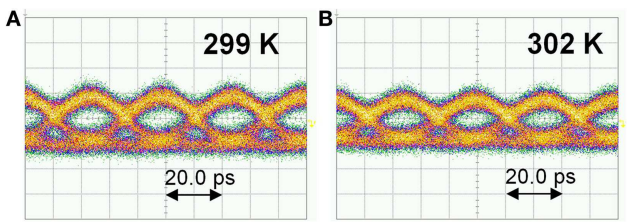

FIGURE 7 | Eye diagrams of Si–SiN-waveguide DL MZI at (A) 299 and (B) 302 K.

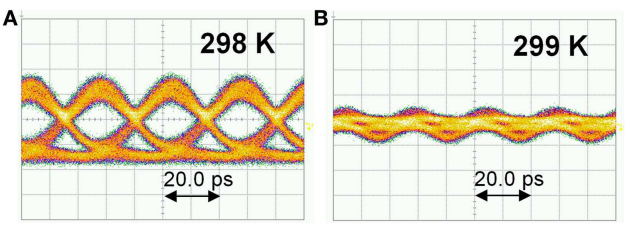

FIGURE 8 | Eye diagrams of Si-waveguide DL MZI at (A) 298 and (B) 299 K.

variation of +4 K is -1.4 GHz, which could cause only about 1-dB penalty for a 40-Gbit/s system (Hoon and Winzer, 2003). By using the state-of-the-art fabrication process, as discussed in the above section, the tolerable temperature variations could be over 90 K. As references, the eye diagrams of the conventional Si-waveguide DL MZI at 298 and 299 K are shown in **Figures 8A,B**, respectively. Here, the vertical axis is 69.7 mV/div and the horizontal axis is 10.0 ps/div. The eye diagram was completely closed with a temperature variation of only +1 K. These results clearly show that the Si–SiN-waveguide DL MZI actually improves the thermal-insensitivity of the Si-photonic DL MZI and that it has a potential to be used in the telecommunications devices. A well-controlled fabrication environment would reduce the insertion loss of the DL MZI and also improves the signal-to-noise ratio.

CONCLUSION

We demonstrated a small sensitivity to temperature variations of DL MZI on a Si-photonics platform. The key technique is to balance the TO effect in two arms by using waveguides made of different materials, which are Si and SiN. The Si–SiN-waveguide DL MZI with an FSR of 40 GHz showed $d\lambda/dT$ of -2.8 pm/K, which is about 24 times smaller than that of the conventional Si-waveguide DL MZI. The technology has the potential to reduce temperature sensitivities of various Si-photonic devices, such as wavelength filters, phase demodulators, and ring resonators.

REFERENCES

Chen, L., Doerr, C. R., Dong, P., and Chen, Y. K. (2011). Monolithic silicon chip with 10 modulator channels at 25 Gbps and 100-GHz spacing. *Opt. Express* 19, B946–B951. doi:10.1364/OE.19.00B946

Fukazawa, T., Ohno, F., and Baba, T. (2004). Very compact arrayed-waveguide-grating demultiplexer using Si photonic wire waveguides. *Jpn. J. Appl. Phys.* 43, L673–L675. doi:10.1143/JJAP.43.L673

Fukuda, H., and Wada, K. (2014). Parallel-core-type polarization rotator for silicon wire waveguide platform. *Photonics Res.* 2, A14–A18. doi:10.1364/PRJ.2.000A14

Fukuda, H., Yamada, K., Tsuchizawa, T., Watanabe, T., Shinojima, H., and Itabashi, S. (2008). Silicon photonic circuit with polarization diversity. *Opt. Express* 16, 4872–4880. doi:10.1364/OE.16.004872

Gnauck, A. H., and Winzer, P. J. (2005). Optical phase-shift-keyed transmission. *J. Lightw. Technol.* 23, 115–130. doi:10.1109/JLT.2004.840357

Gondarenko, A., Levy, J. S., and Lipson, M. (2009). High confinement micron-scale silicon nitride high Q ring resonator. *Opt. Express* 17, 11366–11370. doi:10.1364/OE.17.011366

Guha, B., Gonarenko, A., and Lipson, M. (2010). Minimizing temperature sensitivity of silicon Mach-Zehnder interferometers. *Opt. Express* 18, 1879–1887. doi:10.1364/OE.18.001879

Hai, M. S., and Liboiron-Ladouceur, O. (2011). "Temperature compensated 50 Gb/s DPSK demodulator," in *Conference on Lasers and Electro-Optics* (Baltimore: OSA), JTuI76.

Hiraki, T., Nishi, H., Tsuchizawa, T., Kou, R., Fukuda, H., Takeda, K., et al. (2013). Si-Ge-Silica monolithic integration platform and its application to a 22-Gb/s x 16-ch WDM receiver. *Photonics J.* 5, 4500407. doi:10.1109/JPHOT.2013.2269676

Hoon, K., and Winzer, P. J. (2003). Robustness to laser frequency offset in direct-detection DPSK and DQPSK systems. *J. Lightw. Technol.* 21, 1887–1891. doi:10.1109/JLT.2003.816816

Huang, Y., Song, J., Luo, X., Liow, T. Y., and Lo, G. Q. (2014). CMOS compatible monolithic multi-layer Si_3N_4-on-SOI platform for low-loss high performance

silicon photonics dense integration. *Opt. Express* 22, 21859–21865. doi:10.1364/OE.22.021859

Lazzeri, E., Nguyen, A. T., Serafino, G., Kataoka, N., Wada, N., Bogoni, A., et al. (2010). "All-optical NRZ-DPSK to RZ-OOK format conversion using optical delay line interferometer and semiconductor optical amplifier," in *Photonics in Switching Conference* (Monterey), JTuB45.

Lockwood, D. J., and Pavesi, L. (eds) (2010). *Silicon Photonics*. Berlin: Springer.

Nishi, H., Tsuchizawa, T., Kou, R., Shinojima, H., Yamada, T., Kimura, H., et al. (2012). Monolithic integration of a silica AWG and Ge photodiodes on Si photonic platform for one-chip WDM receiver. *Opt. Express* 20, 9312–9321. doi:10.1364/OE.20.009312

Shimura, D., Horikawa, T., Okayama, H., Jeong, S.-H., Tokushima, M., Sasaki, H., et al. (2014). "High precision Si waveguide devices designed for 1.31μm and 1.55μm wavelengths on 300mm-SOI," in *Conference on Group IV Photonics*. Vancouver: IEEE.

Tsuchizawa, T., Yamada, K., Watanabe, T., Sungbong, P., Nishi, H., Kou, R., et al. (2011). Monolithic integration of silicon-, germanium-, and silica-based optical devices for telecommunications applications. *IEEE J. Sel. Top. Quant. Electron.* 17, 516–525. doi:10.1109/JSTQE.2010.2089430

Uenuma, M., and Motooka, T. (2009). Temperature-independent silicon waveguide optical filter. *Opt. Lett.* 34, 599–601. doi:10.1364/OL.34.000599

Vivien, L., and Pavesi, L. (eds). (2013). *Handbook of Silicon Photonics*. New York: Taylor and Francis.

Winzer, P. J., and Leuthold, J. (2001). Return-to-zero modulator using a single NRZ drive signal and an optical delay interferometer. *IEEE Photon. Technol. Lett.* 13, 1298–1300. doi:10.1109/68.969887

Xia, F., Rooks, M., Sekaric, L., and Vlasov, Y. (2007). Ultra-compact high order ring resonator filters using submicron silicon photonic wires for on-chip optical interconnects. *Opt. Express* 15, 11934–11941. doi:10.1364/OE.15.011934

Conflict of Interest Statement: The authors declare that the research was conducted in the absence of any commercial or financial relationships that could be construed as a potential conflict of interest.

Received: 16 January 2015; accepted: 16 March 2015; published online: 30 March 2015.
*Citation: Hiraki T, Fukuda H, Yamada K and Yamamoto T (2015) Small sensitivity to temperature variations of Si-photonic Mach–Zehnder interferometer using Si and SiN waveguides. Front. Mater. **2**:26. doi: 10.3389/fmats.2015.00026*
This article was submitted to Optics and Photonics, a section of the journal Frontiers in Materials.

frontiers in Materials

ORIGINAL RESEARCH
published: 05 May 2015
doi: 10.3389/fmats.2015.00036

Ultrahigh temperature-sensitive silicon MZI with titania cladding

Jong-Moo Lee [1,2]*

[1] Electronics and Telecommunications Research Institute, Daejeon, South Korea, [2] School of Advanced Device Technology, University of Science and Technology, Daejeon, South Korea

We present a possibility of intensifying temperature sensitivity of a silicon Mach-Zehnder interferometer (MZI) by using a highly negative thermo-optic property of titania (TiO_2). Temperature sensitivity of an asymmetric silicon MZI with a titania cladding is experimentally measured from +18 to −340 pm/°C depending on design parameters of MZI.

Keywords: silicon, photonics, temperature, sensor, titania

OPEN ACCESS

Edited by:
Jifeng Liu,
Thayer School of Engineering, USA

Reviewed by:
Raul J. Martin-Palma,
Universidad Autonoma de Madrid, Spain
Venu Gopal Achanta,
Tata Institute of Fundamental Research, India

***Correspondence:**
Jong-Moo Lee,
Electronics and Telecommunications Research Institute, 161 Gajong-dong, Yusong-gu, Daejeon 305-350, Korea
jongmool@etri.re.kr

Specialty section:
This article was submitted to Optics and Photonics, a section of the journal Frontiers in Materials

Received: *30 January 2015*
Accepted: *08 April 2015*
Published: *05 May 2015*

Citation:
Lee J-M (2015) Ultrahigh temperature-sensitive silicon MZI with titania cladding. Front. Mater. 2:36. doi: 10.3389/fmats.2015.00036

Introduction

There have been many efforts to adjust temperature-dependent wavelength shift (TDWS) of a photonic waveguide device using a cladding material with a negative thermo-optic coefficient (TOC) differently from a core material with a positive TOC (Kokubun et al., 1998; Lee et al., 2007, 2008; Alipour et al., 2010; Guha et al., 2013; Bovington et al., 2014; Lee, 2014). Polymers have been popularly used as the cladding material with a negative TOC (Kokubun et al., 1998; Lee et al., 2007, 2008), and titania (TiO_2) is recently attracting attention with a highly negative TOC (Alipour et al., 2010; Guha et al., 2013; Bovington et al., 2014; Lee, 2014) and its merit of complementary-metal-oxide-semiconductor (CMOS) compatibility in fabrication when it is used for a silicon photonic waveguide device. Silicon has a very high TOC of 1.8×10^{-4}/°C and there have been many efforts to reduce the high TDWS of silicon photonic devices such as a ring resonator by using polymer (Kokubun et al., 1998; Lee et al., 2007, 2008) or titania cladding (Alipour et al., 2010; Guha et al., 2013; Lee, 2014) with a highly negative TOC.

In case of silicon photonic Mach-Zehnder interferometer (MZI), there were reports showing the way to reduce the TDWS of MZI without using a cladding with a negative TOC (Uenuma and Mooka, 2009; Guha et al., 2010; Dwivedi et al., 2013). TDWS of silicon MZI was shown to be reduced by using different widths of waveguide (Uenuma and Mooka, 2009; Guha et al., 2010) or by using different polarization (Dwivedi et al., 2013) in each of the MZI arm, respectively. The difference in each of the MZI arm can induce a different temperature-dependent phase change for the each arm, resulting reduction in TDWS of MZI.

The previous efforts of silicon photonic devices using a negative thermo-optic cladding have been focused on reducing the TDWS, but there have been demands also on high TDWS in such applications of low power temperature tuning (Masood et al., 2013) and integrated-photonic temperature sensors (Irace and Breglio, 2003; Kim et al., 2010; Deng et al., 2014). So, it would also be attractive if there is a method to intensify the TDWS of the silicon device by using a cladding material such as titania with a very high TOC. There have been MZIs using titania for chemical sensing (Qi et al., 2002; Celo et al., 2009), but no reports on temperature sensors using titania cladding to the best of our knowledge.

In this regard, here, we combine the method used to in reducing TDWS of silicon MZI with different dimension for each arm and the method of adding titania cladding on the silicon MZI to show the possibility of ultrahigh temperature-sensitive silicon MZI.

Experiment and Results

Design and Fabrication

Temperature dependence of a silicon MZI can be adjusted by asymmetric geometry of two waveguide arms with different effective refractive indexes induced by different cross-sectional dimension as in reference Uenuma and Moooka (2009) and Guha et al. (2010). Silicon MZIs in this experiment are designed with variations in the length of MZI arm and cross-sectional dimension of each MZI arm as in **Figure 1**. **Figure 1A** shows AsyL, which is for asymmetry in the length of each MZI arm of 80 μm, L for the common length of MZI arm, which is varied from 110 to 360 μm, w0 for the common width of waveguide core, which is 450 nm, w1 for the cross-sectional dimension of a waveguide core which is 1350 nm and shaped as a rib waveguide shown in **Figure 1B** or 450 nm and shaped as a channel waveguide for a comparison, and w2 for the cross-sectional dimension of a waveguide core which is 350 or 450 nm for a comparison. **Figures 1B,C** show the cross-sectional structure of the waveguide with a silica cladding and a titania cladding, respectively. The rib waveguide is formed by shallow etch of 70 nm for the width w1, and there are tapers at the both ends of the rib waveguide for an adiabatic transfer to the channel waveguide with the width of w0.

Figure 2 shows a microscopic image and scanning electron microscope (SEM) image of the fabricated MZIs. There are many variations for the length, L, in design, but we limit our discussion here to the two extreme case of L, 110 and 360 μm. Silicon waveguide core with the width of 450 nm was patterned by DUV lithography on a silicon-on-insulator (SOI) wafer with a 220-nm thick silicon layer on a 2-μm thick buried oxide (BOX) layer. The fabrication of the devices except a deposition of titania cladding were processed using a standard CMOS fabrication process through ePIXfab. There were two types of fabricated device: one with a silica (SiO_2) cladding and the other without an upper cladding. We deposited 400 nm thickness of titania cladding on the fabricated device without an upper cladding, using electron-beam evaporation. The initial vacuum level of the electron-beam evaporation was 5×10^{-7} Torr, and it was kept at 8×10^{-5} Torr with O_2 during the deposition. The temperature of a plate holding SOI chip was maintained at 150°C during the evaporation, and the speed of deposition was about 3Å/s. The refractive index of titania was measured using ellipsometry as 2.13 at 1550 nm.

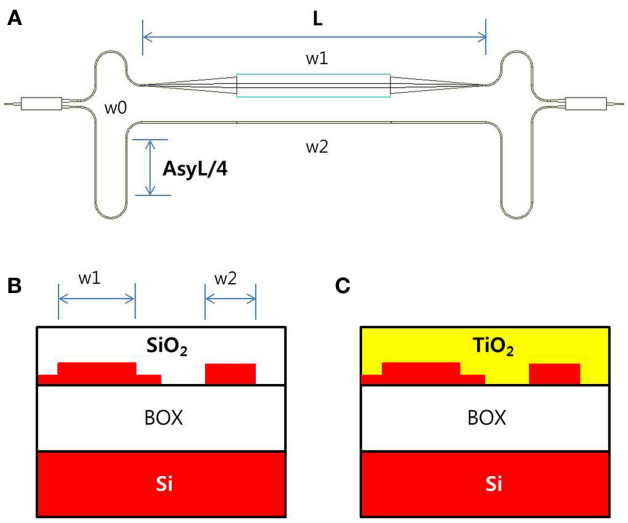

FIGURE 1 | (A) Schematic diagram of asymmetric MZI with arms different in length and cross-sectional dimension of waveguide, and schematic diagram of the cross-section of the arms in **(B)** with silica cladding and **(C)** with titania cladding, respectively.

Measured Results

One pair of single-mode fibers is coupled to the silicon devices for measurement through grating couplers which are with 630-nm pitch and 70 nm depth of the shallow etch. **Figure 3** shows normalized transmission spectra of a silicon MZI with a silica

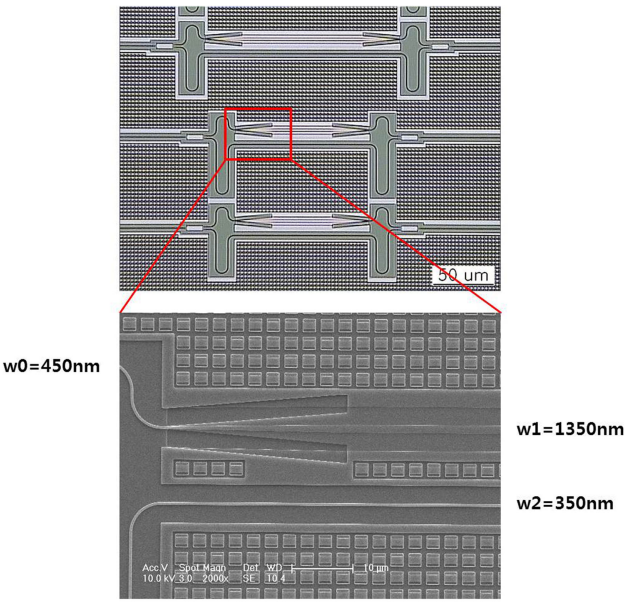

FIGURE 2 | A microscope image and a SEM image of silicon MZIs fabricated in this experiment.

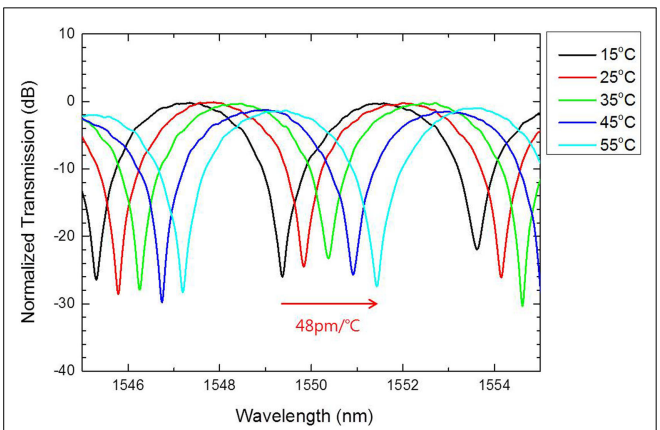

FIGURE 3 | Normalized transmission spectra of MZI with silica cladding as the temperature varied from 15 to 55°C when L = 360 μm, w1 = 1350 nm, and w2 = 350 nm.

cladding when the temperature varied from 15 to 55°C. The main design parameters of the silicon MZI are 360 μm for L, 1350 nm for w1, and 350 nm for w2. **Figure 3** shows TDWS of the silicon MZI is +48 m/°C, which was reduced from +74 pm/°C of a ring resonator included in the same chip for a comparison. The normalized transmissions can be regarded as the insertion loss of the silicon MZI, because they were calculated by subtracting the amount of fiber-to-fiber transmission of a straight silicon waveguide from the amount of fiber-to-fiber transmission of the silicon MZI device. **Figure 3** shows that the insertion loss through the silicon MZI is negligibly small.

Figure 4 shows normalized transmission spectra of a silicon MZI, whose design is the same as in **Figure 3** but with a titania cladding instead of the silica cladding, when the temperature varied from 25 to 35°C. **Figure 4** shows TDWS of the silicon MZI is intensified with opposite sign by the titania cladding as high as −340 pm/°C, which is about seven times bigger than the TDWS of the same design of MZI with a silica cladding and five times bigger than the TDWS of the ring resonator with a silica cladding.

Figure 5 shows the relative wavelength shift of various MZIs with silica or titania cladding in this experiment compared to the TDWS of the ring resonator with the silica cladding. The radius of the ring resonator with the silica cladding was 5 μm and TDWS of the ring resonator was measured at +74 pm/°C as in **Figure 6**. TDWS of a silicon MZI with the same cross-section dimension of 450 nm and titania cladding was measured as +18 pm/°C as in **Figure 5**. TDWS of another titania-covered silicon MZI with 1350 nm for w1, 450 nm for w2, and 110 μm for L was measured as −70 pm/°C as in **Figure 5**.

Discussion

The experimental results show that we can adjust TDWS of the titania-covered silicon MZIs with proper design and can intensify the temperature sensitivity highly enough to be useful in applications requiring an ultrahigh temperature sensitivity such as thermo-optic tuning devices or photonic temperature sensors.

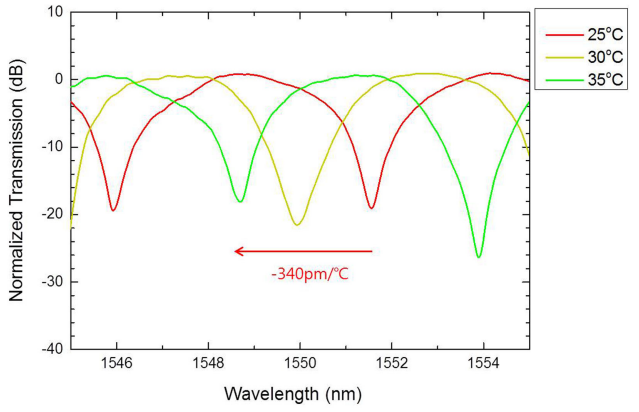

FIGURE 4 | Normalized transmission spectra of MZI with titania cladding as the temperature varied from 25 to 35°C when L = 360 μm, w1 = 1350 nm, and w2 = 350 nm.

The input and output fibers are coupled to the silicon waveguide through grating couplers with the pitch of 630 nm. The fiber was coupled at the vertical angle of 10° for the waveguide with silica cladding and 15° for the waveguide with titania cladding. There was not a big difference in the coupling loss of the grating couplers for the silica cladding and titania cladding. It was about 5 dB/facet for the silica cladding and 5.5 dB/facet for the titania cladding. The slightly excessive loss of the grating coupler in case of titania cladding is expected to be reduced by optimizing the design of gratings or the thickness of titania if it is required. The normalized transmission in **Figures 3** and **4** were calculated by subtracting the amount of fiber-to-fiber transmission of a straight silicon waveguide from the amount of fiber-to-fiber transmission of the silicon MZI device for each case of silica cladding and titania cladding, respectively. So, the normalized transmission spectra show the insertion loss of MZI compared to a straight waveguide.

The refractive index of titania cladding was measured using ellipsometry as 2.13 at 1550 nm, and TOC of titania film was

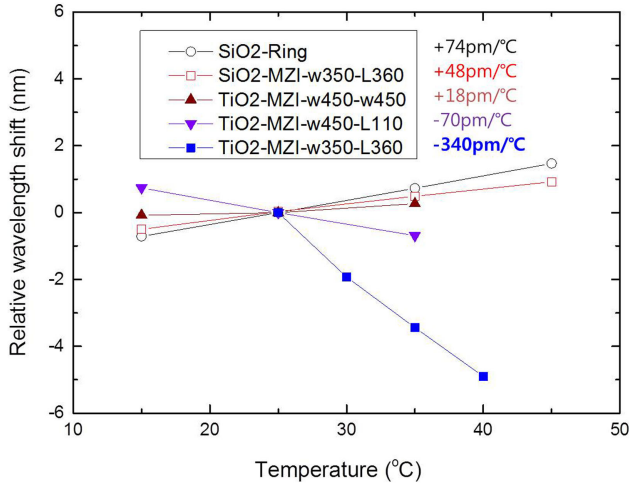

FIGURE 5 | Relative wavelength shift depending on temperature of MZI with silica and titania cladding, respectively, in comparison with +74 pm/°C or a ring resonator with silica cladding. w350 and w450 are for 350 and 450 nm width, respectively, of the MZI narrow arm. L110 and L360 are for 110 and 360 μm length, respectively, of the MZI arm.

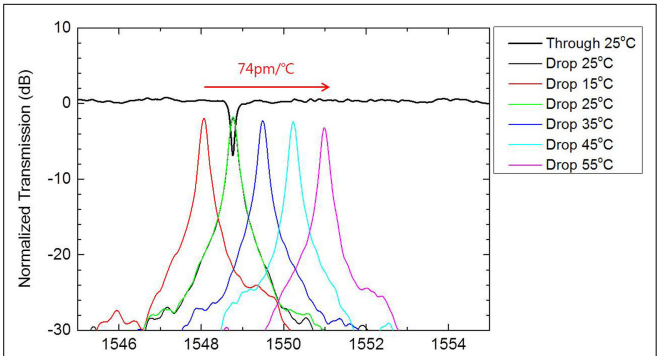

FIGURE 6 | Normalized transmission spectra of the ring resonator with silica cladding mentioned in Figure 5, as the temperature varied from 15 to 55°C.

not directly measured but estimated from -5 to -7×10^{-4}/°C by the measured TDWS of a ring resonator with titania cladding as in reference Lee (2014). The absolute value of TOC of titania is several times higher than TOC of silicon or polymer, and that is the reason we used it as highly negative thermo-optic cladding in this experiment. The reason for the highly negative TOC of the titania cladding and the variation of TOC is not fully understood yet, and finding the reason remains for our future research.

Conclusion

We experimentally showed that TDWS of a silicon MZI can be reduced or intensified by proper design of the width and length of arms of MZI when it is used with a highly negative thermo-optic titania cladding. We experimentally showed temperature sensitivity of an asymmetric silicon MZI with a titania cladding could be adjusted from +18 to −340 pm/°C depending on design parameters such as the width and length of MZI. We believe these results show the possibility of ultrahigh temperature-sensitive silicon MZI for new applications requiring ultrahigh temperature sensitivity such as thermo-optic tuning devices or photonic temperature sensors.

Acknowledgments

We would like to thank ePIXfab (www.epixfab.eu) for the fabrication of SOI waveguide before our deposition of titania cladding. This work was supported by Korean IT R&D program MOTIE [N019800001] and [10044735].

References

Alipour, P., Atabaki, A. H., Eftekhar, A. A., and Adibi, A. (2010). "Athermal performance in titania-clad microring resonators on SOI," in *OSA Technical Digest. Integrated Photonics Research, Silicon and Nanophotonics and Photonics in Switching, Paper IMC6; 2010 Jul 25-28*, (Monterey, CA: Optical Society of America).

Bovington, J., Wu, R., Cheng, K. T., and Bowers, J. E. (2014). Thermal stress implications in athermal TiO2 waveguides on a silicon substrate. *Opt. Express* 21, 661–666. doi:10.1364/OE.22.000661

Celo, D., Post, E., Summers, M., Smy, T., Brett, M. J., and Albert, J. (2009). Interferometric sensing platform with dielectric nanostructured thin films. *Opt. Express* 17, 6655–6664. doi:10.1364/OE.17.006655

Deng, Q. Z., Li, X. B., Chen, R. B., and Zhou, Z. (2014). "Low-cost silicon photonic temperature sensor using broadband light source," in *IEEE 11th International Conference, Group IV Photonics (GFP), WP23; 2014 Aug 27-29*, (Paris).

Dwivedi, S., D'heer, H., and Bogaerts, W. (2013). A compact all-silicon temperature insensitive filter for WDM and bio-sensing applications. *IEEE Photonics Technol. Lett.* 25, 2167–2170. doi:10.1109/LPT.2013.2282715

Guha, B., Cardenas, J., and Lipson, M. (2013). Athermal silicon microring resonators with titanium oxide cladding. *Opt. Express* 21, 26557–26563. doi:10.1364/OE.21.026557

Guha, B., Gondarenko, A., and Lipson, M. (2010). Minimizing temperature sensitivity of silicon Mach-Zehnder interferometers. *Opt. Express* 18, 1879–1887. doi:10.1364/OE.18.001879

Irace, A., and Breglio, G. (2003). All-silicon optical temperature sensor based on multi-mode interference. *Opt. Express* 11, 2807–2812. doi:10.1364/OE.11.002807

Kim, G. D., Lee, H. S., Park, C. H., Lee, S. S., Lim, B. T., Bae, H. K., et al. (2010). Silicon photonic temperature sensor employing a ring resonator manufactured using a standard CMOS process. *Opt. Express* 18, 22215–22221. doi:10.1364/OE.18.022215

Kokubun, Y., Yoneda, S., and Matsuura, S. (1998). Temperature-independent optical filter at 1.55μm wavelength using a silica-based athermal wavelength. *Electron. Lett.* 34, 367–369. doi:10.1049/el:19980245

Lee, J. M. (2014). Influence of titania cladding on SOI grating coupler and 5 μm-radius ring resonator. *Opt. Commun.* 338, 101–105. doi:10.1016/j.optcom.2014.10.039

Lee, J. M., Kim, D. J., Ahn, H. Y., Park, S. H., and Kim, G. O. (2007). Temperature dependence of silicon nanophotonic ring resonator with a polymeric overlayer. *J. Lightwave Technol.* 25, 2236–2243. doi:10.1109/JLT.2007.899792

Lee, J. M., Kim, D. J., Kim, G. H., Kwon, O. K., Kim, K. J., and Kim, G. O. (2008). Controlling temperature dependence of silicon waveguide using slot structure. *Opt. Express* 16, 1645–1652. doi:10.1364/OE.16.001645

Masood, A., Pantouvakiy, M., Lepagey, G., Verheyeny, P., Campenhouty, J. V., Absily, P., et al. (2013). "Comparison of heater architectures for thermal control of silicon photonic circuits," in *IEEE 10th International Conference, Group IV Photonics (GFP), ThC2; 2013 Aug 28-30*, (Seoul).

Qi, Z., Matzuda, N., Itoh, K., Murabayashi, M., and Labers, C. R. (2002). A design for improving the sensitivity of Mach-Zehnder interferometer to chemical and biological measurands. *Sens Actuators B Chem* 81, 254–258. doi:10.1016/S0925-4005(01)00960-1

Uenuma, M., and Moooka, T. (2009). Temperature-independent silicon waveguide optical filter. *Opt. Lett.* 34, 599–601. doi:10.1364/OL.34.000599

Conflict of Interest Statement: The author declares that the research was conducted in the absence of any commercial or financial relationships that could be construed as a potential conflict of interest.

frontiers in Materials

ORIGINAL RESEARCH
published: 27 April 2015
doi: 10.3389/fmats.2015.00034

Silicon-nitride-based integrated optofluidic biochemical sensors using a coupled-resonator optical waveguide

Jiawei Wang, Zhanshi Yao and Andrew W. Poon *

Photonic Device Laboratory, Department of Electronic and Computer Engineering, The Hong Kong University of Science and Technology, Hong Kong, China

OPEN ACCESS

Edited by:
Dan-Xia Xu, National Research Council Canada, Canada

Reviewed by:
Koji Yamada, Nippon Telegraph and Telephone Corporation, Japan
Weidong Zhou, University of Texas at Arlington, USA
Robert Halir, Universidad de Málaga, Spain

***Correspondence:**
Andrew W. Poon, Photonic Device Laboratory, Department of Electronic and Computer Engineering, The Hong Kong University of Science and Technology, Clear Water Bay, Kowloon, Hong Kong, China
eeawpoon@ust.hk

Specialty section:
This article was submitted to Optics and Photonics, a section of the journal Frontiers in Materials

Received: *31 January 2015*
Accepted: *01 April 2015*
Published: *27 April 2015*

Citation:
Wang J, Yao Z and Poon AW (2015) Silicon-nitride-based integrated optofluidic biochemical sensors using a coupled-resonator optical waveguide Front. Mater. 2:34. doi: 10.3389/fmats.2015.00034

Silicon nitride (SiN) is a promising material platform for integrating photonic components and microfluidic channels on a chip for label-free, optical biochemical sensing applications in the visible to near-infrared wavelengths. The chip-scale SiN-based optofluidic sensors can be compact due to a relatively high refractive index contrast between SiN and the fluidic medium, and low-cost due to the complementary metal-oxide-semiconductor (CMOS)-compatible fabrication process. Here, we demonstrate SiN-based integrated optofluidic biochemical sensors using a coupled-resonator optical waveguide (CROW) in the visible wavelengths. The working principle is based on imaging in the far field the out-of-plane elastic-light-scattering patterns of the CROW sensor at a fixed probe wavelength. We correlate the imaged pattern with reference patterns at the CROW eigenstates. Our sensing algorithm maps the correlation coefficients of the imaged pattern with a library of calibrated correlation coefficients to extract a minute change in the cladding refractive index. Given a calibrated CROW, our sensing mechanism in the spatial domain only requires a fixed-wavelength laser in the visible wavelengths as a light source, with the probe wavelength located within the CROW transmission band, and a silicon digital charge-coupled device/CMOS camera for recording the light scattering patterns. This is in sharp contrast with the conventional optical microcavity-based sensing methods that impose a strict requirement of spectral alignment with a high-quality cavity resonance using a wavelength-tunable laser. Our experimental results using a SiN CROW sensor with eight coupled microrings in the 680 nm wavelength reveal a cladding refractive index change of ~1.3×10^{-4} refractive index unit (RIU), with an average sensitivity of ~$281 \pm 271\ \mathrm{RIU}^{-1}$ and a noise-equivalent detection limit of $1.8 \times 10^{-8} \sim 1.0 \times 10^{-4}$ RIU across the CROW bandwidth of ~1 nm.

Keywords: silicon nitride, biochemical sensor, integrated optofluidics, coupled-resonator optical waveguide, microring resonators, CMOS-compatible, elastic light scattering, visible wavelengths

Introduction

In recent years, the increasing demands of medical diagnostics outside a clinic or a laboratory and self-monitoring for personal healthcare have highly motivated the rapid research and development of portable, low-cost biochemical sensors (Estevez et al., 2012). Particularly, miniaturized, label-free

biochemical sensors are highly desired in order to be readily deployed at or carried to the sensing environment and to read-out in real-time, quantitative biochemical information about the environment (Vollmer et al., 2008). Among various demonstrated chip-scale photonic biochemical sensors, optical microresonator-based biosensors featuring optical resonances with a high quality (Q) factor ($10^3 \sim 10^4$) promise a high sensitivity [few tens to hundreds of nanometer resonance shift per refractive index unit (RIU)], a low detection limit ($10^{-7} \sim 10^{-4}$ RIU) and a compact footprint (few to hundreds of micrometer square) (De Vos et al., 2007; Ciminelli et al., 2013; Sedlmeir et al., 2014). However, such high-Q microcavity-based sensors working in the spectral domain are constrained by a narrow resonance bandwidth as the sensing window, which requires a strict resonance alignment and thus may compromise the reliability of the sensor system. Besides, the sensing implementation typically requires a precision wavelength-scanning setup, such as a wavelength-tunable laser, which may limit the portability of the sensor system.

Other than microcavity-based biochemical sensors, integrated interferometric optical biochemical sensors also attract increasing attentions. Various kinds of interferometer structures, including Mach–Zehnder interferometers (MZI) (Densmore et al., 2008; Kozma et al., 2009; Duval et al., 2013; Halir et al., 2013; Dante et al., 2015), Young interferometers (Ymeti et al., 2007), and Hartman interferometers (Xu et al., 2007) have been adopted as integrated interferometric biochemical sensors, demonstrating a high sensitivity ($10^2 \sim 10^4$ rad/RIU) along with a low detection limit ($10^{-7} \sim 10^{-5}$ RIU). One key merit of such integrated interferometric sensors is that they require a relatively simple configuration, which typically comprises a fixed-wavelength laser source and a photodetector. However, these interferometric sensors are not tolerant to equipment noises that cause output intensity variations, such as laser intensity variations.

Previously, our research group has proposed a coupled-resonator optical waveguide (CROW)-based biochemical sensing scheme using what we termed "pixelized pattern detection" in the spatial domain (Lei and Poon, 2011). The scheme employs the discrete transition of the CROW eigenstate excited at a fixed laser wavelength upon a small change in the cladding refractive index, Δn, and detects the resulting change in mode-field-intensity distribution by far-field measurement of the out-of-plane elastic-light-scattering intensity patterns. Such a sensing scheme in principle only requires relatively simple optical sources and imaging systems including a fixed-wavelength laser and a camera. Recently, we have experimentally demonstrated a proof of concept of such a chip-scale CROW-based sensor on the silicon-on-insulator (SOI) platform in the 1550 nm telecommunication wavelengths (Wang et al., 2014). We have extended the scheme by detecting the continuous modulation of the CROW mode-field-intensity distribution at a fixed wavelength upon a Δn by correlating the elastic-light-scattering patterns with reference patterns at the CROW eigenstates. Compared with interferometric sensors, the correlation analysis allows our sensing scheme to be more tolerant to equipment noises that are common to all pixels of the CROW sensor yet do not cause a spectral shift, including laser intensity variations. Our previous experiment demonstrated a Δn of $\sim 1.5 \times 10^{-4}$ RIU and a noise-equivalent detection limit (NEDL) of $2 \times 10^{-7} \sim 9 \times 10^{-4}$ RIU. However, the choice of the SOI platform and the experimental setup configuration (including a 1550 nm laser, an optical amplifier and an InGaAs camera) render our previous work not practical for point-of-care optical biochemical sensing applications. Particularly, in order to leverage the wide availability of smartphones for biochemical sensing (Lakshminarayanan et al., 2015), it would be advantageous to switch the operational wavelength of the sensor from the telecommunication wavelengths to the visible or near-infrared wavelengths that can be readily recorded using high-resolution silicon charge-coupled device (CCD)/complementary metal-oxide-semiconductor (CMOS) cameras.

In this paper, we report our experimental demonstration of the CROW-based biochemical sensors in the visible wavelengths in the silicon-nitride (SiN) platform. The SiN platform is transparent to the visible and near-infrared wavelengths (Gorin et al., 2008; Subramanian et al., 2013) and its fabrication process is CMOS-compatible. After the CROW calibration steps, our sensing scheme in principle only requires a fixed-wavelength, low-output-power, visible laser source, and a silicon CCD/CMOS camera for recording out-of-plane light-scattering patterns from the top-view. This offers a promising opportunity to integrate the CROW sensor with a smartphone that is equipped with a compact laser source and a high-resolution camera with a properly designed optical interface for future smartphone-based point-of-care applications.

Principle and Methods

Principle and the Sensing Algorithm

Figure 1 illustrates the principle of the CROW-based biochemical sensor following our previous work (Wang et al., 2014). Here, we outline the key concepts of the principle for understanding this work. **Figure 1A** schematically shows a SiN CROW sensor comprising eight coupled microring resonators with identical design, coupled to input and output bus waveguides in an add-drop filter configuration. For a perfect CROW comprising C coupled identical single-mode resonators, the inhomogeneously broadened transmission spectrum features a combination of split mode resonances, with each mode slightly shifted from the original resonance frequency due to inter-cavity-coupling effect. Therefore, the eigenstate number N within each transmission band always equals to the resonator number C. While a perfect CROW exhibits distinctive mode-field-amplitude distributions at eigenstates, the pair of symmetric and anti-symmetric split-modes at different eigenfrequencies have non-distinctive mode-field-intensity distributions. In practice, a CROW inevitably suffers from fabrication imperfections. The coupled resonators are no longer identical nor are identically coupled. The symmetry breaking between the pair of symmetric and anti-symmetric split-modes therefore results in distinctive mode-field-intensity distributions at all discernable eigenstates. The resulting phase disorders and coupling disorders can result in the split mode resonances to be spectrally overlapped. Therefore, in the presence of structural non-uniformity, N could be equal to or smaller than C ($N \leq C$).

Figure 1B schematically illustrates the inhomogeneously broadened transmission bands upon applying cladding refractive indices n_0 and $n_0 + \Delta n$, for an imperfect eight-microring

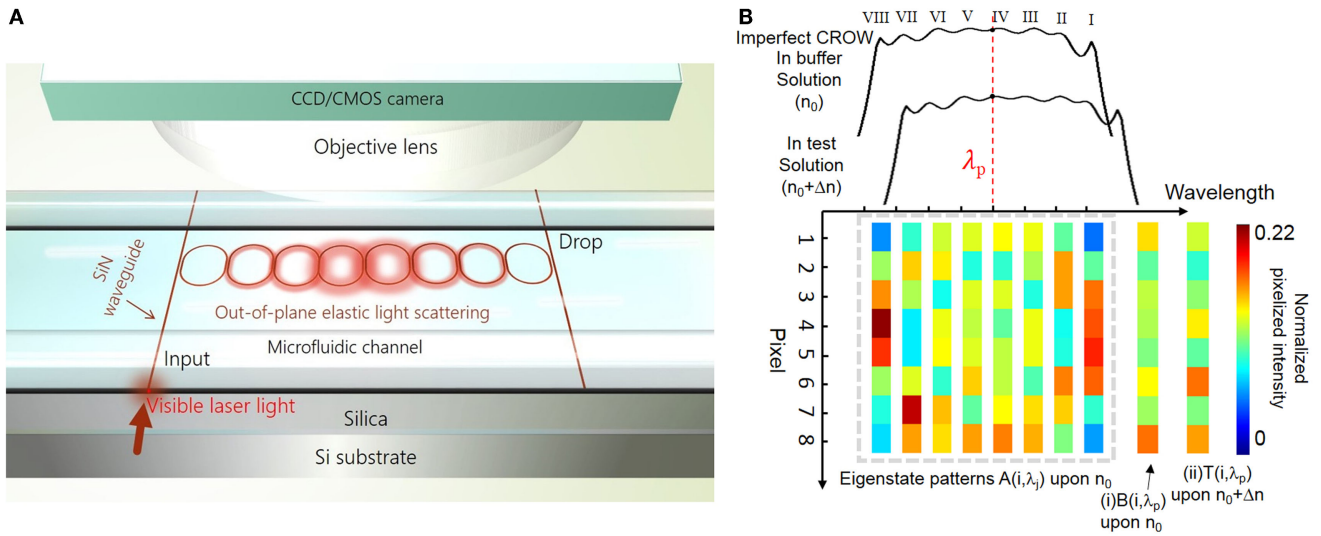

FIGURE 1 | Principle of SiN CROW-based biochemical sensors using out-of-plane elastic light scattering at the visible wavelengths. (A) Schematic of a SiN CROW-based sensor integrated with a microfluidic channel. An objective lens and a CMOS/CCD camera are applied on top of the optofluidic chip in order to image the out-of-plane elastic-light-scattering pattern. **(B)** Illustration of characterizing an imperfect eight-microring CROW, including the inhomogeneously broadened transmission bands upon a buffer solution (n_0) and a test solution ($n_0 + \Delta n$), and pixelized mode-field-intensity distributions at eigenstate wavelength λ_j upon n_0, A(λ_j). Insets: pixelized mode-field-intensity distributions at probe wavelength, λ_p, (i) upon n_0 [B(λ_p)]; and (ii) upon $n_0 + \Delta n$ [T(λ_p)].

CROW exhibiting a complete set of eight distinctive eigenstate mode-field-intensity distributions. With the mode-field intensity of each microring integrated as a pixel, we denote the pixelized one-dimensional pattern at the eigenstate as {A_j}, with j indexing the eigenstate. Any mode-field-amplitude distribution at an arbitrary wavelength, λ_p, within the CROW transmission band upon n_0 can be expressed by a linear superposition of the complete set of eigenstate mode-field-amplitude distributions upon n_0. Therefore, we are able to uniquely identify any pixelized mode-field-intensity profile at λ_p upon n_0, B(λ_p), as shown in inset (i), with {A_j} by a correlation analysis. Upon a small Δn applied homogenously to the cladding, we can uniquely identify by the correlation analysis any pixelized mode-field-intensity distribution at λ_p upon $n_0 + \Delta n$, T(λ_p), as shown in inset (ii), with {A_j}.

As in our previous work (Wang et al., 2014), we adopt the Pearson's correlation coefficient, ρ, in order to analyze the degree of correlation between a pixelized pattern at an arbitrary probe wavelength λ_p, B(λ_p), and the pixelized patterns at the eigenstate wavelengths λ_j, A(λ_j). For a CROW with a number of coupled single-mode cavities, C, and a number of discernable eigenstates, N ($\leq C$), we define ρ at λ_p for A(λ_j) as follows:

$$\rho_j(\lambda_p) = \frac{\sum_{i=1}^{C} (A(i,\lambda_j) - \overline{A(\lambda_j)})(B(i,\lambda_p) - \overline{B(\lambda_p)})}{\sqrt{\sum_{i=1}^{C} (A(i,\lambda_j) - \overline{A(\lambda_j)})^2} \sqrt{\sum_{i=1}^{C} (B(i,\lambda_p) - \overline{B(\lambda_p)})^2}} \quad (1)$$

where $j = 1, 2, \ldots, N$ is the eigenstate number, and $i = 1, 2, \ldots, C$ is the cavity (pixel) number. A(i, λ_j) and B(i, λ_p) are the pixel values normalized to the total intensity of the entire patterns, respectively. The bar sign denotes the mean of the entire pixelized pattern over C pixels.

We adopt the Pearson's correlation coefficient approach to describe the linear dependence of the measured and calibrated intensity distributions. The Pearson's correlation approach is insensitive to both level and scale variations of the intensity distributions. Therefore, the approach is tolerant to equipment noise sources, such as uniform background light imaged onto the camera and the intensity variation of the laser source, which are common to all pixels and do not cause a spectral shift. However, this approach still suffers from the noises that cause a spectral shift, such as a wavelength drift of the laser source and thermal variations in the test environment.

Here, we detail our sensing algorithm following our previous work (Wang et al., 2014). **Figure 2** shows a flow chart illustrating our sensing algorithm including calibration. We first generate a library of correlation coefficients $\{\rho_j'(\lambda_0)\}$, defined at a fixed reference wavelength λ_0 centered at the CROW transmission band. The library is calibrated over a range of Δn values, Δn_d, given by an integer multiple of a minimum refractive index change interval Δn_i. The $\{\rho_j'(\lambda_0)\}$ thus comprises a library of data array of N (rows) × M (columns), where M is given by $\Delta n_d/\Delta n_i$.

For sensing, we first measure the pixelized mode-field-intensity pattern in a buffer solution at a fixed probe wavelength λ_p (which is generally offset from λ_0) as B(λ_p) (**Figure 1B**). We correlate B(λ_p) with the eigenstate patterns {A_j} in order to extract {$\rho_j(\lambda_p)$}. We look for the closest match of {$\rho_j(\lambda_p)$} with the library $\{\rho_j'(\lambda_0)\}$, using only the principal (largest) component, ρ^p, and the second-principal (second-largest) component, ρ^s, of {$\rho_j(\lambda_p)$} in order to streamline the pattern recognition process

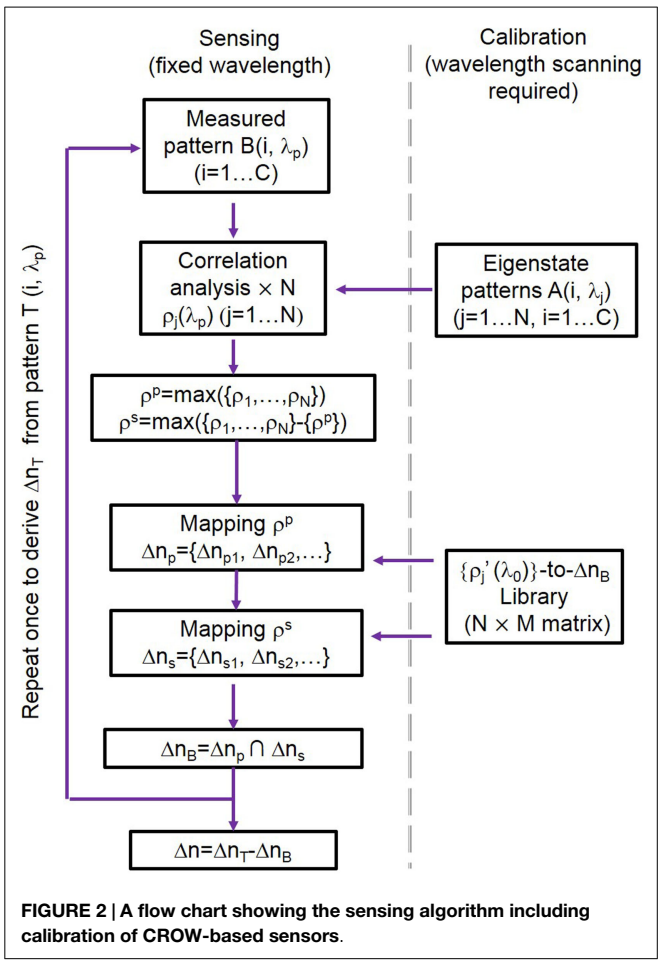

FIGURE 2 | A flow chart showing the sensing algorithm including calibration of CROW-based sensors.

(Wang et al., 2014). We thus obtain a unique equivalent refractive index change for the buffer solution, Δn_B, which is only due to the offset between λ_p and λ_0. We repeat the same procedure for measuring the pattern at λ_p upon the test solution, $T(\lambda_p)$, and obtain another unique equivalent refractive index change Δn_T. Finally, we obtain $\Delta n = \Delta n_T - \Delta n_B$.

Transfer-Matrix Modeling of Imperfect CROW Sensors

We model imperfect SiN CROWs in 680 nm wavelengths using transfer-matrix method with empirical inputs (Wang et al., 2014) (see Supplementary Materials S1 and S2). We measure and accumulate statistics of the measured waveguide widths and coupling gap widths from scanning-electron microscope (SEM) characterization of our fabricated devices. We sample six waveguide widths and three coupling gap width in one coupling region, and measure a total of eighteen coupling regions in two representative eight-microring CROW devices (see Supplementary Material S3). The statistics of the waveguide widths and the coupling gap widths approximately follow two Gaussian distributions. We extract the fabricated waveguide width of 427.5 ± 1.1 nm and coupling gap spacing of 129.1 ± 1.0 nm. In the modeling, we assume that the two Gaussian distributions are independent, and we generate a set of varied waveguide widths and coupling gap spacing randomly distributed across the CROW using the Gaussian number generator in Matlab.

We study the effects of these empirical inputs on the device parameters, including the waveguide effective refractive index, n_{eff}, and the inter-cavity coupling coefficient, κ. We calculate using the numerical finite-element method (FEM) (COMSOL RF module) the n_{eff} of a SiN channel ridge waveguide for the transverse-magnetic (TM)-polarized mode, as a function of waveguide width around 427.5 nm at a fixed waveguide height of 300 nm upon a water upper-cladding. We adopt the measured material refractive index of the deposited 300 nm-thick SiN film as a function of wavelength using ellipsometry. The mean value of the calculated n_{eff} is 1.5994 ± 0.0003 at 686 nm. We choose the TM polarization mode in order to obtain a large evanescent field exposure near the waveguide top surface for better light–analyte interaction. We calculate the coupling coefficient in each directional coupling region as a function of the coupling gap spacing, assuming the waveguide width is fixed at 427.5 nm. We estimate the waveguide propagation loss upon a water upper-cladding to be relatively high at ~17 dB/cm based on our measurements. We attribute this primarily to surface-roughness-induced scattering losses from the waveguide sidewall. We apply the designed racetrack arc radius and interaction length into the modeled CROW. We find from our FEM calculations a linear relationship between Δn and the resulting effective refractive index change Δn_{eff}, which we apply to our transfer-matrix modeling (see Supplementary Materials S1 and S2).

Device Fabrication

We fabricate the CROW devices in a 4″ silicon wafer. The silicon wafer is first grown with a ~2 µm-thick thermal oxide. We grow nitrogen-rich SiN by plasma-enhanced chemical vapor deposition (PECVD) (SiH_4:NH_3 = 25:40 (sccm), 300°C, 13.56 MHz). The thickness of SiN layer is ~300 nm. We fabricate the CROW device pattern by electron-beam lithography (JEOL JBX-6300FS) using a positive electron-beam resist ZEP-520A. We transfer the device pattern to the SiN layer by inductively coupled plasma etching with C_4F_8 and SF_6 gases (STS ICP DRIE Silicon Etcher). **Figure 3A** shows the optical micrograph of the fabricated SiN eight-microring CROW device. The racetrack microring comprises two half circles with a radius of 20 µm and two straight waveguides with an interaction length (L_c) of 4 µm. We design the waveguide width to be 450 nm and the coupling gap spacing to be 100 nm. **Figure 3B** shows a zoom-in-view optical microscope image of the CROW. **Figure 3C** shows a SEM picture of the coupling region.

We fabricate a microfluidic chamber on a polydimethylsiloxane (PDMS) layer. We pattern a SU8 film by contact photolithography as a mold in order to form the PDMS microfluidic channel by imprinting. The designed dimension of microfluidic channel is 8 mm × 2 mm × 50 µm (length, width, and height). We use a puncher to make two holes, each with a diameter of 1 mm, as an inlet and outlet for solution delivery. The diced silicon chip and the PDMS microfluidic layer are treated with oxygen plasma and directly bonded, with the microfluidic channel encompassing the CROW sensor. The bonded PDMS–SiN interface is stable enough for repeating the sensing experiments for many times under a relatively high fluidic pump pressure. **Figure 3D** schematically shows the cross-sectional view of the optofluidic chip.

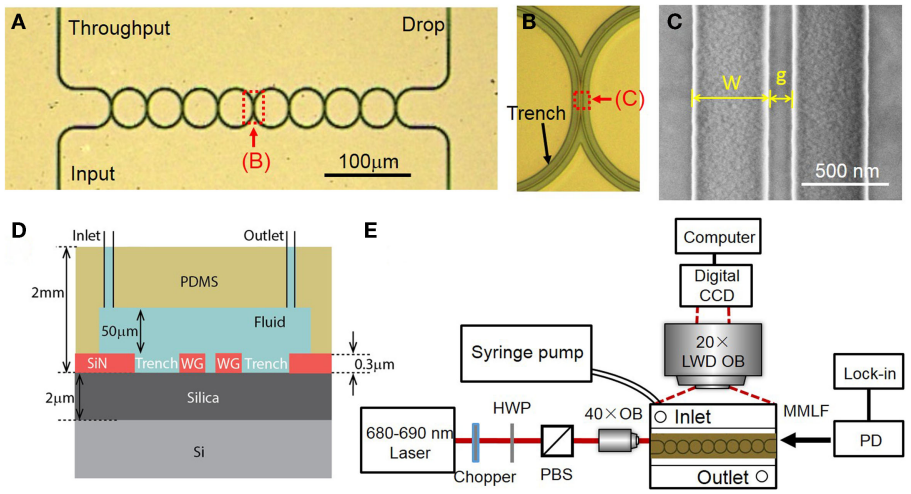

FIGURE 3 | (A) Optical micrograph of the fabricated eight-microring CROW. **(B)** Zoom-in-view picture of the CROW. **(C)** Scanning-electron microscope image of an inter-cavity coupling region of the CROW. **(D)** A cross-sectional view of the SiN chip integrated with a microfluidic channel. **(E)** Schematic of the experimental setup. HWP, half-wave plate; PBS, polarizing beam splitter; LWD OB, long-working-distance objective lens; OB, objective lens; PD, photodetector; MMLF, multimode lensed fiber.

Experimental Method

Figure 3E schematically shows the experimental setup. The wavelength-tunable laser light in the 680 nm wavelengths is end-fired into a tapered 3 μm-wide SiN waveguide through an objective lens (NA = 0.65). The laser power before coupling into the chip is ~2 mW. The polarization is controlled by a half-wave plate before a polarizing beam splitter. The output light from the throughput- or drop-port is collected using a multimode lensed fiber to a silicon power meter and a lock-in amplifier.

For elastic-light-scattering pattern imaging from the top view, we use a long-working-distance microscope objective lens (20× Mitutoyo Plan Apo, NA = 0.42) and a CCD camera (Diagnostic Instruments, Inc., RT3) with 1600 × 1200 pixels (7.4 μm-sized pixels). The camera has an effective differential cooling of −43°C and an 8-bit analog-to-digital conversion in data readout. We fix the exposure time as 60 ms and the gain of ~1. For background subtraction, we set the probe wavelength in between the CROW transmission bands in order to obtain a background image.

In order to acquire the library of calibrated correlation coefficients, we scan the laser wavelength in steps of 0.02 nm over ~2 free spectral ranges (FSRs) of the CROW sensor. We record at each wavelength eight successive images over a time period of 4 s (at 2 frames/s). We take average of these successive images in order to reduce the systematic equipment noise contribution. In the sensing tests, we inject the buffer and test solutions, and start recording the images after the scattering pattern is stabilized upon an essentially static fluidic medium. We record over 50 successive images during a time period of 25 s at a fixed probe wavelength.

In order to calibrate the spectral sensitivity of the CROW, we prepare NaCl solutions with mass concentrations from 1 to 5% (in steps of 1%) and test the transmission band spectral shifts upon a Δn. Between each measurement, we rinse the chip by injecting deionized (DI) water using a fluidic pump. We obtain the resonance spectral shifts by fitting the throughput-transmission spectra with a sum of multiple inverted Lorentzian lineshapes, each centered at the resonance (eigenstate) wavelength. The overall transmission band shift is taken as the average value of the spectral shifts of all the eigenstates.

Results

Modeling Results

Figure 4 shows the modeling results for $N = C$ (see Supplementary Material S4 for modeling results corresponding to the case $N < C$). **Figure 4A** schematically shows an imperfect SiN CROW with varied waveguide width and coupling gap width of each microring. Inset shows the numerically calculated waveguide mode-field-amplitude profile in the TM mode at 686 nm wavelength. **Figure 4B** shows the modeled throughput- and drop-transmission spectra of an imperfect eight-microring CROW. We define the CROW transmission bandwidth, $\Delta\lambda_{BW}$, as the spectral range between the first and last discernable eigenstates within the transmission band. **Figure 4C** shows the modeled pixelized patterns at the eight eigenstates. **Figure 4D** shows the calculated library $\left\{\rho_j'(\lambda_0)\right\}$ as a function of Δn, with $\Delta n_d = 2.523 \times 10^{-2}$ and $\Delta n_i = 3.6 \times 10^{-4}$ RIU. **Figure 4E** shows the calculated differential correlation coefficients per unit Δn, given as $|d\left(\rho_j'(\lambda_0)\right)/d(\Delta n)|$.

We define the CROW sensitivity (in units of RIU^{-1}) at an arbitrary λ_p within the transmission band as the larger $|d\left(\rho_j'(\lambda_p)\right)/d(\Delta n)|$ of the ρ^p and ρ^s. **Figure 4F** shows the modeled sensitivity as a non-linear function of λ_p. The sensitivity in the transmission band spans a range from ~73 to ~1440 RIU^{-1}, with an average sensitivity of ~553 ± 290 RIU^{-1}. We quantify the non-uniformity of the sensitivity by the ratio of SD value to average sensitivity value. A lower ratio value suggests a more uniform sensitivity. The extracted non-uniformity ratio from

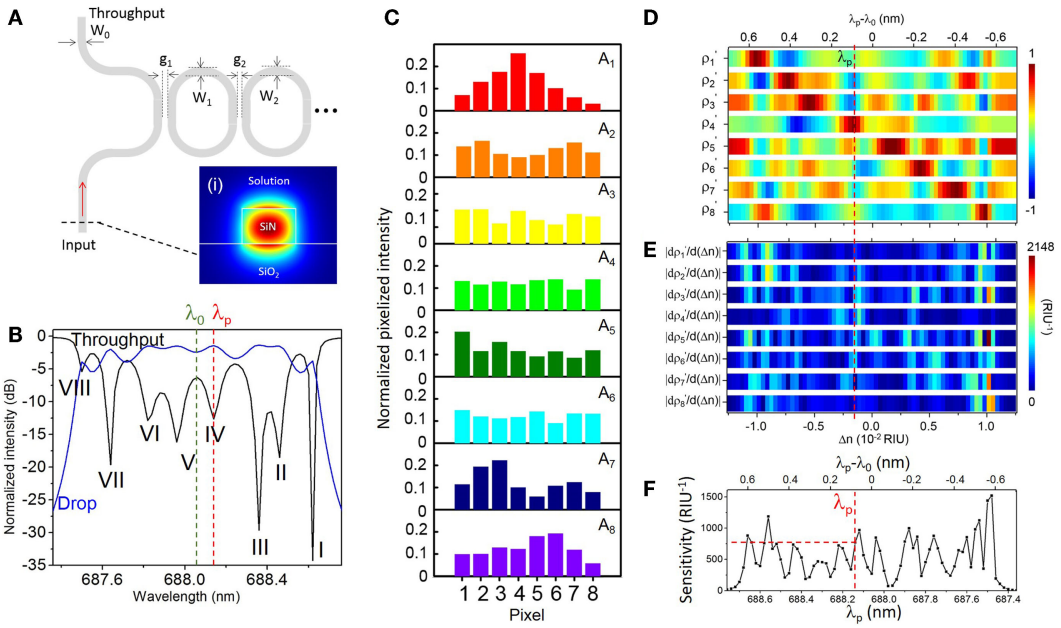

FIGURE 4 | (A) Schematic of an imperfect CROW model with non-uniform waveguide widths (W_0, W_1, W_2, . . . W_{N+1}) and coupling gap spacing (g_1, g_2, . . . g_{N+1}). Inset (i): numerically calculated waveguide mode-field amplitude profile in the TM mode. **(B)** Modeled throughput- and drop-port transmission spectra of an imperfect eight-microring CROW using transfer-matrix modeling. Green and red dashed-lines indicate the reference wavelength λ_0 of 688.06 nm and the probe wavelength λ_p of 688.14 nm, respectively. **(C)** Modeled normalized pixelized intensity patterns at the eight eigenstates, I–VIII. **(D)** Calculated library of the correlation coefficients $\rho_1' - \rho_8'$ as a function of Δn at λ_0, with $\Delta n_d = 2.523 \times 10^{-2}$ and $\Delta n_i = 3.6 \times 10^{-4}$ RIU. **(E)** Calculated library of the differential correlation coefficients as a function of Δn at λ_0, given as $|d\left(\rho_j'(\lambda_0)\right)/d(\Delta n)|$. **(F)** Calculated sensitivity as a function of λ_p. The red dashed-line indicates a sensitivity of 772 RIU^{-1} at $\lambda_p = 688.14$ nm.

Figure 4F is ~0.52. Although such a sensitivity variation is not ideal, we can obtain a practical sensitivity within a wide enough wavelength window without fine-tuning the probe wavelength. As an example, we can set a practical sensitivity of ~100 RIU^{-1} in order to sense a Δn down to 10^{-5} RIU (assuming a noise-induced uncertainty of correlation coefficients of $\sim\pm 10^{-3}$). From **Figure 4F**, the width of the probe wavelength window with a sensitivity >100 RIU^{-1} is 1.1 nm. We consider this sufficiently wide for sensing with a practical sensitivity at an arbitrarily set probe wavelength. If a higher practical sensitivity of, say, 200 RIU^{-1} is desired, the width of the probe wavelength window with a sensitivity >200 RIU^{-1} narrows to ~1.06 nm.

Here, we arbitrarily choose λ_p at 688.14 nm near the center of the CROW transmission band (**Figure 4B**) in order to model the sensing test. The sensitivity at λ_p is ~772 RIU^{-1}. **Figure 5** illustrates the modeled sensing results. **Figure 5A** shows the modeled pixelized patterns at λ_p, $B(\lambda_p)$ and $T(\lambda_p)$, assuming a water buffer ($n_0 = 1.331$) and an arbitrarily chosen Δn value of 2.50×10^{-3} RIU, respectively. **Figure 5B** shows the two sets of correlation coefficients extracted from the two modeled pixelized patterns without and with Δn. The ρ^p and ρ^s without Δn are ρ_4 and ρ_5, respectively. The ρ^p and ρ^s with Δn are ρ_5 and ρ_3, respectively. **Figures 5C,D** show the zoom-in view of the calculated library $\left\{\rho_j'(\lambda_0)\right\}$ as a function of Δn. Insets show the detailed mappings of ρ^p and ρ^s with the library. We extract using linear interpolation from the library $\Delta n = \Delta n_T - \Delta n_B = 2.52 \times 10^{-3}$ RIU, which agrees with the arbitrarily chosen Δn value. We attribute the deviation of 2×10^{-5} RIU to the interpolation error. In principle, the maximum error upon the sampling interval in the library is given by $\pm \Delta n_i/2$, which is ~1.8×10^{-4} RIU given the assumed Δn_i value.

Calibrating the CROW Sensor in a Buffer Solution

Figure 6 summarizes the characterization results upon a buffer solution (DI water). **Figure 6A** shows the measured TM-polarized transmission spectra with DI water upper-cladding. The measured FSR of ~1.80 nm is consistent with the microring circumference. The CROW exhibits an inhomogeneously broadened transmission band, with a $\Delta\lambda_{BW}$ of ~1.10 nm. We discern eight eigenstates within each transmission band (labeled by I to VIII for the first transmission band, and I′–VIII′ for the second transmission band in **Figure 6A**).

Figure 6B shows the measured elastic-light-scattering images at eigenstates I–VIII. We observe a non-uniform scattering image profile across each microring. We attribute this to the extra modulation of the surface roughness and local defects to the intrinsic mode-field-intensity distributions. We notice an obvious "local hotspot" in the coupling region between microring 3 and microring 4 in all the light-scattering images. We attribute that to the larger surface roughness localized in the coupling region between microring 3 and microring 4. We integrate within a certain window the elastic-light-scattering intensity of each microring to form a single pixel. The window excludes the coupling region in order to avoid scattering-induced crosstalks between

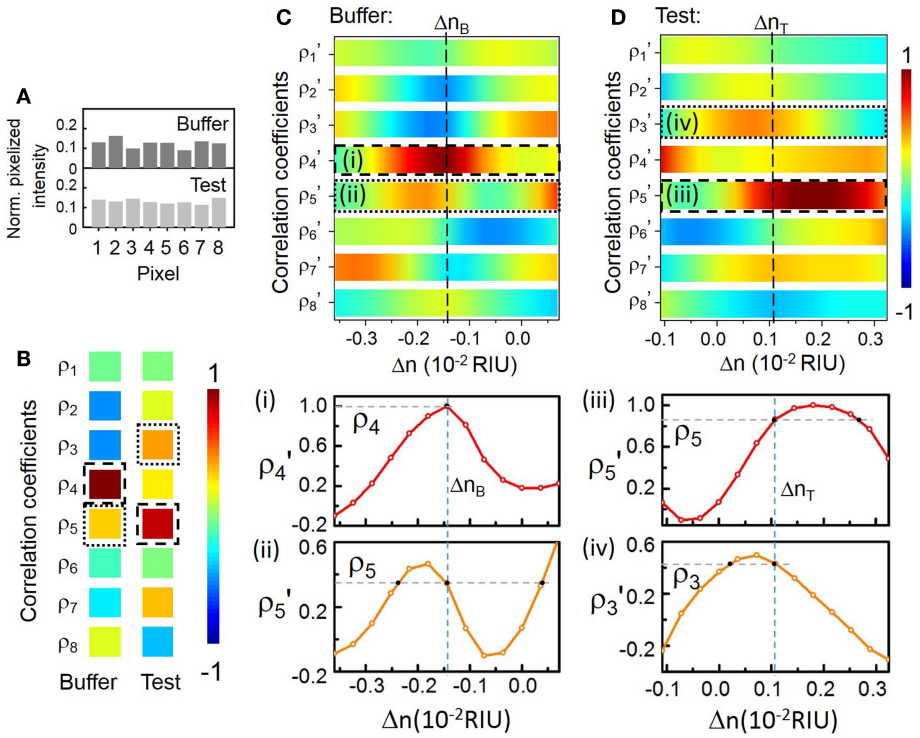

FIGURE 5 | (A) Modeled normalized pixelized patterns at λ_p (688.14 nm) upon n_0 and $n_0 + \Delta n$. **(B)** Calculated correlation coefficients at $\lambda_p = 688.14$ nm upon n_0 and $n_0 + \Delta n$. The dashed-line and the dotted-line boxes indicate ρ^p and ρ^s, respectively. **(C,D)** Zoom-in view of the calculated library of ρ_j' as a function of Δn. Dashed-lines indicate the mapping of Δn_B, Δn_T for buffer solution and test solution, respectively. Insets (i)–(iv): Mapping of ρ^p and ρ^s with the library to extract Δn_B and Δn_T.

the coupled waveguides and local hotspots. Here we normalize the patterns with the estimated contributions of the surface-roughness-induced scattering as a step for pattern correction (see Supplementary Material S5). **Figure 6C** shows the corrected pixelized mode-field-intensity patterns at the eight eigenstates. We use the corrected pixelized patterns for sensing.

Figure 6D shows the measured library of the calibrated correlation coefficients as a function of Δn. Here, we calibrate the sensor by scanning the laser wavelength over $\pm\Delta\lambda$ ($\Delta\lambda = 0.7$ nm) about the center of the CROW transmission band spanning a FSR upon a fixed buffer solution (DI water), with a minimum wavelength step of 0.02 nm. This interval corresponds to a Δn_i of $\sim 3.5 \times 10^{-4}$ RIU, based on the calibrated linear spectral sensitivity of ~57.30 nm/RIU of the CROW sensor (see Supplementary Material S6). We also convert $\Delta\lambda$ back to Δn using the calibrated linear spectral sensitivity. The corresponding range of Δn_d is $\sim \pm 1.2 \times 10^{-2}$ RIU.

Figure 6E shows the calculated $|d\rho_j'/d(\Delta n)|$ as a function of Δn. **Figure 6F** shows the calculated sensitivity as a function of λ_p over the $\lambda_0 \pm \Delta\lambda$ range. The calculated sensitivity value shows highly non-uniform profiles. The sensitivity ranges from ~15 to ~1420 RIU^{-1}, with an average value of $\sim 281 \pm 271$ RIU^{-1}. The extracted non-uniformity ratio from **Figure 6F** is ~0.96. The width of the probe wavelength window with a sensitivity >100 RIU^{-1} is 0.88 nm. Whereas, the width of the probe wavelength window with a sensitivity >200 RIU^{-1} narrows to ~0.48 nm, which is still relatively tolerant to set a probe wavelength. In conventional microcavity-based sensing methods, the sensitivity is only applicable within the high-Q transmission band (~0.1 nm in De Vos et al., 2007), which is generally much narrower than our probe wavelength window.

We define the NEDL at λ_p as the uncertainty of extracted Δn. We repeat the extraction of Δn values based on ρ^p and ρ^s at each λ_p for eight times and calculate the SD of the eight extracted Δn values. **Figure 6G** shows the extracted NEDL values as a function of λ_p, which shows a high dependence on the choice of λ_p. The NEDL values range from $\sim 2 \times 10^{-8}$ to $\sim 1 \times 10^{-4}$ RIU. We observe particularly low NEDL values (~10^{-8} RIU) at λ_p aligning with the eigenstate wavelengths. We attribute the low NEDL at each eigenstate to the particularly low uncertainty of ρ^p ($\sim \pm 10^{-6} - 10^{-4}$) close to 1 at each eigenstate. Upon eight repeated tests at a fixed probe wavelength at each eigenstate, the measured pixelized patterns only slightly deviate from the calibrated eigenstate distributions due to the low noise in the cooled silicon CCD camera and the low thermo-optic coefficient of SiN. The low uncertainties of ρ^p at each eigenstate are converted into particularly low NEDL values.

In order to quantify the sensing resolution, here we define the resolution of the CROW sensor as the lowest refractive index change that can be sensed reliably and repeatedly. In practice, there are two main limiting factors to the resolution. One is the interpolation error in extracting Δn. The other is

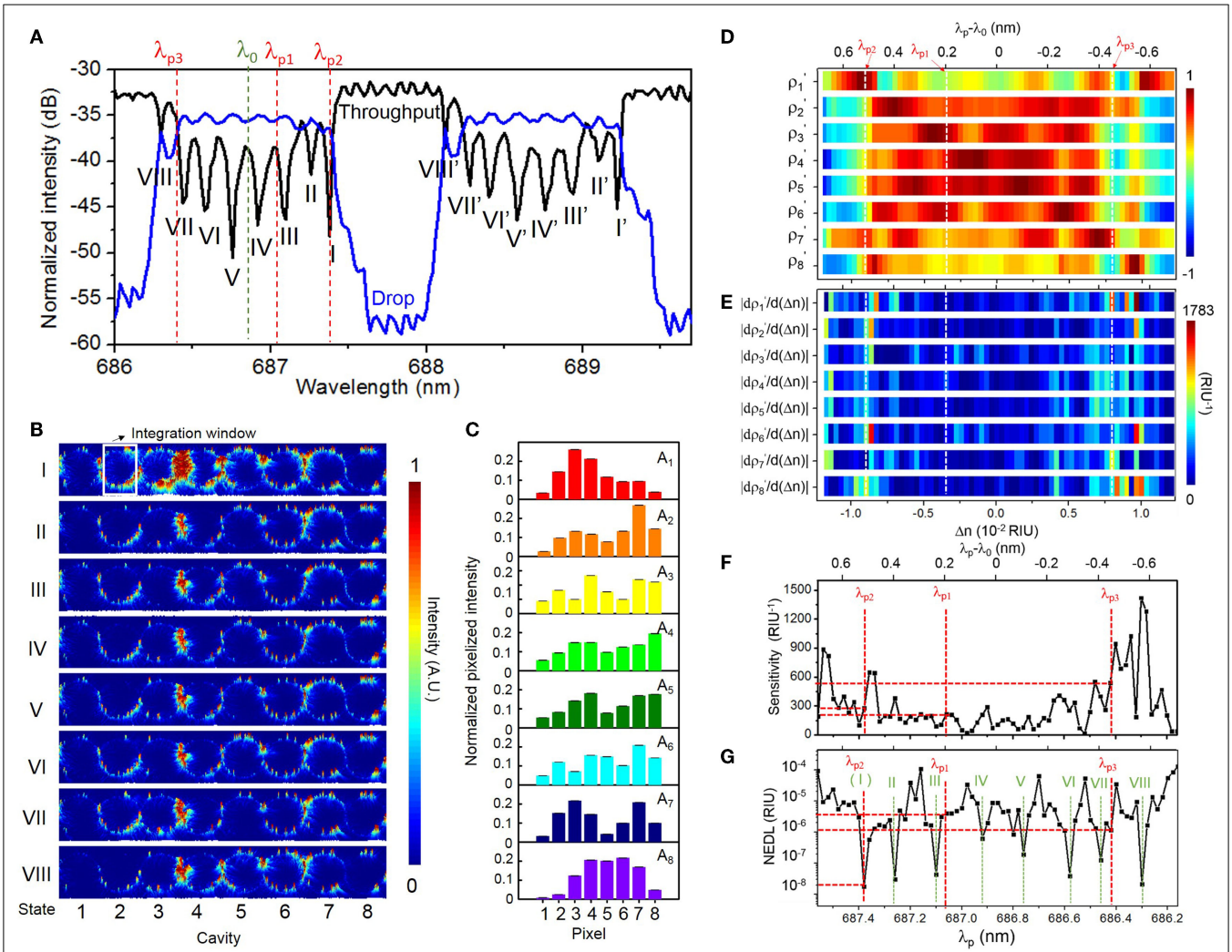

FIGURE 6 | (A) Measured TM-polarized throughput- and drop-port transmission spectra of the eight-microring SiN CROW with DI water upper-cladding. Green and red dashed-lines indicate the reference wavelength λ_0 (686.86 nm) and three probe wavelengths, λ_{p1} (687.06 nm), λ_{p2} (687.38 nm), and λ_{p3} (686.42 nm). **(B)** Measured elastic-light-scattering images with DI water upper-cladding at the eight eigenstates I–VIII. The white-line box indicates the integration window for pixelization. **(C)** Normalized pixelized mode-field intensity patterns at the eight CROW eigenstates I–VIII. **(D)** Calculated library of the calibrated correlation coefficients $\rho_1' - \rho_8'$ as a function of Δn. White dashed-lines indicate the Δn_B values at λ_{p1}, λ_{p2}, and λ_{p3}. **(E)** Calculated differential correlation coefficients as a function of Δn, given as $|d\left(\rho_j'(\lambda_0)\right)/d(\Delta n)|$. **(F)** Calculated sensitivity as a function of λ_p. Red dashed-lines indicate sensitivities of 214, 279, and 541 RIU^{-1} at probe wavelengths λ_{p1}, λ_{p2}, and λ_{p3}, respectively. **(G)** Extracted noise-equivalent detection limit (NEDL) as a function of λ_p. Red dashed-lines indicate NEDL values of ~4×10^{-6}, ~2×10^{-8}, and ~1×10^{-6} RIU at λ_{p1}, λ_{p2}, and λ_{p3}, respectively. Green dashed-lines indicate the eight eigenstate wavelengths λ_j.

the NEDL taking into account all the noise sources that our correlation approach is not tolerant to. Therefore, given a calibration interval of Δn_i (3.5×10^{-4} RIU), the worst resolution is ~1.8×10^{-4} RIU given $\pm \Delta n_i/2$ (1.8×10^{-4} RIU) and the NEDL (~$1.8 \times 10^{-8} - 1.0 \times 10^{-4}$ RIU in **Figure 6G**). The interpolation-error-limited resolution ($\pm\Delta n_i/2$) suggests that a Δn below $\Delta n_i/2$ may not be tested reliably or repeatedly. The resolution can be improved by adopting a finer Δn_i.

We also calibrate the CROW sensor in the adjacent transmission band (see Supplementary Material S7). The pixelized mode-field intensity patterns at eigenstates I′–VIII′ show a high similarity with the corresponding patterns at eigenstates I–VIII, respectively. The extracted sensitivity and NEDL range are both close to the calibrated results of the first transmission band.

Blind Sensing Test Results

We implement blind sensing tests at three different probe wavelengths (λ_{p1}, λ_{p2}, and λ_{p3}) within the CROW transmission band. We prepare one buffer solution (DI water) and three NaCl solutions, X, Y, and Z, with different mass concentration values unknown to the researcher conducting the sensing tests. We study the images upon the buffer solution at the initial stage and upon rinsing after each sensing test. We confirm that the pixelized pattern returns to the baseline pattern (see Supplementary Material S8). **Table 1** summarizes the experimental sensing results.

TABLE 1 | Sensing results at the three probe wavelengths upon the buffer solution and the three test solutions.

λ_p	Solution	ρ^p	ρ^s	Δn_B or Δn_T ($\times 10^{-3}$ RIU)	Δn ($\times 10^{-3}$ RIU)	Sensed concentration (%)
λ_{p1} (687.06 nm)	Buffer (DI water)	ρ_3 (0.927 ± 0.003)	ρ_6 (0.866 ± 0.002)	~−3.54 ± 0.02	–	–
	X (NaCl)	ρ_6 (0.924 ± 0.003)	ρ_2 (0.838 ± 0.003)	~4.21 ± 0.01	~7.75 ± 0.02	~4.35 ± 0.01
	Y (NaCl)	ρ_4 (0.946 ± 0.002)	ρ_5 (0.854 ± 0.003)	~−2.46 ± 0.03	~1.08 ± 0.04	~0.61 ± 0.03
	Z (NaCl)	ρ_3 (0.903 ± 0.002)	ρ_6 (0.854 ± 0.008)	~−3.41 ± 0.01	~0.13 ± 0.03	~0.073 ± 0.014
λ_{p2} (687.38 nm)	Buffer (DI water)	ρ_1 (0.99996 ± 0.00003)	ρ_7 (0.622 ± 0.001)	~−9.1800 ± 0.0001	–	–
	X (NaCl)	ρ_4 (0.941 ± 0.007)	ρ_5 (0.875 ± 0.005)	~−0.79 ± 0.02	~8.39 ± 0.02	~4.70 ± 0.01
	Y (NaCl)	ρ_2 (0.841 ± 0.012)	ρ_6 (0.807 ± 0.012)	~−8.16 ± 0.02	~1.03 ± 0.02	~0.58 ± 0.01
	Z (NaCl)	ρ_1 (0.989 ± 0.001)	ρ_7 (0.622 ± 0.003)	~−9.14 ± 0.01	~0.05 ± 0.01	~0.03 ± 0.01
λ_{p3} (686.42 nm)	Buffer (DI water)	ρ_7 (0.851 ± 0.001)	ρ_2 (0.485 ± 0.002)	~7.775 ± 0.003	–	–
	X (NaCl)	ρ_1 (0.205 ± 0.015)	ρ_7 (−0.013 ± 0.014)	–	–	–
	Y (NaCl)	ρ_2 (0.519 ± 0.006)	ρ_8 (0.305 ± 0.009)	~8.81 ± 0.01	~1.04 ± 0.01	~0.58 ± 0.01
	Z (NaCl)	ρ_7 (0.783 ± 0.005)	ρ_2 (0.477 ± 0.005)	~7.90 ± 0.01	~0.13 ± 0.01	~0.069 ± 0.005

Prepared concentration values: X: (4.5 ± 0.1)%, Y: (0.60 ± 0.02)%, Z: (0.070 ± 0.002)%.

Sensing at an Arbitrarily Set Probe Wavelength λ_{p1}

Figure 7 shows the sensing results at an arbitrarily set probe wavelength λ_{p1} (687.06 nm) near the center of the CROW transmission band. The sensitivity at λ_{p1} is ~214 RIU^{-1} (see **Figure 6F**). The NEDL at λ_{p1} is ~4×10^{-6} RIU (see **Figure 6G**). **Figure 7A** shows the measured elastic-light-scattering images of the CROW upon the buffer solution and the three test solutions at λ_{p1}. **Figure 7B** shows the corresponding pixelized patterns. **Figure 7C** shows the corresponding calculated correlation coefficients. **Figures 7D–G** show the mapping of ρ^p and ρ^s in the buffer solution and the three test solutions with the library. Insets (i)–(viii) show the mapping ρ^p and ρ^s to the corresponding Δn_B or Δn_T using linear interpolations in between Δn_i.

We acquire for solution X a Δn_X of ~$(7.75 \pm 0.02) \times 10^{-3}$ RIU and for solution Y a Δn_Y of ~$(1.08 \pm 0.04) \times 10^{-3}$ RIU, both corresponding to a relatively large Δn but still within Δn_d. We acquire for solution Z (**Figure 7G**) a Δn_Z of ~$(1.3 \pm 0.3) \times 10^{-4}$ RIU. For all three solutions, we convert from the measured Δn values the sensed concentration values (see **Table 1**), which show a good agreement with the prepared values.

Sensing at λ_{p2} Aligned with Eigenstate I

Figure 8 shows the sensing results at a specifically chosen probe wavelength λ_{p2} (687.38 nm) aligned with eigenstate I. The sensitivity at λ_{p2} is ~279 RIU^{-1} (see **Figure 6F**). The NEDL at λ_{p2} is ~2×10^{-8} RIU (see **Figure 6G**), which is much lower compared with that at λ_{p2}. **Figure 8A** shows the measured elastic-light-scattering images upon the buffer solution and the three test solutions. **Figure 8B** shows the corresponding pixelized patterns. **Figure 8C** shows the corresponding calculated correlation coefficients. **Figures 8D–G** show the mapping of ρ^p and ρ^s values in the buffer solution and the three test solutions with the library (see Supplementary Material S9 for detailed mappings).

We acquire for solution X a Δn_X of ~$(8.40 \pm 0.02) \times 10^{-3}$ RIU and for solution Y a Δn_Y of ~$(1.03 \pm 0.02) \times 10^{-3}$ RIU. Both sensing results agree with the prepared concentrations of solutions X and Y. For solution Z (**Figure 8G**), we acquire a Δn_Z of ~$(0.5 \pm 0.1) \times 10^{-4}$ RIU, corresponding to a mass concentration of ~(0.03 ± 0.01)%. This, however, shows a significant deviation from the prepared concentration [~(0.070 ± 0.002)%]. We attribute this deviation to a not sufficiently fine calibration of the library and the error from linear interpolation. The calibrated response of ρ^p around the eigenstate is in the proximity to the maximum (unity). The limited sampling resolution of Δn_i may not be sufficient to describe the response around an extremum.

Sensing at λ_{p3} Near Eigenstate VII

Figure 9 shows the sensing results at another specifically chosen probe wavelength λ_{p3} (686.42 nm). We specifically set λ_{p3} at the blue-edge of the transmission band near eigenstate VII. The sensitivity at λ_{p3} is ~541 RIU^{-1} (see **Figure 6F**). The NEDL at λ_{p3} is ~1×10^{-6} RIU (see **Figure 6G**). We consider λ_{p3} as a near optimized choice with a relatively high sensitivity and a low NEDL. **Figure 9A** shows the measured elastic-light-scattering images upon the buffer solution and the three test solutions. **Figure 9B** shows the corresponding pixelized patterns. **Figure 9C** shows the corresponding calculated correlation coefficients. **Figures 9D–F** show the mapping of ρ^p and ρ^s values with the library (see Supplementary Material S9 for detailed mappings).

For solution X, however, we observe an almost dark scattering pattern, which suggests that λ_{p3} upon solution X is relatively shifted out of the transmission band. Both the extracted ρ^p and ρ^s values out of $\rho_j(\lambda_{p3})$ upon solution X are particularly low. By mapping the extracted $\rho_j(\lambda_{p3})$ values with the library, we find no match to indicate the corresponding Δn_x. Therefore, in the case that there is a chance to measure a large Δn near Δn_d (in the order of $10^{-2} \sim 10^{-3}$ RIU in this case), it is better to position λ_p close to the red-side of the transmission band in order to leverage the dynamic range given by $\Delta\lambda_{BW}$ in full.

For solution Y, we acquire a Δn_Y of ~$(1.04 \pm 0.02) \times 10^{-3}$ RIU. For solution Z, we acquire a Δn_Z of ~$(1.24 \pm 0.1) \times 10^{-4}$ RIU. Both sensing results agree with the prepared concentrations of solutions Y and Z. Compared with the sensing result of solution Z at λ_{p1}, we obtain a more accurate value of Δn_Z with a much improved uncertainty. We attribute this to a higher sensitivity and a lower NEDL at λ_{p3} than those at λ_{p1}.

Discussion

Here, we benchmark our work with other silicon- and SiN-based on-chip optical biochemical sensors that have been demonstrated

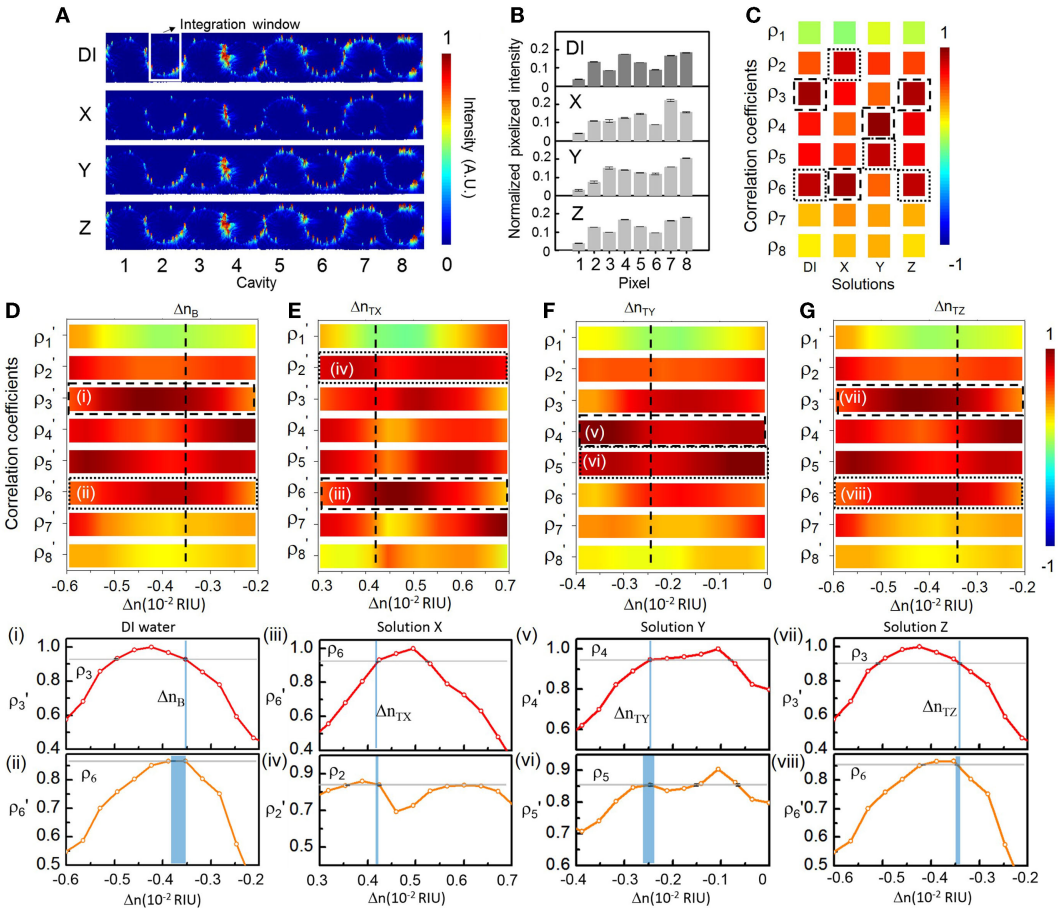

FIGURE 7 | (A) Measured elastic-light-scattering images of CROW upon the buffer solution and the three blind-test solutions X, Y, and Z at an arbitrarily set probe wavelength λ_{p1}. The white-line box indicates the integration window for pixelization. **(B)** Normalized pixelized patterns upon the buffer solution and solutions X, Y, and Z at λ_{p1}. **(C)** Calculated correlation coefficients upon the buffer solution and solutions X, Y and Z at λ_{p1}. Dashed-line and dotted-line boxes indicate ρ^p and ρ^s, respectively. **(D–G)** Zoom-in view of the library to extract Δn. **(D)** Upon the buffer solution. **(E)** Upon solution X. **(F)** Upon solution Y. **(G)** Upon solution Z. Insets (i)–(viii): Mapping of ρ^p and ρ^s upon the buffer solution and solutions X, Y, and Z.

in recent years, including our previous work (Wang et al., 2014), as summarized in **Table 2**. All of the work including this work have attained a detection limit of $10^{-7} \sim 10^{-4}$ RIU. Two of the microcavity-based sensors (Ghasemi et al., 2013; Doolin et al., 2015) and three of the MZI-based sensors (Duval et al., 2013; Misiakos et al., 2014; Dante et al., 2015) operate on the SiN-based platform in the visible wavelengths.

Most of the reported microcavity-based sensors in the literature (except Ghasemi et al., 2013; Doolin et al., 2015) operate in the telecommunication wavelengths (1.3/1.55 μm) and require a wavelength-tunable laser and a non-silicon photodetector. Whereas, our CROW sensor operating in the visible wavelengths only requires in principle a fixed-wavelength visible laser diode and a silicon CCD/CMOS camera after the library preparation.

In terms of the sensor calibration, the main difference between our library preparation and the conventional calibration process for a microcavity-based sensor is the recording of the pixelized patterns instead of single intensity values. A typical calibration for a conventional microcavity-based sensor [e.g., De Vos et al. (2007) and Iqbal et al. (2010)] involves scanning laser wavelength across a narrow transmission band. As an example, in the work of De Vos et al., calibrating the spectral sensitivity of a microring sensor of Q ~ 20,000 involved measuring the microring transmission spectrum three times for each of the four given NaCl solutions with different concentrations (De Vos et al., 2007). In contrast, our library preparation involves scanning laser wavelength across the CROW transmission band, recording the pixelized patterns at each wavelength step corresponding to the refractive index interval Δn_i and deriving the corresponding correlation coefficients with the eigenstate patterns. The pattern recording and additional computation of the correlation coefficients render our library preparation more reliable and tolerant to the equipment noises that are common to all pixels compared with recording single intensity values multiple times.

A major issue requiring further developments is the significant variation of sensitivity values upon different probe wavelengths. We can modify the CROW design in order to attain a more uniform sensitivity (see Supplementary Material S10). Our modeling results suggest that an imperfect CROW with a reduced cavity size along with an enhanced inter-cavity coupling coefficient offers a more uniform sensitivity. Upon a small cavity radius $R = 10$ μm and a strong inter-cavity coupling coefficient

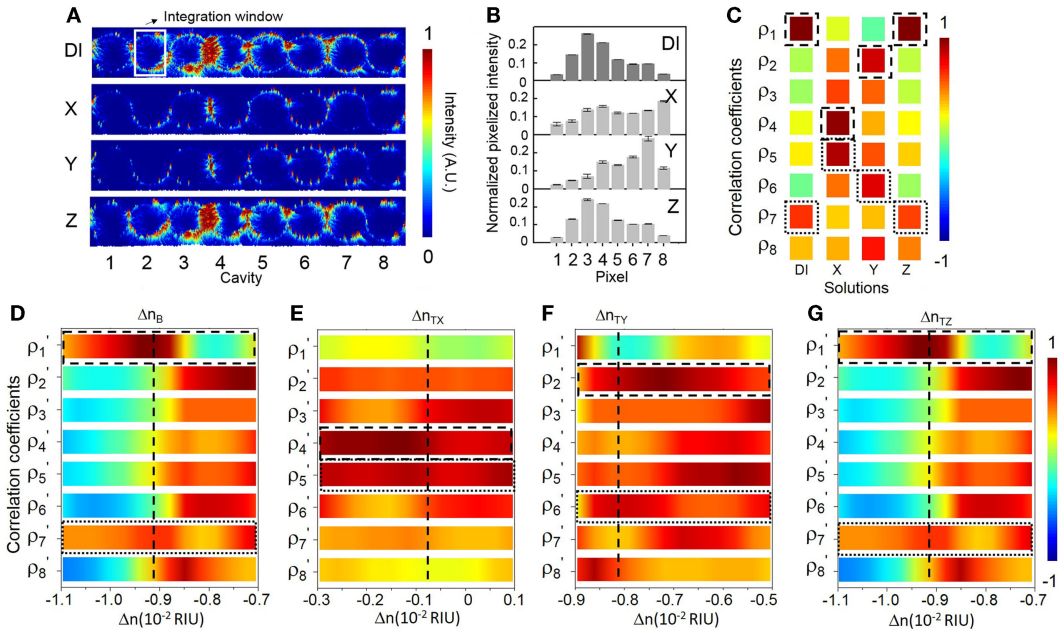

FIGURE 8 | (A) Measured elastic-light-scattering images of CROW upon the buffer solution and the three blind-test solutions X, Y, and Z at a specifically chosen probe wavelength λ_{p2} at eigenstate I. The white-line box indicates the integration window for pixelization. **(B)** Normalized pixelized patterns upon the buffer solution and solutions X, Y, and Z at λ_{p2}. **(C)** Calculated correlation coefficients upon the buffer solution and solutions X, Y, and Z at λ_{p2}. Dashed-line and dotted-line boxes indicate ρ^p and ρ^s, respectively. **(D–G)** Zoom-in view of the library to extract Δn. **(D)** Upon the buffer solution. **(E)** Upon solution X. **(F)** Upon solution Y. **(G)** Upon solution Z.

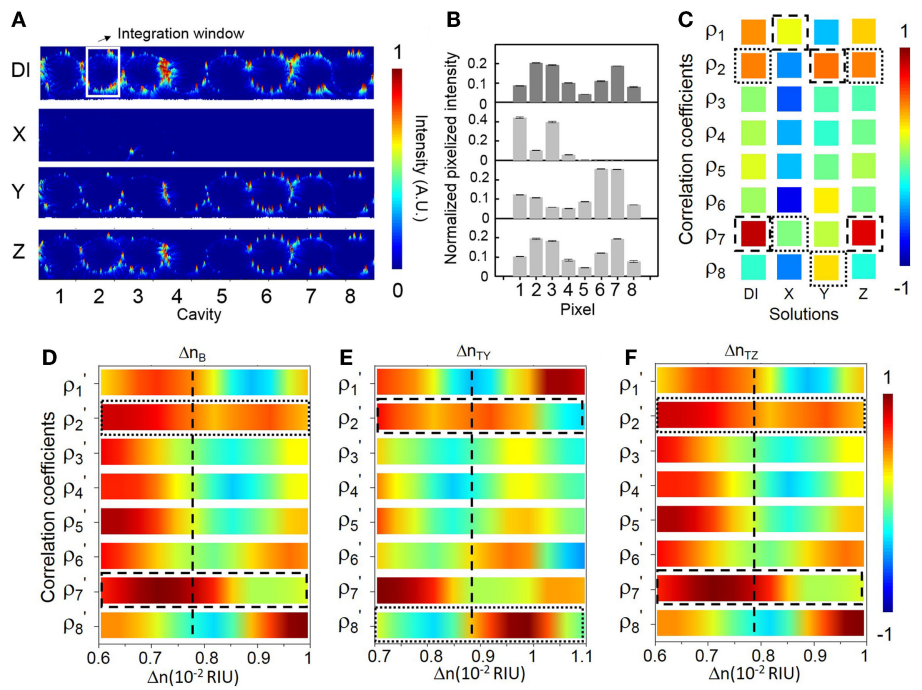

FIGURE 9 | (A) Measured elastic-light-scattering images of CROW upon the buffer solution and the three blind-test solutions X, Y, and Z at a specifically chosen probe wavelength λ_{p3} near eigenstate VII. The white-line box indicates the integration window for pixelization. **(B)** Normalized pixelized patterns upon the buffer solution and solutions X, Y and Z at λ_{p3}. **(C)** Calculated correlation coefficients upon the buffer solution and solutions X, Y, and Z at λ_{p3}. Dashed-line and dotted-line boxes indicate ρ^p and ρ^s, respectively. **(D–F)** Zoom-in view of the library to extract Δn. **(D)** Upon the buffer solution. **(E)** Upon solution Y. **(F)** Upon solution Z.

TABLE 2 | Summary of silicon- and silicon-nitride-based on-chip optical biochemical sensors.

Device config.	Reference	Material platform	Operational wavelength (nm)	Footprint (μm^2)	Q-factor	Sensitivity (RIU^{-1})	Detected Δn (RIU)	Detection limit (RIU)
MZI	Densmore et al. (2008)	SOI	~1550	~40,000	N/A	920 π rad	$\sim 7 \times 10^{-4}$	$\sim 1 \times 10^{-5}$
	Duval et al. (2013)	Si_3N_4	658	$\sim 10^8$	N/A	4950 π rad	$\sim 3 \times 10^{-4}$	$\sim 2 \times 10^{-7}$
	Misiakos et al. (2014)	SiN	~600–900	$\sim 10^7$	N/A	581 rad	$\sim 4 \times 10^{-5}$	$\sim 1 \times 10^{-5}$
	Dante et al. (2015)	Si_3N_4	660	~60,000	N/A	6000 π rad	$\sim 2 \times 10^{-4}$	$\sim 4 \times 10^{-7}$
Microdisk	Wang et al. (2013)	SOI	~1550	~3	~100	130 nm	$\sim 9 \times 10^{-3}$	$\sim 8 \times 10^{-4}$
	Doolin et al. (2015)	Si_3N_4	~770	~900	10000	200 nm	$\sim 4 \times 10^{-4}$	$\sim 10^{-6}$
Microring with slot-waveguide	Barrios et al. (2007)	Si_3N_4	~1300	~20,000	1800	212 nm	$\sim 10^{-3}$	$\sim 2 \times 10^{-4}$
	Claes et al. (2009)	SOI	~1550	~240	~450	298 nm	$\sim 4 \times 10^{-3}$	$\sim 4.2 \times 10^{-5}$
	Carlborg et al. (2010)	Si_3N_4	~1300	~20,000	–	248 nm	$\sim 3 \times 10^{-4}$	$\sim 5 \times 10^{-6}$
Microring	De Vos et al. (2007)	SOI	~1550	~110	20,000	70 nm	$\sim 9 \times 10^{-4}$	$\sim 10^{-5}$
	Iqbal et al. (2010)	SOI	~ 1550	~900	43,000	163 nm	$\sim 10^{-6}$	–
	Ghasemi et al. (2013)	SiN	~656	~400	–	48 nm	–	–
	Liu et al. (2014)	SOI	~1550	~1600	15000	6000 rad	$\sim 4 \times 10^{-4}$	$\sim 2.5 \times 10^{-6}$
Eight-microring CROW in the spatial domain	Wang et al. (2014)	SOI	~1550	~1716	N/A	~199	$\sim 1.5 \times 10^{-4}$	$2 \times 10^{-7} \sim 9 \times 10^{-4}$
	(This work)	SiN	~680	~14080	N/A	$\sim 281 \pm 271$	$\sim 1.3 \times 10^{-4}$	$2 \times 10^{-8} \sim 1 \times 10^{-4}$

$\kappa \sim 0.9$, we obtain for an imperfect eight-microring CROW a modeled sensitivity of $\sim 384 \pm 153\ RIU^{-1}$, with an improved non-uniformity ratio of ~0.40 compared to the modeled ratio of ~0.52 following our experimental device parameters. Assuming a practical sensitivity of $\sim 100\ RIU^{-1}$, the width of the modeled probe wavelength window with a sensitivity $>100\ RIU^{-1}$ is 2.2 nm, which is much improved compared to the modeled width of 1.1 nm following the experimental device parameters. If a higher practical sensitivity of $300\ RIU^{-1}$ is desired, the modeled probe wavelength window width with a sensitivity $>300\ RIU^{-1}$ is ~1.56 nm, which is still sufficiently wide for practical applications. Based on our current imperfect CROW model, we can further design the CROW with tailored non-uniform parameters to optimize the sensitivity and sensitivity variation.

In summary, we demonstrated a SiN CROW-based sensing scheme in the spatial domain in the visible wavelengths. Given a calibrated CROW sensor, this sensing scheme in principle only requires a low-power, fixed-wavelength laser source in the visible wavelengths and a silicon CCD or CMOS camera to image the elastic-light-scattering patterns in the far field. Our proof-of-concept experiment using an eight-microring CROW on the SiN-on-silica platform showed an average sensitivity of $\sim 281 \pm 271\ RIU^{-1}$ and a NEDL of $2 \times 10^{-8} \sim 1 \times 10^{-4}$ RIU. Our blind sensing tests using NaCl solutions showed a detection of $\sim 1.26 \times 10^{-4}$ RIU. Therefore, we have shown that such a chip-scale, microresonator-based SiN CROW sensor operating in the visible wavelengths is promising as a potentially high-performance, portable, and low-cost optical biochemical sensor for applications such as point-of-care biochemical analyses and self-monitoring of personal healthcare using smartphones.

Acknowledgments

This work is supported by grants from the Research Grants Council of the Hong Kong Special Administrative Region, China (Project No. 618010, 617612, and 617913). The authors acknowledge the HKUST Nanoelectronics Fabrication Facility for fabricating the optofluidic chip.

Supplementary Material

The Supplementary Material for this article can be found online at http://www.frontiersin.org/Journal/10.3389/fmats.2015.00034/abstract

References

Barrios, C. A., Gylfason, K. B., Sánchez, B., Griol, A., Sohlström, H., Holgado, M., et al. (2007). Slot-waveguide biochemical sensor. *Opt. Lett.* 32, 3080–3082. doi:10.1364/ol.32.003080

Carlborg, C. F., Gylfason, K. B., Kazmierczak, A., Dortu, F., Polo, M. B., Catala, A. M., et al. (2010). A packaged optical slot-waveguide ring resonator sensor array for multiplex label-free assays in labs-on-chips. *Lab. Chip* 10, 281–290. doi:10.1039/b914183a

Ciminelli, C., Campanella, C. M., Dell'olio, F., Campanella, C. E., and Armenise, M. N. (2013). Label-free optical resonant sensors for biochemical applications. *Prog. Quant. Electron.* 37, 51–107. doi:10.1016/j.pquantelec.2013.02.001

Claes, T., Molera, J. G., De Vos, K., Schachtb, E., Baets, R., and Bienstman, P. (2009). Label-free biosensing with a slot-waveguide-based ring resonator in silicon on insulator. *Photonics J. IEEE* 1, 197–204. doi:10.1109/jphot.2009.2031596

Dante, S., Duval, D., Fariña, D., González-Guerrero, A. B., and Lechuga, L. M. (2015). Linear readout of integrated interferometric biosensors using a periodic wavelength modulation. *Laser Photon. Rev.* 9, 248–255. doi:10.1002/lpor.201400216

De Vos, K., Bartolozzi, I., Schacht, E., Bienstman, P., and Baets, R. (2007). Silicon-on-insulator microring resonator for sensitive and label-free biosensing. *Opt. Express* 15, 7610–7615. doi:10.1364/oe.15.007610

Densmore, A., Xu, D.-X., Janz, S., Waldron, P., Mischki, T., Lopinski, G., et al. (2008). Spiral-path high-sensitivity silicon photonic wire molecular sensor with temperature-independent response. *Opt. Lett.* 33, 596–598. doi:10.1364/ol.33.000596

Doolin, C., Doolin, P., Lewis, B. C., and Davis, J. P. (2015). Refractometric sensing of Li salt with visible-light Si3N4 microdisk resonators. *Appl. Phys. Lett.* 106, 081104. doi:10.1063/1.4913618

Duval, D., Osmond, J., Dante, S., Dominguez, C., and Lechuga, L. M. (2013). Grating couplers integrated on Mach-Zehnder interferometric biosensors operating

in the visible range. *Photonics J. IEEE* 5, 3700108. doi:10.1109/jphot.2013.2251873

Estevez, M.-C., Alvarez, M., and Lechuga, L. M. (2012). Integrated optical devices for lab-on-a-chip biosensing applications. *Laser Photon. Rev.* 6, 463–487. doi:10.1002/lpor.201100025

Ghasemi, F., Eftekhar, A. A., Gottfried, D. S., Song, X., Cummings, R. D., and Adibi, A. (2013). "Self-referenced silicon nitride array microring biosensor for toxin detection using glycans at visible wavelength," in *SPIE BiOS* (San Francisco, CA: International Society for Optics and Photonics).

Gorin, A., Jaouad, A., Grondin, E., Aimez, V., and Charette, P. (2008). Fabrication of silicon nitride waveguides for visible-light using PECVD: a study of the effect of plasma frequency on optical properties. *Opt. Express* 16, 13509–13516. doi:10.1364/oe.16.013509

Halir, R., Vivien, L., Le Roux, X., Xu, D.-X., and Cheben, P. (2013). Direct and sensitive phase readout for integrated waveguide sensors. *Photonics J. IEEE* 5, 6800906. doi:10.1109/jphot.2013.2276747

Iqbal, M., Gleeson, M. A., Spaugh, B., Tybor, F., Gunn, W. G., Hochberg, M., et al. (2010). Label-free biosensor arrays based on silicon ring resonators and high-speed optical scanning instrumentation. *IEEE J. Sel. Top. Quantum Electron.* 16, 654–661. doi:10.1109/jstqe.2009.2032510

Kozma, P., Hamori, A., Cottier, K., Kurunczi, S., and Horvath, R. (2009). Grating coupled interferometry for optical sensing. *Appl. Phys. B* 97, 5–8. doi:10.1007/s00340-009-3719-1

Lakshminarayanan, V., Zelek, J., and Mcbride, A. (2015). "Smartphone Science" in eye care and medicine. *Opt. Photonics News* 26, 44–51. doi:10.1364/opn.26.1.000044

Lei, T., and Poon, A. W. (2011). Modeling of coupled-resonator optical waveguide (CROW) based refractive index sensors using pixelized spatial detection at a single wavelength. *Opt. Express* 19, 22227–22241. doi:10.1364/oe.19.022227

Liu, J., Zhou, X., Qiao, Z., Zhang, J., Zhang, C., Xiang, T., et al. (2014). Integrated optical chemical sensor based on an SOI ring resonator using phase-interrogation. *Photonics J. IEEE* 6, 1–7. doi:10.1109/jphot.2014.2352973

Misiakos, K., Raptis, I., Makarona, E., Botsialas, A., Salapatas, A., Oikonomou, P., et al. (2014). All-silicon monolithic Mach-Zehnder interferometer as a refractive index and bio-chemical sensor. *Opt. Express* 22, 26803–26813. doi:10.1364/OE.22.026803

Sedlmeir, F., Zeltner, R., Leuchs, G., and Schwefel, H. G. (2014). High-Q MgF^2 whispering gallery mode resonators for refractometric sensing in aqueous environment. *Opt. Express* 22, 30934–30942. doi:10.1364/oe.22.030934

Subramanian, A., Dhakal, A., Peyskens, F., Selvaraja, S., Baets, R., Neutens, P., et al. (2013). Low-loss singlemode PECVD silicon nitride photonic wire waveguides for 532–900 nm wavelength window fabricated within a CMOS pilot line. *Photonics J. IEEE* 5, 2202809. doi:10.1109/jphot.2013.2292698

Vollmer, F., Arnold, S., and Keng, D. (2008). Single virus detection from the reactive shift of a whispering-gallery mode. *Proc. Natl. Acad. Sci. U.S.A.* 105, 20701–20704. doi:10.1073/pnas.0808988106

Wang, J., Yao, Z., Lei, T., and Poon, A. W. (2014). Silicon coupled-resonator optical-waveguide-based biosensors using light-scattering pattern recognition with pixelized mode-field-intensity distributions. *Sci. Rep.* 4, 07528. doi:10.1038/srep07528

Wang, X., Guan, X., Huang, Q., Zheng, J., Shi, Y., and Dai, D. (2013). Suspended ultra-small disk resonator on silicon for optical sensing. *Opt. Lett.* 38, 5405–5408. doi:10.1364/ol.38.005405

Xu, J., Suarez, D., and Gottfried, D. S. (2007). Detection of avian influenza virus using an interferometric biosensor. *Anal. Bioanal. Chem.* 389, 1193–1199. doi:10.1007/s00216-007-1525-3

Ymeti, A., Greve, J., Lambeck, P. V., Wink, T., Van Hövell, S. W., Beumer, T. A., et al. (2007). Fast, ultrasensitive virus detection using a Young interferometer sensor. *Nano Lett.* 7, 394–397. doi:10.1021/nl062595n

Conflict of Interest Statement: The authors declare that the research was conducted in the absence of any commercial or financial relationships that could be construed as a potential conflict of interest.

frontiers in
MATERIALS

ORIGINAL RESEARCH ARTICLE
published: 07 April 2015
doi: 10.3389/fmats.2015.00028

High-throughput multiple dies-to-wafer bonding technology and III/V-on-Si hybrid lasers for heterogeneous integration of optoelectronic integrated circuits

Xianshu Luo[1], Yulian Cao[2], Junfeng Song[1], Xiaonan Hu[2], Yuanbing Cheng[2], Chengming Li[2], Chongyang Liu[2], Tsung-Yang Liow[1], Mingbin Yu[1], Hong Wang[2], Qi Jie Wang[2] and Patrick Guo-Qiang Lo[1]*

[1] *Institute of Microelectronics, Agency for Science, Technology and Research (A*STAR), Singapore, Singapore*
[2] *Photonics Center of Excellence (OPTIMUS), School of Electrical and Electronic Engineering, Nanyang Technological University, Singapore, Singapore*

Edited by:
Laurent Vivien, Université Paris-Sud, France

Reviewed by:
Junichi Fujikata, Photonics Electronics Technology Research Association, Japan
Yasuhiko Ishikawa, The University of Tokyo, Japan

***Correspondence:**
*Patrick Guo-Qiang Lo, Institute of Microelectronics, Agency for Science, Technology and Research (A*STAR), Singapore Science Park II, 11 Science Park Road, 117685 Singapore*
e-mail: logq@ime.a-star.edu.sg

Integrated optical light source on silicon is one of the key building blocks for optical interconnect technology. Great research efforts have been devoting worldwide to explore various approaches to integrate optical light source onto the silicon substrate. The achievements so far include the successful demonstration of III/V-on-Si hybrid lasers through III/V gain material to silicon wafer bonding technology. However, for potential large-scale integration, leveraging on mature silicon complementary metal oxide semiconductor (CMOS) fabrication technology and infrastructure, more effective bonding scheme with high bonding yield is in great demand considering manufacturing needs. In this paper, we propose and demonstrate a high-throughput multiple dies-to-wafer (D2W) bonding technology, which is then applied for the demonstration of hybrid silicon lasers. By temporarily bonding III/V dies to a handle silicon wafer for simultaneous batch processing, it is expected to bond unlimited III/V dies to silicon device wafer with high yield. As proof-of-concept, more than 100 III/V dies bonding to 200 mm silicon wafer is demonstrated. The high performance of the bonding interface is examined with various characterization techniques. Repeatable demonstrations of 16-III/V die bonding to pre-patterned 200 mm silicon wafers have been performed for various hybrid silicon lasers, in which device library including Fabry–Perot (FP) laser, lateral-coupled distributed-feedback laser with side wall grating, and mode-locked laser (MLL). From these results, the presented multiple D2W bonding technology can be a key enabler toward the large-scale heterogeneous integration of optoelectronic integrated circuits.

Keywords: silicon photonics, hybrid lasers, heterogeneous integration, die-to-wafer bonding, optoelectronic integrated circuits

INTRODUCTION

In the future generation of datacom and computercom, which demand ever higher bandwidth and lower power, the conventional electrical interconnection routing the electronic signals becomes bandwidth-limited along with prohibitively high power consumption (Beausoleil et al., 2008). One solution to the challenge is the optical interconnect technology (Goodman et al., 1984; Miller, 2000, 2009; Ohashi et al., 2009), in which high bandwidth optical signals are routed by low-loss optical fiber and waveguides. In contrast to the electrical interconnection (i.e., the copper wire), optical interconnect has many merits, e.g., high speed, low crosstalk, immunity to electromagnetic interference, low overall power consumption (Alduino and Paniccia, 2007). Most importantly, with the up scaling potential, optical interconnect is expected to provide much higher transmission capacity and longer signal transmission distance than the electrical interconnect.

Although it was proposed initially 30 years ago (Goodman et al., 1984), there was no significant development progress with solid demonstrations of optical interconnect for very-large-scale integration (VLSI). The situation has changed since the concept of silicon photonics (Pavesi and Lockwood, 2004; Reed and Knights, 2004; Lipson, 2005; Guillot and Pavesi, 2006; Jalali and Fathpour, 2006; Soref, 2006; Poon et al., 2009a,b; Vivien and Pavesi, 2013; Xu et al., 2014), which utilizes low-cost silicon material along with leveraging on the advancement of silicon complementary metal oxide semiconductor (CMOS) process, integration, and mature infrastructure. Envisioned by Soref and Lorenzo (1985), silicon photonics has emerged and progressed steadily. Especially in the past decade, we have been witnessing rapid growth in research and development activities along with product development efforts exploiting silicon photonics technology for the optical interconnect (Pavesi and Lockwood, 2004; Reed and Knights, 2004; Lipson, 2005; Guillot and Pavesi, 2006; Jalali and Fathpour, 2006; Soref, 2006; Fedeli et al., 2008; Poon et al., 2009a,b; Michel et al., 2010; Reed et al., 2010; Feng et al., 2012; Liow et al., 2013; Vivien and Pavesi, 2013; Dong et al., 2014a,b; Lim et al., 2014; Xu et al., 2014). For instance, to minimize the small core silicon waveguide propagation losses, considerable research work has been devoted to minimize the waveguide sidewall roughness by using the deep ultra-violet (DUV) photolithography and optimized patterning technique (Dumon et al., 2004; Bogaerts et al., 2005) and sidewall smoothing technique [e.g., double thermal oxidations (Sparacin

et al., 2005; Xia et al., 2006)]. Indeed, submicrometer-scale silicon wire waveguides have shown a propagation loss of 2 dB/cm and less (Xia et al., 2006). Furthermore, owing to the enabling CMOS fabrication technologies, we have seen the establishment and utilization of a myriad of essential silicon photonic passive and active components including optical filters (Xiao et al., 2007; Zhou and Poon, 2007; Guha et al., 2010; Fang et al., 2012), optical switches (Poon et al., 2009a,b; Van Campenhout et al., 2009; Luo et al., 2012; Song et al., 2013), low-power-consuming modulators with up to 50 Gb/s-speed operation (Dong et al., 2009; Reed et al., 2010; Tu et al., 2013, 2014), and Ge-on-Si photodetectors with bandwidth larger than 40 GHz (Michel et al., 2010; Liow et al., 2013). It is these demonstrated silicon photonic devices and technologies that make ultimate optical interconnection a viable solution to address the distance/bandwidth/cost and power-consumption challenges. To this end, silicon photonics provides nearly all key building blocks for optical interconnection. Furthermore, the CMOS-compatible fabrication processes make it possible to integrate both electronics and photonics either through monolithic or heterogeneous approach. Such significant progress has led the optical interconnect to become a much more practical technology.

However, silicon-based on-chip optical light source, which is one of the key components for the light generation for carrying information, has been the missing piece for optical interconnect. This is mainly because silicon is transparent in the telecommunication wavelengths (i.e., 1310 and 1550 nm wavelengths) due to the indirect bandgap, which prohibits efficient light emission from silicon. Thus, to solve the challenge, numerous research efforts have been devoted to explore various technologies for light source on silicon chips.

REVIEW ON RESEARCH FOR LASERS ON SILICON

Historically, researchers worldwide have devoted many research efforts by exploring various possibilities for the development of lasers on silicon, which mainly focused in the following directions:

(1) silicon material engineering by introducing emissive centers to assist the efficient light emission (Pavesi et al., 2000; Han et al., 2001; Rotem et al., 2007a,b; Shainline and Xu, 2007),
(2) strained Ge (Liu et al., 2007, 2009, 2010; Cheng et al., 2009; Sun et al., 2009b,c; Camacho-Aguilera et al., 2012),
(3) silicon Raman laser (Boyraz and Jalali, 2004, 2005; Rong et al., 2005a,b, 2007), and
(4) heterogeneous integration of III/V gain materials through packaging (Chu et al., 2009; Fujioka et al., 2010; Urino et al., 2011) or wafer bonding (Park et al., 2005; Fang et al., 2007a,b; Liang et al., 2009a,b, 2010; Stanković et al., 2010; Grenouillet et al., 2012).

Here, we will limit our review to the heterogeneous integrated silicon lasers. With regard to the silicon laser through heterogeneous integration of III/V gain materials on silicon, there are two major types of integration strategies, namely the packaging scheme and the bonding scheme. Research groups from Japan devoted many efforts for the development of silicon lasers using packaging methods. Chu et al. (2009) demonstrated the first wavelength-tunable-laser fabricated with silicon photonic technology, which comprised a semiconductor optical amplifier (SOA) chip and a silicon photonic chip, and were hybrid-integrated by using passive alignment technology. An SiON mode-size converter was adopted between the silicon waveguide and III/V SOA for low coupling loss. Later on, silicon photonic-based optical interconnects were also demonstrated by integrating lasers, silicon modulators, and Ge photodetectors on single silicon substrate (Urino et al., 2011). While such demonstrations have shown the advantage in principal of being capable to integrate various building blocks together for optical interconnection, the main issue is the complicated fabrication process. It typically requires precise alignment between the SOA and the silicon waveguide, even with assistance of the mode-size converter. Considering the III/V gain region of <200 nm in thickness, for instance, it became a difficult challenge for alignment with acceptable coupling loss. Such complicated fabrication process is a potential show stopper for future massive production demanding high yield, thus significantly increases the product cost.

Heterogeneous integration of III/V gain materials on silicon through wafer bonding technology is another major directional strategy for silicon lasers. UMR-CNRS and LETI initiated the research work of III/V laser on silicon wafers for photonic integration by using wafer bonding technology. In 2001, they demonstrated the first InP-based microdisk laser integrated on a silicon wafer through SiO_2–SiO_2 molecular bonding (Seassal et al., 2001). Although this work did not show complete integration of III/V optoelectronics with silicon photonics waveguide structures, it showed the potential of such wafer bonding technology for future heterogeneous integrated optoelectronic circuit. Following such demonstration, Hattori et al. (2006) demonstrated an integration scheme of III/V microdisk laser with silicon waveguide in 2006. By aligning the microdisk laser atop silicon waveguide, the laser emissions can be vertically coupled into the underneath silicon waveguide with 35% coupling efficiency. Such demonstration showed the capability of the hybrid photonic integration of III/V laser with silicon waveguide for photonic links application.

The so-called hybrid silicon laser was proposed and first demonstrated by Park et al. (2005) with optical injection. In this work, the III/V wafer with AlGaInAs quantum well structure is directly bonded to pre-patterned silicon wafer using low-temperature oxygen plasma-assisted wafer bonding. The laser cavity was defined by endface-polished silicon waveguide structure, while the III/V provides the optical gain. As the III/V optoelectronic structures are fabricated after the wafer bonding with best precise, only possibly achieved via lithographic process, alignment to the silicon device layer, thus there is no stringent alignment requirement to the bonding process, which significantly simplifies the fabrication process and makes the possibility of wafer-level-oriented manufacturing ability. Subsequently, Fang et al. (2006) demonstrated an electrically pumped AlGaInAs-silicon evanescent laser with continuous-wave (CW) operation in 2006. Subsequently, various hybrid lasers with different structures and also enhanced laser performances are demonstrated by various research groups using molecular wafer bonding technology, including Fabry–Pérot lasers (FP) (Ben Bakir et al., 2011; Dong et al., 2013), racetrack lasers (Fang et al., 2007a,b), distributed Bragg reflector (DBR) lasers (Fang et al., 2008a,b,c),

distributed-feedback (DFB) lasers (Fang et al., 2008a,b,c), microring lasers (Liang et al., 2009a,b, 2012), wavelength tunable lasers (Keyvaninia et al., 2013a,b,c), multiple-wavelength lasers (Van Campenhout et al., 2008; Kurczveil et al., 2011), and mode-locked lasers (MLL) (Fang et al., 2008a,b,c).

Besides such direct bonding method, wafer bonding can also be realized through an adhesive material as the bonding interlayer. Among all kinds of adhesive bonding materials, divinylsiloxane-bisbenzocyclobutene (DVS-BCB or BCB) is the most popular one for hybrid silicon lasers due to the merits such as the high bonding strength and the sustainability in the subsequent III/V process. IMEC has used BCB-assisted adhesive bonding method for heterogeneous integration (Roelkens et al., 2005). In 2006, Roelkens et al. (2006) demonstrated the first electrically injected InP/InGaAsP laser integrated on silicon waveguide circuit using BCB-assisted adhesive bonding technology. Similar to Seassal et al. (2001), the optical laser is purely made with III/V layer with the laser facets being defined by dry etching. With optimized mode-size converter, the optical light can be vertically coupled down to the underneath silicon waveguide with high efficiency. By designing hybrid mode waveguide comprising silicon waveguide and III/V gain medium, they also demonstrated a hybrid FP laser (Stanković et al., 2011) and a DFB laser (Stanković et al., 2012; Keyvaninia et al., 2013a,b,c), and multiple-wavelength laser (Keyvaninia et al., 2013a,b,c) using such adhesive bonding technology.

Apart from BCB, some kinds of metal can also be adopted as the bonding interlayer for adhesive bonding. AuGeNi is one of the most popular metals for metal bonding as it not only functions as a bonding media but can also be used for the Ohmic contact to the InGaAsP structure. Tanabe et al. (2010) demonstrated a InAs/GaAs quantum-dot laser on Si substrate by metal-assisted wafer bonding with room temperature operation at 1.3 μm wavelength. Meanwhile, Hong et al. (2010) also demonstrated an FP laser through selective-area metal bonding using AuGeNi. The silicon waveguide in such demonstration is with 5 μm and 800 nm thickness. The demonstrated FP laser is with threshold current density of 1.7 kA/cm and a maximum output power of 3 mW. However, the drawback of the AuGeNi-assisted bonding is the Au contamination. Thus, Tatsumi et al. (2012) further demonstrated an Au-free metal-assisted wafer bonding for lasers on silicon chip. Besides, Creazzo et al. (2013) also demonstrated another type of silicon laser by using metal-assisted bonding of III/V epitaxial material directly onto the silicon substrate. The demonstrated that silicon laser had a threshold of ~50 mA and maximum optical power of ~8 mW. The benefit of such metal-assisted bonding is the advantage of effective thermal dissipation, which shows a thermal resistant of only 21°C/W.

Beyond these two major heterogeneous integration schemes, there are also other methods for III/V-on-Si lasers, including direct III/V epitaxy on silicon substrate (Liu et al., 2011; Lee et al., 2012) and III/V epitaxial layer transfer-printing to silicon wafers (Justice et al., 2012; Yang et al., 2012). However, while the direct epitaxy method faces major challenges of high-density dislocations due to the lattice mismatch between III/V material and silicon after many years of research, the transfer-printing method for hybrid silicon laser needs further demonstrations to show the repeatability and reliability.

From these analyses, it shows that among various approaches, the hybrid silicon laser through wafer bonding technology can be considered as the most successful and promising one for silicon photonic heterogeneous integration circuits due to the ever-demonstrated advanced performances and the fabrication process compatibility with silicon photonics. **Table 1** summarizes some of the representative demonstrations of hybrid silicon lasers through wafer bonding technology.

WAFER BONDING TECHNOLOGIES FOR ON-CHIP SILICON LASERS

In general, there are two mainstreams of wafer bonding methods applying to heterogeneous integrated silicon photonics, namely the molecular bonding through interfacial bonds, and the adhesive bonding assisted with another adhesive material as bonding interface such as polymer or metal. Such wafer bonding technology is a mature process, which is widely applicable for SOI wafer fabrication, MEMS technology, and optoelectronic device fabrication. As a lot of review papers already exist (Lasky, 1986; Maszara, 1991; Tong and Goesele, 1999; Alexe and Gösele, 2004; Christiansen et al., 2006), we thus only focus the discussion on the application of hybrid silicon lasers. According to the existing demonstrations, we further summarize here the major bonding technologies as below:

(1) wafer-to-wafer (W2W) molecular bonding,
(2) die-to-wafer (D2W) molecular bonding,
(3) BCB-assisted D2W adhesive bonding, and
(4) metal-assisted adhesive bonding.

The W2W molecular bonding for hybrid silicon lasers is mainly driven by the UCSB group. Through such plasma-activated low-temperature W2W molecular bonding (Pasquariello and Hjort, 2002), they, together with their collaborators, have demonstrated various hybrid silicon lasers, starting from the first-hybrid FP laser (Fang et al., 2006), followed by racetrack-shaped laser (Fang et al., 2007a,b), DBR lasers (Fang et al., 2008a,b,c), DFB lasers (Fang et al., 2008a,b,c), MLL (Fang et al., 2008a,b,c), and multi-wavelength arbitrary waveform generation (AWG) laser (Kurczveil et al., 2011). However, for the conventional III/V-to-Si W2W bonding without thick oxide interlayer, the generated gas by-products of H_2 and H_2O are easily trapped inside the bonding interface and form the interfacial voids, which subsequently affect the bonding quality. In order to effectively remove such trapped gases, some proper outgas channels are designed, such as in-plane outgassing channels (IPOC) (Kissinger and Kissinger, 1993) or vertical outgassing channels (VOC) (Liang and Bowers, 2008). IPOS is formed by etching some lateral channels extended to the chip edges, so that the by-product gases can be directed to outside the bonding interface to the chip edge during post bonding annealing. However, for some close-loop structures, such as microrings, there is no way to design such IPOS. In order to solve such issue, VOC is proposed by etching some array of holes down to the BOX layer. The generated by-product gases can migrate to the closest VOC and are absorbed by SOI BOX. As both IPOS and VOC can be formed during the waveguide etching, there is no particular design requirement from the fabrication point of view. However, as the formation of such outgas channels affects the silicon layer

Table 1 | Representative demonstrations of hybrid silicon lasers through wafer bonding technology.

Laser types	Bonding type	Waveguide scheme	Performances						Reference
			λ (nm)	T (°C)	I_{th} (mA)	P_{out} (mW)	SE (mW/mA)	Z_t (°C/W)	
Fabry–Perot laser	Molecular bonding	Hybrid WG (75 vs. 3% mode confinement within Si WG and QW)	1577	CW @ 15	65	1.8	0.013[a]	40	Fang et al. (2006)
DBR laser	Molecular bonding	Hybrid waveguide with inverse taper (66 vs. 4.4% mode confinement within Si WG and QW)	1569	CW @ 15	65	11	0.088[a]	40	Fang et al. (2008a,b,c)
	D2W molecular bonding with oxide interlayer	Hybrid waveguide with adiabatic mode transformer	1570	Pulse @ 20	100	7.2	0.021[a]	–	Ben Bakir et al. (2011)
	W2W molecular bonding with oxide interlayer	Hybrid waveguide with inverse taper, thermal tunable microring for wavelength tuning	1553	CW @ 20	40	4	0.025[a]	–	Keyvaninia et al. (2013a,b,c)
	Metal-assisted D2W bonding	III/V gain material butt-coupling with Si waveguide through a waveguide coupler	1562	CW @ 20	41	8	0.038	21	Creazzo et al. (2013)
DFB laser	Molecular bonding	Hybrid waveguide with inverse taper (59.2 vs. 5.2% mode confinement within Si WG and QW)	1600	CW @ 10	25	5.4	0.072[a]	132	Fang et al. (2008a,b,c)
	D2D BCB adhesive bonding	Hybrid waveguide (70 vs. 3% mode confinement within Si WG and QW)	1308	CW @ 20	20	2.1	0.026	–	Stanković et al. (2011)
	Selective-area metal bonding	Hybrid WG (94% mode confinement within Si)	1554	Pulse @ RT	35	3	0.05	–	Hong et al. (2010)
Microdisk laser	D2W molecular bonding	InP microdisk laser light vertically coupling to Si WG	1590	CW @ 20	0.9	0.012	0.008	–	Van Campenhout et al. (2008)
Microring laser	Molecular bonding	Racetrack microring, hybrid waveguide	1590	CW @ 15	175	29	0.089	–	Fang et al. (2007a,b)
	Molecular bonding	Hybrid microring with side coupled Si WG	–	CW @ 10	7.5	2.5	0.2	–	Liang et al. (2011)

[a] *Data are extracted from the power–current curves.*

pattern density, which will finally affect the bonding strength, it is desirable to take into account the design tradeoff between the bonding strength and the gas removal effectiveness.

Alternatively, plasma-assisted D2W molecular bonding has also been investigated for hybrid silicon lasers mainly by LETI. For large-scale manufacturability for potential massive production, the key enabling capability is the multiple dies to wafer bonding with high yield. Kostrzewa et al. (2006) first demonstrated a molecular bonding of multiple InP dies to a 200 mm silicon CMOS wafer with only 1 mm × 1 mm die size (Kostrzewa et al., 2006). For strong hydrophilic molecular bonding, both InP and silicon wafers were covered with oxide layer. Pick-and-place technology was used in order to align the InP dies to specific spots in silicon wafer, as well as to supply mechanical force to the dies through pick-and-place head. Using such D2W bonding, they demonstrated electrically pumped microdisk lasers integrated with a silicon waveguide circuit (Van Campenhout et al., 2007). However, in such D2W bonding, as the cleaning of the dies is performed ahead of the pick-and-place process, the bonding surface could be contaminated, and subsequently affecting the bonding quality and bonding yield. Furthermore, with the consideration of the pick-and-place time of 30 s/die, it takes approximately an

hour for bonding 100 dies. Such long bonding time through pick-and-place process for individual die would cause the bonding surface deactivation for the molecular bonding with plasma activation.

BCB-assisted D2W adhesive bonding can address such issue with potential capability of bonding unlimited number of dies. Stanković et al. (2010) demonstrated such D2D adhesive bonding technology using BCB. The BCB is first spin-coated on silicon wafer with controlled thickness of <100 nm in order to ensure the vertical light coupling efficiency, followed with die attaching and subsequent curing at 240°C for 1 h in a nitrogen atmosphere at 1000 mbar. With the assistant of BCB adhesion, the stringent requirements of contamination-free and smooth bonding surfaces for molecular bonding are relieved significantly. Furthermore, there is, in principle, no limitation for multiple dies bonding by the assistance of BCB adhesive layer (Keyvaninia et al., 2012). Through such bonding method, various hybrid lasers, including FP laser (Stanković et al., 2011), DFB laser (Stanković et al., 2012), microring and AWG integrated multi-wavelength DBR lasers (Keyvaninia et al., 2013a,b,c), and microdisk laser (Mechet et al., 2013) have been demonstrated. However, although such adhesive bonding is with good robustness and bonding strength, the thermal dissipation could be a major problem due to the low thermal conductivity of the BCB layer. Besides, robust polymer coating process ensuring the controllable BCB thickness is also very important.

Apart from these three major bonding methods, metal-assisted adhesive bonding (Hong et al., 2010; Tanabe et al., 2010; Creazzo et al., 2013) is another one that can be used for hybrid laser integration. However, due to the potential metal contamination and the non-compatibility with the subsequent fabrication process, such as acid etching for substrate removal, the metal-assisted adhesive bonding method might not be an optimal choice for silicon heterogeneous optoelectronic integrated circuits.

In **Table 2**, we summarize and compare these four different bonding methods.

OUTLINE OF THE MANUSCRIPT

The rest of the submission is organized as follows. In the Section "III/V-to-Si Wafer-to-Wafer (W2W) Bonding Technology," we show a demonstration of the wafer-to-wafer bonding by using low-temperature plasma-activated molecular bonding method with oxide as the bonding interlayer. In the Section "High-Throughput Multiple Dies-to-Wafer Bonding Technology," we propose and show the demonstration of an alternative bonding technology that can perform high-throughput D2W bonding for potential massive production of silicon hybrid lasers, which is based on a batch process to simultaneously bonding all the dies to the silicon wafer. In the Section "Design of III/V-on-Si Lasers," we provide some design guidelines of hybrid silicon laser, including the design of III/V multiple quantum wells (MQW) structures, the silicon waveguide thickness selection for hybrid laser, and the design of the vertical coupling structures. The Section "Demonstration of III/V-on-Si Hybrid Lasers" shows some hybrid silicon laser demonstrations using the bonded wafers from the proposed high-throughput D2W bonding, including FP laser, lateral-coupled distributed-feedback (LC-DFB) laser with side wall grating, and MLL. The Section "Summary and Future Outlook" summarizes this paper and addresses some of the future challenges.

III/V-TO-Si WAFER-TO-WAFER BONDING TECHNOLOGY

We have started the development of wafer bonding technology for hybrid silicon photonics integration in 2011. Considering the complete integration with existing silicon photonic integrated circuit, which consisting various silicon passive waveguide devices, high-speed modulator, and photodetectors, and are normally

Table 2 | The major bonding technology for hybrid integration.

Bonding methods	Process description	Fabrication tolerance	Manufacturing scalability	Comments
W2W molecular bonding	O_2 plasma-assisted direct bonding with 12 h annealing at 300°C	Small tolerance of contamination-free, smooth, and flat bonding surfaces	Difficult due to wafer size mismatch	Low utilization of both III/V and silicon wafers Sensitive to the wafer bowing
D2W molecular bonding	O_2 plasma-assisted bonding with oxide interlayer and 3 h annealing at 250°C	Small tolerance of contamination-free and smooth bonding surfaces	Difficult due to contamination and surface deactivation during pick-and-place process for large number of dies bonding	Difficult to ensure high yield with large number of dies bonding
BCB-assisted D2W adhesive bonding	BCB adhesive bonding with post curing of 1 h at 240°C	Large tolerance with low requirement on the bonding surface. Yet it requires controllable polymer coating regarding the thickness and flatness	Easy to be scalable with multiple dies and large-sized wafers	Thermal dissipation problem due to the low thermal conductivity of the BCB layer
Metal-assisted adhesive bonding	Metal-assisted bonding with annealing	Large tolerance with low requirement on the bonding surface. However, potential metal contamination, and process incompatibility. Potential coupling problem due to the metal absorption	Easy to be scalable with multiple dies and large-sized wafers	Enhanced thermal resistant due to the metal utilization

with thick oxide cladding, we adopt the low-temperature plasma-activated molecular bonding method (Pasquariello and Hjort, 2002) with oxide as the bonding interlayer. Furthermore, such thick cladding oxide also serves as the diffusion and absorption medium for the bonding by-products gases, thus with enhanced bonding quality and bonding yield.

For the initial development, we deposit 1.1 μm PECVD oxide on top of silicon wafers, followed with chemical mechanic polishing (CMP) to remove 100 nm oxide in order to ensure the smooth bonding interface. For all the bonding process described hereafter, we will use the similar PECVD oxide as cladding followed with CMP to smooth the bonding surface. Thus, we characterize and compare the oxide properties in terms of wafer-level uniformity and surface roughness before and after CMP. **Figures 1A,B** show the wafer-level oxide thickness before and after CMP. The non-uniformity is only ~1% after CMP, which suggests a very flat surface. **Figures 1C,D** show the AFM results before and after CMP. As deposited, the surface is relatively rough, with RMS of ~2.5 nm, while after CMP, the surface roughness is reduced significantly with RMS of ~0.4 nm, which is more suitable for wafer molecular bonding (Christiansen et al., 2006).

The bonding process starts with the wafer cleaning, separately for silicon wafer and III/V wafer. First, standard SPM clean for 10 min is performed to the silicon wafer in order to remove any organic contaminants, followed with 5 min SC1 clean with megasonic to remove any particle on the surface. The III/V wafer is separately cleaned in the NH_4OH solution (NH_4OH:DI water = 1:15) for 1 min. Second, O_2 plasma activation in a RIE chamber is performed for both silicon wafer and III/V wafer, subsequently followed with DI water rinse. These two bonded wafers are then physically contacted with each other immediately after drying and placed inside to the EVG 520 bonder for pre-bonding under N_2 for 3 min with 1000 N mechanic force. After that, post bonding annealing at 300°C in vacuum is applied to the bonded pair for 12 h. **Figure 2A** shows the optical image of a 50 mm InP wafer bonding to a 200 mm silicon wafer before unloading from the bonder track.

The bonded wafers are first characterized by scanning acoustic microscope (SAM) using Sonix HS3000. **Figure 2B** shows the typical CSAM image for the bonded wafer. We observe that larger than 98% of the 50 mm InP area is bonded to the silicon wafer, with only limited voids, which are attributed to the particles remaining on bonding surface. Besides, the bonding quality in the wafer

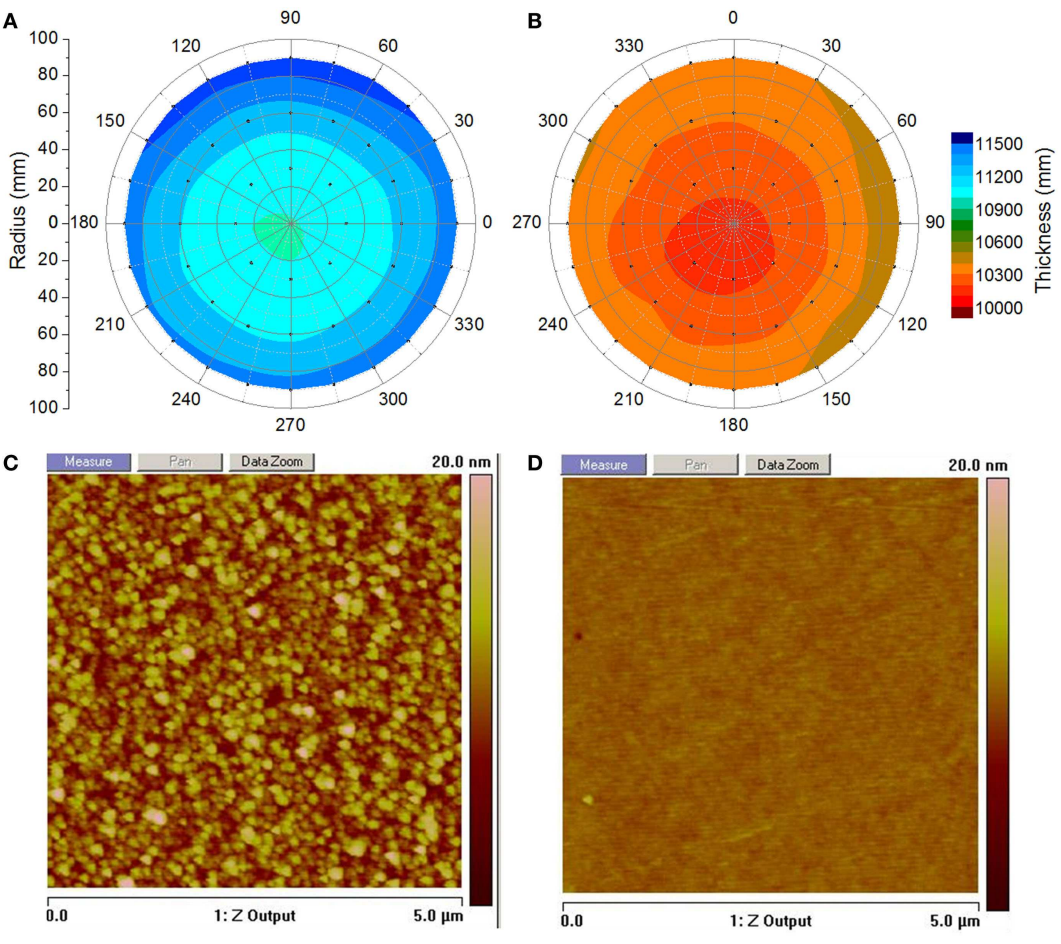

FIGURE 1 | The oxide thickness (A) before and (B) after CMP. The AFM results of the wafer surface roughness **(C)** before and **(D)** after CMP.

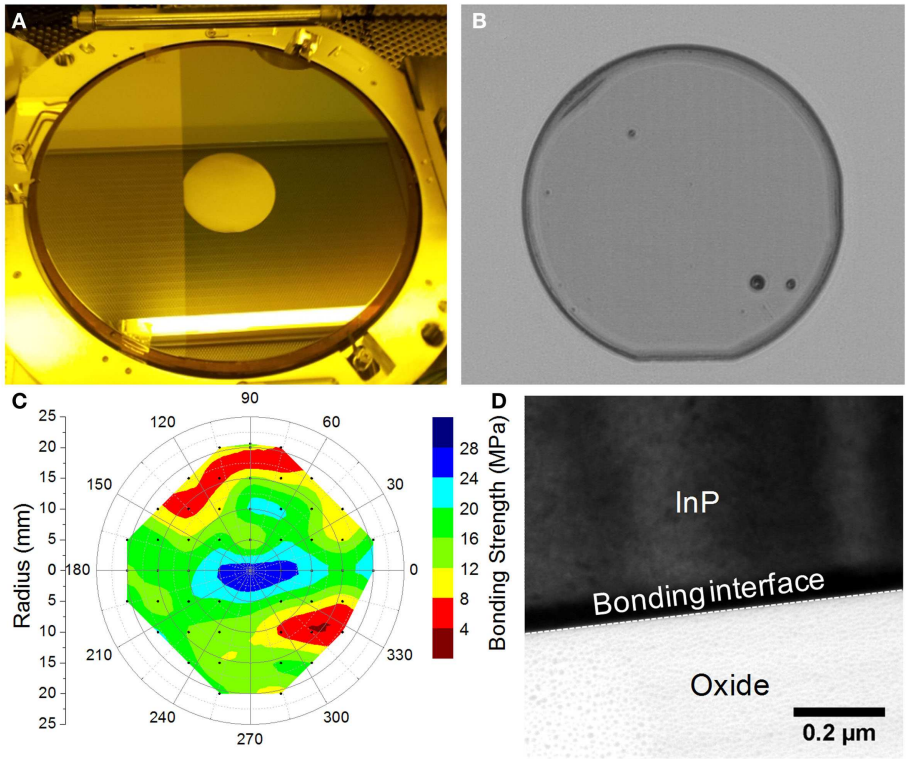

FIGURE 2 | (A) The bonded wafer before unloading from the EVG bonder. **(B)** The CSAM result. **(C)** The shear testing result. **(D)** The TEM results show the high-quality bonding interface.

periphery is also not good enough, which is due to the ring-shaped imperfection of the InP wafer.

The whole wafer is then diced into 5 mm × 5 mm dies for shear testing by using a Die Shear Tester (Dage Series 4000). **Figure 2C** shows the extracted bonding strength, with maximum bonding strength of ~30 MPa in the wafer center region, and the averaged value of 15 MPa. We believe such bonding strength is high enough for any of the post optoelectronic fabrication process. **Figure 2D** shows the TEM results of the bonded wafer, which indicate a very tight bonding between InP and oxide, again suggesting a high-quality bonding.

However, although such W2W bonding has been demonstrated with high quality, there are still existing big challenges, including:

(1) insufficient III/V wafer utilization,
(2) insufficient silicon wafer utilization due to wafer size mismatch,
(3) III/V wafer global stress-induced bonding voids.

First of all, for practical application of optical interconnection, only very small portion of the silicon waveguide area needs to be bonded with III/V material for optoelectronic fabrication to form optical lasers. With whole III/V wafer bonding, most of the III/V material will be subsequently etched away during post optoelectronic fabrication. Giving such precious III/V wafers, the insufficient utilization of the III/V material results in significantly increased device cost and waste, which in turn makes it ineffectual to use the silicon photonics though it is of low cost. Second, the main stream silicon photonics has already adopted 200 mm silicon wafers. However, due to the brittleness of the InP wafers, it is very difficult to make large-sized wafers to match with silicon wafers. Although the largest available III/V epitaxial wafer can go with 150 mm, the commercially available largest-sized III/V epitaxial wafer is only 75 mm. Thus, such wafer size mismatching definitely results in the insufficient utilization of the silicon device wafer, which in turn increased the cost. Furthermore, InP wafers with multiple quantum well structures are normally with high global stress, which induces the wafer bowing. Such stress-induced wafer bowing will easily trap the air between the bonding interfaces with remained voids, thus reducing the bonding quality.

HIGH-THROUGHPUT MULTIPLE DIES-TO-WAFER BONDING TECHNOLOGY

Based on the aforementioned W2W bonding method, we propose an alternative proprietary high-throughput multiple D2W bonding method, which is based on temporarily bonding III/V dies to a handle silicon wafer through pick-and-place process for simultaneous batch processing. Such high-throughput multiple D2W bonding method is the key enabling technique for potential manufacturability of large-scale hybrid optoelectronic integrated circuit (H-OEIC).

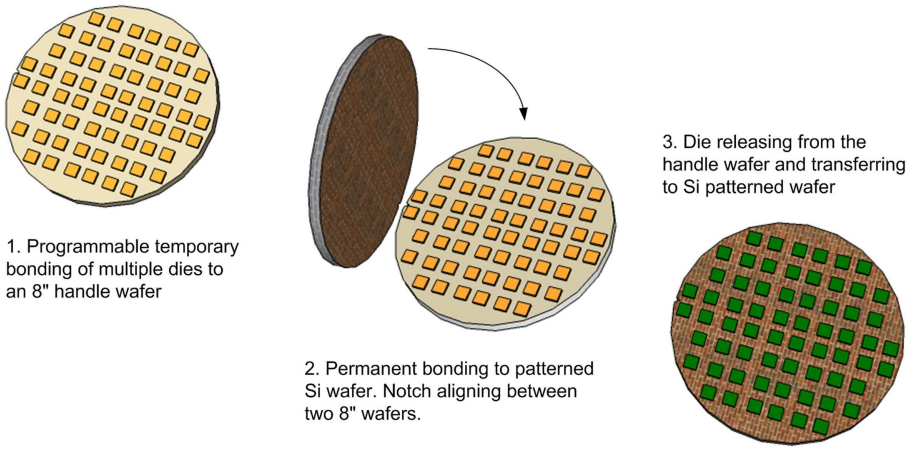

FIGURE 3 | Illustration of the key processing steps of the multiple D2W bonding technology.

Figure 3 shows the key process steps of the proposed multiple D2W bonding technology, which includes:

(a) the programmable reconfiguration of III/V dies onto a handle wafer via pick-and-place process,
(b) the D2W bonding through the notch alignment between the two 8″ wafers, after batch processing of wafer cleaning and plasma activation, and
(c) the dies releasing from the handle wafer and transferring to silicon device wafer.

The most critical step here is the choice of the adhesion layer for the temporary III/V dies bonding to the handle wafer, which includes the following two trade-off considerations.

(1) The adhesion should be strong enough to stick the III/V dies on the handle wafer without peeling off during the subsequent III/V dies batch processing, including InGaAs cap layer wet etching, pre-clean, wafer drying, and plasma activation, etc.
(2) The adhesion should not be excessively strong so that the III/V dies can be successfully released and transferred to the Si device wafer after pre-bonding.

The programmable reconfiguration of the dies onto the handle wafer is realized through pick-and-place process by predetermining the position coordinates of each die with considering the wafer-level silicon device die distribution. Unlike the pick-and-place process in flip-chip bonding, which directly bonds the dies to the actual wafer (Kostrzewa et al., 2006), the pick-and-place in our proposed method only helps to distribute the dies onto a handle wafer without flipping the chips. Thus, all the dies attached to the handle wafer can be simultaneously performed with different process steps for wafer bonding, such as InGaAs cap layer etching, wafer clean, and plasma activation.

The D2W bonding alignment accuracy is mainly determined by the notch alignment, which is performed manually and induces a relatively large misalignment of $\pm 500\,\mu m$, compared to the misalignment of only $\pm 5\,\mu m$ from the programmable reconfiguration by pick-and-place process. However, as the alignment of the III/V devices to the silicon waveguide device is determined through photolithography during optoelectronic fabrication process after wafer bonding, such misalignment can easily be compensated by adopting relatively large-sized III/V dies.

Figure 4 schematically illustrates the detailed bonding process flow starting from the preparations of silicon and III/V wafer. For either blanket silicon wafer or patterned silicon wafer with photonic devices, the wafers are cladded with PECVD oxide, followed with CMP process to smooth the bonding surface. As the hybrid laser performance is largely dependent on the vertical coupling efficiency, which is determined by the inter-layer oxide thickness, it is of very importance to control the oxide thickness by CMP process.

The preparation of the III/V dies includes the III/V wafer dicing into certain sized dies, the preparation of the adhesion layer to the handle wafer, and the programmable reconfiguration of the III/V dies temporary bonding to the handle wafer through pick-and-place process. Typically, the mechanical wafer dicing will result in edge roughness along the dicing lane, thus subsequently cause the low quality bonding near the die periphery. Besides, such dicing process may also introduce particles to the wafer surface cause contamination. Thus, a sacrificial InGaAs cap layer in order to protect the III/V bonding surface is designed in our demonstration. The applied mechanic force by the pick-and-place head also needs to be well controlled in order to ensure the successful die releasing from the handle wafer after pre-bonding. Due to the direct contact of the pick-and-place head, the die surface could be contaminated. However, owing to the sacrificial InGaAs layer, the bonding surface can be well protected without contamination or surface damage. We have checked and compared the surface condition of the III/V dies before and after the etching of the sacrificial InGaAs layer. We observe the particles on the chip surface after the wafer dicing and pick-and-place process, which is with relatively high RMS of 0.198 nm. In comparison, after the etching of InGaAs cap layer, the surface roughness is improved with reduced RMS of

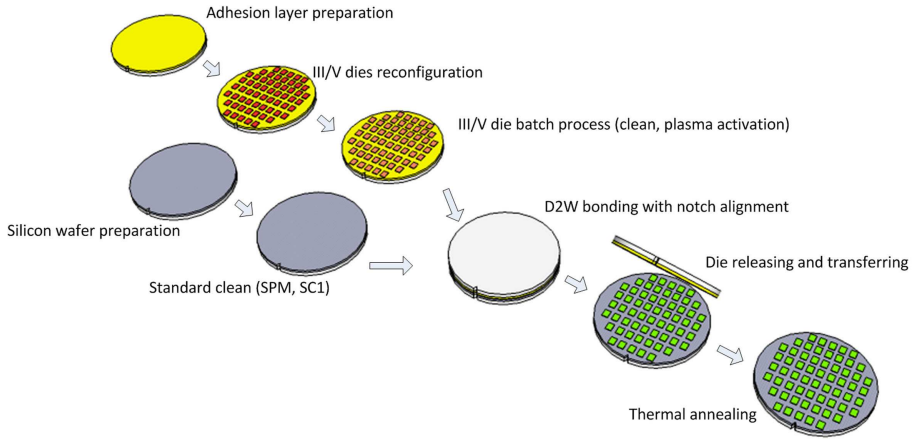

FIGURE 4 | The fabrication process flow of the multiple D2W bonding technology. The process includes two different folds, i.e., the bonding wafers preparation including the III/V dies adhesion to handle wafer for batch process and the silicon device wafer fabrication, and D2W bonding through dies releasing from handle wafer and transferring to silicon device wafer.

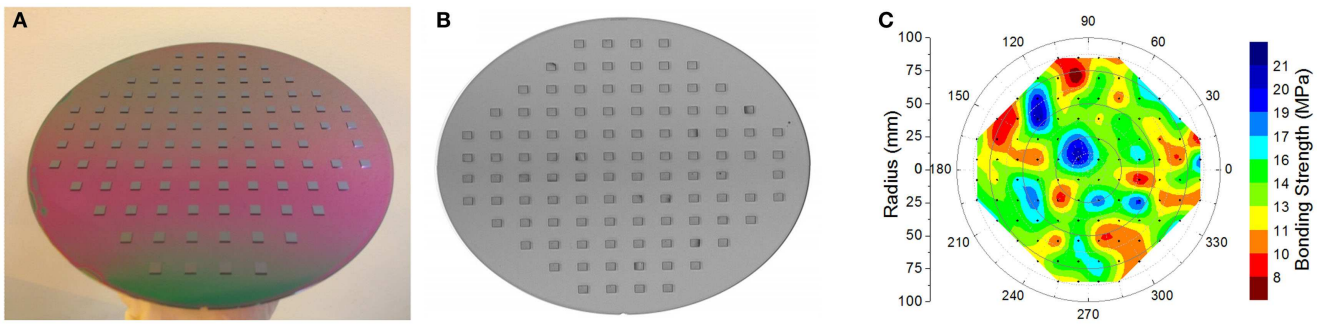

FIGURE 5 | Demonstration of 104 III/V dies bonding to silicon wafer. **(A)** Photo image of the bonded wafer, **(B)** CSAM results, **(C)** shear testing results.

0.182 nm, which is far below the required RMS of <1 nm for wafer direct bonding (Christiansen et al., 2006).

Prior the physical contact of the wafers for molecular bonding, the silicon wafer is performed with standard SPM clean for 10 min and SC1 clean with mega sonic for 5 min, while III/V die-attached handle wafer is first performed with sacrificial InGaAs cap layer etching in H_3PO4 solution for 1 min, followed with standard clean in NH_4OH solution for 2 min. After that, O_2 plasma activation is applied to both silicon wafer and III/V dies in a RIE chamber for 1 min, followed with DI water rinsing and wafer drying. The III/V dies and the silicon wafer are then physically contacted with each other by notch alignment between two 8″ wafers, followed with pre-bonding in the 200 mm EVG bonder for 2 min with 1000 N mechanical force applied. The III/V dies are released from the handle wafer after pre-bonding, and all III/V dies are now transferred to the silicon device wafer. Finally, the bonded pairs are placed back to the EVG bonder for post-bonding annealing at 300°C for 12 h.

As a proof-of-concept demonstration, we show here the bonding of 104 InP dies to an 8″ silicon wafer. The silicon wafer is covered with 1 μm PECVD oxide after CMP. The InP dies are diced into 5 mm × 5 mm in size. **Figure 5A** shows the photo image of the bonded wafers with nearly all InP dies are successfully bonded to the silicon wafer. The only missing piece is peeled off during pick-and-place process. The CSAM shown in **Figure 5B** suggests a successful bonding. The dark areas, which suggest less strong bonding, come from the dies located in the InP wafer edge. **Figure 5C** shows the sheer testing results. The maximum bonding strength is larger than 20 MPa, with an averaged bonding strength of ~13 MPa, which is comparable with that of W2W bonding under the same process.

All in all, we believe that there are at least two significant implications of the proposed multiple D2W bonding technology:

(1) The significantly increased bonding efficiency owing to the simultaneous batch process. Through the batch process of the III/V dies (pre-clean, plasma activation, etc.), it is possible to bond unlimited number of dies. It also helps to avoid potential contamination by performing the pick-and-place before cleaning process, and eliminates the time link constraint of the bonding surface deactivation. This is the most significant processing advantage comparing to the conventional pick-and-place method.

(2) The scalability to whatever-sized silicon wafers. Such multiple D2W bonding technology can easily be adopted for even larger-sized silicon wafers, such as 300 mm wafer. This is the most critical step toward the potential manufacturability of H-OEIC.

DESIGN OF III/V-on-Si LASERS

A hybrid III/V-on-silicon laser consists of a III/V epitaxial-layered structure and a silicon waveguide. It is a device that emits laser beams from silicon waveguides by electrical/optical injection to the III/V region. In this section, we will discuss the design of hybrid III/V-on-silicon lasers with regard to two fundamental laser elements, namely, optical gain medium and optical waveguide cavity.

DESIGN OF III/V MQW STRUCTURES

There are two main material systems for the fabrication of long-wavelength lasers emitting at 1.55 μm, which are InGaAsP/InP and InGaAlAs/InP systems. Both kinds of materials can be used to fabricate hybrid lasers. InGaAlAs MQWs exhibit a larger conduction band discontinuity ($E_c = 0.72E_g$), and smaller valence band discontinuity compared with InGaAsP MQW. This leads to an improved electron confinement, which can improve the temperature characteristics of semiconductor laser diodes. Thus, InGaAlAs/InP material system is more suitable for high speed and uncooled operation of semiconductor laser diode. In this study, we select this material system for the hybrid silicon lasers demonstration. The MQW region includes eight $Al_{0.055}Ga_{0.292}In_{0.653}As$ quantum wells separated by nine $Al_{0.055}Ga_{0.292}In_{0.653}As$ barriers. The gain spectrum of the MQW is calculated and the wavelength of peak gain is designed at 1550 nm when the carrier injection density increases from 5×10^{17} to $5 \times 10^{18}/cm^3$ as shown in **Figure 6A**. **Figure 6B** shows the measured photoluminescence (PL) spectrum for III/V epitaxial wafer at room temperature with the peak wavelength at about 1550 nm.

DESIGN OF HYBRID LASER VERTICAL WAVEGUIDE STRUCTURE

As mentioned, the optical gain comes from overlying III/V stack layer, which needs to be structured to efficiently inject electrons or holes into the MQW regions. A high overlap between the optical mode and the MQW benefits to achieve a high optical gain, which means that the optical mode needs to be well confined in the III/V waveguide. However, on the other hand, the light has to be confined sufficiently inside the silicon output waveguide for the efficient light extraction. In view of this, there are mainly two kinds of waveguide structures considering the optical power distribution for the hybrid laser with optical mode predominantly confined either in the silicon waveguide or in the III/V overlay. This leads to two different optical cavity designs. In the first design, the optical cavity comprises both III/V and silicon waveguides and the mode is mainly guided within the Si waveguide and evanescently coupled with the III/V waveguide. Such structure is also called as overlapped structure with hybrid mode (Fang et al., 2006, 2007a,b, 2008a,b,c, 2009). It has the advantage of making the coupling to a passive silicon waveguide straightforward and wavelength selective features can easily be defined in the silicon waveguide layer using CMOS fabrication techniques, which provides an accurate mechanism to control the emission wavelength of the laser. However, it requires a controllable thin bonding layer (<50 nm) for efficient optical coupling, which may increase the difficulty of bonding process. Furthermore, due to the weak interaction between the optical mode and gain material, it usually requires longer laser cavity, and thus resulting in high power consumption. In the second design, the mode in the hybrid section is mainly guided by the III/V waveguide, and the light is coupled from the III/V waveguide to the silicon waveguide through waveguide mode transformer, such as inverse tapers (Yariv and Sun, 2007; Sun et al., 2009a; Ben Bakir et al., 2011). In such design, the bonding interface can be relatively thick (typically from 30 to 150 nm) due to the released coupling constrain for the bonding interface. The advantage is that the optical mode experiences a high optical gain in the central region of the laser structure. However, the challenge of this structure is the fabrication of low-loss tapered waveguides. Hereafter, we name such design as adiabatic tapered coupling structure.

Silicon waveguide thickness selection

The selection of the silicon waveguide thickness depends on the detailed device dimensions/structures and the fabrication process. For indium phosphide (InP)-based gain waveguides, the effective refractive index is typically larger than 3.2 if the waveguide width and height are larger than 1 μm. In order to achieve this index for silicon waveguides for effective coupling with the InP-based gain

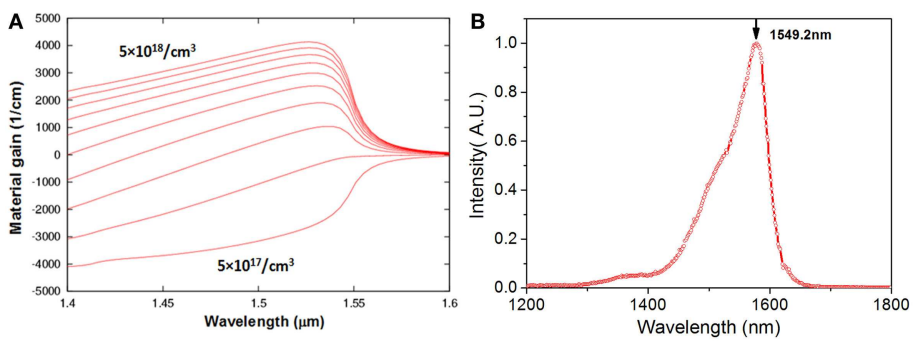

FIGURE 6 | (A) The calculated gain spectrum under different carrier injection concentration. **(B)** The measured photoluminescence (PL) spectrum for III/V epitaxial wafer.

region, the corresponding silicon waveguide thickness needs to be sufficiently large. **Figure 7** shows the calculated effective refractive index of the fundamental mode in silicon waveguide depending on the waveguide thickness. It indicates that the required silicon thickness needs to be larger than 450 nm to achieve an effective index of 3.2 for the waveguide with 2 μm in width. Such thick silicon layer does not match with the current mainstream silicon photonics. However, on the other hand, it is still possible to couple light from 220 nm silicon to InP waveguides by using very narrow InP waveguides (~200 nm) to push down the value of effective index, although the fabrication is difficult to form these narrow InP waveguides by conventional photolithography.

Overlapped structure with hybrid mode

As mentioned above, there is a tradeoff between the optical mode confinement in the III/V and silicon regions for the overlapped structure. The bonded III/V-Si structure forms the hybrid waveguide cavity. The effective refractive index of III/V active and Si regions are critical parameters for the hybrid waveguides, which, respectively, determine the light confinement factors in III/V and Si region. In our design, the confinement factors over the silicon and the quantum well regions are modified by altering the silicon waveguide thickness and the separate confinement heterostructure (SCH) thickness in order to ensure sufficiently low-threshold gain for lasing. While the thicker silicon waveguide pulls the optical mode into the silicon layer, the larger SCH thickness can drag back the optical mode into the III/V region.

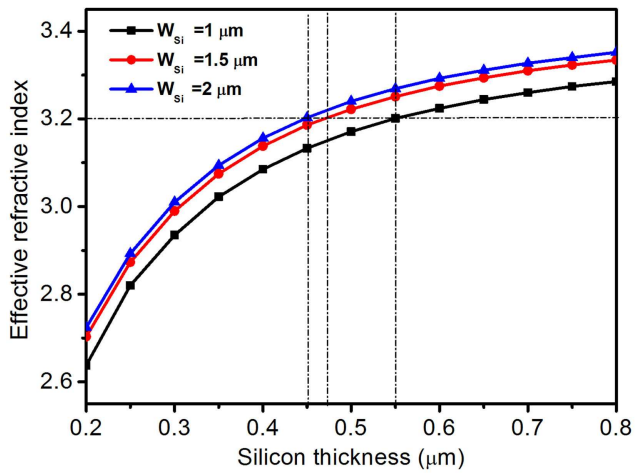

FIGURE 7 | Effective refractive index of the silicon waveguide fundamental mode as the function of silicon waveguide thicknesses. Both top and bottom claddings are oxide ($n = 1.45$) and silicon index is chosen as 3.48 at the wavelength of 1550 nm.

Figure 8A shows the calculated optical confinement factors in MQW and Si depending on the Si waveguide width under different Si thickness, with assuming the III/V ridge width and the SCH thickness of 6 μm and 250 nm, respectively. It shows that when the waveguide widths of III/V and Si are fixed, the optical confinement in Si waveguide can be increased by using a thick Si layer. With the silicon waveguide thickness of 700 nm, large confinement of up to 70% in silicon waveguide is achieved. However, the device performance is very sensitive to the bonding interface quality due to the overlapping of the optical mode with the bonding interface between the III/V and the silicon. Based on the analysis, we adopt silicon thickness of 500 nm for the demonstration of hybrid Si lasers.

Figure 8B shows the simulated optical confinement factor in MQW and in silicon waveguide with different SCH thickness, with the fixed III/V and Si waveguide widths of 4 and 2 μm, and Si waveguide thickness of 500 nm. As the SCH thickness increases, the optical mode confinement in III/V region increase, which in turn significantly decreases the optical mode confinement in silicon waveguide. Inserts in **Figure 8B** show the simulated field distributions with SCH thicknesses of 0.1 and 0.5 μm. It shows obviously that for the small SCH thicknesses, the optical mode lies primarily in the silicon region, while the optical mode is dragged into III/V region with increased SCH thickness. The ability to control the optical mode with the SCH thickness is a key feature of this platform. For hybrid lasers, higher optical confinement is needed to achieve lower threshold current. Thus, we choose an optimized SCH thickness of 0.18 μm for the hybrid lasers.

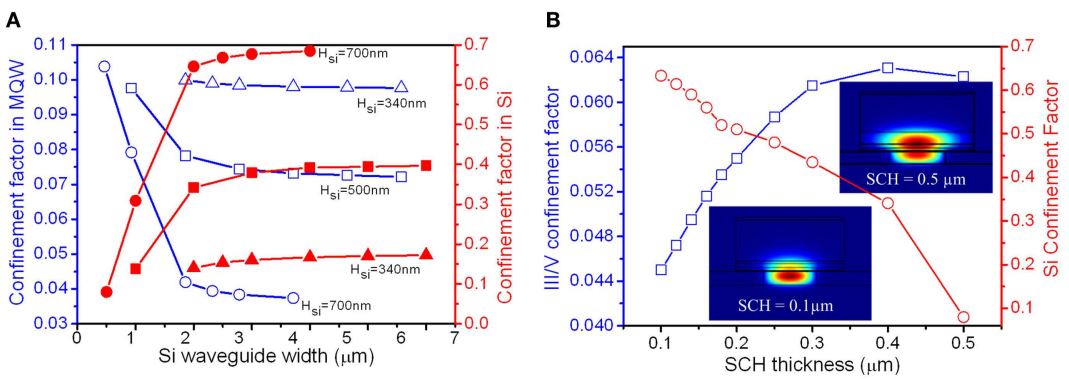

FIGURE 8 | Confinement factor of optical mode in multiple quantum wells (MQW) and Si waveguide as a function of (A) the Si waveguide width under different Si waveguide thicknesses, and (B) the SCH thickness. Insets: the simulated field distributions of the fundamental TE mode with different SCH thicknesses. It shows that by increasing the thickness of SCH layer up to 500 nm, the optical mode is more confined in the III/V active layer.

For such hybrid III/V-on-silicon lasers, another challenge arises from the control of the bonding layer thickness. Generally, a thin bonding layer (<50 nm) is needed for efficient optical coupling between III/V and silicon regions, while the thicker bonding layer benefits to the bonding quality of III/V layer and the bonding yield improvement. For direct bonding without oxide interlayer, it is easy to achieve such thin thickness, which is usually only the native oxide. However, this process is particularly sensitive to surface roughness and particles contamination, which would limit the bonding quality and bonding yield. DVS-BCB bonding can be used for the heterogeneous integration of III/V material on silicon to improve the yield. However, it is difficult to obtain a controllable thin bonding interlayer of <50 nm. In our case, we choose silicon oxide as interlayer between III/V and silicon, which is also compatible with the mainstream silicon phonics, in which all the devices are with oxide cladding.

Figure 9A shows the calculated optical confinement factor in MQW and silicon waveguide as the function of interlayer oxide thickness. In the simulation, we assume the fixed silicon thickness of 500 nm, the silicon waveguide width of 3 μm, and III/V ridge waveguide with of 6 μm. We observe from the results that the Si confinement factor largely decreases when the interlayer thickness increases from 10 to 100 nm. Only approximately 5% optical light is confined in the silicon waveguide when the interlayer thickness is 100 nm.

Additionally, the interlayer of oxide at the bonding interface also affects the characteristics temperature of hybrid III/V-on-silicon laser due to the poor thermal conductivity of as low as 1.3 W/m/K. The modal gain of laser is dependent on the temperature of the active region. As the temperature of active region increases, the modal gain decreases due to the increased carrier leakage out or not reaching the active region, and/or increased non-radiative recombination. The decrease of modal gain leads to high threshold current and low output optical power. In order to investigate the effect of interlayer on the thermal characteristics of the hybrid lasers, a two-dimensional model of the device structure is conducted using COMSOL by mapping out the heat dissipation of each layer. **Figure 9B** shows the simulation structure. In the simulation, the structure parameters are as follows: III/V ridge width, Si ridge width and thickness, and the laser cavity length are assumed to be 6 μm, 1 μm, 500 nm, and 1000 μm, respectively. Injection current is 500 mA and the corresponding voltage is 4 V. **Figure 9C** shows the calculated working temperatures in the III/V active region with different thicknesses of the oxide interlayer. The increase of temperature in the III/V active region versus interlayer thickness is about 0.02 K/nm. For illustration purpose, **Figure 9D** shows as an example the thermal distribution within the layered structure for the oxide interlayer thickness of 0 nm. The thermal distributions for the other thicknesses are similar. Actually, we can conclude from the study that the main hurdle for the heat dissipation is the SOI BOX layer, which can be seen from the results without oxide bonding interlayer (thickness = 0 nm). Thus, for enhanced thermal management, novel designs such as thermal shunt (Liang et al., 2012) are required to effectively remove the generated heat.

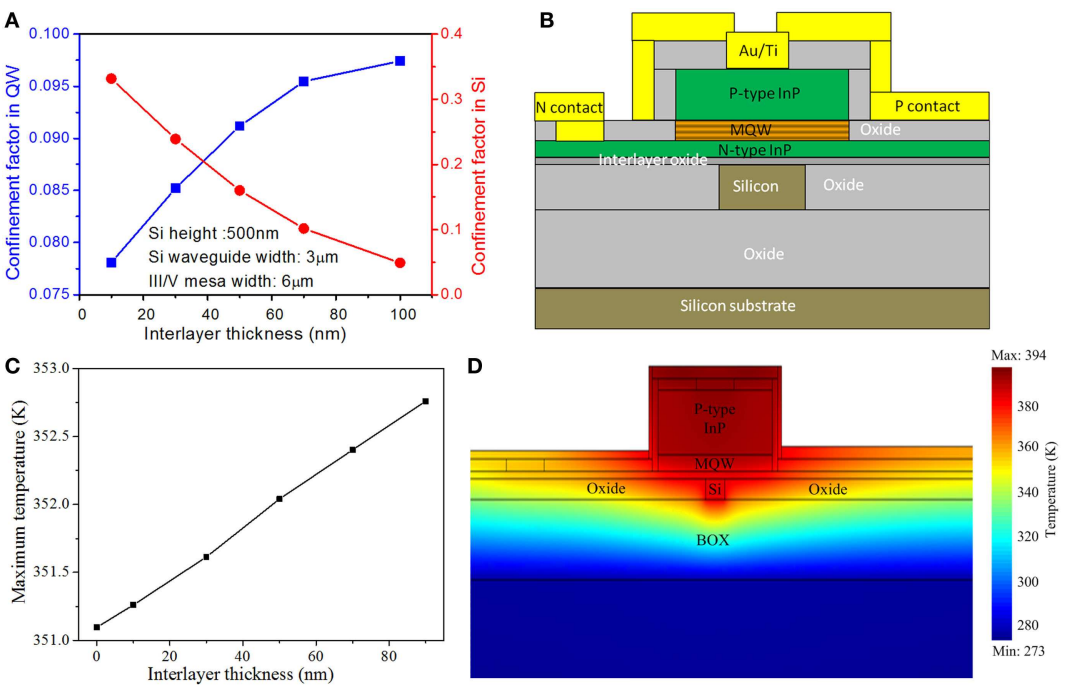

FIGURE 9 | (A) The confinement factor of the optical mode in the MQW and silicon layers, respectively, as a function of the interlayer thickness. **(B)** The simulation structure of the thermal distribution. **(C)** The temperature changes in the III/V active region with regard to the oxide interlayer thickness. **(D)** The simulated thermal distribution with the interlayer thickness is 0 nm.

Adiabatic tapered coupling structure

For the adiabatic tapered coupling structure, the mode in the hybrid section is mainly guided by the III/V waveguide, and the light is coupled from the III/V waveguide to the silicon waveguide through a tapered waveguide. It shows that a tapering length ~100 μm is required for a sufficient light coupling with minimized optical loss. By using such tapered coupling, it eliminates the tricky tradeoff between the modal gain and vertical coupling efficiency, which is inherent in the overlapped waveguide structures. Therefore, hybrid lasers with a short cavity as pure III/V laser are possible. Up to now, the hybrid lasers with the high performances are achieved using such tapered coupling scheme (Levaufre et al., 2014; Zhang et al., 2014).

In order to efficiently couple the light between the Si-III/V hybrid waveguide and the silicon waveguide, the III/V waveguide and silicon waveguides are tapered simultaneously in the same direction. Here, we adopt a three-dimensional approximated model based on beam propagation method (BPM) in order to optimize the tapering structure of the silicon waveguide and III/V waveguide for an efficient coupling. **Figure 10A** schematically illustrates the design of such waveguide tapering structure. The coupling efficiency largely depends on the tapering design, especially the III/V waveguide taper width and taper length. Here, we simulate such dependency by varying the taper width and taper length, while fixing the III/V waveguide width of 5 μm, the silicon waveguide width of 1 μm, and the silicon taper length of 100 μm.

Figures 10B,C, respectively, show the simulated coupling efficiency from III/V-Si hybrid waveguide to silicon waveguide as functions of the III/V waveguide taper width and tape length. It suggests that the coupling efficiency from III/V-Si hybrid waveguide to Si waveguide can be as high as 85% by using an 80-μm-long III/V waveguide taper and a 100-μm-long silicon waveguide

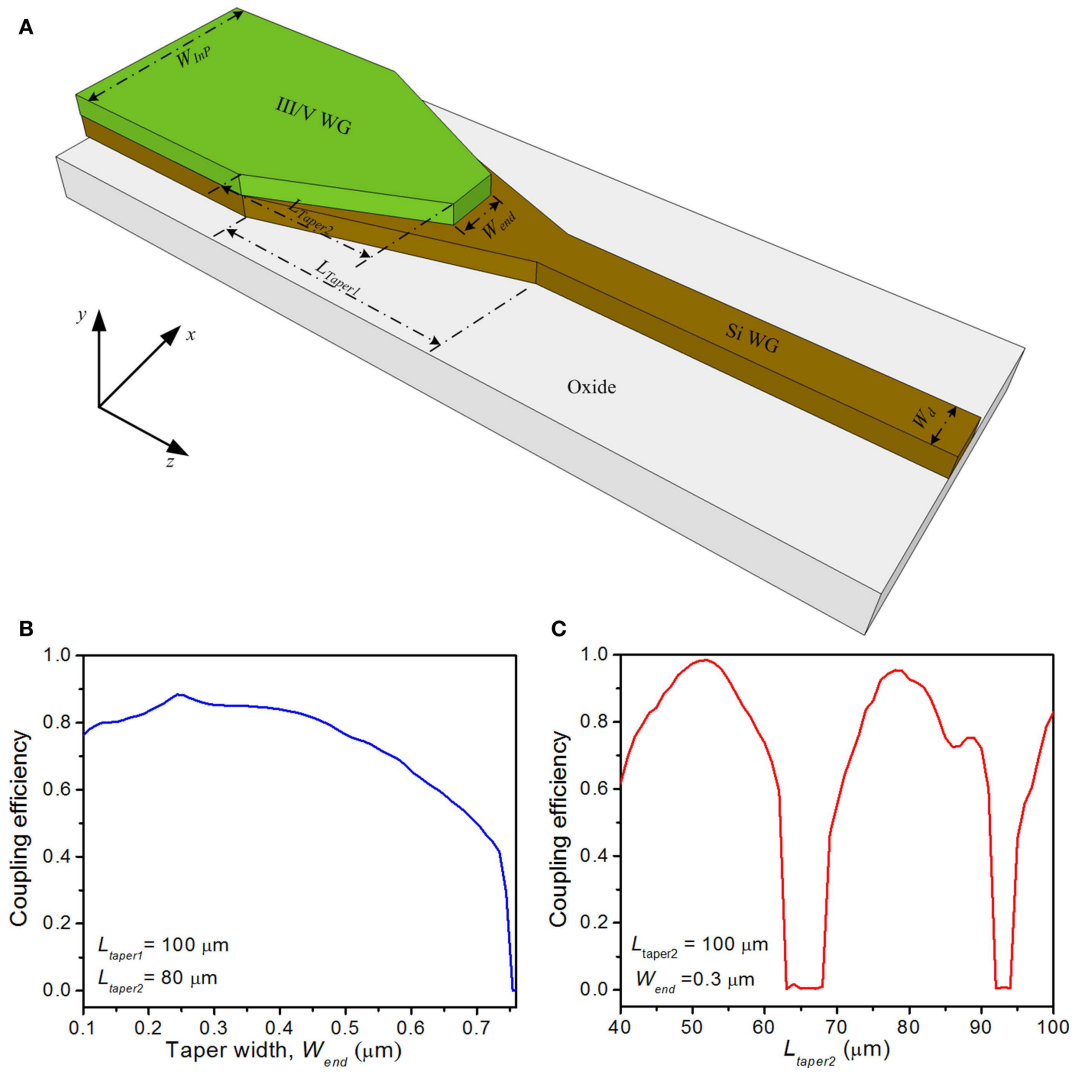

FIGURE 10 | (A) Schematics of the tapering structure for the vertical coupling between III/V waveguide and silicon waveguide. W_{InP}: III/V waveguide width, W_{end}: III/V waveguide taper width, W_d: silicon waveguide width, L_{Taper1}: silicon waveguide taper length, L_{Taper2}: III/V waveguide taper length. The whole structure is cladded with oxide. Coupling efficiency of III/V waveguide to Si waveguide as functions of **(B)** the III/V waveguide taper width, and **(C)** the III/V waveguide taper length.

tape. Through optimizing the III/V waveguide taper width and III/V waveguide taper length, the maximum coupling efficiency can be as high as 99%. However, due to the optoelectronic fabrication limitation, we are not able to demonstrate the hybrid laser using such adiabatic tapered coupling structure.

DEMONSTRATION OF III/V-on-Si HYBRID LASERS

Using the proposed multiple D2W bonding technology, we have demonstrated various hybrid silicon lasers, including FP lasers, DBR lasers, sidewall-grating lasers, racetrack-shaped microring lasers, and MLL. In this section, we will first introduce the hybrid silicon laser fabrication process, leveraging on IME's CMOS-compatible silicon photonic fabrication facilities and NTU's expertise in optoelectronics fabrication capability, followed with showing some hybrid silicon laser demonstrations as the examples.

III/V-on-Si HYBRID LASER FABRICATION PROCESS

The III/V-on-Si hybrid laser fabrication in our demonstrations includes two parts, namely silicon passive device fabrication using IME's CMOS line and multiple D2W bonding in IME's MEMS line, and III/V optoelectronics fabrication in NTU. **Figure 11** shows the fabrication process flow. We adopt commercially available SOI wafer with 340 nm silicon layer sitting on a 2 μm buried oxide (BOX) layer. The fabrication starts with the blanket silicon epitaxy to ~500 nm for refractive index matching between silicon waveguide device and InP gain medium. After the deposition of 70 nm oxide as the hard mask, the waveguide structures, including both grating coupler and inverse taper coupler are patterned by deep UV photolithography and transferred onto the silicon layer by using deep RIE etching. For the grating coupler, the silicon etching thickness is 377 nm. While for other waveguide devices, second silicon etch is applied down to the BOX layer by covering the surface grating coupler area with additional photo resist. Oxide cladding of 650 nm in thickness is deposited followed by a surface planarization step, which includes oxide etch-back with 500 nm in depth and CMP process. Such planarization steps with CMP also help to smooth the bonding surface with very small surface roughness for molecular bonding. The interlayer oxide thickness can be well controlled by the CMP process, with only ~50 nm oxide left atop the silicon waveguide in our demonstration. For enhanced flatness and uniformity of the bonding surface, we only etch away the silicon surrounding the devices, remaining most of the silicon areas forming silicon plateaus.

The multiple D2W bonding is then performed after the preparation of III/V dies, followed with the process described in Section "III/V-to-Si Wafer-to-Wafer (W2W) Bonding Technology." As the designed devices are all within an area of 8 mm × 8 mm, the InP dies are all diced with 9 mm × 9 mm with the consideration of bonding misalignment of ±500 μm for the notch alignment, thus ensuring the full covering of all the silicon photonic devices within the III/V die area. For a 50 mm InP wafer, there are only 16 full dies with 9 mm × 9 mm in size. Thus, for the purpose of hybrid silicon laser demonstration using such D2W bonding technology, we only perform 16-dies bonding to 200 mm silicon wafers, with some of the silicon photonics device area being wasted. **Figure 12A** shows the photo image of the 16-dies bonded silicon wafer. **Figure 12B** shows the CSAM results. Except some particle-induced bonding defects, all the dies are bonded very well. However, we clearly observe that some of the die edge periphery regions are not bonded well due to the wafer dicing induced damage. **Figures 12C,D**, respectively, show the TEM and cross-SEM of the bonding structures, both suggesting very reliable bonding quality.

The III/V optoelectronic fabrication starts from the InP substrate removal using HCl solution. After photolithography, the InP mesa structures are formed by using H_3PO_4, H_2O_2, and HCl mixed solution to etch the InGaAs contact layer and p-InP cladding layer. The SCH layer and QW layer are also etched using H_3PO_4:H_2O_2:H_2O solution, stopping on the n-InP cladding layer.

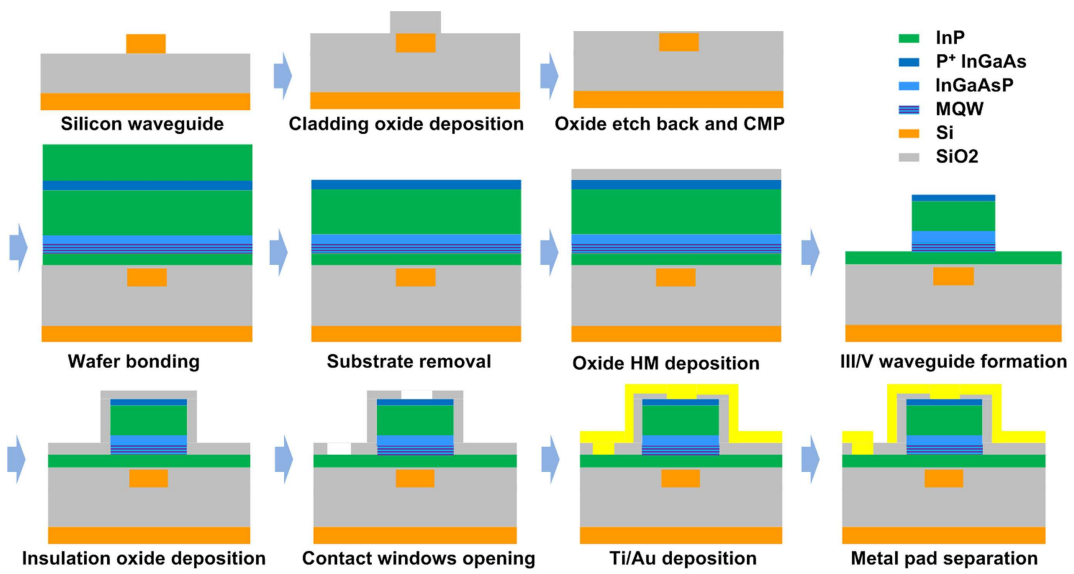

FIGURE 11 | The fabrication process of the hybrid silicon laser in a ridge waveguide structure.

Then, an SiO_2 insulator layer with the thickness of 300 nm is deposited, followed with the contact opening for p-type and n-type injection by one-time photolithography and the oxide is etched by HF solution. After that, Ti/Au metal contacts are formed by sputtering, with wet etching to form a Ti/Au slot between the n-type and p-type contacts using diluted HF and KI solution, respectively.

FABRY–PEROT LASERS

The CW operation of the optical laser requires good thermal management to remove the generated heat. In the case of FP lasers, another way is to design narrow ridge waveguide to generate less heat. In our demonstration, we design a FP laser with ridge waveguide width of 6 μm. The laser facets are formed by lapping down the Si substrate to around 60 μm, followed with mechanical cleaving. The length of the FP laser is ~720 μm. The demonstrated FP laser is able to work at room temperature with CW operation. **Figure 13A** shows the measured *P–I* curves under different temperatures. The threshold current at 264 K is ~45 mA, and increases significantly to ~100 mA at room temperature. We attribute such fast increase of the threshold to the thick oxide interlayer, which prohibits the heat dissipation efficiently. The measured output power from a single facet without any reflection coating is more than 1 mW. This includes the coupling loss due to the un-optimized testing setup for light collection, which is estimated only with ~20% light collection efficiency. The thermal dissipation is very important for CW lasing. **Figure 13B** shows the measured lasing spectra under different temperatures. The wavelength shift with temperature is about 0.75 nm/K.

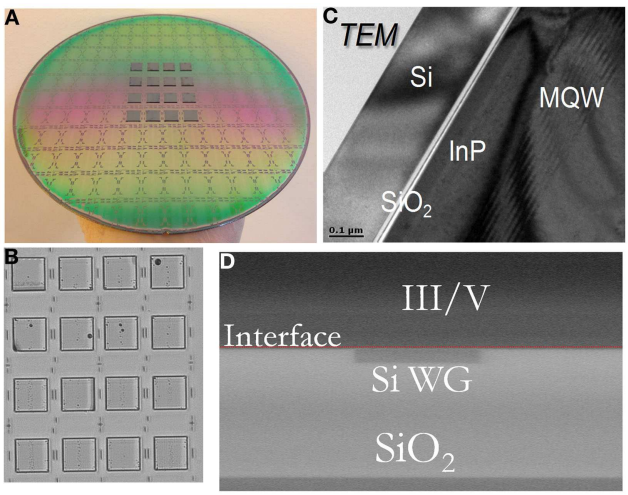

FIGURE 12 | (A) The optical image of the 16-dies bonded silicon wafer. **(B)** CSAM results. **(C)** TEM of the bonding structure. **(D)** Cross-SEM of the bonding structures.

LATERAL-COUPLED DISTRIBUTED-FEEDBACK LASERS WITH SIDE WALL GRATING

The FP laser is fabricated by lapping down the silicon substrate and mechanical cleaving to form the facets. From the optical communication and optical interconnect applications point of view, such FP lasers are not practical for photonic integration. Furthermore, how to achieve good facet is still a main challenge and a key limiting factor for high-performance hybrid lasers as reflection coating is always required in order to optimize the cavity transmission and reflection. In view of this, optical resonators, Bragg grating structures that form the cavities through fabrication are the good candidates for on-chip hybrid laser. We here show as an example of a hybrid laser using LC-DFB structure as the laser cavity.

Figure 14A schematically shows the perspective view of the LC-DFB hybrid laser with illustration of the key parameters, including the Bragg grating period Λ, the silicon ridge width *D*, and the grating teeth width, W_1. Considering the fabrication limitation, we design third-order later Bragg grating in order to achieve single-mode operation. With regard to the silicon thickness of 500 nm, the grating period Λ is 670 nm with filling factor of 0.5. The ridge width *D* and the teeth width W1 are, respectively, designed with 2 and 1 μm. The Bragg grating is centered beneath the III/V gain region, which is with the width of 12 μm. Both LC-DFB structure and III/V gain region are designed with the same lengths. In order to extract the output laser light for easy characterization, the vertical grating couplers are adopted. For the vertical grating coupler, the period is designed to be 640 nm with filling factor of 0.5, and the silicon etch depth is 377 nm. Such grating coupler design is purely based on theoretical calculation, without any process

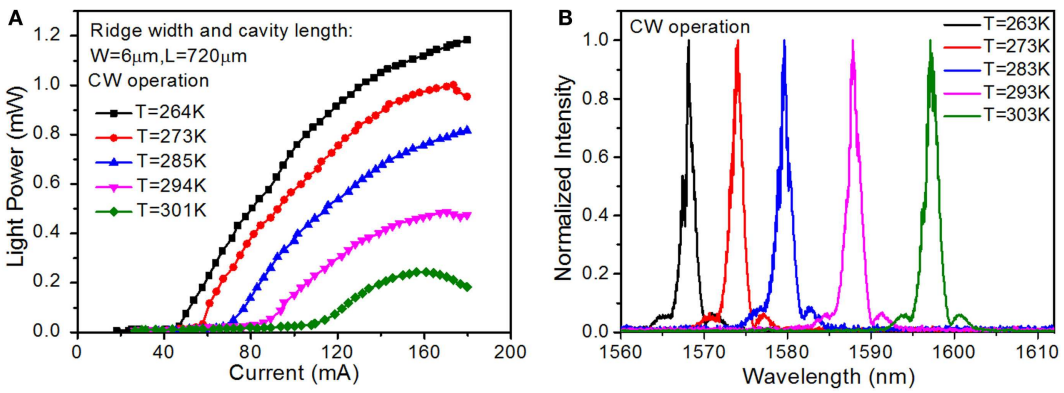

FIGURE 13 | (A) The power–current characteristic curves and **(B)** the lasing spectra of a typical hybrid silicon FP laser measured under different temperature.

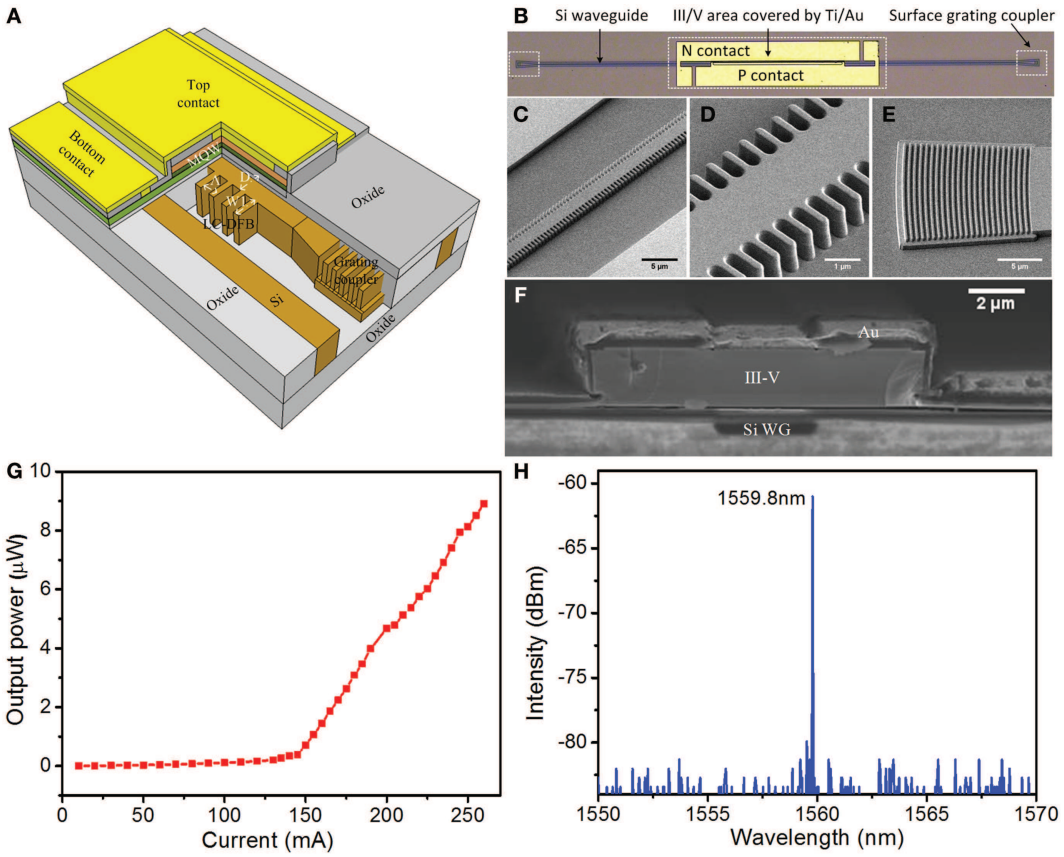

FIGURE 14 | (A) The perspective view of the hybrid LC-DFB laser integrating with surface grating coupler, with illustration of the key design parameters. Λ: grating period, *D*: the ridge width, and W_1: the grating teeth width. **(B)** Top-view optical microscope image of a LC-DFB hybrid laser integrated with vertical surface coupler. **(C–E)** The SEM of the LC-DFB structures and the grating coupler. **(F)** The cross SEM of the vertical layered structure. **(G)** The light power output and **(H)** the laser spectrum of the hybrid silicon laser with sidewall Bragg grating structure. The output power is directly measured from the surface grating coupler.

verification and optimization. For this demonstration, we did not design any mode transformer between III/V layer and silicon waveguide layer, thus expecting some transition loss. **Figure 14B** shows the optical microscope image of the fabricated hybrid LC-DFB laser with integrated vertical grating couplers. The LC-DFB structure and the III/V gain region are designed with same length of 700 μm, while the silicon device including two grating couplers is ~2750 μm. Due to the optoelectronic fabrication limitation, there is no designed taper between III/V waveguide and silicon waveguide, thus expecting relatively high transition loss. **Figures 14C–E** show the SEM images of the fabricated LC-DFB and vertical grating coupler, while **Figure 14F** shows the cross-sectional SEM of the vertical structures, illustrating the Si waveguide, the III/V layer, and the Ti/Au layer.

Figures 14G,H show the measured *P–I* curve and the spectrum of the LC-DFB hybrid laser under pulse operation. The threshold current is ~120 mA, corresponding to a threshold current density of ~1.42 kA/cm^2. From the spectrum, we see clearly single-mode operation with the peak wavelength at 1559.8 nm and a side-mode-suppression ratio (SMSR) larger than 20 dB. This is expected from the LC-DFB design. However, the maximum output power is only ~10 μW upon 250 mA current injection, which also can be observed from the spectrum measurement. We attribute the relatively low output power to the following two reasons, namely, the accumulated optical loss, and the inefficient vertical light coupling. First of all, the optical loss, which mainly includes the surface grating coupler coupling loss, the Bragg grating scattering loss, and the non-radiative recombination loss from the bonding interface, affects the light output significantly. From the reference measurement for the device only with passive silicon waveguide yet bonded III/V layer, the accumulated total loss is >40 dB, which is mainly due to the unoptimized surface grating coupler. Second, the oxide interlayer in our design, which might not be able to control precisely, will affect the light coupling efficiently from III/V layer to silicon waveguide. Furthermore, the polarization sensitivity of the surface grating coupler can also induce additional optical loss. Thus, the optimized grating coupler design for the light extraction from the silicon waveguide and the vertical light transition structure for light coupling from III/V layer to silicon waveguide can significantly increase the laser output power. Besides, by optimization of the Bragg grating period and silicon waveguide thickness, the SMSR can also be enhanced.

PASSIVELY MODE-LOCKED LASERS

Semiconductor MLLs are excellent candidates for generating stable ultra-short optical pulses, which have a corresponding wide optical spectrum of phase correlated modes and high repetition rate. Optical frequency combs emitted by MLLs can have high extinction ratios, low jitter, and low chirp, which can be utilized in a variety of applications including AWG, optical clock generation and recovery, coherent communications systems, high-speed analog-to-digital conversion (ADC), and optical time-division multiplexing (OTDM), etc. Integration of MLLs on silicon is very promising as it combines the low-loss and low-dispersion characteristics of silicon material with high gain III/V material, thus ensuring improved performance. Furthermore, it will be possible for semiconductor MLLs to generate ultra-short optical pulses with low repetition rate on the silicon platform owing to the long cavity length. Here, we show our preliminary demonstration of a passive MLL using the developed heterogeneous integration platform.

The optical cavity of the MLL is defined by a 1250-μm-long gain section, a saturable absorber (SA) with the length of 30-100μm, and cleaved facet at the waveguide end. The gain section and SA are separated by a 20 μm electrical isolation region with isolation resistance >1 kΩ. The SA is made up of the same active material as the gain section. The difference between the SA and gain section is that SA absorbs the light in the cavity upon applying a reverse bias, while the gain section amplifying light upon forward current injections.

The laser optical output is collected by a photodiode located in front of the cleaved facet. The typical threshold current with an unbiased 50-μm-long SA section is 88 mA. The device has a maximum single facet CW output power of 1 mW at room temperature when the injection current is 140 mA. The series resistance is about 8.5 Ω, while the slope efficiency is about 0.02 mW/mA. **Figure 15A** shows the measured optical spectra at different injection currents. It shows that the widest optical emission is centered at about 1605 nm with a full-width at half-maximum (FWHM) of 5.4 nm at the injection current of 110 mA measured by an optical spectrum analyzer (OSA). Assuming the generated optical pulse is chirp-free and the shape of the pulse is with a Sech-function, the width of the optical pulse is calculated to 0.5 ps.

Passive mode locking of the device is obtained by forward biasing the gain section (I_{gain}) and reverse biasing (V_{sa}) or un-biasing the SA section. The mode locking behavior of the device is characterized by measuring the radio frequency (RF) spectrum using the spectrum analyzer (Agilent E4448A). **Figure 15B** shows the measured RF spectrum of the III/V-on-Si MLL at the injection current to the gain section (I_{gain}) of 110 mA and reverse biasing the SA section at −0.9 V. The resolution bandwidth (RBW) during measurement is 1 MHz. The repetition frequency is about 30.0 GHz with signal-to-noise ratio above 30 dB. By changing I_{gain}, it can be tuned to more than 30 GHz, giving clear evidence of passively mode locking of light signal. The measured RF linewidth of the injection locked laser is about 7 MHz by Lorentzian fitting the RF spectrum.

SUMMARY AND FUTURE OUTLOOK

KEY ACHIEVEMENTS

In summary, we reviewed in this paper the recent demonstrations of optical light source in silicon for the application of H-OEIC, with major focus on hybrid silicon lasers through wafer bonding technology. Furthermore, we proposed a proprietary high-throughput multiple dies-to-wafer (D2W) bonding technology by temporarily bonding III/V dies to a handle silicon wafer through pick-and-place process for subsequent simultaneous batch processing. Such high-throughput multiple D2W bonding technology features the merits of high bonding yield with unlimited III/V dies and scalability to whatever-size silicon wafers, thus is the key enabling technique toward potential manufacturability of large-scale H-OEIC. As proof-of-concept demonstration, we showed the III/V dies to silicon wafer bonding with up to 104 dies. Repeatable demonstrations of 16-III/V dies bonding to pre-patterned 200 mm silicon wafers are performed for the fabrication of hybrid silicon lasers with various laser cavities, including FP lasers, LC-DFB laser with side wall grating, and MLL.

CHALLENGES AND FUTURE OUTLOOK

However, there are still many key issues need to be addressed before the hybrid silicon laser applied to optical interconnects system.

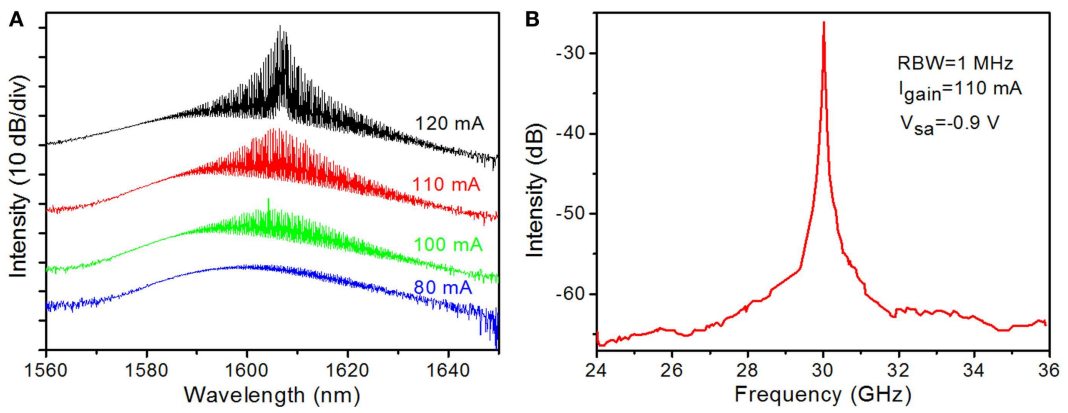

FIGURE 15 | (A) The measured optical spectra of the III/V-on-silicon mode-locked laser at different injection currents to the gain section while the SA section is floating. **(B)** Measured RF spectrum of the III/V-on-Si MLL at 110 mA injection current and saturation voltage of −0.9 V. The RBW during measurement is 1 MHz.

Here, we will only discuss three of the most important issues, including:

(1) the thermal management;
(2) the integration with other silicon photonic devices with full wafer processing capability; and
(3) the new platform beyond silicon for high-performance advanced hybrid lasers.

Thermal management is one of the major obstacles for achieving high-performance hybrid silicon lasers for practical applications (Sysak et al., 2011). Due to the poor thermal conductivity of the SOI BOX layer as well as the inter oxide layer between bonding surface, such layers would prevent the efficient heat dissipation to the silicon substrate, thus resulting in the poor laser performances, such as lower laser power. One of the simple ways to increase the thermal dissipation efficiency is to design the contact electrodes with thick and large area metal, serving as the top surface heat sink. Another efficient way for thermal dissipation is to remove the BOX layer in some areas and refill it with high thermal conductive materials such as polycrystalline silicon or metals, serving as thermal shunt (Liang et al., 2012). However, although such approach has been demonstrated with enhanced thermal management and increased laser performance, it still requires further development in order to further improve the performance.

The integration of such hybrid laser with the existing silicon photonics building blocks is another key issue before it is applied for H-OEIC. For most of the demonstrated hybrid silicon lasers, the silicon waveguide is normally with more than 500 nm thickness in order to ensure the optical index matching with III/V material for efficient light coupling to silicon waveguide. Such thick waveguide design is actually not compatible with the mainstream silicon photonics, with most of the key building blocks are demonstrated in 220 nm silicon wafers (Xu et al., 2014). Thus, novel designs taking care of both of these design considerations are required. Recently, Dong et al. (2014a,b) demonstrated novel integration scheme with associated transition structure via epitaxial growth of silicon in a pre-defined trench. Such epitaxial-grown silicon mesa also serves as the bonding interface with III/V gain material. Thus, the rest of the device area leaves with 220 nm silicon for other existing silicon photonic devices. Such novel demonstration sets a path toward the integration of hybrid silicon laser with existing silicon photonics building blocks. However, for practical integration with high-speed modulator and photodetector, which involves even complicated integration process with multiple oxide etch-back and CMP, it is still very challenging on how to ensure the flatness and smoothness of the bonding surface. More sophisticated design and further demonstration with integration of such are highly demanded.

The third issue is associated with current new demonstration trend that utilizes extremely low-loss SiN or SiON waveguide as the passive waveguide layer (Bovington et al., 2014; Luo et al., 2014). As we know, for some advanced type of hybrid lasers, such as the MLLs, extremely low optical loss is required for achieving high performances. The state-of-the-art demonstration of the silicon waveguide is still with propagation loss of ~2 dB/cm, which is higher comparing that of SiN waveguide of 0.1 dB/m (Bauters et al., 2011). Thus, III/V-SiN platform for hybrid lasers is another interest research area, which can address the loss issue. The integration between SiN waveguide and other SOI-based devices is also CMOS-compatible and ready for further application (Huang et al., 2014).

ACKNOWLEDGMENTS

This work was supported by A*STAR SERC Future Data Center Technologies Thematic Strategic Research Programme under Grant No. 112 280 4038, and A*STAR – MINDEF Science and Technology Joint Funding Programme under Grant No.122 331 0076.

REFERENCES

Alduino, A., and Paniccia, M. (2007). Interconnects: wiring electronics with light. *Nat. Photonics* 1, 153–155. doi:10.1038/nphoton.2007.17

Alexe, M., and Gösele, U. (2004). *Wafer Bonding: Applications and Technology*. Berlin: Springer-Verlag.

Bauters, J. F., Heck, M. J., John, D. D., Barton, J. S., Blumenthal, D. J., Bowers, J. E., et al. (2011). "Ultra-low-loss (< 0.1 dB/m) planar silica waveguide technology," in *Paper Presented at the IEEE Photonics Conference* (Arlington, VA: Marriott Crystal Gateway).

Beausoleil, R. G., Kuekes, P. J., Snider, G. S., Wang, S.-Y., and Williams, R. S. (2008). Nanoelectronic and nanophotonic interconnect. *Proc. IEEE* 96, 230–247. doi:10.1109/JPROC.2007.911057

Ben Bakir, B., Descos, A., Olivier, N., Bordel, D., Grosse, P., Augendre, E., et al. (2011). Electrically driven hybrid Si/III-V Fabry-Pérot lasers based on adiabatic mode transformers. *Opt. Express* 19, 10317–10325. doi:10.1364/OE.19.010317

Bogaerts, W., Baets, R., Dumon, P., Wiaux, V., Beckx, S., Taillaert, D., et al. (2005). Nanophotonic waveguides in silicon-on-insulator fabricated with CMOS technology. *J. Lightwave Technol.* 23, 401–412. doi:10.1109/JLT.2004.834471

Bovington, J., Heck, M., and Bowers, J. (2014). Heterogeneous lasers and coupling to Si 3 N 4 near 1060 nm. *Opt. Lett.* 39, 6017–6020. doi:10.1364/OL.39.006017

Boyraz, O., and Jalali, B. (2004). Demonstration of a silicon Raman laser. *Opt. Express* 12, 5269–5273. doi:10.1364/OPEX.12.005269

Boyraz, O., and Jalali, B. (2005). Demonstration of directly modulated silicon Raman laser. *Opt. Express* 13, 796–800. doi:10.1364/OPEX.13.000796

Camacho-Aguilera, R. E., Cai, Y., Patel, N., Bessette, J. T., Romagnoli, M., Kimerling, L. C., et al. (2012). An electrically pumped germanium laser. *Opt. Express* 20, 11316–11320. doi:10.1364/OE.20.011316

Cheng, S.-L., Lu, J., Shambat, G., Yu, H.-Y., Saraswat, K., Vuckovic, J., et al. (2009). Room temperature 1.6 μm electroluminescence from Ge light emitting diode on Si substrate. *Opt. Express* 17, 10019–10024. doi:10.1364/OE.17.010019

Christiansen, S. H., Singh, R., and Gosele, U. (2006). Wafer direct bonding: from advanced substrate engineering to future applications in micro/nanoelectronics. *Proc. IEEE* 94, 2060–2106. doi:10.1109/JPROC.2006.886026

Chu, T., Fujioka, N., and Ishizaka, M. (2009). Compact, lower-power-consumption wavelength tunable laser fabricated with silicon photonic-wire waveguide micro-ring resonators. *Opt. Express* 17, 14063–14068. doi:10.1364/OE.17.014063

Creazzo, T., Marchena, E., Krasulick, S. B., Yu, P. K., Van Orden, D., Spann, J. Y., et al. (2013). Integrated tunable CMOS laser. *Opt. Express* 21, 28048–28053. doi:10.1364/OE.21.028048

Dong, P., Hu, T.-C., Liow, T.-Y., Chen, Y.-K., Xie, C., Luo, X., et al. (2014a). Novel integration technique for silicon/III-V hybrid laser. *Opt. Express* 22, 26854–26861. doi:10.1364/OE.22.026854

Dong, P., Liu, X., Chandrasekhar, S., Buhl, L. L., Aroca, R., and Chen, Y.-K. (2014b). Monolithic silicon photonic integrated circuits for compact 100 Gb/s coherent optical receivers and transmitters. *IEEE J. Sel. Top. Quantum Electron.* 20, 1–8. doi:10.1109/JSTQE.2013.2295181

Dong, P., Hu, T.-C., Zhang, L., Dinu, M., Kopf, R., Tate, A., et al. (2013). 1.9 μm hybrid silicon/iii-v semiconductor laser. *Electron. Lett.* 49:664. doi:10.1049/el.2013.0674

Dong, P., Liao, S., Feng, D., Liang, H., Zheng, D., Shafiiha, R., et al. (2009). Low V pp, ultralow-energy, compact, high-speed silicon electro-optic modulator. *Opt. Express* 17, 22484–22490. doi:10.1364/OE.17.022484

Dumon, P., Bogaerts, W., Wiaux, V., Wouters, J., Beckx, S., Van Campenhout, J., et al. (2004). Low-loss SOI photonic wires and ring resonators fabricated with deep UV lithography. *IEEE Photonics Technol. Lett.* 16, 1328–1330. doi:10.1109/LPT.2004.826025

Fang, A. W., Jones, R., Park, H., Cohen, O., Raday, O., Paniccia, M. J., et al. (2007a). Integrated AlGaInAs-silicon evanescent racetrack laser and photodetector. *Opt. Express* 15, 2315–2322. doi:10.1364/OE.15.002315

Fang, A. W., Park, H., Kuo, Y.-H., Jones, R., Cohen, O., Liang, D., et al. (2007b). Hybrid silicon evanescent devices. *Mater. Today* 10, 28–35. doi:10.1016/S1369-7021(07)70177-3

Fang, A. W., Koch, B. R., Gan, K.-G., Park, H., Jones, R., Cohen, O., et al. (2008a). A racetrack mode-locked silicon evanescent laser. *Opt. Express* 16, 1393–1398. doi:10.1364/OE.16.001393

Fang, A. W., Koch, B. R., Jones, R., Lively, E., Liang, D., Kuo, Y.-H., et al. (2008b). A distributed Bragg reflector silicon evanescent laser. *IEEE Photonics Technol. Lett* 20, 1667–1669. doi:10.1109/LPT.2008.2003382

Fang, A. W., Lively, E., Kuo, Y.-H., Liang, D., and Bowers, J. E. (2008c). A distributed feedback silicon evanescent laser. *Opt. Express* 16, 4413–4419. doi:10.1364/OE.16.001393

Fang, A. W., Park, H., Cohen, O., Jones, R., Paniccia, M. J., and Bowers, J. E. (2006). Electrically pumped hybrid AlGaInAs-silicon evanescent laser. *Opt. Express* 14, 9203–9210. doi:10.1364/OE.14.009203

Fang, A. W., Sysak, M. N., Koch, B. R., Jones, R., Lively, E., Kuo, Y.-H., et al. (2009). Single-wavelength silicon evanescent lasers. *IEEE J. Sel. Top. Quantum Electron.* 15, 535. doi:10.1364/OE.22.005448

Fang, Q., Song, J., Luo, X., Jia, L., Yu, M., Lo, G., et al. (2012). High efficiency ring-resonator filter with NiSi heater. *IEEE Photonics Technol. Lett.* 24, 350–352. doi:10.1109/LPT.2011.2177816

Fedeli, J., Di Cioccio, L., Marris-Morini, D., Vivien, L., Orobtchouk, R., Rojo-Romeo, P., et al. (2008). Development of silicon photonics devices using microelectronic tools for the integration on top of a CMOS wafer. *Adv. Opt. Tech.* 2008. doi:10.1155/2008/412518

Feng, S., Lei, T., Chen, H., Cai, H., Luo, X., and Poon, A. W. (2012). Silicon photonics: from a microresonator perspective. *Laser Photonics Rev.* 6, 145–177. doi:10.1002/lpor.201100020

Fujioka, N., Chu, T., and Ishizaka, M. (2010). Compact and low power consumption hybrid integrated wavelength tunable laser module using silicon waveguide resonators. *J. Lightwave Technol.* 28, 3115–3120. doi:10.1109/JLT.2010.2073445

Goodman, J. W., Leonberger, F. J., Kung, S.-Y., and Athale, R. A. (1984). Optical interconnections for VLSI systems. *Proc. IEEE* 72, 850–866. doi:10.1109/PROC.1984.12943

Grenouillet, L., Dupont, T., Philippe, P., Harduin, J., Olivier, N., Bordel, D., et al. (2012). Hybrid integration for silicon photonics applications. *Opt. Quant. Electron.* 44, 527–534. doi:10.1038/nnano.2014.215

Guha, B., Kyotoku, B. B., and Lipson, M. (2010). CMOS-compatible athermal silicon microring resonators. *Opt. Express* 18, 3487–3493. doi:10.1364/OE.18.003487

Guillot, G., and Pavesi, L. (2006). *Optical Interconnects: The Silicon Approach.* Berlin: Springer-Verlag.

Han, H.-S., Seo, S.-Y., and Shin, J. H. (2001). Optical gain at 1.54 μm in erbium-doped silicon nanocluster sensitized waveguide. *Appl. Phys. Lett.* 79, 4568–4570. doi:10.1063/1.1419035

Hattori, H. T., Seassal, C., Touraille, E., Rojo-Romeo, P., Letartre, X., Hollinger, G., et al. (2006). Heterogeneous integration of microdisk lasers on silicon strip waveguides for optical interconnects. *IEEE Photonics Technol. Lett.* 18, 223–225. doi:10.1109/LPT.2005.861542

Hong, T., Ran, G.-Z., Chen, T., Pan, J.-Q., Chen, W.-X., Wang, Y., et al. (2010). A selective-area metal bonding InGaAsP–Si laser. *IEEE Photonics Technol. Lett.* 22, 1141–1143. doi:10.1364/OE.22.005448

Huang, Y., Song, J., Luo, X., Liow, T.-Y., and Lo, G.-Q. (2014). CMOS compatible monolithic multi-layer Si3N4-on-SOI platform for low-loss high performance silicon photonics dense integration. *Opt. Express* 22, 21859–21865. doi:10.1364/OE.22.021859

Jalali, B., and Fathpour, S. (2006). Silicon photonics. *J. Lightwave Technol.* 24, 4600–4615. doi:10.1109/JLT.2006.885782

Justice, J., Bower, C., Meitl, M., Mooney, M. B., Gubbins, M. A., and Corbett, B. (2012). Wafer-scale integration of group III-V lasers on silicon using transfer printing of epitaxial layers. *Nat. Photonics* 6, 610–614. doi:10.1038/nphoton.2012.204

Keyvaninia, S., Muneeb, M., Stanković, S., Roelkens, G., Van Thourhout, D., and Fedeli, J. (2012). "Multiple die-to-wafer adhesive bonding for heterogeneous integration," in *Paper Presented at the 16th European Conference on Integrated Optics (ECIO-2012)*. Sitges, Barcelona, Spain.

Keyvaninia, S., Roelkens, G., Van Thourhout, D., Jany, C., Lamponi, M., Le Liepvre, A., et al. (2013a). Demonstration of a heterogeneously integrated III-V/SOI single wavelength tunable laser. *Opt. Express* 21, 3784–3792. doi:10.1364/OE.21.003784

Keyvaninia, S., Verstuyft, S., Pathak, S., Lelarge, F., Duan, G.-H., Bordel, D., et al. (2013b). III-V-on-silicon multi-frequency lasers. *Opt. Express* 21, 13675–13683. doi:10.1364/OE.21.013675

Keyvaninia, S., Verstuyft, S., Van Landschoot, L., Lelarge, F., Duan, G.-H., Messaoudene, S., et al. (2013c). Heterogeneously integrated III-V/silicon distributed feedback lasers. *Opt. Lett.* 38, 5434–5437. doi:10.1364/OL.38.005434

Kissinger, G., and Kissinger, W. (1993). Void-free silicon-wafer-bond strengthening in the 200–400 C range. *Sens. Actuators A* 36, 149–156. doi:10.1016/0924-4247(93)85009-5

Kostrzewa, M., Di Cioccio, L., Zussy, M., Roussin, J., Fedeli, J., Kernevez, N., et al. (2006). InP dies transferred onto silicon substrate for optical interconnects application. *Sens. Actuators A* 125, 411–414. doi:10.1016/j.sna.2005.07.023

Kurczveil, G., Heck, M. J., Peters, J. D., Garcia, J. M., Spencer, D., and Bowers, J. E. (2011). An integrated hybrid silicon multiwavelength AWG laser. *IEEE J. Sel. Top. Quantum Electron.* 17, 1521–1527. doi:10.1109/JSTQE.2011.2112639

Lasky, J. (1986). Wafer bonding for silicon-on-insulator technologies. *Appl. Phys. Lett.* 48, 78–80. doi:10.1063/1.96768

Lee, A., Jiang, Q., Tang, M., Seeds, A., and Liu, H. (2012). Continuous-wave InAs/GaAs quantum-dot laser diodes monolithically grown on Si substrate with low threshold current densities. *Opt. Express* 20, 22181–22187. doi:10.1364/OE.20.022181

Levaufre, G., Le Liepvre, A., Jany, C., Accard, A., Kaspar, P., Brenot, R., et al. (2014). "Hybrid III-V/silicon tunable laser directly modulated at 10Gbit/s for short reach/access networks," in *Paper Presented at the Optical Communication (ECOC), 2014 European Conference on*, Cannes France.

Liang, D., and Bowers, J. (2008). Highly efficient vertical outgassing channels for low-temperature InP-to-silicon direct wafer bonding on the silicon-on-insulator substrate. *J. Vac. Sci Technol. B* 26, 1560–1568. doi:10.1116/1.2943667

Liang, D., Fang, A. W., Chen, H.-W., Sysak, M. N., Koch, B. R., Lively, E., et al. (2009a). Hybrid silicon evanescent approach to optical interconnects. *Appl. Phys. A* 95, 1045–1057. doi:10.1007/s00339-009-5118-1

Liang, D., Fiorentino, M., Okumura, T., Chang, H.-H., Spencer, D. T., Kuo, Y.-H., et al. (2009b). Electrically-pumped compact hybrid silicon microring lasers for optical interconnects. *Opt. Express* 17, 20355–20364. doi:10.1364/OE.17.020355

Liang, D., Fiorentino, M., Srinivasan, S., Bowers, J. E., and Beausoleil, R. G. (2011). Low threshold electrically-pumped hybrid silicon microring lasers. *IEEE J. Sel. Top. Quantum Electron.* 17, 1528–1533. doi:10.1109/JSTQE.2010.2103552

Liang, D., Roelkens, G., Baets, R., and Bowers, J. E. (2010). Hybrid integrated platforms for silicon photonics. *Materials* 3, 1782–1802. doi:10.1038/nnano.2014.215

Liang, D., Srinivasan, S., Fiorentino, M., Kurczveil, G., Bowers, J., and Beausoleil, R. (2012). "A metal thermal shunt design for hybrid silicon microring laser," in *Paper Presented at the Optical Interconnects Conference, 2012* (Santa Fe, NM: IEEE).

Lim, A. E.-J., Song, J., Fang, Q., Li, C., Tu, X., Duan, N., et al. (2014). Review of silicon photonics foundry efforts. *IEEE J. Sel. Top. Quantum Electron.* 20, 8300112. doi:10.1109/JSTQE.2013.2293274

Liow, T.-Y., Song, J., Tu, X., Lim, A.-J., Fang, Q., Duan, N., et al. (2013). Silicon optical interconnect device technologies for 40 Gb/s and beyond. *IEEE J. Sel. Top. Quantum Electron.* 19, 8200312–8200312. doi:10.1109/JSTQE.2012.2218580

Lipson, M. (2005). Guiding, modulating, and emitting light on silicon-challenges and opportunities. *J. Lightwave Technol.* 23, 4222. doi:10.1109/JLT.2005.858225

Liu, H., Wang, T., Jiang, Q., Hogg, R., Tutu, F., Pozzi, F., et al. (2011). Long-wavelength InAs/GaAs quantum-dot laser diode monolithically grown on Ge substrate. *Nat. Photonics* 5, 416–419. doi:10.1364/OE.20.022181

Liu, J., Sun, X., Camacho-Aguilera, R., Kimerling, L. C., and Michel, J. (2010). Ge-on-Si laser operating at room temperature. *Opt. Lett.* 35, 679–681. doi:10.1364/OL.35.000679

Liu, J., Sun, X., Kimerling, L. C., and Michel, J. (2009). Direct-gap optical gain of Ge on Si at room temperature. *Opt. Lett.* 34, 1738–1740. doi:10.1364/OL.34.001738

Liu, J., Sun, X., Pan, D., Wang, X., Kimerling, L. C., Koch, T. L., et al. (2007). Tensile-strained, n-type Ge as a gain medium for monolithic laser integration on Si. *Opt. Express* 15, 11272–11277. doi:10.1364/OE.15.011272

Luo, X., Song, J., Feng, S., Poon, A. W., Liow, T.-Y., Yu, M., et al. (2012). Silicon high-order coupled-microring-based electro-optical switches for on-chip optical interconnects. *IEEE Photonics Technol. Lett.* 24, 821–823. doi:10.1109/LPT.2012.2188829

Luo, X., Song, J., Zhou, H., Liow, T. Y., Yu, M., and Lo, P. G. Q. (2014). United States Patent No. US 2014/0153600 A1.

Maszara, W. (1991). Silicon-on-insulator by wafer bonding: a review. *J. Electrochem. Soc.* 138, 341–347. doi:10.1149/1.2085575

Mechet, P., Verstuyft, S., De Vries, T., Spuesens, T., Regreny, P., Van Thourhout, D., et al. (2013). Unidirectional III-V microdisk lasers heterogeneously integrated on SOI. *Opt. Express* 21, 19339–19352. doi:10.1364/OE.21.019339

Michel, J., Liu, J., and Kimerling, L. C. (2010). High-performance Ge-on-Si photodetectors. *Nat. Photonics* 4, 527–534. doi:10.1038/nphoton.2010.157

Miller, D. A. (2000). Optical interconnects to silicon. *IEEE J. Sel. Top. Quantum Electron.* 6, 1312–1317. doi:10.1109/2944.902184

Miller, D. A. (2009). Device requirements for optical interconnects to silicon chips. *Proc. IEEE* 97, 1166–1185. doi:10.1109/JPROC.2009.2014298

Ohashi, K., Nishi, K., Shimizu, T., Nakada, M., Fujikata, J., Ushida, J., et al. (2009). On-chip optical interconnect. *Proc. IEEE* 97, 1186–1198. doi:10.1109/JPROC.2009.2020331

Park, H., Fang, A., Kodama, S., and Bowers, J. (2005). Hybrid silicon evanescent laser fabricated with a silicon waveguide and III-V offset quantum wells. *Opt. Express* 13, 9460–9464. doi:10.1364/OPEX.13.009460

Pasquariello, D., and Hjort, K. (2002). Plasma-assisted InP-to-Si low temperature wafer bonding. *IEEE J. Sel. Top. Quantum Electron.* 8, 118–131. doi:10.1109/2944.991407

Pavesi, L., Dal Negro, L., Mazzoleni, C., Franzo, G., and Priolo, F. (2000). Optical gain in silicon nanocrystals. *Nature* 408, 440–444. doi:10.1038/35044012

Pavesi, L., and Lockwood, D. J. (2004). *Silicon Photonics*. Berlin: Springer-Verlag.

Poon, A. W., Luo, X., Xu, F., and Chen, H. (2009a). Cascaded microresonator-based matrix switch for silicon on-chip optical interconnection. *Proc. IEEE* 97, 1216–1238. doi:10.1109/JPROC.2009.2014884

Poon, A. W., Luo, X., Zhou, L., Li, C., Lee, J. Y., Xu, F., et al. (2009b). "Microresonator-based devices on a silicon chip: novel shaped cavities and resonance coherent interference," in *Practical Applications of Microresonators in Optics and Photonics*, ed. A. B. Matsko (Boca Raton, FL: CRC Press), 211–263.

Reed, G. T., and Knights, A. P. (2004). *Silicon Photonics: An Introduction*. England: John Wiley & Sons.

Reed, G. T., Mashanovich, G., Gardes, F., and Thomson, D. (2010). Silicon optical modulators. *Nat. Photonics* 4, 518–526. doi:10.1038/nphoton.2010.219

Roelkens, G., Van Thourhout, D., and Baets, R. (2005). Ultra-thin benzocyclobutene bonding of III–V dies onto SOI substrate. *Electron. Lett.* 41, 561–562. doi:10.1049/el:20050807

Roelkens, G., Van Thourhout, D., Baets, R., and Smit, M. (2006). Laser emission and photodetection in an InP/InGaAsP layer integrated on and coupled to a Silicon-on-Insulator waveguide circuit. *Opt. Express* 14, 8154–8159. doi:10.1364/OE.14.008154

Rong, H., Jones, R., Liu, A., Cohen, O., Hak, D., Fang, A., et al. (2005a). A continuous-wave Raman silicon laser. *Nature* 433, 725–728. doi:10.1038/nature03273

Rong, H., Liu, A., Jones, R., Cohen, O., Hak, D., Nicolaescu, R., et al. (2005b). An all-silicon Raman laser. *Nature* 433, 292–294. doi:10.1038/nature03273

Rong, H., Xu, S., Kuo, Y.-H., Sih, V., Cohen, O., Raday, O., et al. (2007). Low-threshold continuous-wave Raman silicon laser. *Nat. Photonics* 1, 232–237. doi:10.1038/nphoton.2007.29

Rotem, E., Shainline, J. M., and Xu, J. M. (2007a). Electroluminescence of nanopatterned silicon with carbon implantation and solid phase epitaxial regrowth. *Opt. Express* 15, 14099–14106. doi:10.1364/OE.15.014099

Rotem, E., Shainline, J. M., and Xu, J. M. (2007b). Enhanced photoluminescence from nanopatterned carbon-rich silicon grown by solid-phase epitaxy. *Appl. Phys. Lett.* 91, 051127. doi:10.1063/1.2766843

Seassal, C., Rojo-Romeo, P., Letartre, X., Viktorovitch, P., Hollinger, G., Jalaguier, E., et al. (2001). InP microdisk lasers on silicon wafer: CW room temperature operation at 1.6 μm. *Electron. Lett.* 37, 222–223. doi:10.1049/el:20010173

Shainline, J. M., and Xu, J. (2007). Silicon as an emissive optical medium. *Laser Photonics Rev.* 1, 334–348. doi:10.1002/lpor.200710021

Song, J., Luo, X., Tu, X., Jia, L., Fang, Q., Liow, T.-Y., et al. (2013). On-chip quasi-digital optical switch using silicon microring resonator-coupled Mach-Zehnder interferometer. *Opt. Express* 21, 12767–12775. doi:10.1364/OE.21.012767

Soref, R. (2006). The past, present, and future of silicon photonics. *IEEE J. Sel. Top. Quantum Electron.* 12, 1678–1687. doi:10.1021/ar900141y

Soref, R., and Lorenzo, J. (1985). Single-crystal silicon: a new material for 1.3 and 1.6 μm integrated-optical components. *Electron. Lett.* 21, 953–954. doi:10.1049/el:19850673

Sparacin, D. K., Spector, S. J., and Kimerling, L. C. (2005). Silicon waveguide sidewall smoothing by wet chemical oxidation. *J. Lightwave Technol.* 23, 2455. doi:10.1109/JLT.2005.851328

Stanković, S., Jones, R., Sysak, M. N., Heck, J. M., Roelkens, G., and Van Thourhout, D. (2011). 1310-nm hybrid III–V/Si Fabry–Pérot laser based on adhesive bonding. *IEEE Photonics Technol. Lett.* 23, 1781–1783. doi:10.1109/LPT.2011.2169397

Stanković, S., Jones, R., Sysak, M. N., Heck, J. M., Roelkens, G., and Van Thourhout, D. (2012). Hybrid III–V/Si distributed-feedback laser based on adhesive bonding. *IEEE Photonics Technol. Lett.* 24, 2155–2158. doi:10.1109/LPT.2012.2223666

Stanković, S., Van Thourhout, D., Roelkens, G., Jones, R., Heck, J., and Sysak, M. (2010). Die-to-die adhesive bonding for evanescently-coupled photonic devices. *ECS Trans.* 33, 411–420. doi:10.1149/1.3483531

Sun, X., Liu, H.-C., and Yariv, A. (2009a). Adiabaticity criterion and the shortest adiabatic mode transformer in a coupled-waveguide system. *Opt. Lett.* 34, 280–282. doi:10.1364/OL.34.000280

Sun, X., Liu, J., Kimerling, L. C., and Michel, J. (2009b). Direct gap photoluminescence of n-type tensile-strained Ge-on-Si. *Appl. Phys. Lett.* 95, 011911–011911–011913. doi:10.1364/OL.38.000652

Sun, X., Liu, J., Kimerling, L. C., and Michel, J. (2009c). Room-temperature direct bandgap electroluminesence from Ge-on-Si light-emitting diodes. *Opt. Lett.* 34, 1198–1200. doi:10.1364/OL.34.001198

Sysak, M. N., Liang, D., Jones, R., Kurczveil, G., Piels, M., Fiorentino, M., et al. (2011). Hybrid silicon laser technology: a thermal perspective. *IEEE J. Sel. Top. Quantum Electron.* 17, 1490–1498. doi:10.1109/JSTQE.2011.2109940

Tanabe, K., Guimard, D., Bordel, D., Iwamoto, S., and Arakawa, Y. (2010). Electrically pumped 1.3 μm room-temperature InAs/GaAs quantum dot lasers on Si substrates by metal-mediated wafer bonding and layer transfer. *Opt. Express* 18, 10604–10608. doi:10.1364/OE.18.010604

Tatsumi, T., Tanabe, K., Watanabe, K., Iwamoto, S., and Arakawa, Y. (2012). 1.3 μm InAs/GaAs quantum dot lasers on Si substrates by low-resistivity, Au-free metal-mediated wafer bonding. *J. Appl. Phys.* 112, 033107. doi:10.1063/1.4742198

Tong, Q.-Y., and Goesele, U. (1999). *Semiconductor Wafer Bonding: Science and Technology*. Wiley, 1998.

Tu, X., Chang, K.-F., Liow, T.-Y., Song, J., Luo, X., Jia, L., et al. (2014). Silicon optical modulator with shield coplanar waveguide electrodes. *Opt. Express* 22, 23724–23731. doi:10.1364/OE.22.023724

Tu, X., Liow, T.-Y., Song, J., Luo, X., Fang, Q., Yu, M., et al. (2013). 50-Gb/s silicon optical modulator with traveling-wave electrodes. *Opt. Express* 21, 12776–12782. doi:10.1364/OE.21.012776

Urino, Y., Shimizu, T., Okano, M., Hatori, N., Ishizaka, M., Yamamoto, T., et al. (2011). First demonstration of high density optical interconnects integrated with lasers, optical modulators, and photodetectors on single silicon substrate. *Opt. Express* 19, B159–B165. doi:10.1364/OE.19.00B159

Van Campenhout, J., Green, W. M., Assefa, S., and Vlasov, Y. A. (2009). Low-power, 2x2 silicon electro-optic switch with 110-nm bandwidth for broadband reconfigurable optical networks. *Opt. Express* 17, 24020–24029. doi:10.1364/OE.17.024020

Van Campenhout, J., Liu, L., Romeo, P. R., Van Thourhout, D., Seassal, C., Regreny, P., et al. (2008). A compact SOI-integrated multiwavelength laser source based on cascaded InP microdisks. *IEEE Photonics Technol. Lett.* 20, 1345–1347. doi:10.1109/LPT.2008.926857

Van Campenhout, J., Rojo Romeo, P., Regreny, P., Seassal, C., Van Thourhout, D., Verstuyft, S., et al. (2007). Electrically pumped InP-based microdisk lasers integrated

with a nanophotonic silicon-on-insulator waveguide circuit. *Opt. Express* 15, 6744–6749. doi:10.1364/OE.15.006744

Vivien, L., and Pavesi, L. (2013). *Handbook of Silicon Photonics*. Boca Raton, FL: CRC Press.

Xia, F., Sekaric, L., and Vlasov, Y. (2006). Ultracompact optical buffers on a silicon chip. *Nat. Photonics* 1, 65–71. doi:10.1038/nphoton.2006.42

Xiao, S., Khan, M. H., Shen, H., and Qi, M. (2007). Multiple-channel silicon micro-resonator based filters for WDM applications. *Opt. Express* 15, 7489–7498. doi:10.1364/OE.15.009386

Xu, D.-X., Schmid, J. H., Reed, G. T., Mashanovich, G. Z., Thomson, D. J., Nedeljkovic, M., et al. (2014). Silicon photonic integration platform-have we found the sweet spot? *IEEE J. Sel. Top. Quantum Electron.* 20, 189–205. doi:10.1109/JSTQE.2014.2299634

Yang, H., Zhao, D., Chuwongin, S., Seo, J.-H., Yang, W., Shuai, Y., et al. (2012). Transfer-printed stacked nanomembrane lasers on silicon. *Nat. Photonics* 6, 615–620. doi:10.1038/nphoton.2012.160

Yariv, A., and Sun, X. (2007). Supermode Si/III-V hybrid lasers, optical amplifiers and modulators: a proposal and analysis. *Opt. Express* 15, 9147–9151. doi:10.1364/OE.15.009147

Zhang, C., Srinivasan, S., Tang, Y., Heck, M. J., Davenport, M. L., and Bowers, J. E. (2014). Low threshold and high speed short cavity distributed feedback hybrid silicon lasers. *Opt. Express* 22, 10202–10209. doi:10.1364/OE.22.010202

Zhou, L., and Poon, A. W. (2007). Electrically reconfigurable silicon microring resonator-based filter with waveguide-coupled feedback. *Opt. Express* 15, 9194–9204. doi:10.1364/OE.15.009194

Conflict of Interest Statement: The authors declare that the research was conducted in the absence of any commercial or financial relationships that could be construed as a potential conflict of interest.

Received: 08 January 2015; paper pending published: 13 February 2015; accepted: 17 March 2015; published online: 07 April 2015.

Citation: Luo X, Cao Y, Song J, Hu X, Cheng Y, Li C, Liu C, Liow T-Y, Yu M, Wang H, Wang QJ and Lo PG-Q (2015) High-throughput multiple dies-to-wafer bonding technology and III/V-on-Si hybrid lasers for heterogeneous integration of optoelectronic integrated circuits. Front. Mater. ***2****:28. doi: 10.3389/fmats.2015.00028*

This article was submitted to Optics and Photonics, a section of the journal Frontiers in Materials.

frontiers in
MATERIALS

REVIEW ARTICLE
published: 17 September 2014
doi: 10.3389/fmats.2014.00015

Group IV light sources to enable the convergence of photonics and electronics

Shinichi Saito[1]*, Frederic Yannick Gardes[1], Abdelrahman Zaher Al-Attili[1], Kazuki Tani[2,3,4], Katsuya Oda[2,3,4], Yuji Suwa[2,3,4], Tatemi Ido[2,3,4], Yasuhiko Ishikawa[5], Satoshi Kako[3,6], Satoshi Iwamoto[3,6] and Yasuhiko Arakawa[3,6]

[1] *Faculty of Physical Sciences and Engineering, University of Southampton, Southampton, UK*
[2] *Photonics Electronics Technology Research Association (PETRA), Tokyo, Japan*
[3] *Institute for Photonics-Electronics Convergence System Technology (PECST), Tokyo, Japan*
[4] *Central Research Laboratory, Hitachi Ltd., Tokyo, Japan*
[5] *Department of Materials Engineering, Graduate School of Engineering, The University of Tokyo, Tokyo, Japan*
[6] *Institute of Industrial Science, The University of Tokyo, Tokyo, Japan*

Edited by:
Jifeng Liu, Dartmouth College, USA

Reviewed by:
Androula Galiouna Nassiopoulou, National Centre for Scientific Research Demokritos, Greece
Raul J. Martin-Palma, Universidad Autonoma de Madrid, Spain
Jifeng Liu, Dartmouth College, USA

****Correspondence:***
Shinichi Saito, Nano Research Group, Electronics and Computer Science, Faculty of Physical Sciences and Engineering, Highfield Campus, University of Southampton, Southampton SO17 1BJ, UK
e-mail: s.saito@soton.ac.uk

Group IV lasers are expected to revolutionize chip-to-chip optical communications in terms of cost, scalability, yield, and compatibility to the existing infrastructure of silicon industries for mass production. Here, we review the current state-of-the-art developments of silicon and germanium light sources toward monolithic integration. Quantum confinement of electrons and holes in nanostructures has been the primary route for light emission from silicon, and we can use advanced silicon technologies using top-down patterning processes to fabricate these nanostructures, including fin-type vertical multiple-quantum-wells. Moreover, the electromagnetic environment can also be manipulated in a photonic crystal nanocavity to enhance the efficiency of light extraction and emission by the Purcell effect. Germanium is also widely investigated as an active material in Group IV photonics, and novel epitaxial growth technologies are being developed to make a high quality germanium layer on a silicon substrate. To develop a practical germanium laser, various technologies are employed for tensile-stress engineering and high electron doping to compensate the indirect valleys in the conduction band. These challenges are aiming to contribute toward the convergence of electronics and photonics on a silicon chip.

Keywords: silicon, photonics, CMOS, germanium, epitaxy, luminescence, quantum, strain

1. INTRODUCTION

As the integration of transistors in a chip increases, the demands of the interconnections are expanding, since more information will be transferred between chips optically (Miller, 2009). The advantage of optical interconnection over electrical wiring is fundamentally coming from the elementary particles, photons, used for signal transmission. We can transmit photons without an electrical connection throughout an optical fiber, since photons do not have charge. Of course, optical loss exists, but still the total energy consumption of the optical interconnection can be much lower than that of the electrical connection, especially for the long-distance communications at higher data rate, even including the energy required to convert electrons to photons and vice versa (Miller, 2009). Si photonics is revolutionizing optical interconnections in terms of cost, power, bandwidth, and scalability (Zimmermann, 2000; Pavesi and Lockwood, 2004; Reed and Knights, 2004; Pavesi and Guillot, 2006; Reed, 2008; Deen and Basu, 2012; Fathpour and Jalali, 2012; Vivien and Pavesi, 2013). III-V (Wale, 2008; Evans et al., 2011) and Si-based platform technologies (Reed and Knights, 2004; Gunn, 2006; Rylyakov et al., 2011; Arakawa et al., 2013; Urino et al., 2013) are competing for the next generation of optical interconnections. The critical missing component for Si photonics is a monolithic light source compatible with the existing infrastructure of complementary-metal-oxide-semiconductor (CMOS) technologies for fabrication. The hybrid integration of III-V devices on an Si substrate (Fang et al., 2006) or feeding of an optical fiber to an Si waveguide coupled with a grating from a III-V laser diode (Gunn, 2006) would be the near-term solution, but it is desirable to realize monolithic light sources for the long term. Comprehensive reviews on developing practical lasers on Si have been published by various authors (Cullis et al., 1997; Ossicini et al., 2006; Daldosso and Pavesi, 2009; Liang and Bowers, 2010; Steger et al., 2011; Liu et al., 2012; Michel and Romagnoli, 2012; Boucaud et al., 2013; Shakoor et al., 2013; Liu, 2014). Here, we review this active field focusing on the progress of Si and germanium (Ge) light sources fabricated by standard CMOS processes.

Photoluminescence (PL) (Canham, 1990) and electroluminescence (EL) (Koshida and Koyama, 1992) from porous-Si are the most famous achievements to overcome the fundamental limitations of the indirect band-gap character of Si. The maximum PL (Gelloz and Koshida, 2000) and EL (Gelloz et al., 2005) quantum efficiency exceeded 23 and 1%, respectively. The mechanism of light emission from porous-Si is considered to originate from quantum confinement effects (Canham, 1990; Koshida and Koyama, 1992; Cullis et al., 1997; Nassiopoulou, 2004; Ossicini et al., 2006; Daldosso and Pavesi, 2009) in the self-organized nanostructure. The typical length scale to expect

quantum confinement would be comparable to the exciton Bohr radius, which is about 5 nm for Si and 18 nm for Ge (Cullis et al., 1997). On the other hand, the gate length fabricated by CMOS technologies is comparable to the exciton Bohr radius so that we can fabricate various quantum structures, including quantum dots (Arakawa and Sakaki, 1982), nano-wires, and quantum-wells, by lithographically controlled top-down processes. In addition, novel cavity structures (Iwamoto and Arakawa, 2012) can be fabricated to enhance the internal quantum efficiency by the Purcell effect (Purcell, 1946) as well as the extraction efficiency by improved coupling to a lens. Ge is also intensively studied, since the direct band-gap energy is closer to the indirect transition energy than that of Si. Highly, *n*-type doping and strain engineering are effective to enhance the light emissions from Ge (Liu et al., 2012; Michel and Romagnoli, 2012; Boucaud et al., 2013; Liu, 2014), and some of these recent advances are reviewed in this paper.

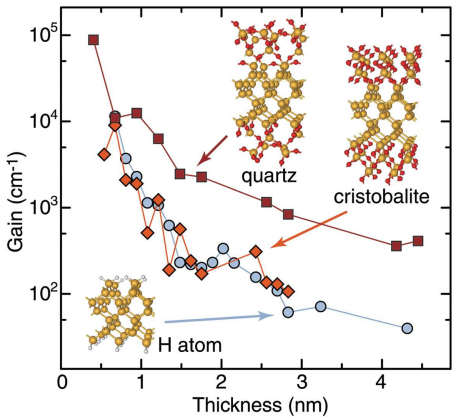

FIGURE 1 | Optical gain of Si(001) thin films calculated from direct transitions across the energy gap only.

2. STRATEGIES TO ENHANCE LIGHT EMISSION FROM GROUP IV MATERIALS

2.1. THEORETICAL STUDY OF LIGHT EMISSION FROM SILICON

Both Si and Ge are known to be poor light emitters because of their indirect band-gap structures. Even so, there are some methods for making direct transitions to occur in these materials. These possibilities were examined theoretically by first-principles calculations based on density functional theory using plane-wave-based ultrasoft pseudo-potentials (Vanderbilt, 1990; Laasonen et al., 1993). Generalized gradient approximation (Perdew et al., 1996) is used for the calculation of Si, and hybrid functional (Perdew et al., 1996) is used for Ge. The optical matrix elements are calculated with the aid of core-repair terms (Kageshima and Shiraishi, 1997).

The lowest conduction band (LCB) of bulk Si has a minimum near the *X*-point, and six electron valleys exist near *X*-points. Two valleys among the six are projected onto Γ-point in two-dimensional momentum (***k***)-space when an Si quantum-well (QW) with (001) surfaces is fabricated; this is called a valley-projection. Because the top of the valence band is also projected onto Γ, direct transitions are possible in an Si(001) QW.

Optical gain of Si(001) QWs is shown in **Figure 1** as a function of the thickness (Suwa and Saito, 2009). Here, losses due to transitions within conduction bands and those within valence bands are not taken into account. The thinner QW shows the larger gain, since the surface of the QW plays an important role in this direct transition and it dominates if the QW is thin. **Figure 1** also shows that the surface structure of the QW affects the efficiency of light emission strongly.

Experimentally, optical gain from the Si quantum dots (Pavesi et al., 2000) embedded in an insulating matrix (Pavesi et al., 2000; Nassiopoulou, 2004; Ossicini et al., 2006; Pavesi and Guillot, 2006) has been reported. It was confirmed that the interface states associated with oxygen atoms were important to explain the positive optical gain (Pavesi et al., 2000; Nassiopoulou, 2004; Ossicini et al., 2006; Pavesi and Guillot, 2006). It will be interesting to make these structures by top-down CMOS processes.

2.2. THEORETICAL STUDY OF LIGHT EMISSION FROM GERMANIUM

Ge has two important differences from Si. One is that Ge has the minimum of the LCB at the *L*-point (*L*-valley), while Si has it near the *X*-point. The other is that Ge has a local minimum of the LCB at the Γ-point (Γ-valley), while Si does not. An *L*-valley is projected onto the Γ-point in the two-dimensional ***k***-space for Ge(111) QW. For Ge(001) QW, no *L*-valley is projected onto the Γ-point. The small Γ-valley, which is not occupied unless a large number of electrons are injected, is always projected onto the Γ-point independently of the direction of the QW. While there are two approaches to obtain efficient light emission from Ge by direct transitions, using *L*-valleys of a Ge(111) QW or using the Γ-valley of bulk Ge, we think the latter is more promising. This is due to the fact that the calculated optical matrix element for the Γ-valley is very large compared to that for the *L*-valleys.

To enhance light emission from bulk Ge, applying tensile strain is known to be effective (Liu et al., 2010). Tensile strain makes the energy difference between the Γ and *L*-valleys small, and that makes electron injection into the Γ-valley easier. Also heavy *n*-type doping is known to be effective, because electrons can be injected into the Γ-valley if the *L*-valleys are already occupied by doped electrons.

In order to predict required strength of strain and amount of doping, we calculated optical gains of bulk Ge with and without strain. **Figure 2** shows calculated optical gain as functions of injected electron density and hole densities. Here, the applied strain is assumed to be 0.25% biaxial tensile strain parallel to (001) surface and optical losses due to free carrier absorptions (Wang et al., 2013) are taken into account. This result shows that even bulk Ge without strain can have a positive optical gain, but number of electrons required for that is very large (10^{20} cm^{-3}). Despite the relatively small amount of the strain (0.25%), the impact on the gain is clear. Owing to this enhancement, only half the electron density (5×10^{19} cm^{-3}) is needed to have positive gain. In experiment, applying 0.25% strain is rather easy, and making higher strain will be possible, as we see in the following sections. Therefore, Ge lasers will be realized when an appropriate strain and carrier injection are achieved.

3. ELECTRO-LUMINESCENCE FROM SILICON QUANTUM-WELL

As we reviewed in Section 1, it is well established that efficient recombination is observed in Si nanostructures by quantum confinement effects (Canham, 1990; Koshida and Koyama, 1992; Cullis et al., 1997; Ossicini et al., 2006; Daldosso and Pavesi, 2009). The nanostructures include quantum dots (Arakawa and Sakaki, 1982), nano-wires (Canham, 1990; Koshida and Koyama, 1992), quantum-well (QW) (Saito et al., 2006a,b, 2008, 2009; Saito, 2011), and fins (Saito et al., 2011a,b). One of the difficulties in developing an efficient light-emitting diode (LED) made of Si comes from the trade-off between quantum confinement and carrier injection. The surface of these Si nanostructures is easily oxidized to SiO_2, and the band offsets between Si and SiO_2 are too high to expect efficient current injection except for tunneling. In order to overcome this trade-off, lateral carrier injection into the Si QW was proposed (Saito et al., 2006a,b, 2008, 2009; Hoang et al., 2007; Noborisaka et al., 2011; Saito, 2011). As shown in **Figures 3A–C**, the Si QW LEDs were fabricated by local thinning of a silicon-on-insulator (SOI) substrate, and the Si QW was directly connected to the thick Si diffusion electrodes (Saito et al., 2006a,b). Both electrons and holes are laterally injected to the Si QW in these planar *p-i-n* diodes (Saito et al., 2006a,b, 2008, 2009; Noborisaka et al., 2011; Saito, 2011). Another advantage of these device structures is the fabrication of the Si QW through the LOCal-Oxidation of Si (LOCOS) process. The LOCOS process was originally developed for isolation of CMOS transistors (Sze and Lee, 2012; Taur and Ning, 2013). It was also used to evaluate the carrier mobility in the ultra-thin Si QW (Uchida and Takagi, 2003). Oxidation is one of the most precisely controlled processes in CMOS technologies, and we can routinely oxidize a large Si wafer (typically 8–10″ in diameter) within the local variation of <0.1 nm. Besides, the interface between Si and SiO_2 is excellent with low interface trap density ($<10^{11}$ cm^{-2}) (Sze and Lee, 2012; Taur and Ning, 2013). The excellent interfacial quality and strong quantum confinement in Si nanostructures are critical to ensure high quantum efficiency (Gelloz et al., 2005). As shown in **Figure 3E**, EL is observed exclusively from the thin Si QW and EL from thick Si electrodes is negligible (Saito et al., 2006a). This supports the mechanism of EL based on quantum confinement (Ossicini et al., 2006; Suwa and Saito, 2009). The high carrier density in the thin Si QW also contributes to enhance the emissions (Saito et al., 2006a). By applying the back gate to the Si substrate, we can modulate the intensities of light emission, and the device can be called as an Si light-emitting transistor (Saito et al., 2006b).

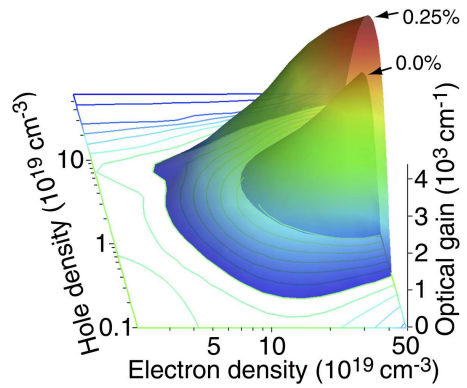

FIGURE 2 | Optical gain of germanium as a function of injected electron density and hole density is shown. Those without strain and with 0.25% biaxial tensile strain parallel to (001) surface are shown.

The next step toward the practical light source for Si photonics is to couple the light from Si to a cavity and a waveguide (WG). An Si-based WG cannot be used for emission from Si QW due to the absorption. An Si_3N_4 WG was fabricated on top of the Si QW by conventional lithography and dry etching (Saito et al., 2008, 2009). To enhance the optical confinement in the WG of the Si Resonant Cavity LED (RCLED), part of the supporting substrate was removed by using double sided aligner and anisotropic wet etching (Saito et al., 2008, 2009), as shown in **Figure 3B**. Evanescent coupling between the propagating optical mode and Si QW was expected, and the enhanced EL from the edge of the waveguide was observed (**Figure 3F**). More recently, SOI substrates with superior uniformities with thick Buried-OXide (BOX) ($>2\,\mu$m) became available, and by using these wafers, strong optical confinement within the Si_3N_4 WG was ensured without removing the supporting Si substrate (Saito, 2011), as shown in **Figure 3C**. In fact, the near-field image of the propagating optical mode was taken at the edge of the WG (**Figure 3G**).

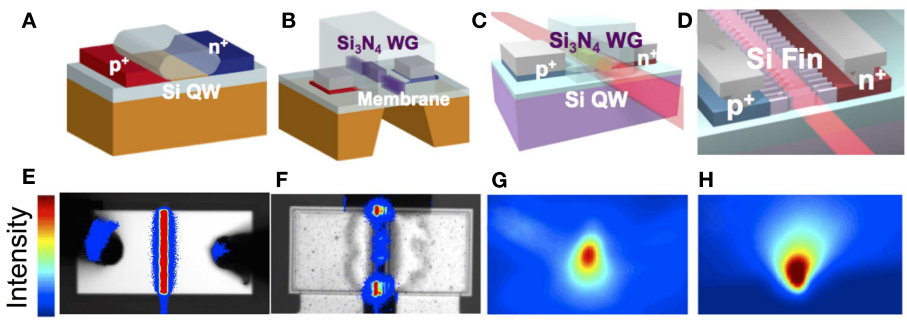

FIGURE 3 | Development of an Si light source. **(A)** Si QW LED, **(B)** Si RCLED, **(C)** Si QW LED with thick BOX, **(D)** Si FinLED, and **(E–H)** EL images from these devices. **(E,F)** are plan views. **(G,H)** are near-field images at the edge of WG.

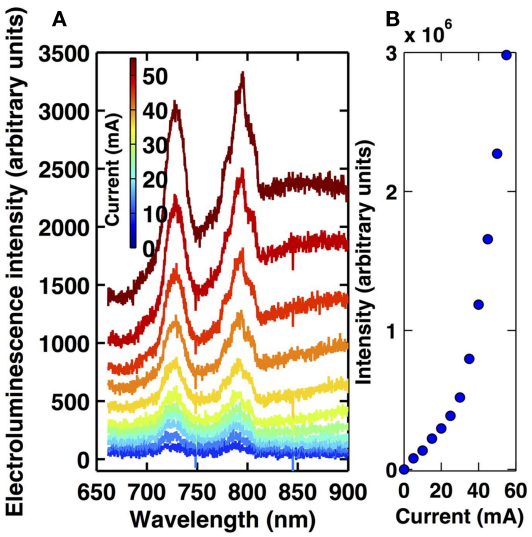

FIGURE 4 | EL from Si FinLED taken from edge of WG. **(A)** Spectra and **(B)** integrated intensity.

The obvious disadvantage of using the planar Si QW is the small confinement factor of the optical mode in the Si QW due to the thin single QW layer. It is not straightforward to make Si Multiple QWs (MQWs) (Fukatsu et al., 1992), if the surface of the Si QW is covered with the amorphous SiO_2. As an alternative to the stacking of the Si MQWs, the Si FinLED has been proposed (Saito et al., 2011b), as shown in **Figure 3D**. Si fin is a vertical QW located perpendicular to an Si substrate, and it was proposed for a self-aligned double-gate CMOS field-effect-transistor, called a FinFET (Hisamoto et al., 2000). FinFETs are already used for mass production and more than one billion of FinFETs are integrated in the most recent MPU (INTEL, 2013[1]; ITRS, 2012[2]). Therefore, we can fabricate thousands of Si fins as MQWs at the same time simply by conventional photolithography and dry etching (Saito et al., 2011b). By applying forward bias to the Si FinLED, we can observe edge emission from the Si_3N_4 WG (**Figure 3H**). The EL spectra from the edge of the Si FinLED are shown in **Figure 4A**. The enhanced peaks from the edge of the stop band were observed due to the distributed-feedback structure of the periodic fins (Saito et al., 2011b). The non-linear increase of the EL intensity against the current is considered to come from stimulated emission (**Figure 4B**), but the estimated gain of $<1\ cm^{-1}$ was too low to overcome the threshold for a laser operation (Saito et al., 2011b).

4. APPLICATION OF PHOTONIC NANOSTRUCTURES TO GROUP IV MATERIALS

4.1. CONTROL OF LIGHT EMISSION BY PHOTONIC CRYSTALS

The light emission properties of materials depend not only on material characteristics such as the dipole moment and the refractive index but also on the electromagnetic environment surrounding the material. In the previous sections, engineering group IV materials themselves such as quantum confinement, doping, and strain engineering have been discussed. Here, we discuss another approach, i.e., tailoring the electromagnetic environment by photonic nanostructures for improving light emission properties. The total efficiency of light-emitting devices can be expressed as a product of three factors: light emission efficiency $\eta_{emission}$, extraction efficiency $\eta_{extraction}$, and collection efficiency $\eta_{collection}$. $\eta_{emission}$ denotes how efficiently injected carriers recombine by emitting photons. $\eta_{extraction}$ takes into account the fact that only a part of emitted photons can be extracted from the material. $\eta_{collection}$ expresses how much extracted photons can be collected by the first lens of the setup. All of them can be improved by photonic nanostructures. Photonic crystal (PhC) (Jannopoulos and Winn, 1995), which has a wavelength-scale periodic variation of refractive index, is an important photonic nanostructure for this application (see discussions in Iwamoto and Arakawa, 2012). **Figure 5A** shows a scanning electron microscope (SEM) image of a two-dimensional (2D) PhC slab, which is the most widely studied PhC structure. The structure can be fabricated by forming air holes in a thin semiconductor plate using conventional lithography and etching processes. In the structure, owing to the periodic modulation in refractive index, in-plane light propagation is governed by the photonic band structure. Strikingly, propagation is forbidden in photonic bandgaps (PBGs). Photonic band structures and PBGs can play roles to improve mainly $\eta_{extraction}$ and $\eta_{collection}$. Another important structure is the PhC nanocavity (**Figure 5B**), which is created by omitting air holes from the regular array. Photons are confined in in-plane and out-of-plane directions due to the PBG effect and total internal reflection, respectively. PhC nanocavities have a high quality factor Q and small mode volume V_c (~1 cubic wavelength or less). These two quantities are key parameters to enhance the spontaneous emission rate through the Purcell effect (Purcell, 1946) and improve $\eta_{emission}$. Particularly, for light emitters with broad linewidth such as bulk Si, V_c has a stronger impact (Ujihara, 1995). Such high-Q PhC nanocavities can uncover the quantum nature of light-matter interaction. Cavity quantum electrodynamics in a high-Q PhC nanocavity coupled with a single semiconductor quantum dot is a hot topic in the field (see, for example, Arakawa et al., 2012). Purcell enhancement factors of as large as 12 (Lo Savio et al., 2011) and 30 (Sumikura et al., 2014) were reported, which would be limited by the emission linewidth and the Q factor, respectively.

4.2. ENHANCED LIGHT EMISSION FROM SILICON PHOTONIC CRYSTAL STRUCTURES

PhC structures without cavities have been firstly applied to control the light emission from crystalline Si. In 2003, Zelsmann et al. (2003) reported enhanced PL extraction from a 2D PhC slab fabricated into the top Si layer of a SOI substrate at low temperature (Zelsmann et al., 2003). Similar enhancements at room temperature have been observed from arrays of Si nanoboxes (Cluzel et al., 2006a) and rods (Cluzel et al., 2006b) formed on SOI substrates. Strong light emission was observed at wavelengths corresponding to photonic band edges at the Γ point. Increasing the number of band edge within the emission spectrum of Si can lead to higher

[1]http://www.intel.com/content/www/us/en/history/museum-transistors-to-transformations-brochure.html
[2]http://www.itrs.net

luminescence intensity. This is experimentally verified by increasing the lattice constant of PhC so that normalized frequencies corresponding to the Si emission wavelengths are increased (Fujita et al., 2008). Si light-emitting diodes (LEDs) with PhC patterns have also been demonstrated (Nakayama et al., 2010a; Iwamoto and Arakawa, 2012). The device schematically shown in **Figure 6A** was fabricated using a SOI substrate. Firstly, a lateral *p-i-n* junction was formed into the top 200-nm-thick Si layer by area-selective implantations of boron and phosphorous ions. Then, a PhC structure was patterned. To keep mechanical stability and better thermal conductivity, the buried-oxide (BOX) layer was not removed. An SEM image of the central part of a device is shown in **Figure 6A**. The *i*-region is 5 μm in length and 250 μm in width. EL spectra from devices with different PhC periods and from a device without PhC are shown in the inset of **Figure 6B**. EL emission increased as the period *a* increased. **Figure 6B** shows the integrated intensities from these devices as a function of injected current. The integrated intensity from the device with $a = 750$ nm is ~14 times stronger than that from an unpatterned LED. This enhancement is mainly caused by the improvement of $\eta_{\text{extraction}}$ and $\eta_{\text{collection}}$ due to the photonic band structures as discussed above. η_{emission} is also expected to be enhanced in PhC nanocavities. **Figure 7** shows room-temperature μ-PL spectra measured at the center of an L3-type PhC nanocavity compared to a non-patterned region (see the inset). The L3 PhC nanocavity was also fabricated into an SOI substrate. In this sample, the BOX layer was etched out in order to confine the photons strongly in the vertical direction. The PL intensity from the cavity was much larger than that from the non-patterned region. In addition, sharp peaks are observed only in the spectrum from the cavity. These peaks originate from the cavity resonant modes. For this particular sample with the air hole radius $r = 0.37a$, large enhancement of PL over 300 times was obtained for a cavity mode at 1,191 nm. As discussed in Section 1, this enhancement can be attributed to three factors. Detailed analysis including numerical simulation indicated that η_{emission} is improved by ~5 times (Iwamoto et al., 2007). The enhancement factors in η_{emission} ranging ~5−10 have been reported for Si interband transition (Fujita et al., 2008) and for light emission from optically active defects in Si (Lo Savio et al., 2011). The temperature dependence of cavity mode emission (Hauke et al., 2010; Lo Savio et al., 2011) and the dependence of PL on cavity mode volume V_c (Nakayama et al., 2012) suggest that the Purcell effect plays a role in this enhancement. The enhancement in η_{emission} reported so far is still too small for practical applications. However, this research would provide important insights for further development of light-emitting devices using group IV materials. Indeed, these pioneering works have stimulated theoretical investigations, which discuss the possibility of lasing oscillation in Si (Escalante and Martínez, 2012, 2013). Recent advances in this field are developments of Si LEDs with PhC nanocavities (Nakayama et al., 2011; Shakoor et al., 2013). Shakoor et al. (2013) recently reported Si LEDs using L3-type nanocavity structure, in which optically active defects created by hydrogen bombardment are used as light emission centers. They carefully designed the cavity structure to improving $\eta_{\text{collection}}$ and obtained sharp light emission at around 1.5 μm with a power density of 0.4 mW/cm^2. The strain-induced dislocations (Ng et al., 2001; Kittler et al., 2013) will also be compatible to PhC nanocavities, since the emission energies are smaller than the band gap of Si. The combination of PhC nanocavities and defect engineering is very promising, and a wall plug efficiency of 0.7×10^{-8} was reported (Shakoor et al., 2013).

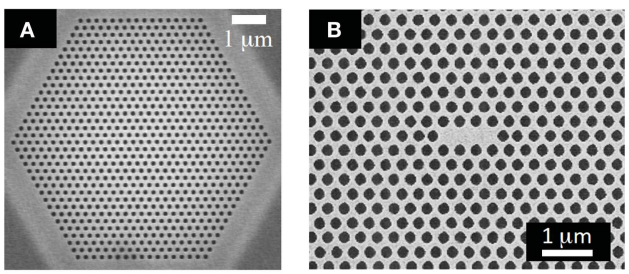

FIGURE 5 | SEM images of a regular PhC structure with a triangular lattice (A) and a L3-type PhC nanocavity, in which three air holes along a Γ-K direction are omitted (B).

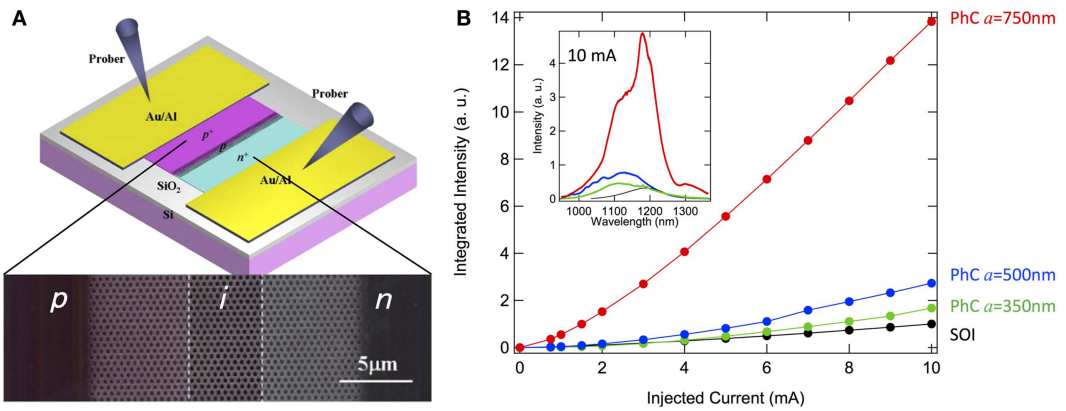

FIGURE 6 | (A) Schematic representation of a silicon PhC LED is shown. The SEM image shows the center area of a device. **(B)** Integrated EL intensities for silicon PhC LED with various periods *a* and for an SOI LED with a flat surface. The inset shows corresponding EL spectra at 10 mA.

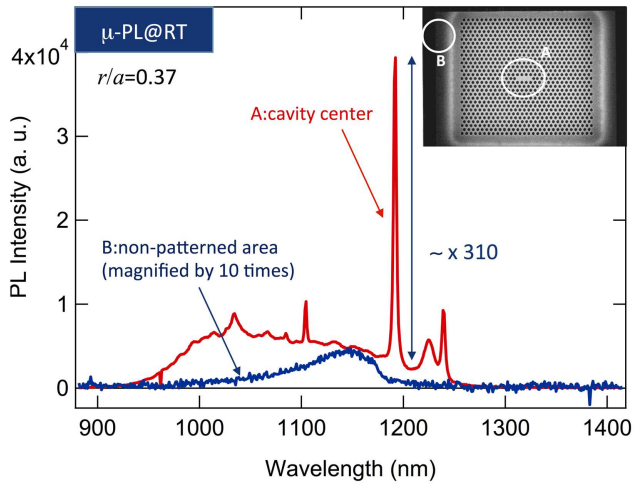

FIGURE 7 | Room-temperature μ-PL spectra measured at the center of a PhC nanocavity and at a non-patterned area. The spectrum for the latter is magnified by ten times for better viewing.

4.3. APPLICATION OF PHOTONIC CRYSTAL STRUCTURES TO OTHER EMITTERS IN GROUP IV MATERIALS

Erbium ions have been investigated as one of the promising light emitters in Si. PhC nanocavities have been also applied to enhance the light emission from Er ions (Wang et al., 2012; Savio et al., 2013). Narrowing the cavity linewidth in Er-doped silicon nitride PhC nanocavities has been also demonstrated under optical pumping condition (Gong et al., 2010). As discussed in the previous sections, Ge is, at present, the most important material for future light-emitting devices in Si photonics. PhC (Nakayama et al., 2010b) and PhC nanocavities (Kurdi et al., 2008; Ngo et al., 2008) have been applied to increase the light emission from bulk Ge. Applying advanced strain/doping engineering technologies to photonic nanostructures would open a new route for boosting the light emission efficiency of Ge.

5. GENERATION OF TENSILE STRAIN IN Ge LAYERS EPITAXIALLY GROWN ON Si SUBSTRATE

In epitaxial growth of Ge on an Si substrate, a compressive strain in Ge, derived from the 4.2% lattice mismatch with Si, should be relaxed after growth beyond the critical thickness, while it has been reported by one of the authors that, during the cooling from the growth temperature to room temperature, a biaxial tensile strain as large as 0.2% is built-in due to the thermal expansion mismatch (Ishikawa et al., 2003, 2005; Cannon et al., 2004; Liu et al., 2005). It is known that the strain in semiconductors causes shifts in band edge energies, e.g., de Walle, 1989, modifying the gap energies, i.e., properties of optical transitions. The 0.2% tensile strain in Ge reduces the direct bandgap energy from 0.80 to ~0.77 eV, and as a result, the optical absorption edge (or the longer limit of detection wavelength) shifts from 1.55 to >1.60 μm, causing the increase of optical absorption coefficient at 1.55 μm (Ishikawa et al., 2003, 2005; Cannon et al., 2004; Liu et al., 2005). This property is effective for the detection of near-infrared (NIR) light used in the optical fiber communications (1.3–1.6 μm). A further attractive feature of the tensile strain in Ge is the reduction of energy difference in the conduction band between the direct Γ valley and indirect L-valley (e.g., Fischetti and Laux, 1996; Wada et al., 2006; Camacho-Aguilera et al., 2012; Nama et al., 2013; Süess et al., 2013). This feature stimulates researchers to obtain efficient NIR light emission from tensile-strained Ge due to the enhanced direct transition around the Γ point (e.g., Liu et al., 2007; Lim et al., 2009). In this section, the grown-in tensile strain in Ge on Si, generated due to the thermal expansion mismatch, is described. **Figure 8A** shows typical $\omega - 2\theta$ x-ray diffraction (XRD) curves taken for 0.6-μm-thick Ge grown on a 525-μm-thick Si(001) substrate with the Cu Kα radiation as the x-ray source (0.15406 nm in wavelength). The samples were grown by ultrahigh-vacuum chemical vapor deposition with a source gas of GeH_4 (9%) diluted in Ar. The growth temperature was 600°C, while a lower temperature of 370°C was used at the initial stage of Ge growth (~50 nm) in order to prevent the islanding, leading to Ge layers uniform in thickness (Luan et al., 1999; Ishikawa and Wada, 2010). After the growth, high-temperature annealing was carried out for one of the samples at 800°C for 20 min. Such annealing is often performed in order to reduce the threading-dislocation density (Luan et al., 1999). In our case, the density was reduced from 1×10^9 to $1 - 2 \times 10^8$ cm^{-2}. In **Figure 8A**, the peaks due to the (004) diffraction are clearly seen at around $2\theta \sim 66°$ for both of the as-grown and annealed samples. It is important that the peaks were located at larger diffraction angles than that for unstrained Ge, indicating the reduction of out-of-plane lattice constant, i.e., the increase of in-plane lattice constant due to the generation of tensile strain. According to the peak positions, the in-plane biaxial tensile strain was estimated to be 0.11 and 0.22% for the as-grown and annealed samples, respectively.

As mentioned above, such a tensile strain is generated in Ge due to the mismatch of thermal expansion coefficient with Si. As schematically shown in **Figure 8B**, the compressive strain in Ge due to the 4.2% lattice mismatch should be relaxed at the growth/annealing temperature, while the shrinkage in the Ge lattice during the cooling should be prevented by the thick Si substrate, since Si has a smaller thermal expansion coefficient than that of Ge. This means that a tensile (compressive) stress/strain is generated in Ge (Si), as in the bottom of **Figure 8B**. Taking into account the balance of forces together with the balance of moments in the stacked structure of Ge and Si, the tensile (compressive) strain in Ge (Si) is theoretically expressed as:

$$\epsilon_{||}\,(\mathrm{Ge}) = \frac{1}{R}\left[\frac{Y_1 t_1^3 + Y_2 t_2^3}{6 Y_1 t_1 (t_1 + t_2)} + \left(\frac{t_1}{2} - z_1\right)\right] \quad (1)$$

$$\epsilon_{||}\,(\mathrm{Si}) = \& - \frac{1}{R}\left[\frac{Y_1 t_1^3 + Y_2 t_2^3}{6 Y_2 t_2 (t_1 + t_2)} - \left(\frac{t_2}{2} - z_2\right)\right], \quad (2)$$

where, α_i, Y_i, t_i, and z_i represent the thermal expansion coefficient, the Young's modulus, the layer thickness, and the location in the layer measured from the bottom of the layer for the i-th layer (1 for Ge and 2 for Si), respectively. The radius of curvature R is

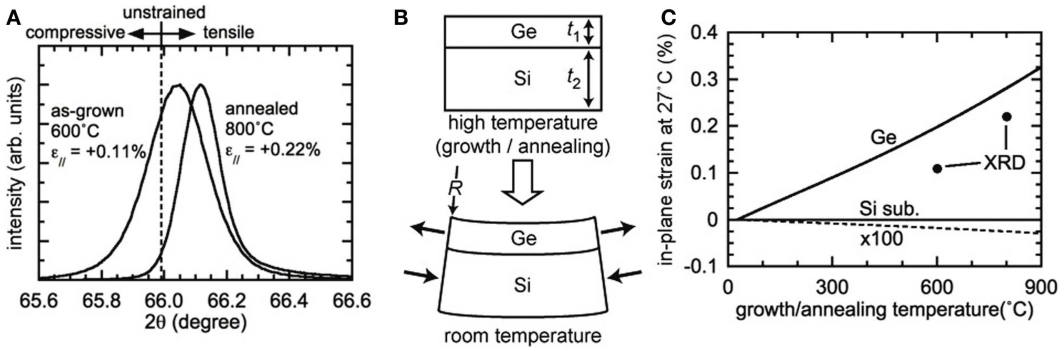

FIGURE 8 | (A) $\omega - 2\theta$ XRD curves for 0.6-μm-thick Ge on Si (001) substrate, **(B)** schematic illustration showing the generation of tensile stress/strain in Ge, and **(C)** theoretical curves and experimental data for biaxial tensile strain in Ge.

represented from

$$\frac{1}{R} = \frac{6\,(t_1 + t_2)\,Y_1 Y_2 t_1 t_2 \int_{T_{GR/AN}}^{T_{RT}} (\alpha_1 - \alpha_2)\,dT}{3(t_1 + t_2)^2 Y_1 Y_2 t_1 t_2 + \left(Y_1 t_1^3 + Y_2 t_2^3\right)(Y_1 t_1 + Y_2 t_2)}, \quad (3)$$

where $T_{GR/AN}$ and T_{RT} represent the growth/annealing temperature before cooling and the room temperature (after the cooling), respectively. Since the first term is dominant in the right side of equation (1), the strains are almost independent of z_i, the location within the layer. Therefore, equations (1) and (2) are simplified to:

$$\in_{||}(\mathrm{Ge}) \sim \frac{1}{R}\frac{Y_1 t_1^3 + Y_2 t_2^3}{6 Y_1 t_1 (t_1 + t_2)} \quad (4)$$

$$\in_{||}(\mathrm{Si}) \sim -\frac{1}{R}\frac{Y_1 t_1^3 + Y_2 t_2^3}{6 Y_2 t_2 (t_1 + t_2)}. \quad (5)$$

The lines in **Figure 8C** represent the strains calculated for the Ge thickness of 0.6 μm and the Si thickness of 525 μm. Note that almost identical results can be obtained when the thickness of Si substrate t_2 is much larger (more than ~100 times) than the Ge thickness t_1. The parameters used in the calculation can be found in Ishikawa et al. (2005). It is found that a tensile strain on the order of 0.1% is generated in Ge at room temperature, while the compressive strain in Si is negligible. It is also found that higher growth/annealing temperature generates larger tensile strain after the cooling. These properties are qualitatively in good agreement with the XRD results in **Figure 8A**. However, quantitatively, the tensile strain observed by XRD was smaller than the theoretical one. This is probably ascribed to the residual compressive strain in Ge at the growth/annealing temperature (Ishikawa et al., 2005). From the viewpoint of optoelectronic integration of Ge devices on an Si platform, Si-on-insulator (SOI) wafers have been widely used. For Ge layers grown on SOI wafers, a similar amount of tensile strain should be generated, since the elastic deformation, derived from the thermal expansion mismatch, is governed by the thick Si substrate, rather than the buried SiO_2 and the top Si layers with the thicknesses on the order of 1 μm or below. Patterning of the Ge layer as well as deposition of dielectric films embedding a strain could intentionally modify the strain in the Ge.

6. DIRECT GERMANIUM EPITAXIAL GROWTH PROCESS ON SILICON

The Ge was epitaxially grown by using a cold-wall rapid thermal chemical vapor deposition system. Germane (GeH_4) was used as a source gas, which was supplied with H_2 carrier gas. As the starting point of improving the crystallinity and controlling the lattice strain, Ge layers with good surface morphology were grown at 420°C under relatively high pressure of 7,000 Pa. Then, the Ge layers were annealed in the same H_2 atmosphere to improve the crystallinity. **Figure 9** shows a reciprocal space map (RSM) of XRD (XRD-RSM) from the 130-nm-thick Ge layer directly grown on the Si substrate before and after H_2 annealing. An intense Si (-1-13) peak was observed, which represented the diffraction from the Si substrate under the Ge layer. Since the XRD-RSM was measured by using semiconductor array detectors, errors in the counts occur if the diffraction intensity is very high; therefore, the streak line observed around the Si (-1-13) peak does not represent any actual diffraction. Since a Ge (-1-13) diffraction peak was observed from the Ge layer without annealing (**Figure 9A**), it could be confirmed that a single crystalline Ge layer was obtained by using low-temperature epitaxial growth. The displacement of the diffraction peak shows that the as-grown Ge layer still contained a compressive strain just after the low-temperature epitaxial growth at 420°C due to the larger lattice constant of Ge compared to that of the Si substrate. It has been reported that cyclic annealing at a relatively higher temperature can reduce the threading-dislocation density (Luan et al., 1999) in Ge layers. This has led to studies on the effect of annealing on the crystallinity and lattice strain of Ge layers. After low-temperature epitaxial growth of Ge layers at 420°C, the temperature was increased to the annealing temperature in the same H_2 atmosphere as that during the epitaxial growth, and the Ge layers were then annealed at various temperatures for 10 min. XRD-RSMs of Ge layers annealed at a temperature ($T_{GR/AN}$) of 700°C after the low-temperature epitaxial growth are shown in **Figure 9B**. The Ge (-1-13) diffraction peaks became much steeper and the peak intensity increased when the annealing temperature

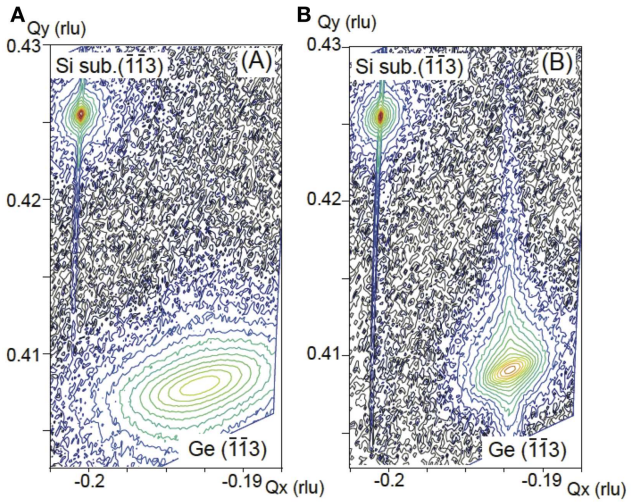

FIGURE 9 | XRD-RSM of (-1-13) diffraction from Ge layer grown on Si substrate, (A) after low-temperature epitaxial growth and (B) after post-annealing.

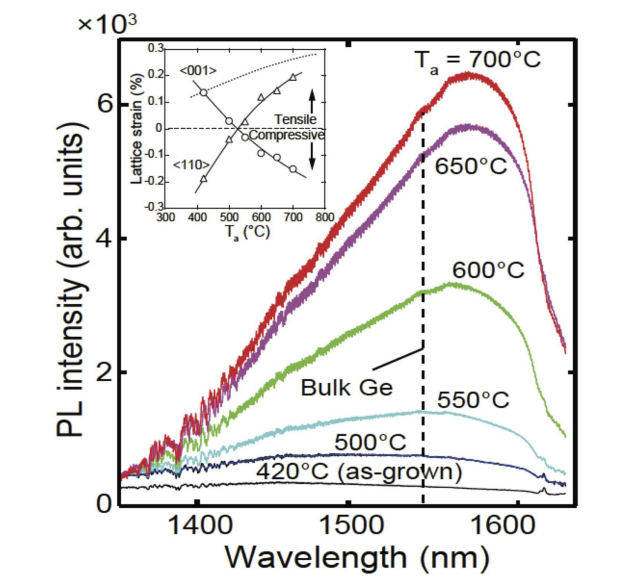

FIGURE 10 | Photoluminescence spectra from Ge layers annealed with different temperatures are shown. Peak wavelength of photoluminescence from Ge layers red-shifted as annealing temperature increased, consistent with temperature induced tensile strain. Inset shows lattice strain of Ge layers grown on Si substrate along <001> and <110> crystal orientations as a function of annealing temperature. Dotted line indicates lattice strain calculated with difference between thermal expansion coefficients of Si and Ge.

was increased, indicating that the crystallinity of the Ge layers was increased by the post-annealing.

The inset of **Figure 10** shows the lattice strain in the Ge layers in the <001> and <110> crystal orientations as a function of the annealing temperature. We used standard Si wafers for this experiment, so that <001> is perpendicular to the surface of the Ge film, while <110> is in the plane of Ge film. The lattice strain in the <110> crystal orientation increased as $T_{GR/AN}$ increased, and the strain in the <001> crystal orientation showed an opposite dependence. Although the Ge layer contained a compressive strain in the <110> crystal orientation at $T_{GR/AN} = 420$°C, i.e., without annealing, this strain started decreasing when $T_{GR/AN}$ was increased, and the Ge was completely un-strainedat $T_{GR/AN} = 530$°C. Furthermore, the sign of the lattice strain changed from compressive to tensile after annealing at $T_{GR/AN} > 530$°C, and the tensile strain at $T_{GR/AN} = 700$°C reached 0.19%. This result is consistent with previous studies (Cannon et al., 2004). Normally, a grown layer with a larger lattice constant compared to a substrate contains a compressive strain within the growth plane. However, since the Ge layers grown on the Si substrate were almost completely relaxed even after low-temperature growth, the Ge lattice could be dislocated at the Ge/Si interface by post-annealing, and the lattice strain of the Ge layer was relaxed during annealing at the relatively higher temperature with the volumes of Ge and Si determined by the thermal expansion coefficients (Singh, 1968; Okada and Tokumaru, 1984). After annealing, the volume of the Ge layer and the Si substrate both shrunk as the temperature decreased, and there was barely any change to the lattice alignment at low-temperature. The volume of the Si substrate returned to its original value because it was thick enough. However, the volume of the Ge layer could not return due to its larger thermal expansion coefficients. Therefore, the tensile lattice strain remained only in the Ge layers after cooling (Cerdeira et al., 1972). The ideal lattice strain in <110> crystal orientation was also plotted in the inset of **Figure 10**, which was calculated with only the difference of the thermal expansion coefficients between Si and Ge, so these values indicate the maximum lattice strain. Since there are large discrepancies between calculation and measured values, it seems that relaxation ratio has a large effect on the lattice strain even at the lower temperatures. PL spectra from the post-annealed Ge layers with various annealing temperatures are shown in **Figure 10**. Although Ge is an indirect bandgap material and the *L*-valley has the lowest energy level in the conduction band, we were able to observe recombination between electrons and holes at the Γ-valley as luminescence at a wavelength of 1,550 nm, even from the bulk Ge (dashed line in **Figure 10**). A comparison with the post-annealed Ge layers shows that although the spectrum was very weak and broad for the as-grown Ge layer, an obvious peak could be observed from annealed samples at $T_{GR/AN} > 530$°C. Moreover, the PL intensity increased and the peak shape became sharper as the annealing temperature was increased. The PL spectrum is strongly affected by crystallinity, because non-radiative recombination was significantly increased with defects such as dislocation and stacking faults. Therefore, these results suggest that the crystallinity of the Ge layers was improved by the post-annealing. The peak was observed at a shorter wavelength from the Ge layer annealed at 500°C compared with that from bulk Ge, and a red shift of the PL peaks occurred after post-annealing at a higher temperature. In addition, the peak wavelength from the unstrained Ge was 1,550 nm, which is almost the same value as that of the bulk Ge. These results show that the bandgap energy at the Γ-point was varied by the lattice strain in the Ge layers (Cerdeira

et al., 1972; de Walle and Martin, 1986; de Walle, 1989), which is consistent with the XRD measurements. These results indicate that, in the range of this study, the most favorable PL characteristic can be obtained from the Ge layer after post-annealing at higher temperatures.

7. GERMANIUM LIQUID-PHASE EPITAXY AND DEVICES FOR PHOTONIC APPLICATION

Liquid-phase epitaxy (LPE) is a technique that was invented in the 1960s (Nelson, 1963) and developed in the 1970s (Wieder et al., 1977) for the fabrication of detectors, solar cells, LEDs (Saul and Roccasecca, 1973), and laser diodes (Panish et al., 1970). Originally used for III-V crystal growth, it has been adapted for SiGe-on-insulator (SGOI) and Ge-on-Insulator (GOI) growth by various groups (Liu et al., 2004; Tweet et al., 2005; Feng et al., 2008; Hashimoto et al., 2009; Miyao et al., 2009; Ohta et al., 2011) and is also referred to as rapid melt growth (RMG). The GOI technique was pioneered by Liu et al. (2004) for Ge-on-insulator fabrication. In this technique, a thin insulating layer is deposited on an Si substrate and patterned to open up seed windows. The target material, in this case Ge, is deposited using a non-selective method and patterned to form the desired features. This is then encapsulated using an insulating layer and heated up in a rapid-thermal-annealer (RTA) in order to melt the Ge. The micro-crucible holds the melt in place until the liquid epitaxial growth is complete. Upon cooling, liquid-phase epitaxial growth starts from the seed and propagates to the extremities of the strip structure. For the realization of single crystal Ge, epitaxial growth must proceed faster than unseeded random nucleation, so that the crystal regrowth starting from the seed is uninterrupted. Misfit dislocations arising at the SiGe interface in the seed area are necked down to the seed window as shown in **Figure 11**. The RMG is limited to the growth of structures of the order of around 3 μm in width and with a length of above 100 μm. The limitation is largely due to the surface tension of the insulator causing the Ge to form ball shapes while in the liquid phase.

RMG is very attractive for the heterogeneous integration of Ge-based devices on insulator for electronics and photonics and has been demonstrated for Gate all around P-MOSFET (Feng et al., 2008), P-Channel FinFET (Feng et al., 2007), waveguide integrated Ge/Si heterojunction photodiodes (Tseng et al., 2013), or Ge Gate PhotoMOSFET (Going et al., 2014). These devices demonstrate the possibility of using RMG to obtain high quality Ge crystalline layers to create a bridge between electronic components and photonic components. This vision is clearly demonstrated by Going et al. (2014) in a Ge Gate PhotoMOSFET (Carroll et al., 2012) where a Ge-gated NMOS phototransistor is integrated on an Si photonics platform on SOI substrate. The resulting device, with 1-μm channel length, and 8-μm channel width, demonstrates a responsivity of over 18 A/W at 1550 nm with 583 nW of incident light. By increasing the incident power to 912 μW, the device operates at 2.5 GHz. Ge RMG or LPE on Si is therefore a promising technology for the fabrication of heterogeneous devices requiring high quality Ge layers such as MOSFETs, near-infrared detectors but also Ge-based lasers that are still to be demonstrated using this specific process technique. In fact, a highly tensile strain of 0.4% has successfully been applied to a Ge film grown by RMG process (Matsue et al., 2014), which is quite promising for light emission.

8. TIME-RESOLVED PHOTOLUMINESCENCE STUDY OF GERMANIUM ON SILICON

The use of *n*-type tensile-strained Ge grown on Si substrates is one promising way to realize an efficient light source for Si photonics through the enhanced direct recombination from the Γ valley. However, the large lattice mismatch between Ge and Si inherently causes misfit dislocations at the interface, and threading dislocations during the growth. Besides, epitaxially grown Ge is usually a thin layer, so that both the interface and the surface become important. Therefore, investigation of the excess carrier lifetime is crucial for the realization of efficient light-emitting devices. Recently, the excess carrier dynamics of thin Ge film grown on either Si or SOI substrates have been investigated by time-resolved photoluminescence (Kako et al., 2012), microwave photoconductive decay (Sheng et al., 2013), and pump-probe transmission (Geiger et al., 2014) methods. Here, we present the time-resolved photoluminescence study of both non-doped and *n*-type Ge samples grown on Si.

The Ge samples were epitaxially grown on (100) Si substrates by using a cold-wall rapid thermal chemical vapor deposition system (Oda et al., 2014). There were two primary growth steps. The first step was the growth of an intrinsic Ge thin layer (≈100 nm) at low temperature followed by an annealing process. The second step was the regrowth of Ge on the first layer with another annealing

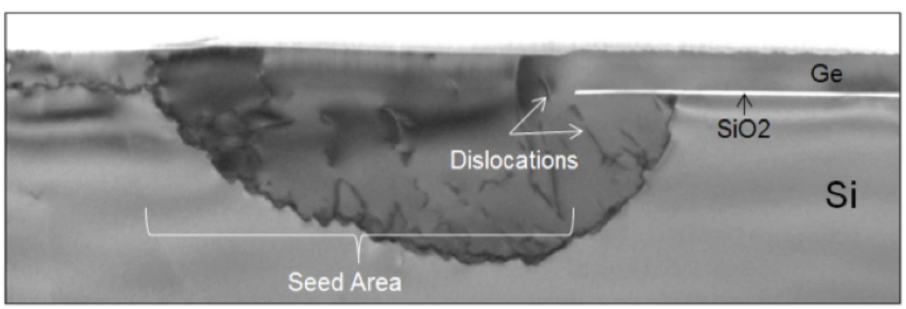

FIGURE 11 | Transmission-electron-microscope (TEM) image of a high quality single crystalline Ge-on-insulator obtained using RMG. It can clearly be seen that the misfit dislocations from the lattice mismatch are confined to the seed region and that the crystalline Germanium lateral overgrowth is free from defects.

process. *In situ n*-type doping was carried out during the second growth step by supplying phosphine. The Ge becomes biaxially strained (≈0.15%) due to the difference of the thermal expansion coefficients between Si and Ge. Time-resolved photoluminescence measurements were performed using a time-correlated single-photon counting method employing a superconducting single-photon detector (SSPD) with a time resolution of about 50 ps. A Ti:Sapphire pulsed laser was used as the excitation source (wavelength 710 nm, repetition rate 80 MHz, and pulse-duration 100 fs). The laser beam was focused on the sample surface using an objective lens. The photoluminescence from the samples was collected by the same objective and focused on to an optical fiber connected to the SSPD. Photoluminescence ranging from 1.2 to 1.8 μm was detected.

Figure 12A shows a time-resolved photoluminescence decay curve measured from a nominally undoped Ge sample (thickness 500 nm). In order to limit the effects of lateral diffusion, the laser spot size was set to ≈10 μm. The decay is a single exponential with a lifetime of 1 ns, which corresponds to the excess carrier lifetime of 2 ns. Germanium has an indirect bandgap, and as such, its excess carrier dynamics are determined by non-radiative recombination processes, such as Shockley-Read Hall (SRH) recombination and surface recombination processes. The photoluminescence decay lifetime, τ_{PL}, of undoped Ge is then related to the excess carrier lifetime, τ_{ex}, as $2\tau_{PL} = \tau_{ex}$. The lifetime of excess carriers τ_{ex} of an indirect semiconductor film depends on the thickness and can be represented by Sproul (1994) and Gaubas and Vanhellemont (2006) as:

$$\frac{1}{\tau_{ex}} = \frac{1}{\tau_B} + \frac{1}{\frac{d}{2S} + \frac{d^2}{\pi^2 D}}, \tag{6}$$

where τ_B is the bulk lifetime, S is the surface recombination velocity, D is the ambipolar diffusion constant, and d is the layer thickness. The excess carrier lifetimes obtained for undoped Ge layers with different thicknesses (filled black circles) are shown in the inset of **Figure 12A** together with the black curve, which is a fit to the data using equation (6) with parameters of $\tau_B = 3.5$ ns, $S = 5.5 \times 10^3$ cm/s, and $D = 30$ cm^2/s (The ambipolar diffusion constant D_a could be estimated by changing the spot size and measuring the photoluminescence decay time). Both SRH bulk recombination and the surface recombination processes determine the excess carrier dynamics in our undoped Ge samples.

Figure 12B shows time-resolved photoluminescence decay curves measured at two different excitation power densities from an *n*-type Ge sample (thickness 500 nm, doping concentration 7×10^{19} cm^{-3}). The measured decay depends on both the excitation power density and time (in contrast to those measured from undoped samples, which are independent of the excitation power). The instantaneous lifetime (that measured at a particular point during the decay) depends on the photoluminescence intensity, and thus the excess carrier density. Based on the SRH non-radiative recombination model, the lifetime of excess carriers depends on their density (Linnros, 1998). This dependence can be simplified to $\tau_{hl} = \tau_n + \tau_p$ ($\tau_{ll} = \tau_p$ for *n*-type doping) in the two extreme conditions where the carrier density is high (low) when compared to the doping concentration (τ_n and τ_p are the inverse capture rates of the electrons and holes, respectively). The photoluminescence lifetime can be expressed as $2\tau_{PL} = \tau_{hl}$ (high excess carrier density) and $\tau_{PL} = \tau_{ll}$ (low excess carrier density). Therefore, from our measurements, we estimate $\tau_{ll} = 0.14$ ns, $\tau_{hl} = 0.8$ ns based on SRH theory. The estimated τ_{hl} value is shorter than those found from the undoped samples. This difference might be attributed to an increased dislocation density introduced by the doping, but the estimation of τ_{hl} could be underestimation because the Auger process becomes important for doped samples (Gaubas and Vanhellemont, 2006). Further investigation is needed in order to obtain a better understanding.

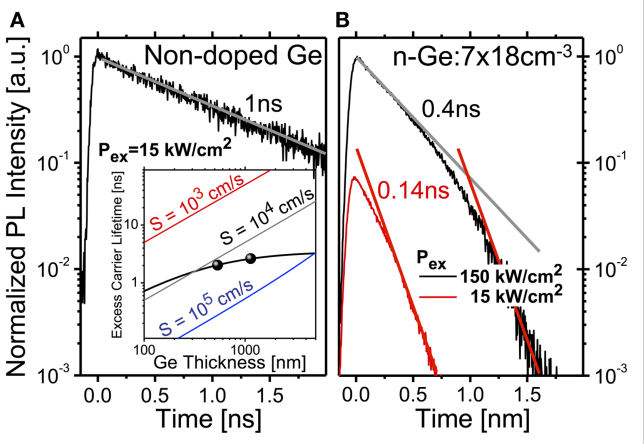

FIGURE 12 | (A) Time-resolved PL curve for an undoped Ge sample. The inset shows the measured excess carrier lifetimes for two Ge thicknesses with simulated lifetimes using the equations shown in the text. **(B)** Time-resolved PL curves of an *n*-type sample for two excitation powers, 150 kW/cm^2 (black line) and 15 kW/cm^2 (red line).

9. ELECTRO-LUMINESCENCE FROM GERMANIUM

Realization of monolithic light sources compatible with the existing Si photonics platform is one of the most difficult challenges. Ge has attracted much attention as for possible future monolithic light sources owing to its emission wavelengths of ~1.6 μm suitable for an Si-based WG, in addition to the CMOS compatibility and the pseudo-direct band-gap character (Menéndez and Kouvetakis, 2004; Liu et al., 2007, 2012; Liang and Bowers, 2010; Michel et al., 2010; Boucaud et al., 2013; Liu, 2014). Recently, laser operation from Ge pumped optically (Liu et al., 2010) and electrically (Cheng et al., 2007; Camacho-Aguilera et al., 2012) has been reported. However, there is no report so far to reproduce their results. The optical gain from Ge is also achieved by the tensile-stress engineering (de Kersauson et al., 2011). The precise nature of the optical gain in Ge is still controversial (Carroll et al., 2012), but the high crystalline quality of Ge is one of the most critical factor to avoid non-radiative recombinations at dislocations. It is confirmed by several groups (Michel et al., 2010; Liu et al., 2012; Boucaud et al., 2013; Liu, 2014) that the primary challenges for engineering Ge as an active layer are: (i) crystallinity, (ii) high *n*-type doping, (iii) tensile strain, as confirmed theoretically (Suwa and Saito, 2010,

2011; Virgilio et al., 2013a,b). Here, we review some of the Ge light sources developed on SOI substrates.

9.1. DEVICE STRUCTURE AND FABRICATION PROCESS

As we discussed in section for Si light sources, lateral carrier injection is a natural choice for electrical pumping, since fabrication processes are based on planar CMOS technologies. We show several candidates for Ge light sources suitable for lateral carrier injection in **Figure 13**.

Figures 13A,E,I show schematic views and a transmission-electron-microscope (TEM) image of a Ge FinLED (Saito et al., 2011a), which uses Ge fins as MQWs embedded in Si_3N_4 WG. Ge fins were fabricated by the oxidation condensation technique (Tezuka et al., 2009) applied to SiGe fins (Saito et al., 2011a). Relatively, high crystallinity is expected in Ge fins, since the lattice mismatch between Si and Ge would be relaxed by stretching the fins during the oxidation (Saito et al., 2011a). In fact, the low dark current density of 1.86×10^{-5} A/cm^{-2} at a reverse bias of $1 - V$ and the strong breakdown current density of >1 MA/cm^{-2} were confirmed (Saito et al., 2011a).

In order to enhance the overlap between an optical mode and fins, Ge fins with (111) orientation at the sidewall were also developed (Tani et al., 2012), as shown in **Figures 13B,F,J**. To improve the patterning accuracy, Si (111) fins were fabricated by anisotropic wet etching, and *n*-Ge was re-grown after the condensation oxidation of SiGe fins (Tani et al., 2011).

Further increase of the coupling is realized by using a bulk Ge WG (Liu et al., 2007; Camacho-Aguilera et al., 2012; Tani et al., 2013a,b), as shown in **Figures 13C,G,K** for schematic views and the scanning electron microscope (SEM) image, rather than using Ge QW or Ge fins. The *p*- and *n*-type diffusion regions were formed in the 40 nm-thick SOI layer, and the Ge waveguide with 500-nm width and 500-μm length was directly grown on the SOI diode. The SOI thickness was designed to minimize the optical loss due to free carrier absorption in the diffusion electrodes. The Ge waveguide was doped with 1×10^{19} cm^{-3} of phosphorus, and the surface of the Ge waveguide was then passivated with GeO_2 formed by low-temperature oxidation to reduce interfacial traps (Tani et al., 2012, 2013a). Then, metal electrodes were made on both diffusion regions.

To enhance light emission efficiency from Ge by tensile stress, several techniques have been developed, e.g., the use of the thermal expansion of relaxed Ge grown on Si (Ishikawa et al., 2003), the growth on buffer layers with larger lattice parameter (Huo et al., 2011), the mechanical deformation using membrane structures (Kurdi et al., 2010), the stress concentration in a membrane structure (Nama et al., 2013), and using external stressors (Ortolland et al., 2009; Ghrib et al., 2013). Considering the process compatibility to the lateral carrier injection, the Si_3N_4 film with the tensile stress of 250-MPa was employed (Tani et al., 2013a), as shown in **Figures 13D,H,L**.

9.2. IMPACT OF STRESS ENGINEERING FOR LATERAL GERMANIUM ON SILICON DIODE

Figure 14A shows EL spectra of the Ge waveguide with 500-nm width and 500-μm length taken from the top of the substrate under continuous current injection of 60-mA. EL peak wavelength of the device with an SiN stressor is slightly longer than that without the SiN stressor due to the tensile strain-induced band-gap shrinkage, although the exact band-gap energy cannot be quantitatively estimated due to the additional peak shifts caused by heating under high currents. Moreover, as shown in **Figure 14B**, the peak intensity of the EL of the device with SiN stressor is 1.65 times larger than that without SiN stressors. **Figure 14C** shows two-dimensional stress mapping calculated by a finite element modeling of the Ge waveguide on the Si substrate covered by Si_3N_4 stressor. The tensile stress of 100 MPa

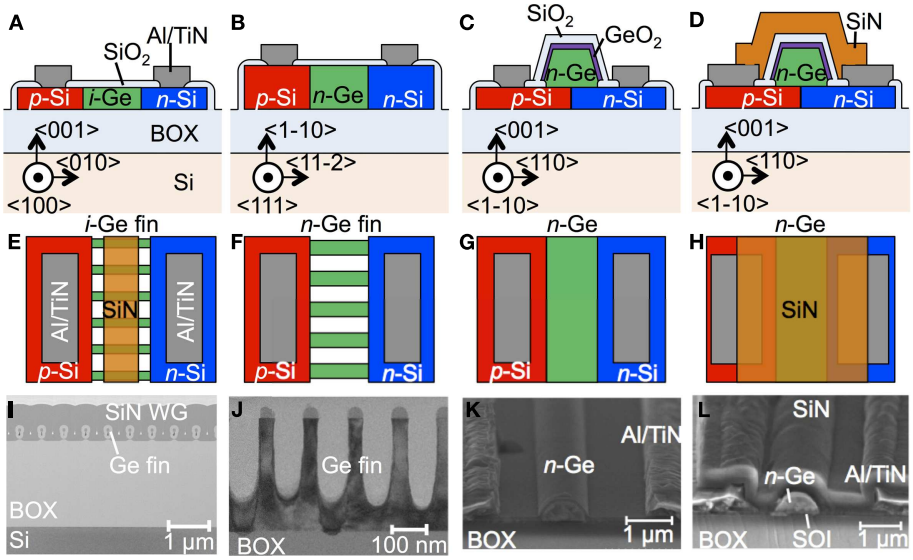

FIGURE 13 | Development of a Ge light source. **(A)** *i*-Ge FinLED, **(B)** *n*-Ge FinLED, **(C)** *n*-Ge-WG-on-Si LED without SiN, and **(D)** *n*-Ge-WG-on-Si LED with SiN. **(A–D)** Cross section, **(E–H)** plan views, and **(I–L)** microscope images.

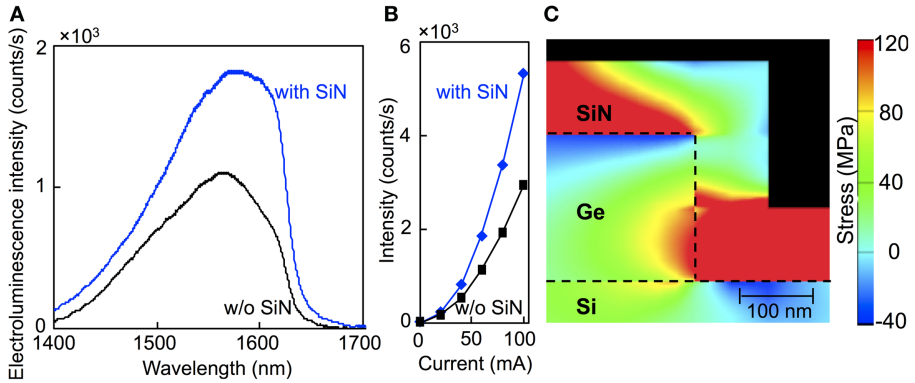

FIGURE 14 | Strain engineering for *n*-Ge-WG-on-Si LED. **(A)** Spectra and **(B)** integrated intensity from experiments. **(C)** Stress mapping simulation.

is localized on the side wall of the Ge waveguide, while the in-plane compressive stress of 40 MPa exists on the top part of the Ge waveguide. The increase of the light emission efficiency was 22% caused by the tensile stress, after subtracting of the additional increase of 35% caused by the light extraction efficiency due to the reduced reflectance at the surface of the Ge waveguide by the 500 nm-thick Si_3N_4 layer (Tani et al., 2013a). Therefore, the stress engineering by Si_3N_4 is an appropriate option to improve the performance of Ge light sources. Recently, there are significant advances in stress engineering by manipulating free-standing Ge structures (Jain et al., 2012; Boztug et al., 2013; Süess et al., 2013; Sukhdeo et al., 2014), and enhanced direct recombination has been achieved.

10. CONCLUSION AND FUTURE OUTLOOK

In this paper, we reviewed the recent progress on the developments of silicon and germanium light sources. There are many process options to fabricate silicon- and germanium-based nanostructures by using modern silicon technologies. For active materials, planar silicon single-quantum-well (Saito et al., 2006a,b, 2008, 2009; Hoang et al., 2007; Noborisaka et al., 2011; Saito, 2011) or multiple-quantum-wells made of silicon or germanium fins (Saito et al., 2011a,b) can be used. To enhance the recombination rates and the extraction efficiencies, photonic crystal structures have been introduced (Fujita et al., 2008; Nakayama et al., 2010a; Iwamoto and Arakawa, 2012). The further increase of the efficiency can be achieved by introducing tensile strain and *n*-type doping of the germanium (Ishikawa et al., 2003; Menéndez and Kouvetakis, 2004; Liu et al., 2007, 2012; Kurdi et al., 2010; Michel et al., 2010; Huo et al., 2011; Boucaud et al., 2013; Ghrib et al., 2013; Nama et al., 2013; Tani et al., 2013a; Liu, 2014).

Considering the success of the laser operation using the bulk germanium waveguides (Liu et al., 2010; Camacho-Aguilera et al., 2012), the next step will be to reduce the threshold current for pumping. It is critical to develop a process technology to fabricate a high crystalline quality germanium quantum-well compatible with the silicon photonics platform. If practical silicon or germanium laser diodes are available in the future, these group IV lasers will realize the convergence of electronics and photonics on a silicon chip.

ACKNOWLEDGMENTS

We would like to thank research collaborators, engineers, and line managers in Hitachi, the University of Tokyo, and University of Southampton for supporting this project. We are also grateful to Prof. H. N. Rutt for his careful reading of the manuscript and constructive comments. Funding: parts of the studied discussed here was supported by Japan Society for the Promotion of Science (JSPS) through its "Funding Program for World-Leading Innovation R&D on Science and Technology (FIRST Program)," the Project for Developing Innovation Systems, and Kakenhi 216860312, MEXT, Japan. This work is also supported by EU, FP7, Marie-Curie, Carrier Integration Grant (CIG), PCIG13-GA-2013-618116, and University of Southampton, Zepler Institute, Research Collaboration Stimulus Fund.

REFERENCES

Arakawa, Y., Iwamoto, S., Nomura, M., Tandaechanurat, A., and Ota, Y. (2012). Cavity quantum electrodynamics and lasing oscillation in single quantum dot-photonic crystal nanocavity coupled systems. *IEEE J. Selec. Top. Quant. Elec.* 18, 1818–1829. doi:10.1109/JSTQE.2012.2199088

Arakawa, Y., Nakamura, T., and Urino, Y. (2013). Silicon photonics for next generation system integration platform. *Commun. Mag. IEEE* 51, 72–77. doi:10.1109/MCOM.2013.6476868

Arakawa, Y., and Sakaki, H. (1982). Multidimensional quantum well laser and temperature dependence of its threshold current. *Appl. Phys. Lett.* 40, 939–941. doi:10.1063/1.92959

Boucaud, P., Kurdi, M. E., Ghrib, A., Prost, M., de Kersauson, M., Sauvage, S., et al. (2013). Recent advances in germanium emission. *Photon. Res.* 1, 102–109. doi:10.1364/PRJ.1.000102

Boztug, C., Sanchez-Perez, J. R., Yin, J., Lagally, M. G., and Paiella, R. (2013). Graiting-coupled mid-infrared light emission from tensile strained germanium nanomembranes. *Appl. Phys. Lett.* 103, 201114. doi:10.1002/smll.201201090

Camacho-Aguilera, R. E., Cai, Y., Patel, N., Bessette, J. T., Romagnoli, M., Kimerling, L. C., et al. (2012). An electrically pumped germanium laser. *Opt. Express* 20, 11316–11320. doi:10.1364/OE.20.011316

Canham, L. T. (1990). Silicon quantum wire array fabrication by electrochemical and chemical dissolution of wafers. *Appl. Phys. Lett.* 57, 1046–1048. doi:10.1063/1.103561

Cannon, D. D., Liu, J., Ishikawa, Y., Wada, K., Danielson, D. T., Jongthammanurak, S., et al. (2004). Tensile strained epitaxial Ge film on Si(100) substrate with potential application to L-band telecommunications. *Appl. Phys. Lett.* 84, 906. doi:10.1063/1.1645677

Carroll, L., Friedli, P., Neunschwander, S., Sigg, H., Cecchi, S., Isa, F., et al. (2012). Direct-gap gain and optical absorption in germanium correlated to the density

of photoexcited carriers, doping, and strain. *Phys. Rev. Lett.* 109, 057402. doi:10.1103/PhysRevLett.109.057402

Cerdeira, F., Buchenauer, C. J., Pollak, F. H., and Cardona, M. (1972). Stress-induced shifts of first-order Raman frequencies of diamond- and zinc-blende-type semiconductors. *Phys. Rev. B* 5, 580–593. doi:10.1103/PhysRevB.5.580

Cheng, T. H., Kuo, P. S., Lee, C. T., Liao, M., Hung, T. A., and Liu, C. W. (2007). "Electrically pumped Ge laser at room temperature," in *IEEE Int. Conf. Electron Devices Meeting (IEDM)*, Washington, 659–662.

Cluzel, B., Pauc, N., Calvo, V., Charvolin, T., and Hadji, E. (2006a). Nanobox array for silicon-on-insulator luminescence enhancement at room temperature. *Appl. Phys. Lett.* 88, 133120. doi:10.1063/1.2191089

Cluzel, B., Calvo, V., Charvolin, T., Picard, E., Noé, P., and Hadji, E. (2006b). Single-mode room-temperature emission with a silicon rod lattice. *Appl. Phys. Lett.* 89, 201111. doi:10.1063/1.2364876

Cullis, A. G., Canham, L. T., and Calcott, P. D. J. (1997). The structural and luminescence properties of porous silicon. *J. Appl. Phys.* 82, 909–965. doi:10.1063/1.366536

Daldosso, N., and Pavesi, L. (2009). Nanosilicon photonics. *Laser Photon. Rev.* 3, 508–534. doi:10.1002/lpor.200810045

de Kersauson, M., Kurdi, M. E., David, S., Checoury, X., Fishman, G., Sauvage, S., et al. (2011). Optical gain in single tensile-strained germanium photonic wire. *Opt. Express* 19, 17925–17934. doi:10.1364/OE.19.017925

de Walle, C. G. V. (1989). Band lineups and deformation potentials in the model-solid theory. *Phys. Rev. B* 39, 1871. doi:10.1103/PhysRevB.39.1871

de Walle, C. G. V., and Martin, R. M. (1986). Theoretical calculations of heterojunction discontinuities in the Si/Ge system. *Phys. Rev. B* 34, 5621–5634. doi:10.1103/PhysRevB.34.5621

Deen, M. J., and Basu, P. K. (2012). *Silicon Photonics Fundamentals and Devices*. West Sussex: Wiley.

Escalante, J. M., and Martínez, A. (2012). Theoretical study about the gain in indirect bandgap semiconductor optical cavities. *Physica B Condens. Matter* 407, 2044–2049. doi:10.1016/j.physb.2012.02.002

Escalante, J. M., and Martínez, A. (2013). Optical gain by simultaneous photon and phonon confinement in indirect bandgap semiconductor acousto-optical cavities. *Opt. Quant. Electron.* 45, 1045–1056. doi:10.1007/s11082-013-9715-z

Evans, P., Fisher, M., Malendevich, R., James, A., Studenkov, P., Goldfarb, G., et al. (2011). "Multi-channel coherent PM-QPSK InP transmitter photonic integrated circuit (PIC) operating at 112 gb/s per wavelength," in *Optical Fiber Communication Conference (OFC)* (Los Angeles: (IEEE) PDPC, OSA).

Fang, A. W., Park, H., Cohen, O., Jones, R., Paniccia, M. J., and Bowers, J. E. (2006). Electrically pumped hybrid AlGaInAs-silicon evanescent laser. *Opt. Express* 14, 9203–9210. doi:10.1364/OE.14.009203

Fathpour, S., and Jalali, B. (eds) (2012). *Silicon Photonics for Telecommunications and Biomedicine*. Boca Raton: CRC Press.

Feng, J., Thareja, G., Kobayashi, M., Chen, S., Poon, A., Bai, Y., et al. (2008). High-performance gate-all-around GeOI p-MOSFETs fabricated by rapid melt growth using plasma nitridation and ALD Al_2O_3 gate dielectric and self-aligned NiGe contacts. *IEEE Electron Device Lett.* 29, 805–807. doi:10.1109/LED.2008.2000613

Feng, J., Woo, R., Chen, S., Liu, Y., Griffin, P. B., and Plummer, J. D. (2007). P-channel germanium FinFET based on rapid melt growth. *IEEE Electron Device Lett.* 28, 637–639. doi:10.1109/LED.2007.899329

Fischetti, M. V., and Laux, S. E. (1996). Band structure, deformation potentials, and carrier mobility in strained Si, Ge, and SiGe alloys. *J. Appl. Phys.* 80, 2234. doi:10.1063/1.363052

Fujita, M., Tanaka, Y., and Noda, S. (2008). Light emission from silicon in photonic crystal nanocavity. *IEEE J. Selec. Top. Quant. Elec.* 14, 1090–1097. doi:10.1109/JSTQE.2008.918941

Fukatsu, S., Usami, N., Chinzei, T., Shiraki, Y., Nishida, A., and Nakagawa, K. (1992). Electroluminescence from strained SiGe/Si quantum well structures grown by solid source si molecular beam epitaxy. *Jpn. J. Appl. Phys.* 31, L1015–L1017. doi:10.1143/JJAP.31.L1015

Gaubas, E., and Vanhellemont, J. (2006). Dependence of carrier lifetime in germanium on resistivity and carrier injection level. *Appl. Phys. Lett.* 89, 142106. doi:10.1063/1.2358967

Geiger, R., Frigerio, J., Süess, M. J., Chrastina, D., Isella, G., Spolenak, R., et al. (2014). Excess carrier lifetimes in Ge layers on Si. *Appl. Phys. Lett.* 104, 062106. doi:10.1063/1.4865237

Gelloz, B., Kojima, A., and Koshida, N. (2005). Highly efficient and stable luminescence of nanocrystalline porous silicon treated by high-pressure water vapor annealing. *Appl. Phys. Lett.* 87, 031107. doi:10.1063/1.2001136

Gelloz, B., and Koshida, N. (2000). Electroluminescence with high and stable quantum efficiency and low threshold voltage from anodically oxidized thin porous silicon diode. *J. Appl. Phys.* 88, 4319–4324. doi:10.1063/1.1290458

Ghrib, A., Kurdi, M. E., de Kersauson, M., Prost, M., Sauvage, S., Checoury, X., et al. (2013). Tensile-strained germanium microdisks. *Appl. Phys. Lett.* 102, 221112. doi:10.1063/1.4809832

Going, R. W., Loo, J., Liu, T.-J. K., and Wu, M. C. (2014). Germanium gate PhotoMOSFET integrated to silicon photonics. *IEEE J. Selec. Top. Quant. Elec.* 20, 8201607. doi:10.1109/JSTQE.2013.2294470

Gong, Y., Makarova, M., Selçuk Yerci, R. L., Stevens, M. J., Baek, B., Nam, S. W., et al. (2010). Linewidth narrowing and Purcell enhancement in photonic crystal cavities on an Er-doped silicon nitride platform. *Opt. Express* 18, 2601–2612. doi:10.1364/OE.18.002601

Gunn, C. (2006). Cmos photonics for high-speed interconnects. *Micro IEEE* 26, 58–66. doi:10.1109/MM.2006.32

Hashimoto, T., Yoshimoto, C., Hosoi, T., Shimura, T., and Watanabe, H. (2009). Fabrication of local Ge-on-insulator structures by lateral liquid-phase epitaxy: effect of controlling interface energy between Ge and insulators on lateral epitaxial growth. *Appl. Phys. Express* 2, 066502. doi:10.1143/APEX.2.066502

Hauke, N., Zabel, T., Müller, K., Kaniber, M., Laucht, A., Bougeard, D., et al. (2010). Enhanced photoluminescence emission from two-dimensional silicon photonic crystal nanocavities. *New J. Phys.* 98, 053005. doi:10.1088/1367-2630/12/5/053005

Hisamoto, D., Lee, W., Kedzierski, J., Takeuchi, H., Asano, K., Kuo, C., et al. (2000). FinFET-a self-aligned double-gate MOSFET scalable to 20 nm. *IEEE Trans. Electron Devices* 47, 2320–2325. doi:10.1109/16.887014

Hoang, T., LeMinh, P., Holleman, J., and Schmitz, J. (2007). Strong efficiency improvement of SOI-LEDs through carrier confinement. *IEEE Electron Device Lett.* 28, 383–385. doi:10.1109/LED.2007.895415

Huo, Y., Lin, H., Chen, R., Makarova, M., Rong, Y., Li, M., et al. (2011). Strong enhancement of direct transition photoluminescence with highly tensile-strained Ge grown by molecular beam epitaxy. *Appl. Phys. Lett.* 98, 011111. doi:10.1063/1.3534785

Ishikawa, Y., and Wada, K. (2010). Germanium for silicon photonics. *Thin Solid Films* 518, S83–S87. doi:10.1016/j.tsf.2009.10.062

Ishikawa, Y., Wada, K., Cannon, D. D., Liu, J., Luan, H.-C., and Kimerling, L. C. (2003). Strain-induced band gap shrinkage in Ge grown on Si substrate. *Appl. Phys. Lett.* 82, 2044. doi:10.1063/1.1564868

Ishikawa, Y., Wada, K., Liu, J., Cannon, D. D., Luan, H.-C., Michel, J., et al. (2005). Strain-induced enhancement of near-infrared absorption in Ge epitaxial layers grown on Si substrate. *J. Appl. Phys.* 98, 013501. doi:10.1063/1.1943507

Iwamoto, S., and Arakawa, Y. (2012). Enhancement of light emission from silicon by utilizing photonic nanostructures. *IEICE Trans. Electron* E95-C, 206–212. doi:10.1587/transele.E95.C.206

Iwamoto, S., Arakawa, Y., and Gomyo, A. (2007). Observation of enhanced photoluminescence from silicon photonic crystal nanocavity at room temperature. *Appl. Phys. Lett.* 91, 211104. doi:10.1063/1.2816892

Jain, J. R., Hryciw, A., Baer, T. M., Miller, D. A. B., Brongersma, M. L., and Howe, R. T. (2012). A micromachining-based technology for enhancing germanium light-emission via tensile strain. *Nat. Photonics* 6, 398–405. doi:10.1038/nphoton.2012.111

Jannopoulos, J. D., and Winn, R. D. M. J. N. (1995). *Photonic Crystals*. Princeton, NJ: Princeton University Press.

Kageshima, H., and Shiraishi, K. (1997). Momentum-matrix-element calculation using pseudopotentials. *Phys. Rev. B* 56, 14985. doi:10.1103/PhysRevB.56.14985

Kako, S., Okumura, T., Oda, K., Suwa, Y., Saito, S., Ido, T., et al. (2012). "Time-resolved photoluminescence study of highly n-doped germanium grown on silicon," in *The 9th International Conference on Group IV Photonics (GFP)*, Vol. 7, San Diego, 340–342.

Kittler, M., Reiche, M., and Arguirov, T. (2013). "1.55 μm light emitter based on dislocation d1-emission in silicon," in *Microelectronics Technology and Devices (SBMicro), Symposium on* IEEE, Curitiba.

Koshida, N., and Koyama, H. (1992). Visible electroluminescence from porous silicon. *Appl. Phys. Lett.* 60, 347–349. doi:10.1063/1.106652

Kurdi, M. E., Bertin, H., Martincic, E., de Kersauson, M., Fishman, G., Sauvage, S., et al. (2010). Control of direct band gap emission of bulk germanium by mechanical tensile strain. *Appl. Phys. Lett.* 96, 041909. doi:10.1063/1.3297883

Kurdi, M. E., Davida, S., Checourya, X., Fishmana, G., Boucauda, P., Kermarrecb, O., et al. (2008). Two-dimensional photonic crystals with pure germanium-on-insulator. *Opt. Commun.* 281, 846–850. doi:10.1016/j.optcom.2007.10.008

Laasonen, K., Pasquarello, A., Car, R., Lee, C., and Vanderbilt, D. (1993). Car-Parrinello molecular dynamics with Vanderbilt ultrasoft pseudopotentials. *Phys. Rev. B* 47, 10142. doi:10.1103/PhysRevB.47.10142

Liang, D., and Bowers, J. E. (2010). Recent progress in lasers on silicon recent progress in lasers on silicon recent progress in lasers on silicon recent progress in lasers on silicon. *Nat. Photonics* 4, 511–517. doi:10.1088/0034-4885/76/3/034501

Lim, P. H., Park, S., Ishikawa, Y., and Wada, K. (2009). Enhanced direct bandgap emission in germanium by micromechanical strain engineering. *Opt. Express* 17, 16358–16365. doi:10.1364/OE.17.016358

Linnros, J. (1998). Carrier lifetime measurements using free carrier absorption transients. I. Principle and injection dependence. *J. Appl. Phys.* 84, 275. doi:10.1063/1.368024

Liu, J. (2014). Monolithically integrated Ge-on-Si active photonics. *Photonics* 1, 162–197. doi:10.3390/photonics1030162

Liu, J., Camacho-Aguilera, R., Bessette, J. T., Sun, X., Wang, X., Cai, Y., et al. (2012). Ge-on-Si optoelectronics. *Thin Solid Films* 520, 3354–3360. doi:10.1016/j.tsf.2011.10.121

Liu, J., Cannon, D. D., Wada, K., Ishikawa, Y., Jongthammanurak, S., Danielson, D. T., et al. (2005). Tensile strained Ge *p-i-n* photodetectors on Si platform for C and L band telecommunications. *Appl. Phys. Lett.* 87, 011110. doi:10.1063/1.2037200

Liu, J., Sun, X., Camacho-Aguilera, R., Kimerling, L. C., and Michel, J. (2010). Ge-on-Si laser operating at room temperature. *Opt. Lett.* 35, 679–681. doi:10.1364/OL.35.000679

Liu, J., Sun, X., Pan, D., Wang, X., Kimerling, L. C., Koch, T. L., et al. (2007). Tensile-strained, n-type Ge as a gain medium for monolithic laser integration on Si. *Opt. Express* 15, 11272–11277. doi:10.1364/OE.15.011272

Liu, Y., Deal, M. D., and Plummer, J. D. (2004). High-quality single-crystal Ge on insulator by liquid-phase epitaxy on Si substrates. *Appl. Phys. Lett.* 84, 2563. doi:10.1063/1.1691175

Lo Savio, R., Portalupi, S. L., Gerace, D., Shakoor, A., Krauss, T. F., O'Faolain, L., et al. (2011). Room-temperature emission at telecom wavelengths from silicon photonic crystal nanocavities. *Appl. Phys. Lett.* 98, 201106. doi:10.1063/1.3591174

Luan, H.-C., Lim, D. R., Lee, K. K., Chen, K. M., Sandland, J. G., Wada, K., et al. (1999). High-quality Ge epilayers on Si with low threading-dislocation densities. *Appl. Phys. Lett.* 75, 2909. doi:10.1063/1.125187

Matsue, M., Yasutake, Y., Fukatsu, S., Hosoi, T., Shimura, T., and Watanabe, H. (2014). Strain-induced direct band gap shrinkage in local Ge-on-insulator structures fabricated by lateral liquid-phase epitaxy. *Appl. Phys. Lett.* 104, 031106. doi:10.1063/1.4862890

Menéndez, J., and Kouvetakis, J. (2004). Type-I $Ge/Ge_{1-x-y}Si_xSn_y$ strained-layer heterostructure with a direct Ge bandgap. *Appl. Phys. Lett.* 85, 1175. doi:10.1063/1.1784032

Michel, J., Liu, J., and Kimerling, L. C. (2010). High-performance ge-on-si photodetectors. *Nat. Photonics* 4, 527–534. doi:10.1038/nphoton.2010.157

Michel, J., and Romagnoli, M. (2012). *Germanium as the Unifying Material for Silicon Photonics.* Bellingham: SPIE. doi:10.1117/2.1201206.004285

Miller, D. A. B. (2009). Device requirements for optical interconnections to silicon chips. *Proc. IEEE* 97, 1166–1185. doi:10.1109/JPROC.2009.2014298

Miyao, M., Tanaka, T., Toko, K., and Tanaka, M. (2009). Giant Ge-on-insulator formation by Si-Ge mixing-triggered liquid-phase epitaxy. *Appl. Phys. Express* 2, 045503. doi:10.1143/APEX.2.045503

Nakayama, S., Ishida, S., Iwamoto, S., and Arakawa, Y. (2012). Effect of cavity mode volume on photoluminescence from silicon photonic crystal nanocavities. *Appl. Phys. Lett.* 98, 171102.

Nakayama, S., Iwamoto, S., Ishida, S., and Arakawa, Y. (2010a). "Demonstration of a silicon photonic crystal slab led with efficient electroluminescence," in *International Conference on Solid State Devices and Materials (SSDM 2010)* D-4-3, Tokyo.

Nakayama, S., Iwamoto, S., Ishida, S., Bordel, D., Augedre, E., Calvelier, L., et al. (2010b). Enhancement pf photoluminescence from germanium by utilizing air-bridge-type photonic crytsal slab. *Physica E* 42, 2556–2559. doi:10.1016/j.physe.2010.05.026

Nakayama, S., Iwamoto, S., Kako, S., Ishida, S., and Arakawa, Y. (2011). "Demonstration of silicon nanocavity led with enhanced luminescence," in *International Conference on Solid State Devices and Materials*, Nagoya, I–8–2.

Nama, D., Sukhdeo, D. S., Kang, J.-H., Petykiewicz, J., Lee, J. H., Jung, W. S., et al. (2013). Strain-induced pseudoheterostructure nanowires confining carriers at room temperature with nanoscale-tunable band profiles. *Nano Lett.* 13, 3118–3123. doi:10.1021/nl401042n

Nassiopoulou, A. G. (2004). *Silicon Nanocrystals in SiO_2 Thin Layers*, Vol. 9. Valencia: American Scientific Publishers, 793–813.

Nelson, H. (1963). Epitaxial growth from the liquid state and its application to the fabrication of tunnel and laser diodes. *RCA Rev.* 24, 603–615.

Ng, W. L., Lourenço, M. A., Gwilliam, R. M., Ledain, S., Shao, G., and Homewood, K. P. (2001). An efficient room-temperature silicon-based light-emitting diode. *Nature* 410, 192–194. doi:10.1038/35069092

Ngo, T.-P., Kurdi, M. E., Checoury, X., Boucaud, P., Damlencourt, J. F., Kermarrec, O., et al. (2008). Two-dimensional photonic crystals with germanium on insulator obtained by a condensation method. *Appl. Phys. Lett.* 93, 241112. doi:10.1063/1.3054332

Noborisaka, J., Nishiguchi, K., Ono, Y., Kageshima, K., and Fujiwara, A. (2011). Strong stark effect in electroluminescence from phosphorous-doped silicon-on-insulator metal-oxide-semiconductor field-effect transistors. *Appl. Phys. Lett.* 98, 033503. doi:10.1063/1.3543849

Oda, K., Tani, K., Saito, S.-I., and Ido, T. (2014). Improvement of crystallinity by post-annealing and regrowth of Ge layers on Si substrates. *Thin Solid Films* 550, 509–514. doi:10.1016/j.tsf.2013.10.136

Ohta, Y., Tanaka, T., Toko, K., Sadoh, T., and Miyao, M. (2011). Growth-direction-dependent characteristics of Ge-on-insulator by Si-Ge mixing triggered melting growth. *Solid State Electron.* 60, 18–21. doi:10.1016/j.sse.2011.01.039

Okada, Y., and Tokumaru, Y. (1984). Precise determination of lattice parameter and thermal expansion coefficient of silicon between 300 and 1500 K. *J. Appl. Phys.* 56, 314. doi:10.1063/1.333965

Ortolland, C., Okuno, Y., Veheyen, P., Kerner, C., Stapelmann, C., Aoulaiche, M., et al. (2009). Stress memorization technique-fundamental understanding and low-cost integration for advanced CMOS technology using a nonselective process. *IEEE Trans. Electron Devices* 56, 1690–1697. doi:10.1109/TED.2009.2024021

Ossicini, S., Pavesi, L., and Priolo, F. (2006). *Light Emitting Silicon for Microphotonics.* Berlin: Springer.

Panish, M. B., Hayashi, I., and Sumski, S. (1970). Double heterostructure injection lasers with room temperature thresholds as low as 2300 a/cm^2. *Appl. Phys. Lett.* 16, 326. doi:10.1063/1.1653213

Pavesi, L., and Guillot, G. (eds) (2006). *Optical Interconnects The Silicon Approach.* Berlin: Springer.

Pavesi, L., and Lockwood, D. J. (eds) (2004). *Silicon Photonics.* Berlin: Springer.

Pavesi, L., Negro, L. D., Mazzoleni, C., Franzò, G., and Priolo, F. (2000). Optical gain in silicon nanocrystals. *Nature* 408, 440–444.

Perdew, J. P., Burke, K., and Wang, Y. (1996). Generalized gradient approximation for the exchange-correlation hole of a many-electron system. *Phys. Rev. B* 54, 16533. doi:10.1103/PhysRevB.54.16533

Purcell, E. M. (1946). Spontaneous emission probabilities at radio frequencies. *Phys. Rev* 69, 681.

Reed, G. (2008). *Silicon Photonics the State of the Art.* West Sussex: Wiley.

Reed, G. T., and Knights, A. P. (2004). *Silicon Photonics.* West Sussex: Wiley.

Rylyakov, A., Schow, C., Lee, B., Green, W., Campenhout, J. V., Yang, M., et al. (2011). "A 3.9ns 8.9mW 4×4 silicon photonic switch hybrid integrated with CMOS driver," in *Int. Solid-State Circuits Conference (ISSCC)* (San Francisco: IEEE), 222–224.

Saito, S. (2011). "Silicon and germanium quantum well light-emitting diode," in *IEEE 8th Int. Conf. Group IV Photonics*, London, 166–168.

Saito, S., Hisamoto, D., Shimizu, H., Hamamura, H., Tsuchiya, R., Matsui, Y., et al. (2006a). Electro-luminescence from ultra-thin silicon. *Jpn. J. Appl. Phys.* 45, L679–L682. doi:10.1143/JJAP.45.L679

Saito, S., Hisamoto, D., Shimizu, H., Hamamura, H., Tsuchiya, R., Matsui, Y., et al. (2006b). Silicon light-emitting transistor for on-chip optical interconnection. *Appl. Phys. Lett.* 89, 163504. doi:10.1063/1.2360783

Saito, S., Oda, K., Takahama, T., Tani, K., and Mine, T. (2011a). Germanium fin light-emitting diode. *Appl. Phys. Lett.* 99, 241105. doi:10.1364/OE.22.005927

Saito, S., Takahama, T., Tani, K., Takahashi, M., Mine, T., Suwa, Y., et al. (2011b). Stimulated emission of near-infrared radiation in silicon fin light-emitting diode. *Appl. Phys. Lett.* 98, 261104. doi:10.1063/1.3605255

Saito, S., Sakuma, N., Suwa, Y., Arimoto, H., Hisamoto, D., Uchiyama, H., et al. (2008). "Observation of optical gain in ultra-thin silicon resonant cavity light-emitting diode," in *IEEE Int. Conf. Electron Devices Meeting (IEDM)*, San Francisco, 19.5.

Saito, S., Suwa, Y., Arimoto, H., Sakuma, N., Hisamoto, D., Uchiyama, H., et al. (2009). Stimulated emission of near-infrared radiation by current injection into silicon (100) quantum well. *Appl. Phys. Lett.* 95, 241101. doi:10.1063/1.3273367

Saul, R. H., and Roccasecca, D. D. (1973). Vapor-doped multislice LPE for efficient GaP green LED's. *J. Electrochem. Soc.* 120, 1128–1131. doi:10.1149/1.2403644

Savio, R. L., Miritello, M., Shakoor, A., Cardile, P., Welna, K., Andreani, L. C., et al. (2013). Enhanced 1.54 μm emission in Y-Er disilicate thin films on silicon photonic crystal cavities. *Opt. Express* 21, 10278–10288. doi:10.1364/OE.21.010278

Shakoor, A., Lo Savio, R., Cardile, P., Portalupi, S. L., Gerace, D., Welna, K., et al. (2013). Room temperature all-silicon photonic crystal nanocavity light emitting diode at sub-bandgap wavelengths. *Laser Photon. Rev.* 7, 114–121. doi:10.1002/lpor.201200043

Sheng, J. J., Leonhardt, D., Han, S. M., Johnston, S. W., Cederberg, J. G., and Carroll, M. S. (2013). Empirical correlation for minority carrier lifetime to defect density profile in germanium on silicon grown by nanoscale interfacial engineering. *J. Vac. Sci. Technol. B Microelectron.* 31, 051201. doi:10.1116/1.4816488

Singh, H. P. (1968). Determination of thermal expansion of germanium, rhodium and iridium by x-rays. *Acta Crystallogr. A* 24, 469–471. doi:10.1107/S056773946800094X

Sproul, A. B. (1994). Dimensionless solution of the equation describing the effect of surface recombination on carrier decay in semiconductors. *J. Appl. Phys.* 76, 2851. doi:10.1063/1.357521

Steger, M., Yang, A., Sekiguchi, T., Saeedi, K., Thewalt, M. L. W., Henry, M. O., et al. (2011). Photoluminescence of deep defects involving transition metals i Si: new insights from highly enriched ^{28}Si. *J. Appl. Phys.* 110, 081301. doi:10.1063/1.3651774

Süess, M. J., Geiger, R., Minamisawa, R. A., Schiefler, G., Frigerio, J., Chrastina, D., et al. (2013). Analysis of enhanced light emission from highly strained germanium microbridges. *Nat. Photonics* 7, 466–472. doi:10.1038/nphoton.2013.67

Sukhdeo, D. S., Nam, D., Kang, J. H., Brongersma, M. L., and Saraswat, K. C. (2014). Direct bandgap germanium-on-silicon inferred from 5.7% <100> uniaxial tensile strain. *Photon. Res.* 2, A8–A13. doi:10.1364/PRJ.2.0000A8

Sumikura, H., Kuramochi, E., Taniyama, H., and Notomi, M. (2014). Ultrafast spontaneous emission of copper-doped silicon enhanced by an optical nanocavity. *Sci. Rep.* 4, 5040. doi:10.1038/srep05040

Suwa, Y., and Saito, S. (2009). Intrinsic optical gain of ultrathin silicon quantum wells from first-principles calculations. *Phys. Rev. B* 79, 233308. doi:10.1103/PhysRevB.79.233308

Suwa, Y., and Saito, S. (2010). "First-principles study of light emisson from germanium guantum-well," in *IEEE 22nd Int. Semiconductor Laser Conference (ISLC)*, Kyoto, 131–132.

Suwa, Y., and Saito, S. (2011). "First-principles study of light emission from silicon and germanium due to direct transitions," in *IEEE 8th Int. Conf. Group IV Photonics*, London, 222–224.

Sze, S. M., and Lee, M. K. (2012). *Semiconductor Devices: Physics and Technology*, 3rd Edn. Singapore: John Wiley and Sons.

Tani, K., Oda, K., Kasai, J., Okumura, T., Mine, T., Saito, S., et al. (2013a). "Germanium waveguides on lateral silicon-on-insulator diodes for monolithic light emitters and photo detectors," in *Group IV Photonics (GFP), IEEE 10th International Conference* (Seoul: IEEE), 134–135.

Tani, K., Oda, K., Okumura, T., Takezaki, T., Kasai, J., Mine, T., et al. (2013b). "Enhanced electroluminescence from germanium waveguides by local tensile strain with silicon nitride stressors," in *International Conference on Solid State Devices and Materials (SSDM)* (Fukuoka: SSDM), K–6–3.

Tani, K., Saito, S., Oda, K., Miura, M., Mine, T., Sugawara, T., et al. (2011). "Ge(111)-fin light-emitting diodes," in *IEEE 8th Int. Conf. Group IV Photonics*, London, 217–219.

Tani, K., Saito, S., Oda, S., Okumura, T., Mine, T., and Ido, T. (2012). "Lateral carrier injection to germanium for monolithic light sources," in *Group IV Photonics (GFP), IEEE 9th Int. Conf*, San Diego, 328–330.

Taur, Y., and Ning, T. H. (2013). *Fundamentals of Modern VLSI Devices*, 2nd Edn. Cambridge: Cambridge University Press.

Tezuka, T., Toyoda, E., Irisawa, T., Hirashita, N., Moriyama, Y., Sugiyama, N., et al. (2009). Structural analyses of strained SiGe wires formed by hydrogen thermal etching and Ge-condensation processes. *Appl. Phys. Lett.* 94, 081910. doi:10.1063/1.3086884

Tseng, C.-K., Chen, W.-T., Chen, K.-H., Liu, H.-D., Kang, Y., Na, N., et al. (2013). A self-assembled microbonded germanium/silicon heterojunction photodiode for 25 Gb/s high-speed optical interconnects. *Sci. Rep.* 3, 3225. doi:10.1038/srep03225

Tweet, D. J., Lee, J. J., Maa, J.-S., and Hsu, S. T. (2005). Characterization and reduction of twist in Ge on insulator produced by localized liquid phase epitaxy. *Appl. Phys. Lett.* 87, 141908. doi:10.1063/1.2077860

Uchida, K., and Takagi, S. (2003). Carrier scattering induced by thickness fluctuation of silicon-on-insulator film in ultrathin-body metal–oxide–semiconductor field-effect transistors. *Appl. Phys. Lett.* 82, 2916. doi:10.1063/1.1571227

Ujihara, K. (1995). "Effects of atomic broadening on spontaneous emission in an optical microcavity," in *Spontaneous Emission and Laser Oscillation in Microcavities*, eds H. Yokoyama and K. Ujihara (Boca Raton, FL: CRC Press), 81–107.

Urino, Y., Horikawa, T., Nakamura, T., and Arakawa, Y. (2013). "High density optical interconnects integrated with lasers, optical modulators and photodetectors on a single silicon chip," in *Optical Fiber Communication Conference (OFC)*, (Anaheim: OSA), OM2J.

Vanderbilt, D. (1990). Soft self-consistent pseudopotentials in a generalized eigenvalue formalism. *Phys. Rev. B* 41, 7892(R). doi:10.1103/PhysRevB.41.7892

Virgilio, M., Manganelli, C. L., Grosso, G., Pizzi, G., and Capellini, G. (2013a). Radiative recombination and optical gain spectra in biaxially strained *n*-type germanium. *Phys. Rev. B* 87, 235313. doi:10.1103/PhysRevB.87.235313

Virgilio, M., Manganelli, C. L., Grosso, G., Schroeder, T., and Capellini, G. (2013b). Photoluminescence, recombination rate, and gain spectra in optically excited *n*-type and tensile strained germanium layers. *J. Appl. Phys.* 114, 243102. doi:10.1063/1.4849855

Vivien, L., and Pavesi, L. (eds) (2013). *Handbook of Silicon Photonics*. Taylor and Francis.

Wada, K., Liu, J., Jongthammanurak, S., Cannon, D. D., Danielson, D. T., Ahn, D., et al. (2006). *Si Microphotonics for Optical Interconnection*. Berlin: Springer Verlag.

Wale, M. (2008). "Photonic integration – an industrial perspective," in *European Photonic Integration Forum* (Brussels: European Photonics Integration Forum).

Wang, X., Li, H., Camacho-Aguilera, R., Cai, Y., Kimerling, L. C., Michel, J., et al. (2013). Infrared absorption of *n*-type tensile-strained Ge-on-Si. *Opt. Lett.* 38, 652–654. doi:10.1364/OL.38.000652

Wang, Y., Zhang, J., Wu, Y., An, J., Li, J., Wang, H., et al. (2012). Light emission enhancement from Er-doped silicon photonic crystal double-heterostructure microcavity. *IEEE Photon. Technol. Lett.* 24, 1041–1135. doi:10.1109/LPT.2011.2173183

Wieder, H. H., Clawson, A. R., and McWilliams, G. E. (1977). $In_xGa_{1-x}As_yP_{1-y}$/InP heterojunction photodiodes. *Appl. Phys. Lett.* 31, 468. doi:10.1063/1.89718

Zelsmann, M., Picard, E., Charvolin, T., Hadji, E., Heitzmann, M., Dalzotto, B., et al. (2003). Seventy-fold enhancement of light extraction from a defectless photonic crystal made on silicon-on-insulator. *Appl. Phys. Lett.* 83, 2542–2544. doi:10.1063/1.1614832

Zimmermann, H. (2000). *Integrated Silicon Opto-Electronics*. Berlin: Springer.

Conflict of Interest Statement: The authors declare that the research was conducted in the absence of any commercial or financial relationships that could be construed as a potential conflict of interest.

Received: 12 June 2014; paper pending published: 28 July 2014; accepted: 29 August 2014; published online: 17 September 2014.

*Citation: Saito S, Gardes FY, Al-Attili AZ, Tani K, Oda K, Suwa Y, Ido T, Ishikawa Y, Kako S, Iwamoto S and Arakawa Y (2014) Group IV light sources to enable the convergence of photonics and electronics. Front. Mater. **1**:15. doi: 10.3389/fmats.2014.00015*

This article was submitted to Optics and Photonics, a section of the journal Frontiers in Materials.

frontiers in Materials

REVIEW
published: 15 July 2015
doi: 10.3389/fmats.2015.00052

Group IV direct band gap photonics: methods, challenges, and opportunities

*Richard Geiger, Thomas Zabel and Hans Sigg**

Laboratory for Micro- and Nanotechnology, Paul Scherrer Institut, Villigen, Switzerland

The concept of direct band gap group IV materials may offer a paradigm change for Si-photonics concerning the monolithic implementation of light emitters: the idea is to integrate fully compatible group IV materials with equally favorable optical properties as the chemically incompatible group III–V-based systems. The concept involves either mechanically applied strain on Ge or alloying of Ge with Sn, which permits to drastically improve the radiative efficiency of Ge. The favorable optical properties result from a modified band structure transformed from an indirect to a direct one. The first demonstration of such a direct band gap laser has recently been accomplished in GeSn. This demonstration proves the capability of this new concept, which may permit a qualitative as well as a quantitative expansion of Si-photonics in not only traditional but also new areas of applications. This review aims to discuss the challenges along this path in terms of fabrication, characterization, and fundamental understanding, and will elaborate on evoking opportunities of this new class of group IV-based laser materials.

Keywords: Si photonics, germanium, strain, GeSn, direct band gap, laser

OPEN ACCESS

Edited by:
Koji Yamada, National Institute of Advanced Industrial Science and Technology, Japan

Reviewed by:
Shinichi Saito, University of Southampton, UK
Krishna C. Saraswat, Stanford University, USA

***Correspondence:**
Hans Sigg, Laboratory for Micro- and Nanotechnology, Paul Scherrer Institut, Villigen PSI, CH 5232, Switzerland
hans.sigg@psi.ch

Specialty section:
This article was submitted to Optics and Photonics, a section of the journal Frontiers in Materials

Received: *13 May 2015*
Accepted: *29 June 2015*
Published: *15 July 2015*

Citation:
Geiger R, Zabel T and Sigg H (2015) Group IV direct band gap photonics: methods, challenges, and opportunities. Front. Mater. 2:52. doi: 10.3389/fmats.2015.00052

Introduction

The Si-based optical platform is rapidly changing the landscape of photonics by offering powerful solutions, for example, for data links (Miller, 2010) and sensing (Passaro et al., 2012) to name only two out of many. This development has taken place in spite of the fact that Si itself is a poor emitter of light. This is without a doubt due to the fact that Si technology as used in very large-scale integration (VLSI) and complementary metal-oxide-semiconductor (CMOS) technology is extremely mature and advanced. This fact seemingly compensates for the shortfalls in concepts for Si to generate light.

Nowadays, group III–V materials are implemented to integrate active light sources onto the Si platform by using involved coupling schemes and/or heterogeneous integration (Fang et al., 2013). However, because these materials are chemically intolerant to Si, their integration bears a lot of burdens, which raises the fabrication costs. Strongly preferred are materials that are compatible to Si, tolerated by the technology (preferentially CMOS), and capable of producing light similar in efficiency to traditional group III–V semiconductor systems.

In direct band gap systems, light generation is based on radiative recombination of electrons and holes, both with practically the same momentum as schematically shown in **Figure 1A**. In unstrained, i.e., "regular" bulk Ge, however, the excited electrons will preferentially occupy the lower conduction band energy states of the L-valley. In Ge, the momentum of the electrons does, thus, not match those of the holes, which occupy the degenerated heavy- and light-mass valence bands at the Γ-point (c.f. **Figure 1B**). The appearing momentum mismatch requires a phonon for the recombination. But note that except the position of the indirect L-valley, which is in Ge 140 meV below the Γ valley minimum, the band alignments near the Γ-point in system A (say InGaAs, one of the most prominent group III–V systems used for lasing) and B are very similar. To achieve the favorable direct recombination

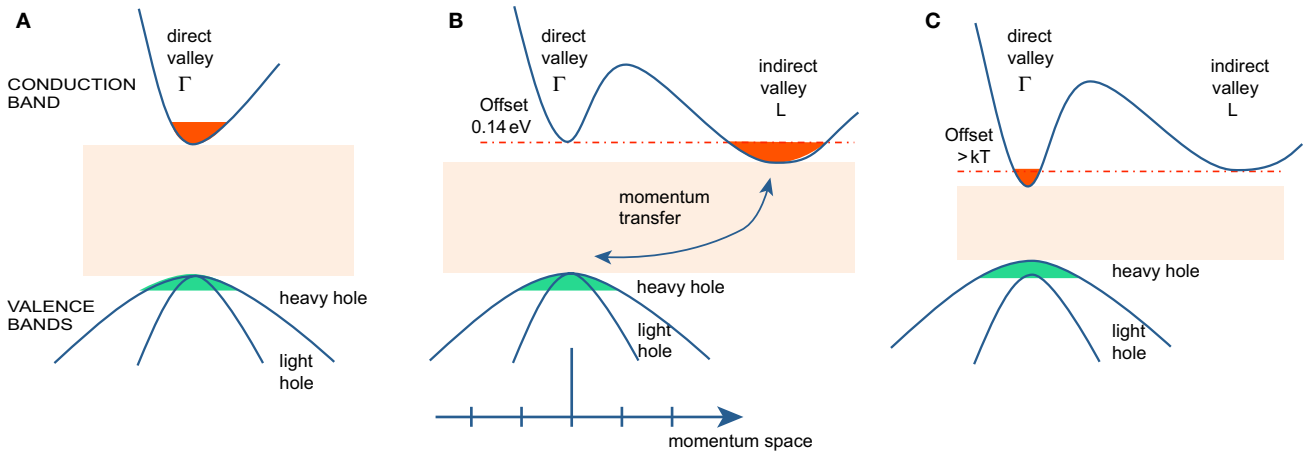

FIGURE 1 | Band structure in momentum space (A) direct band gap semiconductor. Electron/hole recombination occurs at the Γ-point. **(B)** Unstrained Ge. Electrons occupy the conduction band states of the L-valleys. Radiative recombination is hindered by the momentum mismatch. **(C)** Due to strain (or alloying with Sn), the band gap of Ge (GeSn) shrinks and the population of electrons at the Γ-point increases.

condition also for Ge, we need to find a way to inject electrons into that conduction band valley with its energetic minimum at the Γ-point. This is realized in the most straightforward fashion when all unwanted electron levels are energetically shifted above the Γ-states, which is equivalent to transfer the system from a fundamentally indirect to a fundamentally direct one.

We will discuss the two methods that make this conversion possible. One involves the application of tensile strain, while the second approach relies on alloying Ge with Sn. Thus, the obtained band alignments are depicted in **Figure 1C**. With either one of the methods, the Γ-valley can be reduced below the indirect one at L enabling efficient carrier injection into the Γ-valley. Moreover, the VB degeneracy is lifted depending on the strain state and its loading, biaxial or uniaxial, c.f. Section "Modeling" for more details.

In **Figure 2**, we show the state-of-the-art of the strain and alloying approach toward the realization of a direct band gap group IV material. For our discussion, we selected those approaches that are potentially compatible with CMOS fabrication and are suited for optical applications. Very thin membranes (Sánchez-Pérez et al., 2011), nanowires clamped in bulky mechanical strain apparatus (Greil et al., 2012), Ge bulk layers on III–V substrates (Huo et al., 2011), etc., are not considered here because they are unpractical for integration on Si. Not considered either is light emission from Si-based quantum wells and defects; for a recent review, see Saito et al. (2014). In our compilation, **Figure 2**, we benchmark the two strain loadings (uniaxial and biaxial) and Sn alloy composition against the achieved relative band offset, $\Delta E/E_0$, where an offset ΔE of 100% is equal to $E_0 \sim 140$ meV for the case of unstrained Ge. An offset parameter of 0 meV (0%) corresponds, thus, to Γ- and L-valleys having their band edges at the same energy.

The black arrow on the left hand side of the second line in **Figure 2** marks the case of highly *n*-doped Ge (Liu et al., 2010), where a maximum of 0.25% biaxial strain is accomplished. This value of 0.25% is the one typically obtained from direct epitaxy of Ge on Si. It arises due to the difference between the thermal expansion coefficients of Si and Ge (Michel et al., 2010). High *n*-doping

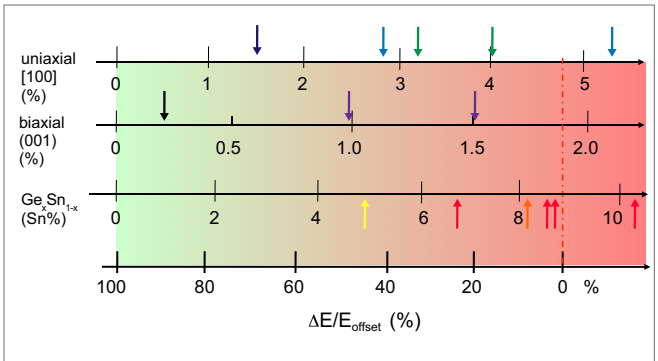

FIGURE 2 | Relative offset of the Γ- and L-conduction band minima realized in Ge either by uniaxial tensile strain along [100] direction [dark blue: (Capellini et al., 2013), light blue: (Nam et al., 2013; Sukhdeo et al., 2014), olive: (Süess et al., 2013; Geiger et al., 2014c)], biaxial tensile strain on (001) oriented substrate [black: (Liu et al., 2010); violet: (Ghrib et al., 2013, 2015)] or by alloying with Sn [yellow: (Chen et al., 2013a); orange (Gupta et al., 2013b); red: (Wirths et al., 2015)]. The shown offset versus Sn concentration relates to the unstrained case. About 100% (0%) offset refers to 140 meV (vanishing energy offset). Hence, the dash-dotted line marks the transition from an indirect to a direct band gap semiconductor.

is introduced to fill the parasitic indirect states (Xiaochen et al., 2010). Such doping does not transform the material into a direct gap system, but it appeared that under optical excitation and electrical pumping the light emission shows an intensity threshold as well as linewidth narrowing (Liu et al., 2010; Camacho-Aguilera et al., 2012). These results became widely known as the optically and electrically pumped Ge-laser. However, since the time when these announcements were made in 2010 and 2012, only one other demonstration of these effects has been reported so far (Koerner et al., 2015). This very recent and only result concerns a Ge diode structure with an unstrained active region doped at 3×10^{19} cm^{-3}. The obtained emission spectra are similar to the one from the original work from the MIT group. However, as we will show

below, these spectra significantly differ in several aspects – the intensity, the linewidth, and the Fabry–Perot (FP) multi-mode behavior – from those obtained with the here discussed direct band gap lasers. Moreover, as will be discussed in Section "Lifetime, Gain, and Loss," these Ge-lasing observations are contradicted by gain experiments (Carroll et al., 2012) as well as by theoretical analysis performed by several groups (Liu et al., 2007; Chow, 2012; Dutt et al., 2012; Peschka et al., 2015) when the lasing current density threshold is calculated using realistic non-radiative lifetimes (Geiger et al., 2014a). As the experimental foundation for understanding this peculiar threshold behavior of low strained (and in one case even unstrained) Ge is ambiguous, we will focus here on reports concerning direct band gap group IV systems, which includes the first unmistakable proof of interband lasing in a group IV system. Without doubt, with the advent of direct band gap systems showing unambiguous lasing, an excellent opportunity is created, which will help to unravel in the very near future above raised questions regarding the lasing in highly *n*-doped Ge.

Coming back to **Figure 2**: the arrows colored in violet depict 1.0 and 1.5% biaxially tensilely strained structures that have been achieved via deposition of Si–Nitride (SiN) stressor layers (Ghrib et al., 2013, 2015). This strain is equivalent to a band offset of ~70 and 30 meV, which corresponds to 50 and 30% of the unstrained band offset value, respectively. So far, the highest strain values are obtained in suspended microbridges under uniaxial loading as is shown on the top stroke. There, the ~0.25% biaxial prestrain is enhanced and transformed into uniaxial strain. The arrows in olive (Süess et al., 2013; Geiger et al., 2014c) and blue (Nam et al., 2013; Sukhdeo et al., 2014) mark recent achievements from the two leading groups. The latest result (Sukhdeo et al., 2014) indicates that the bridge technology can indeed provide direct band gap strained Ge. SiN stressor layers on suspended microbridges or FP cavities deliver far less strain and offset reductions (Capellini et al., 2013, 2014). As shown by the red arrows on the third stroke, alloying Ge with Sn also provides optical group IV material with a fundamental direct band gap. The transition from fundamental indirect to direct occurs at a Sn concentration of ~9% for relaxed GeSn. Depending on the strain loading, i.e., tensile or compressive, the crossover shifts to a higher or lower Sn concentration. Hence, a 20-nm thick GeSn layer with 8% Sn sandwiched between Ge claddings and processed into microdisks is not as close to the direct transition as a relaxed layer with 6% Sn because of the −1% biaxial compressive loading (Chen et al., 2013a). The GeSn alloy above the crossover in **Figure 2** exhibits 0.7% in-plane strain at a Sn concentration of 13%. This system shows lasing at low temperature (Wirths et al., 2015). We will present this recent result and will, thereby, clarify the characteristic of the experimental observation of lasing.

The availability of direct band gap group IV semiconductors as compiled in **Figure 2**, together with the rise of promising results, in particular, the demonstration of lasing in the GeSn system, has motivated the writing of this review. It is meant to present the current understanding evoked from the research undertaken at many places worldwide. Although some of the following descriptions are exemplified for only one of the systems (strain or Sn alloying), we will argue that the physics of this two direct gap systems can be understood by analogy. By merely emphasizing the similarities of the physics and the characterization methods used for investigations, we hope to provide a comprehensive overview that will support and interest many scientists to enter this highly relevant field of research.

In Section "Direct Band Gap Group IV Materials," the band structure in Ge is given in dependence of strain. We then summarize the fabrication steps for strain engineering and Sn alloying. In Section "Characterization Methods: Optical Properties," several optical characterization methods are introduced, such as pump and probe spectroscopy developed for this very purpose at the infrared beamline of the Swiss light source (SLS). Gain and loss studies performed on Ge layers as well as carrier lifetime measurements are shown in Section "Lifetime, Gain, and Loss." These results impact the discussion on lasing in *n*-doped Ge, which is briefly repeated to exemplify the capability of these experimental methods. The analysis of temperature-dependent photoluminescence (PL) is found to deliver a quantitative measure for the directness of GeSn layers, shown in Section "Photoluminescence – Direct Band Gap," and narrow emission spectra together with an intensity versus excitation-threshold represent the first observation of lasing in a direct band gap group IV system, shown in Section "Optically Pumped Laser." Investigation challenges, such as the quantitative analysis of the Auger recombination and the carrier transport, are appointed in Section "Challenges" together with other fundamental device-related issues, such as cavity design, band gap renormalization, and thermal budgets for alloys. We speculate about the opportunities for Si photonics offered by an efficient monolithically integrated laser source in Section "Opportunities," and furthermore discuss the prospect of a Ge and/or GeSn electro-optical data processing platform. We conclude in Section "Conclusion and Outlook" and give a short outlook.

Direct Band Gap Group IV Materials

Modeling

Band Structure

The effect of tensile strain on Ge's band edges shown in **Figure 3** illustrates the path of the transitions' energies going from an indirect to a direct band gap system. The energies for interband- (solid lines) and intervalence-band transitions (broken lines) between the respective conduction- and valence-band edges are calculated via deformation potential theory as implemented in the nextnano® modeling software (Birner et al., 2007). Due to the fact that the Γ-valley energy reduces faster than the one of the L-valley, Ge transforms into a direct band gap semiconductor at ~4.7% uniaxial strain along [100] when the direct transition (black line) decreases below the energy of the indirect recombination (green line). For Ge under biaxial tensile strain or GeSn alloys, the band edges behave similarly with an indirect-to-direct band gap crossover at ~1.6–2.0% strain (El Kurdi et al., 2010; Virgilio et al., 2013; Wen and Bellotti, 2015) or and at a Sn-content of ~9% (Low et al., 2012; Gupta et al., 2013b; Wirths et al., 2015) for a fully relaxed layer.

In the valence band, strain lifts the degeneracy of light hole and heavy hole bands and introduces a mixing such that this distinction becomes meaningless, especially under high strain. For low strain, VB1 and VB2 in **Figure 3** are mostly "heavy hole"- and

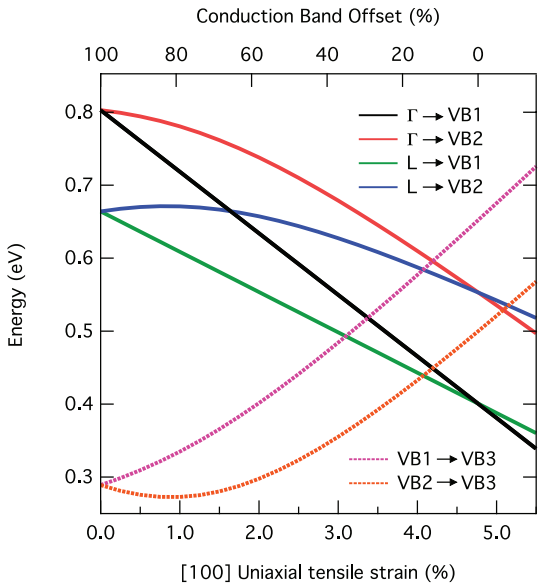

FIGURE 3 | Transition energies between the direct and indirect conduction band valleys and the two top valence bands and within the valence band of uniaxially, tensilely stressed Ge. For a strain of ~4.7%, the conduction band minimum at the Γ-point reaches a lower energy than the indirect L-valleys. The upper *x*-axis denotes the offset between the Γ- and L-band edges in relative units.

"light hole"-like, respectively. VB3 refers to the split-off band. The energetic order of the heavy and light hole bands is reverted when moving from the uniaxial to the biaxial case.

Most of the theoretical work concerning Ge light emission utilizes $k \cdot p$ theory including 6 bands (Aldaghri et al., 2012; Chang and Cheng, 2013; Virgilio et al., 2013), 8 bands (Zhu et al., 2010; Wirths et al., 2013b), or 30 bands (El Kurdi et al., 2010). The latter is not restricted to the Brillouin-zone center but describes the full energy dispersion. In other works, the empirical pseudopotential method (Dutt et al., 2013; Wen and Bellotti, 2015), density functional theory (Tahini et al., 2012), and the tight-binding model (Dutt et al., 2012) are employed. The agreement between the models is generally found to be satisfactory.

Gain

In **Figure 4**, we show gain calculations for uniaxially stressed Ge in dependence of *n*-type doping and conduction band offset (c.f. the scale of the upper *x*-axis in **Figure 3**). The band structure was computed with an 8-band $k \cdot p$ approach (Birner et al., 2007). The gain was calculated via Fermi's golden rule, assuming cylindrical symmetry for the valence bands to simplify the calculation of the joint density of states (JDOS), c.f. Virgilio et al. (2013). More details of the calculation can be found in Süess et al. (2013), supplementary information. The peak gain at room temperature (RT) is plotted after subtraction of the loss following the experimentally determined electron- and hole-absorption cross-sections from Carroll et al. (2012) (Süess et al., 2013). The black, broken line indicates when transparency is reached. As an example, for a system at the crossover to a direct band gap system, transparency is nearly reached at a low injection of 1×10^{18} cm^{-3} as depicted in **Figure 4A**. Applying a moderate doping of 1×10^{19} cm^{-3} results in a gain of >500 cm^{-1}, which is sufficient to overcome typical resonator losses. When the doping level is increased to 2×10^{19} cm^{-3}, the gain approximately triples to ~1500 cm^{-1} according to our model. This suggests that *n*-doping is a very effective method to promote high gain for correspondingly low excitation in direct band gap systems. This is due to the fact that as long as the offset is not much larger than kT (Sukhdeo et al., 2014), electrons will nevertheless spread into the L-band from where they cannot contribute to gain.

Transparency can also be achieved for an undoped and still indirect, strained Ge system under higher excitation. We obtain transparency at an injection of 1×10^{19} cm^{-3} for a system with a remaining offset of 25% (35 meV) and an *n*-doping level below 1×10^{18}cm^{-3} (see **Figure 4B**). When the direct band gap is reached (0% offset), the net gain amounts to 1000 cm^{-1}, which can be increased up to 2000 cm^{-1} at a doping of 2×10^{19} cm^{-3}. In contrast to the indirect band gap Ge, a reduction in temperature helps to increase the gain as soon as the Γ valley constitutes the lowest conduction band energy due to condensation of the carriers into the direct gap states. For example, an intrinsic direct band gap Ge system with 25 meV band offset exhibits a net gain of the order of 4500 cm^{-1} at a temperature of 20 K and an injection of 1×10^{19} cm^{-3} compared to 1700 cm^{-1} at RT.

When comparing gain predictions in literature, we experience larger differences than between predictions of energy levels and their relative positions. The reason for this stems from the uncertainty in the loss. For weakly strained and relaxed Ge, experimental values are available as discussed in Section "Lifetime, Gain, and Loss." Hence, the overall agreement of the predictions is largely coherent. For example, calculations consistently predict gain for Ge with a large offset (80%) only for the case of very high doping of $>5 \times 10^{19}$ cm^{-3}. For strained and alloyed systems, however, the interband energies approach the one of the intervalence band transitions. The energies may even cross, as shown in **Figure 3**. Hence, loss processes related to these transitions will become critical. Furthermore, the gain as predicted by a Green's functional approach (Wen and Bellotti, 2015) tend to be smaller than the commonly used joint density of state formalism as applied for **Figure 4**.

Fabrication

Microbridges

Strain engineering is nowadays a standard tool in microelectronics to improve device performance, where the lattice mismatch between Si and Ge is used to generate strain via epitaxy. However, the pseudomorphic deposition of Ge on Si leads to compressive strain, which deteriorates the light emission efficiency and is, furthermore, limited to small layer thicknesses. Therefore, the main method used to introduce strain is the application of external stressor layers, such as silicon nitride (SiN), which is compatible with CMOS processing. Some work following this approach includes the deposition of stressors on the back side of Ge membranes (Nam et al., 2011, 2012), on micropillars (Velha et al., 2013), or on selectively grown Ge (Oda et al., 2013).

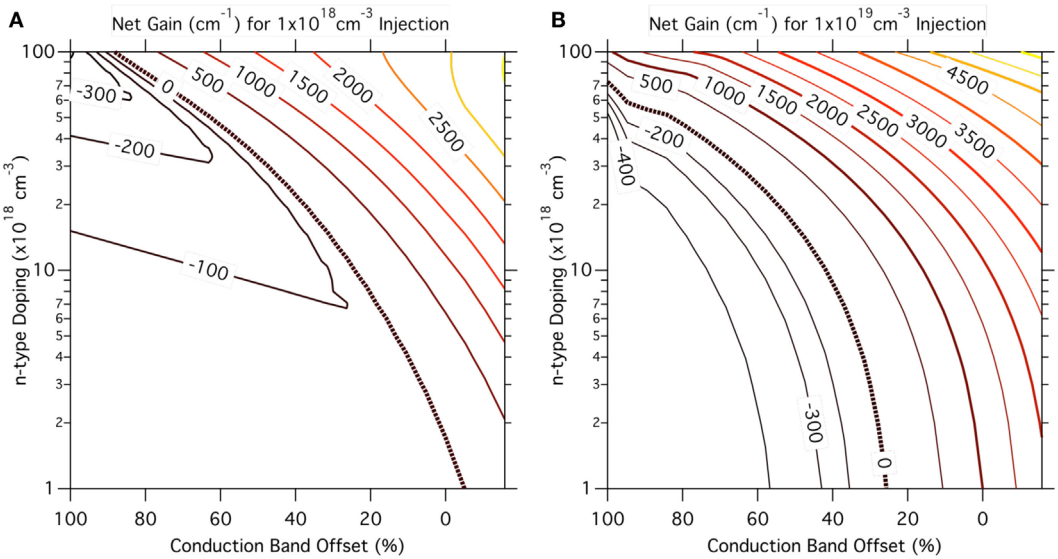

FIGURE 4 | Maximum net gain at room temperature for uniaxially stressed Ge in dependence of *n*-type doping and conduction band offset. An 8-band *k·p* model was employed to calculate the band structure parameters. The map is calculated for a carrier injection of **(A)** 1×10^{18} cm^{-3} and **(B)** 1×10^{19} cm^{-3}. The black, broken line depicts the transparency condition when the gain equals the losses.

An advantage of using external stressor layers is the simplicity to combine the strain transfer with standard cavity structures like FP waveguides (Capellini et al., 2014). However, the achieved strain is so far limited to a predominantly uniaxial strain of 1.5%. In other efforts, SiN layers were deposited on Ge microdisks, resulting in a biaxial strain of 1.0% (Ghrib et al., 2013) and 1.5% (Ghrib et al., 2015). However, these stressor layer approaches suffer from a large strain inhomogeneity across the Ge layer, and elaborated all-around stressor techniques using wafer transfer and bonding. These results are included in **Figure 2**.

Following a different route, it was shown that high levels of tensile strain can be locally induced without the use of any external stressor layers (Minamisawa et al., 2012; Süess et al., 2013). In the approach by Süess et al., the starting substrate is the commonly used tensilely strained Ge layer with a biaxial strain of ~0.2%. Subsequently, the layer is patterned into a microbridge with a narrow central cross-section (the "constriction") and larger outer cross-sections (the "pads") as shown in **Figures 5A,B**. As last processing step, the structure is underetched by selectively removing the underlying buried oxide with hydrofluoric acid, c.f. **Figure 5C**. Releasing the structure leads to a relaxation of the strain in the pads, which in turn increases the strain in the constriction. Due to Hooke's law and force balance, strain accumulated in the constriction will depend on the ratio of pad and constriction widths as well as the ratio between their lengths (Minamisawa et al., 2012; Süess et al., 2013). Hence, following this principle, any strain can be generated in the constriction by solely varying the geometrical parameters independent of the actual dimensions of the structure. In contrast to external stressors where the achievable strain is limited by the efficiency of strain transfer, this strain enhancement is only limited by the material strength. **Figure 5A** shows enhancement factors of more than 20× realized from 0.15% biaxial strain in Ge on Si (blue squares) or Ge on silicon-on-insulator (SOI) (green circles and red triangles) for bridges with varying geometrical dimensions. The agreement of the experimental values with the ones predicted by finite element modeling (red triangles) is excellent. For Ge on SOI, the highest strain achieved in 6 μm × 2 μm constrictions is 3.1%. When starting from 200 nm thick germanium-on-insulator substrates (GOI), which feature a significantly reduced dislocation density (Akatsu et al., 2006; Hartmann et al., 2010), a strain of 5.7% was observed in a 5.0 μm × 0.2 μm constriction (Sukhdeo et al., 2014). According to **Figures 2** and **3**, such a strain is by far sufficient to transform Ge into a direct band gap material showing the prospect of the strain-enhancement technique given a starting material with high-crystal quality.

GeSn Alloying

The epitaxial growth of GeSn alloys poses several challenges, such as a large lattice mismatch between α-Sn and Si (17%) or Ge (15%), and a low solid-solubility of <1%. Therefore, the fabrication of high quality and smooth epilayers was a demanding task for many years and the development of new growth processes to deposit GeSn under non-equilibrium conditions at low temperatures was required. Whereas the first attempts to grow GeSn alloys were based on molecular beam epitaxy (MBE) in 1980s and 1990s (Pukite et al., 1989; Harwit et al., 1990; Wegscheider et al., 1990; Fitzgerald et al., 1991; He and Atwater, 1997), device-grade GeSn epilayers could be synthesized since the early 2000s when the first chemical vapor deposition (CVD) processes were developed (Bauer et al., 2003).

Nowadays, several groups established growth processes for GeSn utilizing either MBE (Bratland et al., 2003; Chen et al., 2011a; Bhargava et al., 2013; Oehme et al., 2013) or CVD

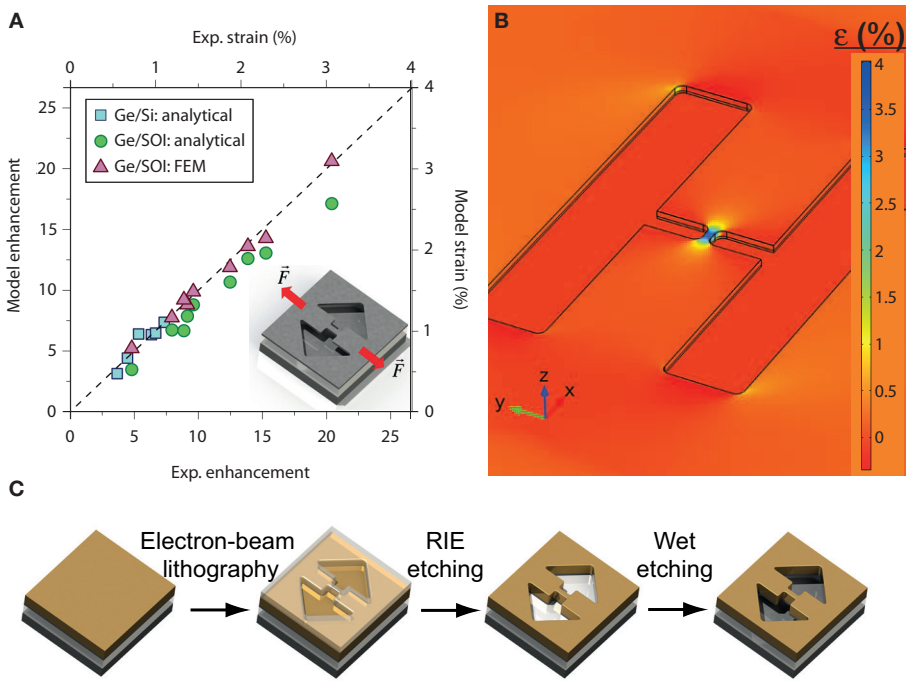

FIGURE 5 | Suspended microbridges from thermally pre-strained Ge. **(A)** Experimental and modeled strain for Ge microbridges fabricated on Si and SOI. The analytical strain-enhancement model is given in Süess et al. (2013). The enhancement of 22× corresponds to 3.1% uniaxial strain (Süess et al., 2013). **(B)** Strain profile of a suspended bridge structure as obtained by finite element modeling (FEM). Due to the relaxation in the pads, the strain in the central constriction is enhanced. **(C)** Process flow for the fabrication of suspended microbridges.

(Vincent et al., 2011; Chen et al., 2013b; Wirths et al., 2013a; Xu et al., 2013; Du et al., 2014) for a variety of applications, e.g., photodiodes, photodetectors, or MOSFETs. Here, due to the reduced lattice mismatch compared to Si, Ge is preferred as virtual substrate (VS) in order to ensure layers of high monocrystalline quality. Regarding the epitaxial growth of direct band gap GeSn alloys, nearly strain relaxed or even tensilely strained layers are highly desired, since for compressively strained GeSn layers, i.e., GeSn coherently grown on Ge VS, higher Sn contents are necessary for the indirect to direct transition (Gupta et al., 2013b). Owing to an advantageous relaxation mechanism for GeSn layers on Ge VS, dislocations seem to mostly protrude into the Ge VS rather than into the GeSn layer, which is beneficial for optical properties as the density of non-radiative recombination centers is reduced (Takeuchi et al., 2006; Senaratne et al., 2014; Wirths et al., 2015). Although relaxation takes place, a certain level of compressive biaxial strain (typically between −0.6 to −0.8%) remains nevertheless, which, as already said in connection with **Figure 2**, shifts the indirect-to-direct band gap crossover to higher Sn concentrations with respect to fully relaxed GeSn. Therefore, several approaches are being followed to reduce the compressive strain, such as growth on lattice-matched InGaAs VS (Chen et al., 2011a), which is not acceptable within a CMOS processing line, or deposition of ever thicker layers to enforce further strain relaxation (Senaratne et al., 2014; Wirths et al., 2015). Gupta et al. (2013b) introduced a robust etching approach enabling to selectively dry etch the Ge VS underneath the epitaxial GeSn layers. The authors envision their method to enable the fabrication of direct band gap GeSn micro disks.

Figures 6A–C show transmission electron microscopy images of a GeSn layer with 13% Sn grown via reduced pressure CVD on a Ge VS (Wirths et al., 2015). The advantageous relaxation mechanism mentioned above can be seen here with dislocation-loops (blue arrows) emitted into the Ge VS. Despite the high-Sn content, the thickness of the GeSn layer could be increased up to 560 nm without deteriorating the high-crystalline quality. Owing to the large thickness, a relaxation of 60% could be achieved such that only a mild compressive strain of −0.6% was present. As will be shown in Section "Photoluminescence – Direct Band Gap," this epilayer was proven to be a direct band gap group IV semiconductor that provides net gain and, hence, shows lasing under optical pumping.

We conclude this section on the fabrication of GeSn alloys by summarizing the list of beneficial assets GeSn epitaxy brings to the current Si technology facilitating future developments and integration. Apart from the prospect to fabricate a fundamental direct band gap group IV material, GeSn alloys are attractive because of (i) low-temperature deposition on Si(001) compatible with existing CMOS processes; (ii) strain relaxation with reasonably low threading dislocation density; (iii) available option for selective growth on silicon, which is attractive for photonic integration; (iv) GeSn/SiGeSn heterojunction layers to generate carrier confinement in quantum wells; (v) and therefore, tunability of the lattice constant offering opportunities to combine the alloys with the strained membrane method.

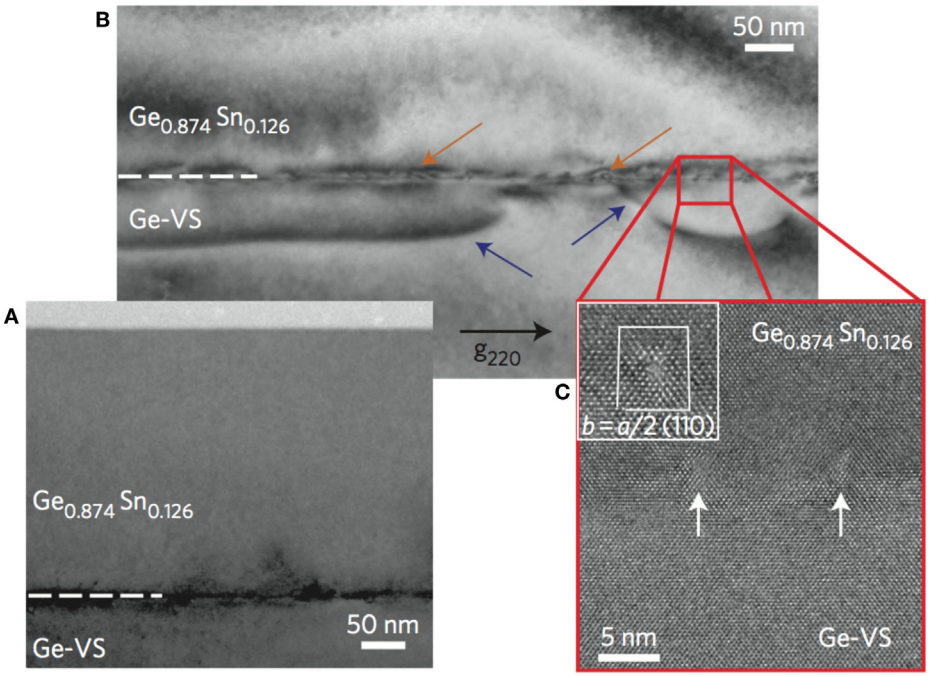

FIGURE 6 | Cross-sectional transmission electron microscopy (TEM) image of a $Ge_{0.87}Sn_{0.13}$ alloy. **(A)** Expanded view showing the high-crystalline quality of the GeSn epilayer. The defects are located near the interface to the Ge virtual substrate. **(B)** Dislocation-loops (blue arrows) emitted below the GeSn/Ge-interface (orange arrows) penetrating only into the Ge virtual substrate. **(C)** High-resolution TEM image of the interface used for Burgers vector calculations. Lomer dislocations with $b = a/2[110]$ are observed (Wirths et al., 2015).

Characterization Methods: Optical Properties

Lifetime, Gain, and Loss

When describing a material with regards to its suitability as an efficient laser source, key properties that decide upon adequacy are the gain and loss, i.e., the material's ability to amplify light, as well as the non-radiative lifetime, which determines the internal quantum efficiency as well as the achievable steady-state carrier density. These characteristics can be extracted in a direct way using broadband, time-resolved pump–probe transmission, and reflection spectroscopy. Possible ways for performing such experiments could be via tunable lasers or supercontinuum sources. However, particularly synchrotron-based infrared pump–probe spectroscopy has been shown to offer advantageous conditions for measuring the carrier density, their lifetime as well as gain and loss due to its extended bandwidth and suitable pulse lengths (Carroll et al., 2012; Geiger et al., 2014a,b). At the infrared beamline of the SLS, 100 ps long pulses of infrared light are supplied from the synchrotron and serve as broadband probe pulses, whereas the excess charge carriers are optically excited by a 100 ps Nd:YAG laser at 1064 nm (Carroll et al., 2011). The delay time between pump and probe pulses can be varied electronically, which offers the possibility to follow the dynamics of a system over a long time period by probing at different times after excitation. In the following, we review some of the pump–probe measurements performed at the SLS and give the most important results that challenge the interpretation of the Ge-lasing observations. We renarrate this discussion at the end of this chapter.

Figure 7A shows the mid-infrared reflection of a Ge layer grown on Si plotted as the ratio of pumped (R_P) and unpumped (R_U) reflection signal. The different colors depict different optical excitation strengths between 1 and 160 MW cm^{-2}. All of the spectra were taken for a pump–probe delay time of 250 ps. The distinct minimum observed in the spectra is attributed to the carriers' plasma frequency. For an increasing excitation power, the minimum shifts to higher energy and becomes at the same time more pronounced. As the plasma frequency shifts in first order proportional to the square root of the total amount of charge carriers in the system, such reflection measurements facilitate a convenient method for the quantitative determination of the carrier density. Thus, the extracted carrier concentration in dependence of the optical pump power for delay times of 0 and 250 ps is shown in the inset of **Figure 7A**. Moreover, by analyzing the carrier density at a fixed pump power for varying delay times, the reflection spectra can be used to extract the carrier decay times. In the case shown here, the carrier density drops to ~4×10^{19} cm^{-3} within 250 ps for all generated carrier concentrations larger than 4×10^{19} cm^{-3}. This behavior indicates an increasingly faster decay time at high-carrier concentrations, which is attributed to Auger recombination (Carroll et al., 2012).

While the analysis of mid-infrared reflection spectra enables to directly access charge carrier concentration and decay time, the latter can also be extracted from near-infrared transmission

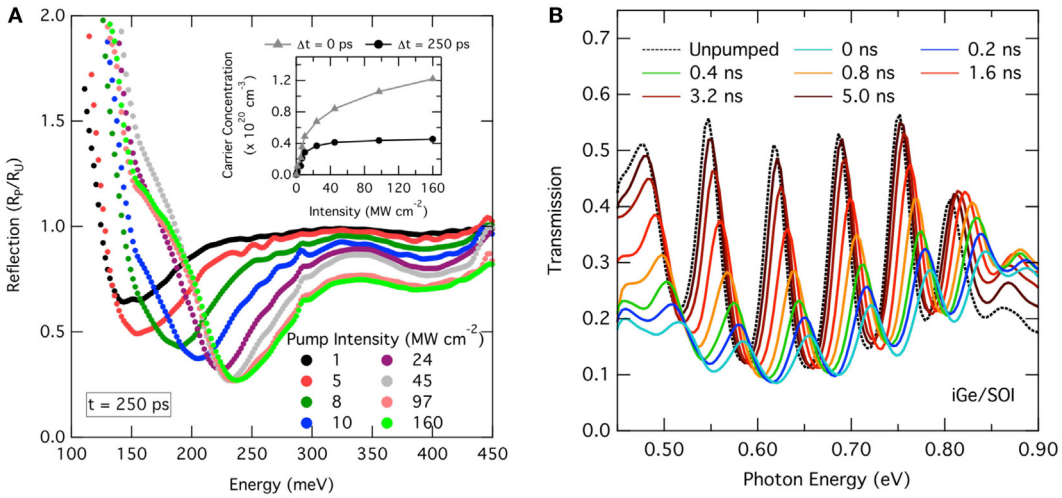

FIGURE 7 | Time-resolved infrared reflection and transmission spectroscopy: (A) mid-infrared reflection spectra of Ge on Si expressed as the ratio of pumped (R_P) and unpumped reflection (R_U) for varying excitation power at a pump–probe delay of 250 ps. The resonance in the spectra is attributed to the carrier plasma frequency, which enables to extract the total amount of charge carriers. The inset shows the carrier concentration for 0 and 250 ps delay time in dependence of the excitation power. **(B)** Normal-incidence pump–probe transmission spectra for Ge on SOI for varying delay times. Strong Fabry–Perot oscillations are observed from the thin film interference. Analyzing the peak-shifts facilitates the extraction of the decay time.

measurements. In **Figure 7B**, normal-incidence transmission spectra of intrinsic Ge are plotted, while the delay time between pump and probe is varied. As SOI is used as substrate, distinct FP oscillations are observed due to standing wave interferences between the Ge/air and Si/SiO_2 interfaces. For short delay times, the transmission is significantly reduced due to absorption. Above the direct band gap of ~0.8 eV, there is an increase compared to the unpumped transmission due to gain or bleaching. By following the shifts of the minima or maxima, the dynamics of the refractive index is obtained, which enables the extraction of the carriers' decay time. Compared to the decay time analysis from the mid-infrared reflection, the sensitivity to detect small carrier densities is higher in such a measurement because the refractive index – and, hence, the oscillation extrema – follows the carrier densities linearly, which enables to follow the decay processes within an extended time window.

In **Figure 8**, the time-dependent FP peak shifts are shown for differently prepared Ge layers. The shifts were normalized to unity at $t = 0$ ns and the decay fitted to an exponential curve (Geiger et al., 2014a). The defective Ge/Si interface was identified as the main non-radiative loss channel, as (i) Ge selectively grown via ultrahigh vacuum CVD (selGe in **Figure 8**) and a full epilayer grown via low-energy plasma-enhanced CVD (iGe in **Figure 8**) feature the same surface recombination velocity (SRV) – i.e., the carrier lifetime normalized to the layer thickness – of ~800 m s^{-1}, (ii) a built-in field introduced by modulation doping (nGe/iGe) increases the lifetime compared to iGe by keeping electrons away from the interface, and (iii) the longest lifetime was observed for an overgrown GOI wafer, where the defective Ge/Si interface is removed (SRV = 490 m s^{-1}). These results demonstrate the importance of engineering the material- and, in the case of Ge on Si, especially the interface quality to obtain a high-internal quantum efficiency and, thus, a low-threshold laser. Furthermore, similar pump–probe transmission studies on strained microbridges showed that neither strain, at least up to ~2%, nor processing affects the lifetime (Geiger et al., 2014b), indicating that a high-crystal quality can be maintained using the microbridge strain-enhancement technology.

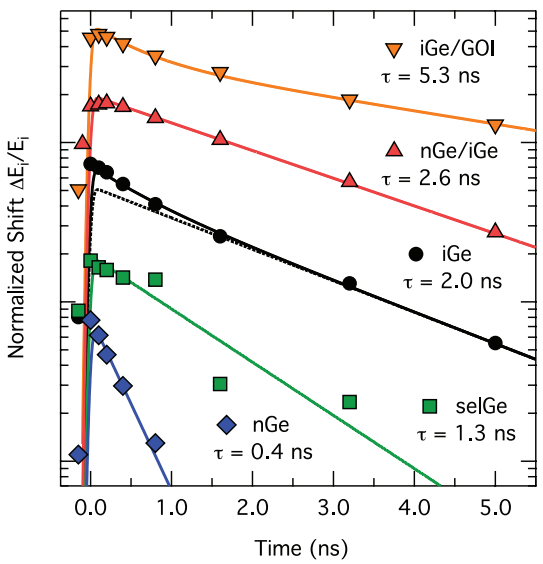

FIGURE 8 | Normalized peak shifts taken from normal-incidence transmission spectra (as, e.g., in Figure 6B) for a series of differently prepared Ge layers: iGe, nGe, selGe refers to intrinsic, *n*-doped, and selectively grown Ge, respectively. GOI refers to Ge on insulator. The non- radiative lifetime is obtained through an exponential fit to the data (Geiger et al., 2014a).

For the analysis of gain and loss, the transmission spectra should be recorded under the Brewster angle such that the obstructing FP resonances do not occur, c.f. **Figure 9A** for the case of unstrained Ge on Si for different pump–probe delay times. $\Delta t = 0$ ps refers to the maximum overlap between pump and probe and, hence, to the highest carrier density. The thick lines in blue and red show modeled transmission spectra for the unpumped and pumped case. Under excitation, a strong absorption occurs with a linear dependence on energy. At the direct band gap, the absorption gets reduced due to gain, but the gain is too small to generate a negative absorption and, hence, light amplification. This situation holds true for all other delay times, i.e., carrier concentrations, as well.

In **Figure 9B**, the situation for $\Delta t = 0$ ps is shown again in terms of the absorption coefficient with the modeled functions being plotted separately for (i) direct gap absorption before pumping (blue, thick line), (ii) direct gap absorption under excitation (red, thick line), and (iii) the featureless pump-induced absorption decreasing linearly in energy (red, thin line). Even though a gain of ~850 cm^{-1} is observed as displayed by a negative absorption, the loss from that spectrally distributed absorption at the same energy is >6000 cm^{-1} making light amplification impossible. To show the contrast to an established laser material featuring a direct band gap, the same absorption properties are plotted in **Figure 9C** for the case of InGaAs. Here, the pump-induced losses are independent on energy and amount to ~1000 cm^{-1}, which is compensated by a direct gap gain of ~1700 cm^{-1} such that a net gain of 700 cm^{-1} is revealed. We should mention here that the theoretical analysis of Carroll et al. (2012) has been questioned (Dutt et al., 2012) concerning the strength of the gain (red line, **Figure 9B**) but not the experiments, which clearly show that the loss is by far larger than the gain.

From the preceding analysis, it is clear that a solid understanding and consideration of the loss processes is required for an accurate description of gain in Ge. For illustration, the absorption cross-sections for three Ge samples (Ge#1: $N_d = 0$, $\varepsilon_{xx} = 0$; Ge#2: $N_d = 2.5 \times 10^{19}$ cm^{-3}, $\varepsilon_{xx} = 0$; Ge#3: $N_d = 0$, $\varepsilon_{xx} = 0.25\%$) are plotted in **Figure 10** in dependence of the total carrier density $N_T = N_d + N_P$, where N_d refers to the doping concentration and N_P to the pump-induced carrier density. As a comparison, the cross-sections of three InGaAs layers (InGaAs#1: $N_d = 0$, InGaAs#2: $N_d = 5.3 \times 10^{18}$ cm^{-3}; InGaAs#3: $N_d = 2.1 \times 10^{19}$ cm^{-3}) are plotted as well. Therefore, **Figure 10** reveals that the absorption scales predominantly with N_P indicating that the absorption cross-section from holes σ_h is much larger than the cross-section for electrons σ_e. Indeed, describing the absorption via a linearly dependent cross-section as $\alpha = \sigma_e N_e + \sigma_h N_h$ (where subscripts e and h refer to electrons and holes, respectively) offers a good representation of the experimental data with $\sigma_h/\sigma_e > 10$. The absorption cross-section for holes is significantly larger than for electrons, because in addition to the non-momentum conserving intraband or Drude-type free carrier absorption, the holes can undergo vertical intervalence band transitions (Newman and Tyler, 1957), which are hereby identified as the main loss channel in Ge. A similar conclusion concerning the cross-section ratio can be deduced from the InGaAs data shown in **Figure 10** in agreement with common knowledge for direct band gap lasing materials (Adams et al., 1980; Childs et al., 1986). Furthermore, the absolute values of the hole cross-section are in a similar range but larger for InGaAs than for Ge, c.f. **Figure 10**. However, the absorption is much higher in Ge due to a much larger total carrier density needed to achieve a gain like in the InGaAs sample.

Finally, we would like to relate the above presented data of gain and loss as well as of lifetimes in Ge layers on Si to the observation

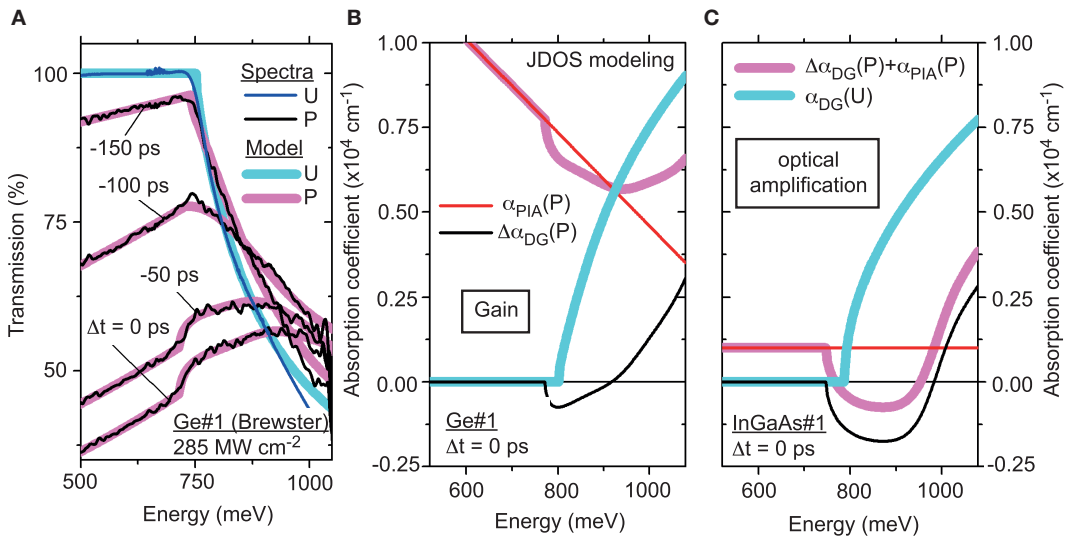

FIGURE 9 | Analysis of pump and probe measurements. **(A)** Transmission spectra for Ge on Si measured under Brewster angle for different delay times. **(B)** Modeled direct gap absorption unpumped (blue, thick line) and pumped (red, thick line) as well as pump-induced absorption (red, thin line) obtained from the spectra in **(A)** at 0 time delay. **(C)** Similar extraction of direct gap gain and losses for undoped InGaAs showing light amplification, as the gain surpasses the pump-induced losses (Carroll et al., 2012).

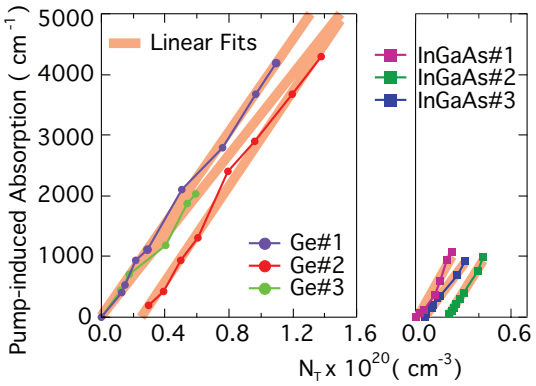

FIGURE 10 | Absorption coefficients for differently doped and strained Ge and InGaAs layers. The data are well described with a linear absorption cross-section model.

of lasing in highly *n*-doped and weakly strained Ge (Liu et al., 2010; Camacho-Aguilera et al., 2012), which was recently repeated at the University of Stuttgart with an unstrained, highly *n*-doped light emitting diode (LED) (Koerner et al., 2015). First, as is shown above by the gain and loss experiment (Carroll et al., 2011), the loss in Ge layers strongly exceeds the gain at all the investigated carrier densities up to 10^{20} cm^{-3} and in all investigated cases, i.e., Ge with and without weak strain and/or *n*-doping. Hence, Carroll's results are apparently in conflict with the observation of lasing (Liu et al., 2010) in similar but not identical material. Second, the non-radiative lifetimes, which have been determined for such Ge layers only recently by Geiger et al. (2014a), c.f **Figure 8**, shine a new light on previous and recent gain and threshold current density calculations (Dutt et al., 2012; Peschka et al., 2015). Using the obtained carrier lifetime of the order of 1–2 ns for threshold current estimates, the calculated threshold of the order of 100 kA cm^{-2} – obtained by assuming a lifetime of 100 ns – needs to be rescaled by a factor of 50–100. Surely, such a current density is above the material's limit and also exceeds the observed threshold values by ~2 orders of magnitude. Therefore, not only the gain/loss experiments but also the theory (when fed with properly valued parameters) shows that more research is needed to understand the MIT results. The recent paper by the Stuttgart group (Koerner et al., 2015) may give the directions for further thinking: a "lasing" threshold was reached only shortly before their devices failed, hinting at a carrier breakthrough. The heat pulse related to the breakthrough may have caused the peaked emission signal.

Photoluminescence – Direct Band Gap

Photoluminescence spectroscopy offers a convenient tool for probing the changes of the electronic band structure induced via strain or Sn alloying. As shown in **Figure 11A**, the reduced offset between Γ- and L-valleys manifests in an increased emission intensity of the PL signal (Süess et al., 2013). A similar effect has also been observed by Chen et al. (2011a).

A quantitative analysis of the relative alignment between Γ- and L can be obtained from the temperature dependence of the PL, as has been demonstrated recently in Wirths et al. (2015). In **Figure 11B**, the temperature-dependent PL intensity for a set of samples with Sn content from 8 to 13% is shown. The data have been normalized to unity at 300 K. For the sample with the lowest Sn content, a rapid drop in intensity on lowering the temperature is observed, whereas for the three other samples a steady increase in intensity can be seen with the intensity increase being dependent on the Sn concentration. Qualitatively, the increase from sample to sample can be explained by the reduced conduction band offset with increasing Sn, whereas cooling down leads to a condensation of the carriers into the lowest energy states such that the direct gap emission either vanishes for indirect band gap materials as sample $Ge_{0.92}Sn_{0.08}$ because the Γ valley is not populated anymore or increases strongly when the electrons condense at the minimum of the Γ valley. To quantify the band offsets for the set of GeSn samples, the emission efficiency is calculated via a similar JDOS model as the one used for calculating the gain in **Figure 4**. Therein, the offset ΔE between Γ- and L-valleys as well as the injected charge carrier density N_i represent the free fitting parameters. Furthermore, the temperature dependence of the lifetime is assumed to be identical for all samples and follows the Shockley–Read–Hall (SRH) recombination characteristics (Shockley and Read, 1952; Schubert, 2006) that describes non-radiative recombination via trap states. Using this model, an excellent agreement with the experimental data is obtained (Wirths et al., 2015). The GeSn sample with 13% Sn content is, hence, identified as a true direct band gap group IV semiconductor with its Γ-valley being 25 meV below the indirect L-valleys. From the second fit parameter, a RT carrier density N_i of 4×10^{17} cm^{-3} is deduced consistent with a carrier lifetime of 0.35 ns, which corresponds to a SRV of 570 m s^{-1}. This value is close to the ones reported for elemental Ge on Si (Geiger et al., 2014a), c.f. **Figure 8**, which is an indication of the high-crystalline quality of the investigated GeSn epilayers.

The temperature dependence of the non-radiative carrier lifetime is obtained as:

$$\tau = (1/\tau_0 + 1/\tau_{SRH} + 1/\tau_{Auger})^{-1} \quad (1)$$

where τ_0 describes the lifetime at low temperature, and τ_{SRH} describes the decay due to the capture of charge carriers by mid-gap states, i.e., $\tau_{SRH} = A \times (1 + \cosh(E_T/kT))$. τ_{Auger} describes the Auger recombination time, which can be neglected here due to the low-carrier densities. Furthermore, E_T is the difference between the trap level energy and the intrinsic Fermi-level, k is the Boltzmann constant, and A is to normalize τ to 0.35 ns at 300 K as obtained from the temperature-dependent PL. For $\Delta E = 19$ meV and $\tau_0 = 2.1$ ns, a good agreement between the extracted lifetimes and the lifetime model is obtained (Wirths et al., 2015). For temperatures >50 K, there is a drastic decrease in carrier lifetime from ~2 ns to 350 ps for higher temperatures. As the temperature dependence of this process is well described via the SRH model, the lifetime decay is attributed to the capture of carriers via mid-gap states originating from defects (Wirths et al., 2015). These defects could potentially be related to defects located at the GeSn/Ge-interface (Geiger et al., 2013; Wirths et al., 2015), but further studies are needed to unambiguously identify the origin of this deterioration and, subsequently, improve the material quality.

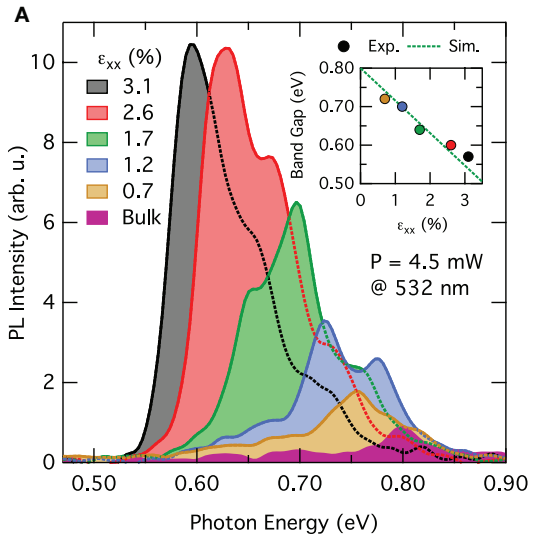

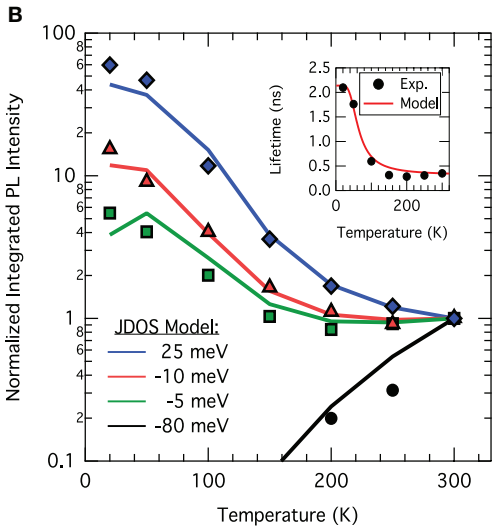

FIGURE 11 | Photoluminescence investigation of strained Ge and GeSn alloys. **(A)** Room-temperature PL spectra for Ge samples with increasing uniaxial strain up to 3.1%. The inset shows the good agreement between the experimental and modeled band edges. **(B)** Temperature-dependent integrated PL intensity normalized to unity at 300 K for a series of GeSn layers with Sn-content ranging from 8 to 13%. An increase in Sn-concentration leads to a more pronounced increase in intensity. The offset between Γ- and L-valleys is extracted from JDOS modeling (solid lines), which reveals $Ge_{0.87}Sn_{0.13}$ to have a fundamental, direct band gap. The inset shows the experimentally extracted non-radiative lifetime modeled with a Shockley–Read–Hall-like temperature dependence (red line).

Optically Pumped Laser

According to the modeling results shown in Section "Modeling," a direct band gap Ge-based system should feature a net gain and, hence, enable light amplification at low excitation. In the previous analysis of low-temperature PL on GeSn alloys in Section "Photoluminescence – Direct Band Gap," a fundamental direct band gap could be identified for a Sn content of 13% in a strain-relaxed layer with 0.7% compressive biaxial strain. To show lasing, a 560-nm epilayer of such $Ge_{0.87}Sn_{0.13}$ material was grown providing an overlap of 60% for the fundamental transverse electric mode in a 5 μm wide FP cavity (Wirths et al., 2015). For this layer, modal gain could be observed at 20 K via the variable-stripe-length (VSL) method under pulsed optical excitation at 1064 nm with a differential gain of ≈0.4 cm kW^{-1} and a threshold excitation density of ≈325 kW cm^{-2} (c.f. **Figure 12**). Above threshold, the gain increases linearly with excitation and can easily pass 100 cm^{-1}. The stripe length-dependent PL analysis is a widely applied technique to measure net modal gain, but it does not allow to resolve the gain and loss as by pump and probe spectroscopy. More evidentially, a gain statement, such as provided by **Figure 12**, becomes respected only after showing lasing.

Indeed, when pumping a FP cavity over its full length, a strongly enhanced emission and narrowing of the line spectra is observed as soon as the modal gain surpasses the cavity losses. This behavior is shown in **Figure 13** where the edge-emission spectra from a 1-mm long FP cavity at 20 K are plotted for varying optical excitation powers. The curves are offset for clarity. The threshold obtained from the lasing experiments matches well with the one obtained from the VSL method. For an excitation density of 1 MW cm^{-2}, lasing could be observed up to 90 K. This temperature is equivalent to the temperature range where the lifetime was found to drop substantially from ~2 ns to 350 ps. Hence, it is tempting to attribute the limitation of lasing to temperatures <100 K to the carrier capture by defect-induced mid-gap states, as has appealed from the analysis shown in **Figure 11B**, inset. However, carrier transfer to the L-valleys and carrier out diffusion into the Ge may be a determining factor, as well.

Despite the breakthrough of presenting for the first time a direct band gap group IV material that is lasing under optical pumping, there still remain open questions. For example, with an excitation power of 325 kW cm^{-2}, a non-radiative lifetime of 2 ns, as shown in **Figure 11**, and a typical absorbance of 1×10^4 cm^{-1} at 1064 nm, a steady-state carrier density of ~3.5×10^{19} cm^{-3} is estimated. With this number, the gain at low temperature from our model is found to be >5000 cm^{-1}. And, interpolating from **Figure 4**, at excitation density of 0.6×10^{18} cm^{-3} we would expect for a system with positive offset of about 15%, a material gain of ~300 cm^{-1} at RT. We assign this large discrepancy from what is observed at low temperature and what a RT calculation predicts to resonant intervalence band absorption. As mentioned above, due to the lack of experimental data for direct gap Ge or GeSn, the energy dependence of the loss as measured by pump–probe experiments for Ge (Carroll et al., 2012) has been used for **Figure 4**. Its proper inclusion possibly adds significant contribution to the loss (Wen and Bellotti, 2015).

In order to improve such gain calculations, which critically depend on the knowledge of the band structure, mappings of the entire valence, and conduction band in reciprocal space would certainly be highly valuable. This could be possible via angle-resolved

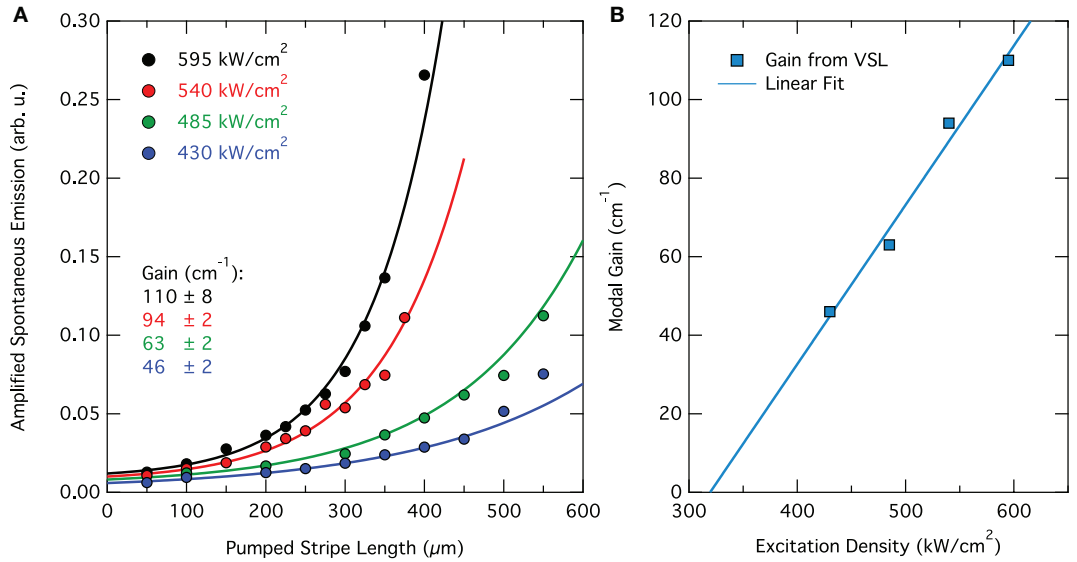

FIGURE 12 | Gain extraction via the variable-stripe-length method (VSL). **(A)** Edge-emitted intensity of $Ge_{0.87}Sn_{0.13}$ at 20 K in dependence of the pumped waveguide length for varying excitation densities. The modal gain is extracted by an exponential fit to the data. **(B)** Differential gain extracted from the spectra in **(A)** indicating a linear dependence on excitation density with a threshold at 325 kW cm^{-2}.

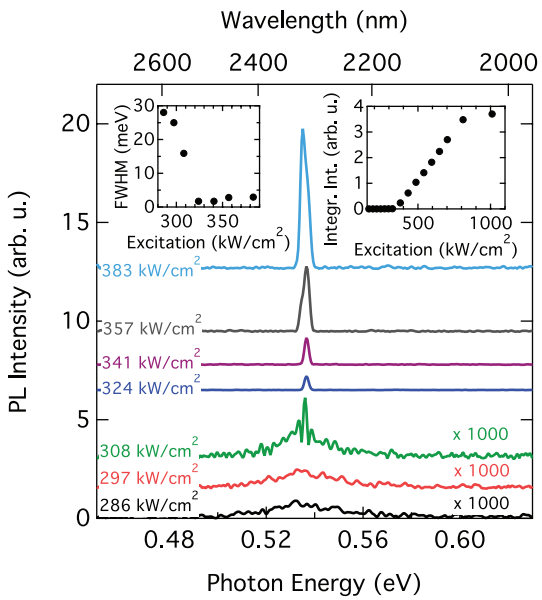

FIGURE 13 | Lasing emission spectra measured from the facet of a 5-μm wide and 1 mm long FP waveguide cavity under optical pumping at 20 K. A clear threshold behavior can be observed in the spectra with respect to output intensity and linewidth, c.f. inset to the right and left hand side, respectively.

photoelectron spectroscopy (ARPES) at high energy (Gray et al., 2011) or the soft x-ray regime (Strocov et al., 2014). Other promising experimental techniques not covered because of lack of space include lifetime measurements via time-resolved PL measurements (He and Atwater, 1997; Nam et al., 2014; Saito et al., 2014). In fact, similar lifetimes for Ge as obtained from synchrotron measurements (Geiger et al., 2014a) were found (Nam et al., 2014).

Challenges

In the previous section, we reviewed experiments and results related to the dependence of the optical properties on strain and alloying of Ge with Sn. Furthermore, we summarized investigations concerning the first lasing of a direct band gap group IV semiconductor and expounded on the temperature dependence of the PL as a powerful tool to determine the directness of a group IV material. We illustrated optical methods based on pump and probe spectroscopy using synchrotron light to determine the carrier lifetime, gain, and loss under optical pumping related to the injected carrier density.

Future experiments along these lines on both, the strained Ge system and GeSn alloys at various strain and Sn concentration, respectively, will allow to establish the fundamentals of lasing in direct band gap group IV systems. The impact of doping on gain, loss, and carrier lifetime should also be addressed in dependence of the directness of the respective system to verify the picture elucidated by **Figure 4** of Section "Gain."

As an example, intervalence band absorption, Auger recombination, and the electrical injection are some of the many fundamental aspects of group IV direct band gap lasing pending to be understood and quantified.

Intervalence Band Absorption

One of the most essential parameters determining the efficiency of a laser is associated to the parasitic absorption due to the injected holes (Adams et al., 1980; Childs et al., 1986). As shown

experimentally by Carroll et al. (2012) for Ge, this absorption depends linearly on the excitation and inclines with decreasing energy. This can be understood from the Drude dependence of the free carrier absorption modified by dipole allowed intervalence band transitions. Because the emission wavelength increases when approaching the direct band gap configuration, and the initially degenerate heavy and light hole bands split due to strain, the parasitic absorption will strongly increase in direct band gap systems and may, thus, obstruct the efficiency of lasing (Wen and Bellotti, 2015). Applying the above introduced optical characterization methods should allow to investigate these effects in detail, which, together with evolving theoretical results, will enable to complete our understanding.

Auger Recombination

On the material level, the performance of optical devices depends strongly on the charge carrier recombination lifetime similarly as described by rate Eq. 1. Here, both the radiative and the Auger recombination lifetime depend on the carrier density n: $1/\tau_{rad} = B \times n$, $1/\tau_{Auger} = C \times n^2$. The quadratic carrier density dependence implicates that Auger recombination becomes a dominant loss mechanism at high-charge carrier densities, which can be the order of $>10^{19}$ cm^{-3} for typical laser devices.

Extensive theoretical work based on perturbation theory has shown that, despite its indirect band gap, the band structure of both, Si and Ge, is favorable for direct Auger recombination (Huldt, 1974; Lochmann, 1978) with Auger recombination coefficients of the order of 10^{-30} cm^{6}s^{-1}. This is comparable to direct band gap materials like GaAs or GaN used for optical devices in the visible part of the spectrum but still much smaller than for low band gap materials like InAs (Metzger et al., 2001).

Significantly, less is known about direct band gap group IV Auger recombination. For direct band gap $Ge_{0.9}Sn_{0.1}/Ge_{0.75}Si_{0.1}Sn_{0.15}$ multi-quantum-well structures, Sun et al. recently showed theoretically that the RT Auger recombination lifetime is of the order of 50 ns compared to a radiative lifetime of 10 ns (Sun et al., 2010). Other work on GeSn (Dutt et al., 2013) and *n*-doped or tensile strained Ge (Liu et al., 2007; Jain et al., 2012) only refers to unstrained bulk Ge recombination coefficients to include in their gain models.

We believe, however, that this is unjustified considering that there is an exponential dependence of the Auger lifetime on the band gap and effective masses (Beattie and Landsberg, 1959; Huldt, 1971; Adams et al., 1980), both being strongly altered in direct band gap Ge. Using the simple exponential dependence derived by Beattie and Landsberg (1959) to scale the experimentally determined Auger recombination coefficient of $C_{Ge} = 10^{-30}$ cm^{6}s^{-1} (Carroll et al., 2012) via the effective masses and band gaps of direct band gap Ge, an Auger coefficient of the order of 10^{-26}–10^{-27} cm^{6}s^{-1} is obtained. Despite the overly strong simplicity of this comparison, it shows that Auger coefficients will most probably increase and need to be addressed and investigated in the future.

Carrier Injection

From an electronic point of view, Ge is one of the most interesting materials as it offers both, high electron and hole mobilities ($\mu_e = 3900$ cm^2/Vs and $\mu_h = 1900$ cm^2/Vs, respectively) (Golikova et al., 1962; Jacoboni et al., 1981). For optical devices, this is appealing because it results in diffusion lengths of several 100 μm, more than sufficient for, e.g., typical detector absorber sizes and laser cavity lengths. However, at the same time, Ge suffers from its low band gap, which causes large leakage currents in Ge pn junctions (Metzger et al., 2001; Satta et al., 2006), thus, requiring extensive work on surface passivation due to the lack of a native oxide.

The already beneficial mobility properties can be further improved by employing tensile strain as has been shown for both, uniaxially and biaxially strained Ge (Schetzina and McKelvey, 1969; Chu et al., 2009; Chen et al., 2011b). Here, we would like to highlight that all these studies have been performed on indirect band gap Ge where the increase in electron mobility is mediated by a reduction of the effective mass in the L valley. Even without strain, the Γ-valley already offers an ~8 times smaller effective mass and correspondingly higher electron mobility. Similarly, an increase in hole mobility is expected due to the lifting of the valence band degeneracy (Beattie and Landsberg, 1959; Fischetti and Laux, 1996). This is advantageous as a high mobility strongly reduces the resistivity of the device allowing an efficient injection and extraction of charge carriers.

GeSn emerged as a material of interest in electronics only recently; therefore, less transport data are available. However, theoretical studies predict very large electron mobilities as well as hole mobilities of the order of 4500 cm^2/Vs for direct band gap GeSn (Sau and Cohen, 2007). The first reported experimental mobility study has been done on low Sn content (<6%) indirect band gap GeSn layers yielding a Hall mobility of the order of ~200–300 cm^2/Vs (Nakatsuka et al., 2010). Slightly better results have been obtained thereafter investigating p-MOSFETs hole channel mobility (Gupta et al., 2013a; Wang et al., 2013).

In summary, we see that a vast amount of knowledge concerning the mobility exists leaving a good base for further studies. Moreover, many electrical devices and the corresponding fabrication techniques, e.g., passivation, contacting, or annealing, have been conceived allowing for a fast implementation in optical devices.

However, besides the tremendous changes in the carrier mobility, there are additional effects coming into play with electrical injection of charge carriers from indirect to direct band gap Ge. Exemplarily in **Figure 14**, such an injection scheme in form of a pin diode is discussed for the case of tensile strained Ge bridges where the strain profile is shown in **Figure 5B**.

Far from the strained constriction, electrons can be injected into the L-valleys of the conduction band as in standard Ge diodes. However, close to the center the strain profile alters the band structure with L- and γ-valley starting to cross, which allows for intervalley scattering (Boucaud et al., 2013) from a high- into a low-effective mass valley with a higher mobility, a process inverse to the Gunn effect (Gunn, 1963). This may support current extraction and injection in optical devices. However, an actual impact still needs to be proven.

Cavity Design

For the usage of direct band gap materials in lasing structures, high-quality factor optical resonators are necessary confining the

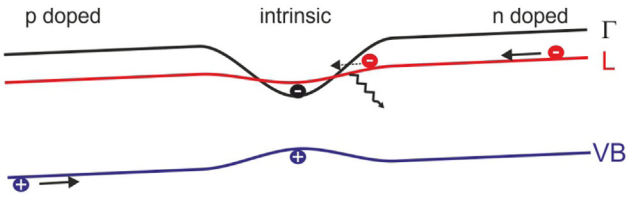

FIGURE 14 | Schematic of the band structure of a forward biased pin strained Ge bridge diode where the intrinsic layer and strained region overlap.

light in the gain region and, thus, allowing for stimulated emission. Helpful in this regard is the high-refractive index contrast of the Ge–air and GeSn–air interfaces (Kasper et al., 2013), which should allow for good confinement properties. The design of suitable cavities seems to be straightforward for GeSn lasers where the wafer-scale direct band gap on Si or Ge already facilitated the implementation of well-known laser cavities, such as FP cavities (Wirths et al., 2015) or microdisks (Cho et al., 2011). At the same time, optical microdisk cavities with quality factors of ~1400 have been demonstrated in tensile strained Ge using external SiN stressors (Ghrib et al., 2013) as well as waveguide cavities (Capellini et al., 2014).

The situation is much more complex for uniaxially strained Ge bridges where patterning of the bridge inevitably relaxes the strain and, hence, prohibits a fundamental direct band gap. This excludes many popular cavity designs, in particular, microdisks, photonic crystals, and FP cavities. Hence, distributed feedback structures, which do not rely on patterning of the strained region, are currently under investigation (Marin et al., 2015).

Band Gap Renormalization and Material Stability

Relevant for both here discussed direct band gap systems is a quantitative analysis of the band gap renormalization of the involved Γ and L valleys in dependence of their respective carrier population. So far, experiments suggest that the renormalization corrections are comparable for the two valleys. Hence, the offset between the Γ and L states would not depend on the injection density, which is essential for a stable injection.

Moreover, material specific investigation concerns, for example, the thermal stability of GeSn and SiGeSn metastable alloys with regards to Sn diffusion and segregation where extensive segregation can result in changes of the emission wavelength and/or emission efficiency. Recently, investigations have been pursued to examine the temperature budget a GeSn or SiGeSn device would be able to withstand, e.g., by *in situ* studies (Fournier-Lupien et al., 2014) or annealing experiments (Wirths et al., 2014). First, *in situ* results indicate phase separation of a 12% Sn containing ternary SiGeSn and binary GeSn alloys at ~420 and 460°C, respectively, which is surprising considering that the higher mixing entropy usually results in a higher thermal stability of ternary alloys (Fournier-Lupien et al., 2014). Annealing experiments revealed distinct Sn diffusion at 300°C for GeSn with approximately the same composition (Wirths et al., 2014).

Finding the intrinsic stress limits of Ge is another item of interest in this context.

By saying this, we conclude our listing of fundamental and materials-related challenges. This list may be incomplete. However, it confirms that the research and development of a laser source from a group IV material will involve many disciplines from fundamental to device physics and from wave optics to material and transport properties. To progress fast, a collaborative effort is demanded.

Opportunities

Photonics

Direct band gap group IV laser systems may permit a qualitative as well as a quantitative expansion of Si-photonics (group IV photonics) into traditional but also new areas of applications. However, it is requested that such lasers can be operated energy efficiently, under ambient conditions and can be fully integrated with current Si technology. An answer to whether this is possible cannot be given yet as the research is at an early stage. We can only speculate about the specifications of such a laser and, thus, have to guess which of the applications would profit most from a successful implementation of group IV lasers. Hence, for the following discussion, let us assume that this all-group-IV laser does indeed exist and it operates (i) under electrical injection, (ii) at RT or above, and (iii) with reasonable power conversion efficiency. What could we do with such a device, where is the highest impact, and what is the platform of choice?

A high return is merely achievable when this laser device will be combined with the current Si photonics by using the same platform. Most advanced are photonic elements fabricated on SOI, except for applications in the visible part of the spectrum – not covered here – where SiN-based structures are often used. SOI for photonics typically consists of Si layers with a thickness of ~200–250 nm and a several micrometer thick buried oxide to avoid leakage of the propagating modes into the Si substrate. For strain engineering, the compatibility with SOI has already been shown (Süess et al., 2013), c.f. Section "Microbridges," and, as mentioned above, bridges with even higher mechanical strength are fabricated from GOI using wafer transfer (Sukhdeo et al., 2014). In fact, wafer-scale fabrication of GOI using the SmartCut® process has already been established several years ago for electronics (Augendre et al., 2009). GOI for photonic applications, where thicker layers and a thicker BOX are required, has been presented recently by Reboud et al. (2015). A photonic platform based on GOI, in comparison to SOI, has the advantage that all photonic elements, such as waveguides, bends, and the resonant structures, can be reduced in size because of the larger refractive index contrast. This allows for the potential fabrication of more dense optical circuits and, hence, for an easier integration with electronics. Furthermore, Ge provides coverage of the longer wavelengths toward 10 μm and more. Moreover, by using processes that are selective for either Ge or Si, the GOI platform may provide additional fabrication opportunities. The high quality (Si)GeSn presented by Wirths et al. (2013b) has been deposited on a Ge VS on Si(001) indicating that the growth on SOI and certainly GOI is possible, as well.

With a laser device implemented on the currently used SOI or similarly on GOI, various new applications will emerge. Before speculating, we may picture the many already existing photonic elements. To select a few: Low-loss (<1 dB cm^{-1}) single mode waveguides in various designs, tapers to adiabatically match the waveguide modes to fibers, and low-loss grating couplers (<1 dB) in 1D or 2D providing polarization splitting. Other standard elements include directional couplers, Mach Zehnder interferometers, ring resonators, and light modulators based on free carrier injections or quantum confined Stark effect. Detectors based on slightly tensile strained (0.2%) Ge provide more than 10 GHz speed for high-data rate transmission. Other device elements include add-drop filters, buffers, and switches, which can be integrated with fluidic channels for (bio-) sensing. The short wavelength infrared at which the here discussed group IV direct band gap lasers emit (see **Figure 3**) is certainly a clear asset for sensing applications (Soref, 2010; Nedeljkovic et al., 2013).

Silicon-on-insulator is (and GOI could become) a very convenient platform to realize high-performing photonic crystal structures enabling unique photonic circuits, such as compact high-Q cavities, which can operate stably at single and dual-wavelength, and as wavelength division multiplexer as desired for optical signal processing. This listing can be extended almost indefinitely, naming, e.g., switching and steering of optical signals, slow light, pulse compression, customized reflectors, and filters. Together with the expectation that such photonic circuits will be very cost effective, compact, reliable, and efficient, a monolithically integrated laser source will certainly bring new functionality, in particular when optics can be merged with electronics.

CMOS Integration

The combination of optics with CMOS electronics to realize an on-chip data distribution network (Heck and Bowers, 2014) is – without any doubt – one of the most advanced and challenging applications for direct band gap group IV lasers. The requirements are so complex (Miller, 2009) that before the start of such a development, many fundamental questions have to be answered, such as the efficiency issues among other challenges, which have been addresses in the previous section. However, once these hurdles are taken, we expect to arise a highly competitive and attractive platform solution for future data processing applications. In fact, the extension of CMOS by integration of Ge and (Si)GeSn may not just resolve the demands for a monolithic laser gain medium, but, as discussed widely elsewhere (Kao et al., 2014), (Si)GeSn would already advance the performance of the electronic circuits. This appealing double benefit, together with the potential compatibility to CMOS of such an all-group-IV solution, bears an essential advantage in comparison to other emerging technologies, such as spin- and/or valley-based electronics, which rely in part on non-conform chemical elements and non-CMOS fabrication processes.

Hence, we expect that as soon as the fundamental lessons of direct band gap lasing are learnt and a gain medium well-qualified for injection pumping at RT is defined, research and development of a new opto-electronic platform will quickly advance. Experts in CMOS technology, group IV epitaxy, laser physics, and Si electronics and photonics will cooperate and define the routes to opto-electronics for fast and energy-efficient data processing.

Conclusion and Outlook

We reviewed the methods for achieving a direct band gap in group IV semiconductors in the most promising material system for the prospect of a Si compatible laser, namely, Ge modified either via tensile strain or by alloying with Sn. We expanded on the methods to characterize these systems and gave examples on their optical properties. The recent advances in numerous approaches to achieve a direct band gap have finally concluded in the first demonstration of lasing in a direct band gap GeSn alloy (Wirths et al., 2015).

With this demonstration, we are at the beginning of an exciting journey in the field of silicon photonics. As shown in great detail, the many optical characterization tools at hand allow us to address a large amount of fundamental questions, including band gap renormalization, various recombination processes, and doping level-dependent lasing performance, but also material- and technology-related issues, such as high Q-factor cavity design, diffusive carrier transport, stress, and thermal diffusion limits.

We hope that with outlining these challenges, we can motivate a vast amount of new researchers from various backgrounds in optics, material science, and device physics to join this interesting research field. We believe that combined efforts will converge in a reasonable time to a demonstration of a practical laser source being electrically pumped, highly efficient, and fully integrated on an electro-optical CMOS platform. This building block will finally pave the way for true monolithic on-chip integration of photonics and CMOS electronics for new sensors in the long wavelength infrared, and will eventually enable to build an on-chip or off-chip electro-optical data distribution network for high-performance computing.

Acknowledgments

We would like to acknowledge the many scientific collaborators we were fortunate to work with over the last few years. They supported us in building up a strong portfolio in the investigation and understanding of lasing in group IV systems, and the fabrication of direct band gap group IV materials. In particular, we thank our previous group members Gustav Schiefler, Martin J. Süess, and Renato Minamisawa for their contributions, which led to this appealing strain concept, and the group of Dan Buca (FZ Jülich), who contacted us for investigating their high quality material and thus gave us the opportunity to learn also about GeSn alloys. The tremendous progress achieved in a short time is a shining example of our good collaboration. We also thank Jérôme Faist and Ralph Spolenak (ETHZ) for their whole-hearted support to this subject and their many essential contributions. Finally, we acknowledge the Swiss Science Foundation (SNF) for supporting part of the here reviewed studies over several years.

References

Adams, A. R., Asada, M., Suematsu, Y., and Arai, S. (1980). The temperature dependence of the efficiency and threshold current of In 1- xGa xAs yP 1- y lasers related to intervalence band absorption. *Jpn. J. Appl. Phys.* 19, L621–L624. doi:10.1143/JJAP.19.L621

Akatsu, T., Deguet, C., Sanchez, L., Allibert, F., Rouchon, D., Signamarcheix, T., et al. (2006). Germanium-on-insulator (GeOI) substrates – a novel engineered substrate for future high performance devices. *Mater. Sci. Semicond. Process.* 9, 444–448. doi:10.1016/j.mssp.2006.08.077

Aldaghri, O., Ikonić, Z., and Kelsall, R. W. (2012). Optimum strain configurations for carrier injection in near infrared Ge lasers. *J. Appl. Phys.* 111, 053106. doi:10.1063/1.3691790

Augendre, E., Sanchez, L., Benaissa, L., Signamarcheix, T., Hartmann, J.-M., Le Royer, C., et al. (2009). Challenges and progress in germanium-on-insulator materials and device development towards ULSI integration. *ECS Trans.* 25, 351–362. doi:10.1149/1.3203972

Bauer, M. R., Tolle, J., Bungay, C., Chizmeshya, A. V. G., Smith, D. J., Menéndez, J., et al. (2003). Tunable band structure in diamond-cubic tin-germanium alloys grown on silicon substrates. *Solid State Commun.* 127, 355–359. doi:10.1016/S0038-1098(03)00446-0

Beattie, A. R., and Landsberg, P. T. (1959). Auger effect in semiconductors. *Proc. R. Soc. A Math. Phys. Eng. Sci.* 249, 16–29. doi:10.1098/rspa.1959.0003

Bhargava, N., Coppinger, M., Gupta, J. P., Wielunski, L., and Kolodzey, J. (2013). Lattice constant and substitutional composition of GeSn alloys grown by molecular beam epitaxy. *Appl. Phys. Lett.* 103, 041908. doi:10.1063/1.4816660

Birner, S., Zibold, T., Andlauer, T., Kubis, T., Sabathil, M., Trellakis, A., et al. (2007). Nextnano: general purpose 3-D simulations. *IEEE Trans. Electron Devices* 54, 2137–2142. doi:10.1109/TED.2007.902871

Boucaud, P., Kurdi El, M., Ghrib, A., Prost, M., de Kersauson, M., Sauvage, S., et al. (2013). Recent advances in germanium emission. *Photon. Res.* 1, 102. doi:10.1364/PRJ.1.000102

Bratland, K., Foo, Y., Soares, J., Spila, T., Desjardins, P., and Greene, J. (2003). Mechanism for epitaxial breakdown during low-temperature Ge(001) molecular beam epitaxy. *Phys. Rev. B* 67, 125322. doi:10.1103/PhysRevB.67.125322

Camacho-Aguilera, R. E., Cai, Y., Patel, N., Bessette, J. T., Romagnoli, M., Kimerling, L. C., et al. (2012). An electrically pumped germanium laser. *Opt. Express* 20, 11316. doi:10.1364/OE.20.011316

Capellini, G., Kozlowski, G., Yamamoto, Y., Lisker, M., Wenger, C., Niu, G., et al. (2013). Strain analysis in SiN/Ge microstructures obtained via Si-complementary metal oxide semiconductor compatible approach. *J. Appl. Phys.* 113, 013513. doi:10.1063/1.4772781

Capellini, G., Reich, C., Guha, S., Yamamoto, Y., Lisker, M., Virgilio, M., et al. (2014). Tensile Ge microstructures for lasing fabricated by means of a silicon complementary metal-oxide-semiconductor process. *Opt. Express* 22, 399–410. doi:10.1364/OE.22.000399

Carroll, L., Friedli, P., Lerch, P., Schneider, J., Treyer, D., Hunziker, S., et al. (2011). Ultrabroadband infrared pump-probe spectroscopy using synchrotron radiation and a tuneable pump. *Rev. Sci. Instrum.* 82, 063101–063101–9. doi:10.1063/1.3592332

Carroll, L., Friedli, P., Neuenschwander, S., Sigg, H., Cecchi, S., Isa, F., et al. (2012). Direct-gap gain and optical absorption in germanium correlated to the density of photoexcited carriers, doping, and strain. *Phys. Rev. Lett.* 109, 057402. doi:10.1103/PhysRevLett.109.057402

Chang, G.-E., and Cheng, H. H. (2013). Optical gain of germanium infrared lasers on different crystal orientations. *J. Phys. D Appl. Phys.* 46, 065103. doi:10.1088/0022-3727/46/6/065103

Chen, R., Gupta, S., Huang, Y.-C., Huo, Y., Rudy, C. W., Sanchez, E., et al. (2013a). Demonstration of a Ge/GeSn/Ge quantum-well microdisk resonator on silicon: enabling high-quality Ge(Sn) materials for micro- and nanophotonics. *Nano Lett.* 14, 37–43. doi:10.1021/nl402815v

Chen, R., Huang, Y.-C., Gupta, S., Lin, A. C., Sanchez, E., Kim, Y., et al. (2013b). Material characterization of high Sn-content, compressively-*strained* GeSn epitaxial films after rapid thermal processing. *J. Cryst. Growth* 365, 29–34. doi:10.1016/j.jcrysgro.2012.12.014

Chen, R., Lin, H., Huo, Y., Hitzman, C., Kamins, T. I., and Harris, J. S. (2011a). Increased photoluminescence of strain-reduced, high-Sn composition Ge1−xSnx alloys grown by molecular beam epitaxy. *Appl. Phys. Lett.* 99, 181125. doi:10.1063/1.3658632

Chen, Y. T., Lan, H. S., Hsu, W., Fu, Y. C., Lin, J. Y., and Liu, C. W. (2011b). Strain response of high mobility germanium n-channel metal-oxide-semiconductor field-effect transistors on (001) substrates. *Appl. Phys. Lett.* 99, 022106. doi:10.1063/1.3604417

Childs, G. N., Brand, S., and Abram, R. A. (1986). Intervalence band absorption in semiconductor laser materials. *Semicond. Sci. Technol.* 1, 116–120. doi:10.1088/0268-1242/1/2/004

Cho, S., Chen, R., Koo, S., Shambat, G., Lin, H., Park, N., et al. (2011). Fabrication and analysis of epitaxially grown Ge1-xSnx microdisk resonator with 20-nm free-spectral range. *IEEE Photon. Technol. Lett.* 23, 1535–1537. doi:10.1109/LPT.2011.2163929

Chow, W. W. (2012). Model for direct-transition gain in a Ge-on-Si laser. *Appl. Phys. Lett.* 100, 191113. doi:10.1063/1.4714540

Chu, M., Sun, Y., Aghoram, U., and Thompson, S. E. (2009). Strain: a solution for higher carrier mobility in nanoscale MOSFETs. *Annu. Rev. Mater. Res.* 39, 203–229. doi:10.1146/annurev-matsci-082908-145312

Du, W., Ghetmiri, S. A., Conley, B. R., Mosleh, A., Nazzal, A., Soref, R. A., et al. (2014). Competition of optical transitions between direct and indirect bandgaps in Ge1−xSnx. *Appl. Phys. Lett.* 105, 051104. doi:10.1063/1.4892302

Dutt, B., Lin, H., Sukhdeo, D. S., Vulovic, B. M., Gupta, S., Nam, D., et al. (2013). Theoretical analysis of GeSn alloys as a gain medium for a Si-compatible laser. *IEEE J. Sel. Top. Quantum Electron.* 19, 1502706–1502706. doi:10.1109/JSTQE.2013.2241397

Dutt, B., Sukhdeo, D. S., Nam, D., Vulovic, B. M., Ze, Y., and Saraswat, K. C. (2012). Roadmap to an efficient germanium-on-silicon laser: strain vs. n-type doping. *IEEE Photon. J.* 4, 2002–2009. doi:10.1109/JPHOT.2012.2221692

El Kurdi, M., Fishman, G., Sauvage, S., and Boucaud, P. (2010). Band structure and optical gain of tensile-strained germanium based on a 30 band k·p formalism. *J. Appl. Phys.* 107, 013710. doi:10.1063/1.3279307

Fang, Z., Chen, Q. Y., and Zhao, C. Z. (2013). A review of recent progress in lasers on silicon. *Opt. Laser Technol.* 46, 103–110. doi:10.1088/0034-4885/76/3/034501

Fischetti, M. V., and Laux, S. E. (1996). Band structure, deformation potentials, and carrier mobility in strained Si, Ge, and SiGe alloys. *J. Appl. Phys.* 80, 2234–2252. doi:10.1063/1.363052

Fitzgerald, E. A., Xie, Y. H., Green, M. L., Brasen, D., Kortan, A. R., Michel, J., et al. (1991). Totally relaxed GexSi1−x layers with low threading dislocation densities grown on Si substrates. *Appl. Phys. Lett.* 59, 811. doi:10.1063/1.105351

Fournier-Lupien, J. H., Chagnon, D., Levesque, P., AlMutairi, A. A., Wirths, S., Pippel, E., et al. (2014). In situ studies of germanium-tin and silicon-germanium-tin thermal stability. *ECS Trans.* 64, 903–911. doi:10.1149/06406.0903ecst

Geiger, R., Frigerio, J., Süess, M. J., Chrastina, D., Isella, G., Spolenak, R., et al. (2014a). Excess carrier lifetimes in Ge layers on Si. *Appl. Phys. Lett.* 104, 062106–062106. doi:10.1063/1.4865237

Geiger, R., Süess, M. J., Bonzon, C., Frigerio, J., Chrastina, D., Isella, G., et al. (2014b). *Carrier Lifetimes in Uniaxially Strained Ge Micro Bridges*. IEEE, 227–228.

Geiger, R., Süess, M. J., Bonzon, C., Spolenak, R., Faist, J., and Sigg, H. (2014c). *Strained Ge Microbridges to Obtain a Direct Bandgap Laser*. IEEE, 7–8.

Geiger, R., Frigerio, J., Süess, M. J., Minamisawa, R. A., Chrastina, D., Isella, G., et al. (2013). *Excess Carrier Lifetimes in Ge Layers on Si*. IEEE, 103–104.

Ghrib, A., Kurdi El, M., de Kersauson, M., Prost, M., Sauvage, S., Checoury, X., et al. (2013). Tensile-strained germanium microdisks. *Appl. Phys. Lett.* 102, 221112. doi:10.1364/OE.23.006722

Ghrib, A., Kurdi El, M., Prost, M., Sauvage, S., Checoury, X., Beaudoin, G., et al. (2015). All-around SiN stressor for high and homogeneous tensile strain in germanium microdisk cavities. *Adv. Opt. Mater.* 3, 353–358. doi:10.1002/adom.201400369

Golikova, O. A., Moizhes, B. Y., and Stilbans, L. S. (1962). Hole mobility of germanium as a function of concentration and temperature. *Sov. Phys. Solid State* 3, 2259–2265.

Gray, A. X., Papp, C., Ueda, S., Balke, B., Yamashita, Y., Plucinski, L., et al. (2011). Probing bulk electronic structure with hard X-ray angle-resolved photoemission. *Nat. Mater.* 10, 759–764. doi:10.1038/nmat3089

Greil, J., Lugstein, A., Zeiner, C., Strasser, G., and Bertagnolli, E. (2012). Tuning the electro-optical properties of germanium nanowires by tensile strain. *Nano Lett.* 12, 6230–6234. doi:10.1021/nl303288g

Gunn, J. B. (1963). Microwave oscillations of current in III–V semiconductors. *Solid State Commun.* 1, 88–91. doi:10.1016/0038-1098(63)90041-3

Gupta, S., Chen, R., Vincent, B., Lin, D., Magyari-Kope, B., Caymax, M., et al. (2013a). (Invited) GeSn channel n and p MOSFETs. *ECS Trans.* 50, 937–941. doi:10.1149/05009.0937ecst

Gupta, S., Magyari-Köpe, B., Nishi, Y., and Saraswat, K. C. (2013b). Achieving direct band gap in germanium through integration of Sn alloying and external strain. *J. Appl. Phys.* 113, 073707. doi:10.1063/1.4792649

Hartmann, J. M., Sanchez, L., Van Den Daele, W., Abbadie, A., Baud, L., Truche, R., et al. (2010). Fabrication, structural and electrical properties of compressively strained Ge-on-insulator substrates. *Semicond. Sci. Technol.* 25, 075010. doi:10.1088/0268-1242/25/7/075010

Harwit, A., Pukite, P. R., Angilello, J., and Iyer, S. S. (1990). Properties of diamond structure SnGe films grown by molecular beam epitaxy. *Thin Solid Films* 184, 395–401. doi:10.1016/0040-6090(90)90437-I

He, G., and Atwater, H. A. (1997). Interband transitions in SnxGe1−xAlloys. *Phys. Rev. Lett.* 79, 1937–1940. doi:10.1103/PhysRevLett.79.1937

Heck, M. J. R., and Bowers, J. E. (2014). Energy efficient and energy proportional optical interconnects for multi-core processors: driving the need for on-chip sources. *IEEE J. Sel. Top. Quantum Electron.* 20, 332–343. doi:10.1109/JSTQE.2013.2293271

Huldt, L. (1971). Band-to-band auger recombination in indirect gap semiconductors. *Phys. Status Solidi A* 8, 173–187. doi:10.1002/pssa.2210080118

Huldt, L. (1974). Auger recombination in germanium. *Phys. Status Solidi A* 24, 221–229. doi:10.1088/0957-4484/22/43/435401

Huo, Y., Lin, H., Chen, R., Makarova, M., Rong, Y., Li, M., et al. (2011). Strong enhancement of direct transition photoluminescence with highly tensile-strained Ge grown by molecular beam epitaxy. *Appl. Phys. Lett.* 98, 011111. doi:10.1063/1.3534785

Jacoboni, C., Nava, F., Canali, C., and Ottaviani, G. (1981). Electron drift velocity and diffusivity in germanium. *Phys. Rev. B* 24, 1014–1026. doi:10.1103/PhysRevB.24.1014

Jain, J. R., Hryciw, A., Baer, T. M., Miller, D. A. B., Brongersma, M. L., and Howe, R. T. (2012). A micromachining-based technology for enhancing germanium light emission via tensile strain. *Nat. Photonics* 6, 398–405. doi:10.1038/nphoton.2012.111

Kao, K.-H., Verhulst, A. S., Rooyackers, R., Douhard, B., Delmotte, J., Bender, H., et al. (2014). Compressively strained SiGe band-to-band tunneling model calibration based on p-i-n diodes and prospect of strained SiGe tunneling field-effect transistors. *J. Appl. Phys.* 116, 214506. doi:10.1063/1.4903288

Kasper, E., Kittler, M., Oehme, M., and Arguirov, T. (2013). Germanium tin: silicon photonics toward the mid-infrared [Invited]. *Photon. Res.* 1, 69. doi:10.1364/PRJ.1.000069

Koerner, R., Oehme, M., Gollhofer, M., Schmid, M., Kostecki, K., Bechler, S., et al. (2015). Electrically pumped lasing from Ge Fabry-Perot resonators on Si. *Opt. Express* 23, 14815–14822. doi:10.1364/OE.23.014815

Liu, J., Sun, X., Camacho-Aguilera, R., Kimerling, L. C., and Michel, J. (2010). Ge-on-Si laser operating at room temperature. *Opt. Lett.* 35, 679. doi:10.1364/OL.35.000679

Liu, J., Sun, X., Pan, D., Wang, X., Kimerling, L. C., Koch, T. L., et al. (2007). Tensile-strained, n-type Ge as a gain medium for monolithic laser integration on Si. *Opt. Express* 15, 11272. doi:10.1364/OE.15.011272

Lochmann, W. (1978). Phonon-assisted auger recombination in indirect gap semiconductors. *Phys. Status Solidi A* 45, 423–432. doi:10.1002/pssa.2210450208

Low, K. L., Yang, Y., Han, G., Fan, W., and Yeo, Y.-C. (2012). Electronic band structure and effective mass parameters of Ge1-xSnx alloys. *J. Appl. Phys.* 112, 103715. doi:10.1063/1.4767381

Marin, E., Bonzon, C., Geiger, R., Zabel, T., Sigg, H., and Faist, J. (2015). *Proceedings CLEO-Europe 2015.* (in print)

Metzger, W. K., Wanlass, M. W., Ellingson, R. J., Ahrenkiel, R. K., and Carapella, J. J. (2001). Auger recombination in low-band-gap n-type InGaAs. *Appl. Phys. Lett.* 79, 3272–3274. doi:10.1063/1.1418032

Michel, J., Liu, J., and Kimerling, L. C. (2010). High-performance Ge-on-Si photodetectors. *Nat. Photonics* 4, 527–534. doi:10.1038/nphoton.2010.157

Miller, D. A. B. (2009). Device requirements for optical interconnects to silicon chips. *Proc. IEEE* 97, 1166–1185. doi:10.1109/JPROC.2009.2014298

Miller, D. A. B. (2010). Optical interconnects to electronic chips. *Appl. Opt.* 49, F59. doi:10.1364/AO.49.000F59

Minamisawa, R. A., Süess, M. J., Spolenak, R., Faist, J., David, C., Gobrecht, J., et al. (2012). Top-down fabricated silicon nanowires under tensile elastic strain up to 4.5%. *Nat Commun* 3, 1096. doi:10.1038/ncomms2102

Nakatsuka, O., Tsutsui, N., Shimura, Y., Takeuchi, S., Sakai, A., and Zaima, S. (2010). Mobility behavior of Ge1-xSnx layers grown on silicon-on-insulator substrates. *Jpn. J. Appl. Phys.* 49, 04DA10. doi:10.1143/JJAP.49.04DA10

Nam, D., Kang, J.-H., Brongersma, M. L., and Saraswat, K. C. (2014). Observation of improved minority carrier lifetimes in high-quality Ge-on-insulator using time-resolved photoluminescence. *Opt. Lett.* 39, 6205. doi:10.1364/OL.39.006205

Nam, D., Sukhdeo, D., Cheng, S.-L., Roy, A., Chih-Yao Huang, K., Brongersma, M., et al. (2012). Electroluminescence from strained germanium membranes and implications for an efficient Si-compatible laser. *Appl. Phys. Lett.* 100, 131112. doi:10.1063/1.3699224

Nam, D., Sukhdeo, D., Roy, A., Balram, K., Cheng, S.-L., Huang, K. C.-Y., et al. (2011). Strained germanium thin film membrane on silicon substrate for optoelectronics. *Opt. Express* 19, 25866–25872. doi:10.1364/OE.19.025866

Nam, D., Sukhdeo, D. S., Kang, J.-H., Petykiewicz, J., Lee, J. H., Jung, W. S., et al. (2013). Strain-induced pseudoheterostructure nanowires confining carriers at room temperature with nanoscale-tunable band profiles. *Nano Lett.* 13, 3118–3123. doi:10.1021/nl401042n

Nedeljkovic, M., Khokhar, A. Z., Hu, Y., Chen, X., Penades, J. S., Stankovic, S., et al. (2013). Silicon photonic devices and platforms for the mid-infrared. *Opt. Mater. Express* 3, 1205. doi:10.1364/OME.3.001205

Newman, R., and Tyler, W. (1957). Effect of impurities on free-hole infrared absorption in p-type germanium. *Phys. Rev.* 105, 885–886. doi:10.1103/PhysRev.105.885

Oda, K., Okumura, T., Tani, K., Saito, S.-I., and Ido, T. (2013). Improvement of photoluminescence from Ge layer with patterned Si3N4 stressors. *Thin Solid Films* 557, 355–362. doi:10.1016/j.tsf.2013.08.117

Oehme, M., Buca, D., Kostecki, K., Wirths, S., Holländer, B., Kasper, E., et al. (2013). Epitaxial growth of highly compressively strained GeSn alloys up to 12.5% Sn. *J. Cryst. Growth* 384, 71–76. doi:10.1016/j.jcrysgro.2013.09.018

Passaro, V., Tullio, C., Troia, B., Notte, M., Giannoccaro, G., and Leonardis, F. (2012). Recent advances in integrated photonic sensors. *Sensors* 12, 15558–15598. doi:10.3390/s121115558

Peschka, D., Thomas, M., Glitzky, A., Nurnberg, R., Gartner, K., Virgilio, M., et al. (2015). Modeling of edge-emitting lasers based on tensile strained germanium microstrips. *IEEE Photon. J.* 7, 1–15. doi:10.1109/JPHOT.2015.2427093

Pukite, P. R., Harwit, A., and Iyer, S. S. (1989). Molecular beam epitaxy of metastable, diamond structure SnxGe1-x alloys. *Appl. Phys. Lett.* 54, 2142–2144. doi:10.1063/1.101152

Reboud, V., Widiez, J., Hartmann, J.-M., Dias, G. O., Fowler, D., Chelnokov, A., et al. (2015). Structural and optical properties of 200 mm germanium-on- insulator (GeOI) substrates for silicon photonics applications. *Proc. SPIE 9367, Silicon Photonics X* 2015. doi:10.1117/12.2079393

Saito, S., Gardes, F. Y., Al-Attili, A. Z., Tani, K., Oda, K., Suwa, Y., et al. (2014). Group IV light sources to enable the convergence of photonics and electronics. *Front. Mater.* 1:15. doi:10.3389/fmats.2014.00015

Sánchez-Pérez, J. R., Boztug, C., Chen, F., Sudradjat, F. F., Paskiewicz, D. M., Jacobson, R. B., et al. (2011). Direct-bandgap light-emitting germanium in tensilely strained nanomembranes. *Proc. Natl. Acad. Sci. U.S.A.* 108, 18893–18898. doi:10.1073/pnas.1107968108

Satta, A., Nicholas, G., Simoen, E., Houssa, M., Dimoulas, A., De Jaeger, B., et al. (2006). Impact of germanium surface passivation on the leakage current of shallow planar p-n junctions. *Mater. Sci. Semicond. Process.* 9, 716–720. doi:10.1016/j.mssp.2006.08.037

Sau, J., and Cohen, M. (2007). Possibility of increased mobility in Ge-Sn alloy system. *Phys. Rev. B* 75, 045208. doi:10.1103/PhysRevB.75.045208

Schetzina, J. F., and McKelvey, J. P. (1969). Strain dependence of the minority carrier mobility in p-type germanium. *Phys. Rev.* 181, 1191. doi:10.1103/PhysRev.181.1191

Schubert, E. F. (2006). *Light-Emitting Diodes*, 2nd Edn. Cambridge University Press.

Senaratne, C. L., Gallagher, J. D., Jiang, L., Aoki, T., Smith, D. J., Menendez, J., et al. (2014). Ge1-ySny (y = 0.01-0.10) alloys on Ge-buffered Si: synthesis, microstructure, and optical properties. *J. Appl. Phys.* 116, 133509. doi:10.1063/1.4896788

Shockley, W., and Read, W. (1952). Statistics of the recombinations of holes and electrons. *Phys. Rev.* 87, 835–842. doi:10.1103/PhysRev.87.835

Soref, R. (2010). Mid-infrared photonics in silicon and germanium. *Nat. Photonics* 4, 495–497. doi:10.1038/nphoton.2010.171

Strocov, V. N., Wang, X., Shi, M., Kobayashi, M., Krempasky, J., Hess, C., et al. (2014). Soft-X-ray ARPES facility at the ADRESS beamline of the SLS: concepts, technical realisation and scientific applications. *J. Synchrotron. Radiat.* 21, 32–44. doi:10.1107/S1600577513019085

Süess, M. J., Geiger, R., Minamisawa, R. A., Schiefler, G. L., Frigerio, J., Chrastina, D., et al. (2013). Analysis of enhanced light emission from highly strained germanium microbridges. *Nat. Photonics* 7, 466–472. doi:10.1038/nphoton.2013.67

Sukhdeo, D. S., Nam, D., Kang, J.-H., Brongersma, M. L., and Saraswat, K. C. (2014). Direct bandgap germanium-on-silicon inferred from 5.7% ⟨100⟩ uniaxial tensile strain [Invited]. *Photon. Res.* 2, A8. doi:10.1364/PRJ.2.0000A8

Sun, G., Soref, R. A., and Cheng, H. H. (2010). Design of a Si-based lattice-matched room-temperature GeSn/GeSiSn multi-quantum-well mid-infrared laser diode. *Opt. Express* 18, 19957–19965. doi:10.1364/OE.18.019957

Tahini, H., Chroneos, A., Grimes, R. W., Schwingenschlögl, U., and Dimoulas, A. (2012). Strain-induced changes to the electronic structure of germanium. *J. Phys. Condens. Matter* 24, 195802. doi:10.1088/0953-8984/24/19/195802

Takeuchi, S., Sakai, A., Yamamoto, K., Nakatsuka, O., Ogawa, M., and Zaima, S. (2006). Growth and structure evaluation of strain-relaxed Ge 1− xSn xbuffer layers grown on various types of substrates. *Semicond. Sci. Technol.* 22, S231–S235. doi:10.1088/0268-1242/22/1/S54

Velha, P., Dumas, D. C., Gallacher, K., Millar, R., Myronov, M., Leadley, D. R., et al. (2013). *Strained Germanium Nanostructures on Silicon Emitting at >2.2 μm Wavelength*. IEEE, 142–143.

Vincent, B., Gencarelli, F., Bender, H., Merckling, C., Douhard, B., Petersen, D. H., et al. (2011). Undoped and in-situ B doped GeSn epitaxial growth on Ge by atmospheric pressure-chemical vapor deposition. *Appl. Phys. Lett.* 99, 152103. doi:10.1063/1.3645620

Virgilio, M., Manganelli, C. L., Grosso, G., Schroeder, T., and Capellini, G. (2013). Photoluminescence, recombination rate, and gain spectra in optically excited n-type and tensile strained germanium layers. *J. Appl. Phys.* 114, 243102. doi:10.1063/1.4849855

Wang, L., Su, S., Wang, W., Gong, X., Yang, Y., Guo, P., et al. (2013). Strained germanium-tin (GeSn) p-channel metal-oxide-semiconductor field-effect-transistors (p-MOSFETs) with ammonium sulfide passivation. *Solid State Electron.* 83, 66–70. doi:10.1016/j.sse.2013.01.031

Wegscheider, W., Eberl, K., Menczigar, U., and Abstreiter, G. (1990). Single-crystal Sn/Ge superlattices on Ge substrates: growth and structural properties. *Appl. Phys. Lett.* 57, 875. doi:10.1063/1.104264

Wen, H., and Bellotti, E. (2015). Rigorous theory of the radiative and gain characteristics of silicon and germanium lasing media. *Phys. Rev. B* 91, 035307. doi:10.1103/PhysRevB.91.035307

Wirths, S., Buca, D., Mussler, G., Tiedemann, A. T., Holländer, B., Bernardy, P., et al. (2013a). Reduced pressure CVD growth of Ge and Ge1-xSnx alloys. *ECS J. Solid State Sci. Technol.* 2, N99–N102. doi:10.1149/2.006305jss

Wirths, S., Ikonić, Z., Tiedemann, A. T., Holländer, B., Stoica, T., Mussler, G., et al. (2013b). Tensely strained GeSn alloys as optical gain media. *Appl. Phys. Lett.* 103, 192110. doi:10.1063/1.4829360

Wirths, S., Geiger, R., den Driesch von, N., Mussler, G., Stoica, T., Mantl, S., et al. (2015). Lasing in direct-bandgap GeSn alloy grown on Si. *Nat. Photonics* 9, 88–92. doi:10.1038/nphoton.2014.321

Wirths, S., Stange, D., Pampillón, M.-A., Tiedemann, A. T., Mussler, G., Fox, A., et al. (2014). High-k gate stacks on low bandgap tensile strained Ge and GeSn alloys for field-effect transistors. *ACS Appl. Mater. Interfaces* 7, 62–67. doi:10.1021/am5075248

Xiaochen, S., Jifeng, L., Kimerling, L. C., and Michel, J. (2010). Toward a germanium laser for integrated silicon photonics. *IEEE J. Sel. Top. Quantum Electron.* 16, 124–131. doi:10.1109/JSTQE.2009.2027445

Xu, C., Beeler, R. T., Jiang, L., Grzybowski, G., Chizmeshya, A. V. G., Menéndez, J., et al. (2013). New strategies for Ge-on-Si materials and devices using non-conventional hydride chemistries: the tetragermane case. *Semicond. Sci. Technol.* 28, 105001. doi:10.1088/0268-1242/28/10/105001

Zhu, Y.-H., Xu, Q., Fan, W.-J., and Wang, J.-W. (2010). Theoretical gain of strained GeSn0.02/Ge1−x−y′SixSny′ quantum well laser. *J. Appl. Phys.* 107, 073108. doi:10.1063/1.3329424

Conflict of Interest Statement: The authors declare that the research was conducted in the absence of any commercial or financial relationships that could be construed as a potential conflict of interest.

frontiers in
MATERIALS

ORIGINAL RESEARCH ARTICLE
published: 27 April 2015
doi: 10.3389/fmats.2015.00030

Direct growth of $Ge_{1-x}Sn_x$ films on Si using a cold-wall ultra-high vacuum chemical-vapor-deposition system

Aboozar Mosleh[1,2]*, Murtadha A. Alher[2,3], Larry C. Cousar[1,4], Wei Du[2], Seyed Amir Ghetmiri[1,2], Thach Pham[2], Joshua M. Grant[5], Greg Sun[6], Richard A. Soref[6], Baohua Li[4], Hameed A. Naseem[2] and Shui-Qing Yu[2]

[1] Microelectronics-Photonics Graduate Program (μEP), University of Arkansas, Fayetteville, AR, USA
[2] Department of Electrical Engineering, University of Arkansas, Fayetteville, AR, USA
[3] Mechanical Engineering Department, University of Karbala, Karbala, Iraq
[4] Arktonics, LLC, Fayetteville, AR, USA
[5] Engineering-Physics Department, Southern Arkansas University, Magnolia, AR, USA
[6] Department of Engineering, University of Massachusetts Boston, Boston, MA, USA

Edited by:
Jifeng Liu, Dartmouth College, USA

Reviewed by:
Fabio Iacona, National Research Council, Italy
Christophe Labbé, Ecole Nationale Supérieure d'Ingénieurs de Caen, France

***Correspondence:**
Aboozar Mosleh, Engineering Research Center (ENRC), 700 Research Center Boulevard, Fayetteville, AR 72701, USA
e-mail: amosleh@gmail.com

Germanium–tin alloys were grown directly on Si substrate at low temperatures using a cold-wall ultra-high vacuum chemical-vapor-deposition system. Epitaxial growth was achieved by adopting commercial gas precursors of germane and stannic chloride without any carrier gases. The X-ray diffraction analysis showed the incorporation of Sn and that the $Ge_{1-x}Sn_x$ films are fully epitaxial and strain relaxed. Tin incorporation in the Ge matrix was found to vary from 1 to 7%. The scanning electron microscopy images and energy-dispersive X-ray spectra maps show uniform Sn incorporation and continuous film growth. Investigation of deposition parameters shows that at high flow rates of stannic chloride the films were etched due to the production of HCl. The photoluminescence study shows the reduction of band-gap from 0.8 to 0.55 eV as a result of Sn incorporation.

Keywords: chemical-vapor-deposition, Si photonics, Ge alloys, photoluminescence, Ge–Sn

INTRODUCTION

The discovery and development of $Ge_{1-x}Sn_x$ epitaxy technology has enabled silicon photonics to be explored in a different scope of a material platform. The ability of band-gap engineering by varying Sn mole fraction, along with its compatibility to the complementary metal–oxide–semiconductor (CMOS) process, has paved the way for highly competitive Si-based near and mid-infrared optoelectronic devices. Recent reports on the fabrication and characterization of high performance $Ge_{1-x}Sn_x$ devices such as modulators (Kouvetakis et al., 2005), photodetectors (Conley et al., 2014a,b), and light emitting diodes (LEDs) (Du et al., 2014a) show great potential for $Ge_{1-x}Sn_x$ being adopted by industry in the near future. Cutting-edge reports on $Ge_{1-x}Sn_x$, achieving a direct band-gap group IV alloy (Du et al., 2014b; Ghetmiri et al., 2014a; Li et al., 2014; Wirths et al., 2014), is a turning point for the technology to be pursued for the demonstration of an efficient group IV laser. In addition, due to the tunable lattice constant and formation of Lomer dislocations, $Ge_{1-x}Sn_x$ has been shown to work as a universal compliant buffer layer to grow high quality lattice mismatched materials, like III–Vs, on Si (Beeler et al., 2011a; Mosleh et al., 2014).

A variety of challenges exist for the growth of $Ge_{1-x}Sn_x$ alloys on Si such as large lattice mismatch between $Ge_{1-x}Sn_x$ and Si (more than 4.2%), low solid solubility of Sn in Ge (less than 0.5%), and instability of diamond lattice Sn (α-Sn) above 13°C. Therefore, growth can only possibly be done under non-equilibrium conditions. Different growth methods have been demonstrated for $Ge_{1-x}Sn_x$ growth in which molecular beam epitaxy (MBE) and chemical-vapor-deposition (CVD) have obtained device quality material and high Sn incorporation. For the MBE method, both gas source and solid source MBE have been used by different groups to grow $Ge_{1-x}Sn_x$ films (Gurdal et al., 1998; Takeuchi et al., 2007; Chen et al., 2011; Werner et al., 2011; Stefanov et al., 2012; Bhargava et al., 2013; Oehme et al., 2013; Wang et al., 2013).

The other parallel approach of $Ge_{1-x}Sn_x$ growth is CVD. The early results of CVD growth by Kouvetakis and Chizmeshya (2007) at Arizona State University (ASU) showed the ability to grow $Ge_{1-x}Sn_x$ film directly on Si using a hot-wall ultra-high vacuum CVD (UHV-CVD) system with deuterated Stannane (SnD_4) as the Sn precursor along with different chemistries of germanium. Due to the high cost and instability of SnD_4, other precursors such as tetramethyl tin [$Sn(CH_3)_4$] and stannic chloride ($SnCl_4$) have been explored to grow $Ge_{1-x}Sn_x$ alloys. Vincent et al. (2011) (from IMEC using atmospheric pressure CVD) and Kim et al. (Chen et al., 2013) [from Applied Materials/Stanford University using reduced pressure-CVD (RP-CVD)] have reported successful growth of $Ge_{1-x}Sn_x$ by using $SnCl_4$ and a high cost Ge precursor digermane (Ge_2H_6) and carrier gases on a Ge-buffered Si substrate. Using the same $SnCl_4$ and Ge_2H_6 precursors and carrier gases, Mantl et al. (Wirths et al., 2013) (from PGI9-IT) demonstrated direct growth of $Ge_{1-x}Sn_x$ on Si using showerhead technology in an RP-CVD chamber. In the recent report, Tolle et al. (Margetis et al., 2014; Mosleh et al., 2014a) (ASM company) have achieved $Ge_{1-x}Sn_x$ growth using an industry prevail RP-CVD reactor in collaboration with University of Arkansas (UA). Low-cost Germane (GeH_4) and $SnCl_4$ with carrier gasses of N_2/H_2 were used to grow $Ge_{1-x}Sn_x$. A Ge buffer was deposited between the Si substrate and the $Ge_{1-x}Sn_x$ layer in order to compensate the lattice mismatch between the layers. **Table 1** lists the different research groups that have grown $Ge_{1-x}Sn_x$ using CVD. Different

Table 1 | A summary of reports on $Ge_{1-x}Sn_x$ growth using CVD methods by different research groups.

Growth team	Deposition system	Deposition gas precursors				Carrier gas	Buffer layer
		Ge	Cost	Sn	Cost		
ASU (Kouvetakis and Chizmeshya, 2007)	UHV-CVD	Different chemistries	High	SnD_4	High	Yes	No
IMEC (Vincent et al., 2011)	AP-CVD	Ge_2H_6	High	$SnCl_4$	Low	Yes	Ge
Applied materials (Chen et al., 2013)	RP-CVD	Ge_2H_6	High	$SnCl_4$	Low	Yes	Ge
PGI9-IT (Wirths et al., 2013)	RP-CVD	Ge_2H_6	High	$SnCl_4$	Low	Yes	No
ASM/UA (Margetis et al., 2014; Mosleh et al., 2014a)	RP-CVD	GeH_4	Low	$SnCl_4$	Low	Yes	Ge
UA (this work)	UHV-CVD	GeH_4	Low	$SnCl_4$	Low	No	No

growth methods and the cost effectiveness of the gas precursors are compared.

In this paper, we report direct growth of strain-relaxed $Ge_{1-x}Sn_x$ films on Si substrates with Sn mole fractions up to 7% using a cold-wall UHV-CVD system. Stannic chloride and germane were chosen as the precursors which are low-cost and commercially available. The growth of $Ge_{1-x}Sn_x$ films was achieved without using any carrier gases and buffer layers. In order to investigate the material quality, the X-ray diffraction (XRD), high-resolution transmission electron microscopy (TEM), energy-dispersive X-ray spectroscopy (EDX), Raman spectroscopy, and photoluminescence (PL) measurements have been conducted.

EXPERIMENT

GROWTH METHOD

A cold-wall UHV-CVD system was adopted to grow $Ge_{1-x}Sn_x$ films (see **Figure 1** for machine schematic). The system composes a load-lock chamber with a base pressure of 10^{-6} Pa and a process chamber whose base pressure reaches 10^{-8} Pa using the turbo-molecular and cryogenic pumps, respectively. Due to low-temperature growth of the films, removal of oxygen and water vapor is critical which was achieved by using a cryogenic pump. The turbo-molecular pumps are backed by mechanical pumps. The heating stage consisted of a pyrolytic graphite heater with a thermocouple placed at the same distance away from the heater as the wafer. The sample holder rotates up to 80 rpm for uniform film growth. The gas flow is through a side entry port, controlled by mass flow controllers (MFCs). Stannic chloride is a volatile liquid with vapor pressure of 2.4 kPa at one atmospheric pressure. Therefore, the evaporation could produce enough pressure to be passed through the MFC.

Germanium–tin films were grown on 4″ (001) p-type Si substrates with 5–10 Ω cm resistivity. Prior to loading the samples, they were cleaned in a two-step process: (1) Piranha etch solution [H_2SO_4:H_2O_2 (1:1)], (2) oxide strip HF dipping [H_2O:HF (10:1) using 48% pure HF] followed by nitrogen blow drying. The final oxide strip step was not followed by a water rinse as it reduces the life-time of hydrogen passivation and exposes the surface to ambient oxygen (Mosleh et al., 2013, 2014b). The experiments were carried out at reduced pressures of 13, 40, 65, 95, 130, 200, and 260 Pa and at temperatures as low as 300°C. Germane (GeH_4) and stannic chloride ($SnCl_4$) were used as the precursors for $Ge_{1-x}Sn_x$ growth. The gas flow ratio ($GeH_4/SnCl_4$) was set to 5, 3.3, 2.5, and 1.6. Depending on the growth parameters such as gas flow ratio and deposition pressure, a growth rate of 20–3.3 nm/min was achieved.

CHARACTERIZATION METHOD

Analysis of Sn mole fraction, lattice constant, growth quality, and strain in the $Ge_{1-x}Sn_x$ films were conducted using a high-resolution X-ray diffractometer. High-resolution TEM (TITAN) with an accelerating voltage of 300 kV was used to investigate crystal orientation and defects in the grown epi-layers as well as determining the thicknesses of the samples. Surface morphology of the samples was investigated by a scanning electron microscope equipped with EDX. Room temperature PL measurements were carried out using a 690-nm excitation laser. The PL signal was collected by a grating-based spectrometer equipped with a thermoelectric-cooled PbS detector (cut-off at 3 μm) for spectral analysis.

RESULTS AND DISCUSSION

MATERIAL CHARACTERIZATION

The 2θ-ω XRD scan was performed from the symmetric (004) plane to obtain the out-of-plane lattice constant of the $Ge_{1-x}Sn_x$ films. **Figure 2A** shows the peak at 69° corresponding to a satisfaction of the Bragg condition by Si (001) substrate, and the peaks at lower angles of 66–65° due to larger lattice size of the $Ge_{1-x}Sn_x$ layers. The difference in the position of $Ge_{1-x}Sn_x$ peaks is due to the difference in the Sn mole fractions of $Ge_{1-x}Sn_x$ layers. Different compositions were achieved from 1 to 7% with desirable crystal quality. The $Ge_{1-x}Sn_x$ peaks are broadened for two reasons: (1) thin film thickness of the layers and (2) presence of mosaicity in the Ge–Sn crystal and formation of defects as a result of strain relaxation. The full width at half maximum (FWHM) of the $Ge_{1-x}Sn_x$ peaks are between 0.28 for 1% Sn film and 0.36 for 7% Sn film. The change in FWHM depends on various factors such as film thickness, relaxation, and quality and there is no trend showing that the FWHM of the peaks change as the Sn composition increases.

In order to calculate the total lattice constant and the strain in the film, an asymmetric reciprocal space mapping (RSM) from (−2, −2, 4) plane was performed. The RSM scans provide measurement of the in-plane ($a_{\parallel}$) and out-of-plane ($a_{\perp}$) lattice constant of $Ge_{1-x}Sn_x$ alloys. The total lattice constant a_0^{GeSn} was calculated by taking into account the elastic constants of $Ge_{1-x}Sn_x$ (Beeler et al., 2011b). Knowing the total lattice constant, the Sn mole fractions is calculated through Vegard's law with the bowing factor of $b = 0.0166$ Å (Moontragoon et al., 2012). **Figure 2B**

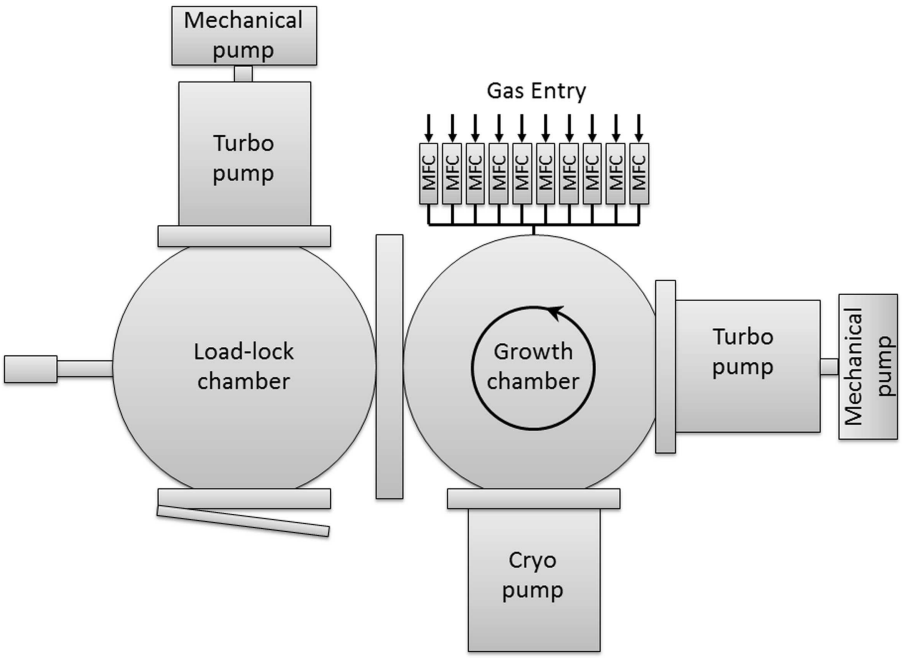

FIGURE 1 | Cold-wall UHV-CVD system with a substrate rotation. Samples are transferred through a load-lock chamber equipped with a turbo-molecular pump. The growth chamber is equipped with a turbo-molecular pump and a cryogenic pump. Side entry of the gases is controlled by mass flow controllers.

shows the RSM of 6% Sn sample. The x-axis shows Q_z in reciprocal lattice unit (rlu) which is related to the out-of-plane lattice constant (L) and the y-axis shows Q_x which is related to the in-plane lattice constant (H or K). Direction of the spread in the $Ge_{0.94}Sn_{0.06}$ peak does not show a compositional gradient in the sample because it is related to the relaxation of the lattice on Si substrate. Large lattice mismatch between Sn and Ge is the main reason for a large spread in the omega direction. The relaxation line in **Figure 2B** shows that the films which are grown above are tensile strained and the films grown underneath are compressively strained. The $Ge_{0.94}Sn_{0.06}$ peak is observed to be on the relaxation line and the relaxation is measured to be 97%.

Calculation of total strain in other samples shows that all the films are more than 95% relaxed. **Table 2** shows the lattice constants of the $Ge_{1-x}Sn_x$ alloys, their Sn mole fraction, and strain relaxation percentage. $Ge_{1-x}Sn_x$ films were almost fully relaxed mainly due to large lattice mismatch between Si (5.431 Å) and $Ge_{1-x}Sn_x$ (above 5.658 Å) and small critical thickness (Mosleh et al., 2014a). The other reason for relaxation of Ge (and similarly $Ge_{1-x}Sn_x$) films on Si is the thermal mismatch between these two materials. High temperature growth (above 500°C) and rapid cool down has been the main method for achieving tensile strained Ge on Si (Conley et al., 2014a). The $Ge_{1-x}Sn_x$ samples were grown at 300°C for 30 min and we have not achieved tensile strained films; however, the thermal mismatch between Si and $Ge_{1-x}Sn_x$ has helped relaxing the compressive strain. The strain has been mainly relieved through formation of misfit dislocations including Lomer misfit dislocation. The cross-sectional TEM image in **Figure 2C** shows formation of such dislocations at the $Ge_{1-x}Sn_x$/Si interface. In addition, **Figure 2B** shows that strain relaxation occurred by formation of misfit dislocations at the interface. The TEM image shows that the grown film was fully epitaxial. Film thickness of the samples is listed in **Table 2**.

The SEM scan/EDX spectra of the samples show surface morphology of the sample as well as Sn incorporation in the Ge matrix. The EDX spectra in **Figure 2D** show the presence of Ge, Si, and Sn in the $Ge_{0.94}Sn_{0.06}$ film. Due to the high count collection of secondary electrons from the substrate, the ratio of Sn and Ge cannot exactly reveal the percentage of Sn in Ge. The presence of carbon and oxygen in the EDX spectra is mainly due to the contamination and oxidation of the film after exposure to ambient air. The EDX maps for Ge (**Figure 2E**) and Sn (**Figure 2F**) display uniform incorporation of Sn. The SEM image shows continuous growth of $Ge_{1-x}Sn_x$ without observation of locally crystalline patches. No segregation and precipitation of Sn was observed on the films which indicates robust and stable growth of the films.

GROWTH MECHANISM

Growth of $Ge_{1-x}Sn_x$ on a Si substrate requires considering the reaction of byproducts and reduction of activation energy by introducing carrier gases. Stannic chloride has a tendency to etch Ge due to the presence of chlorine in the chemistry of the molecule. The byproduct of $GeH_4 + SnCl_4$ reaction is HCl which is an etchant gas for germanium and silicon (Bogumilowicz et al., 2005). Following reactions show different mechanisms of film deposition as well as HCl production in the chamber:

$$GeH_4 \rightarrow Ge + 2H_2 \quad (1)$$

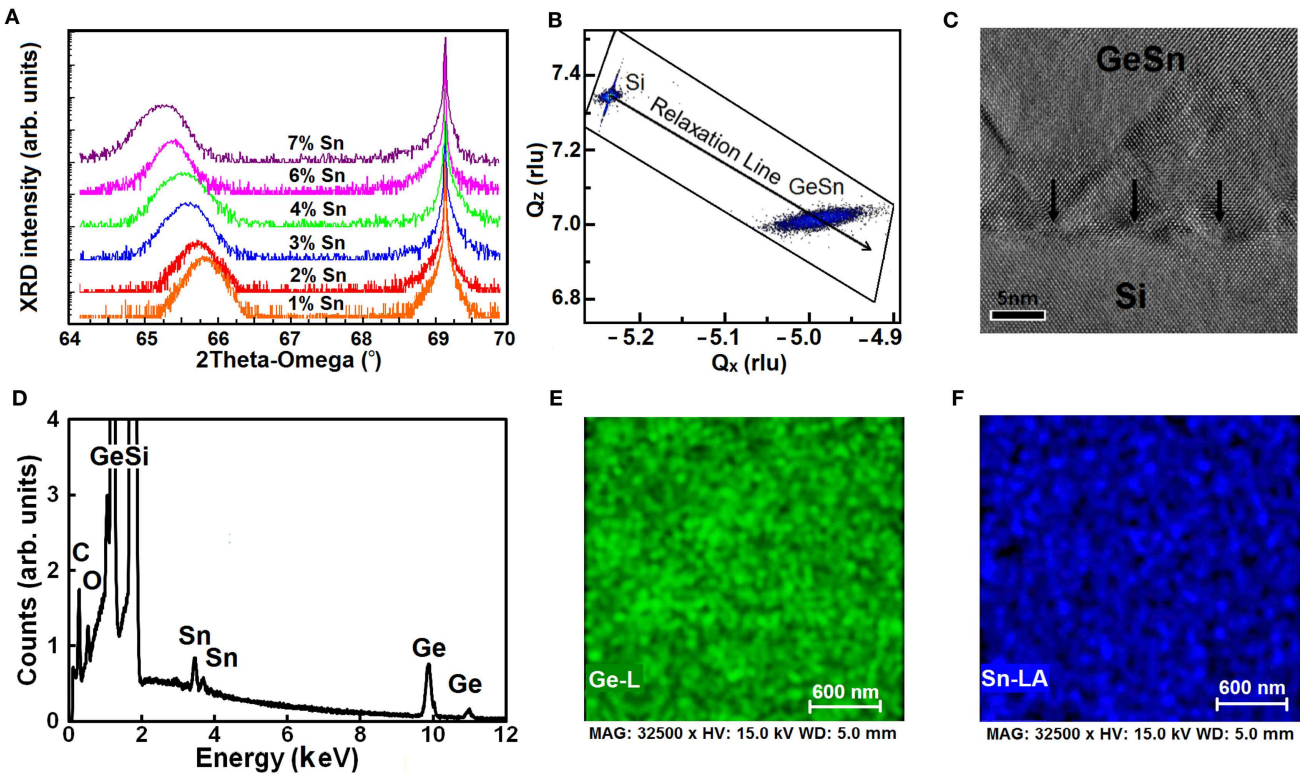

FIGURE 2 | (A) Symmetric (004) 2θ-ω scan of $Ge_{1-x}Sn_x$ films which are grown on a Si substrate. The peak at 69° shows the Si substrate peak and the peaks between 66° and 65° belong to $Ge_{1-x}Sn_x$ films. **(B)** Reciprocal space map from asymmetrical plane (−2, −2, 4) for $Ge_{0.94}Sn_{0.06}$ grown on a Si substrate. The *x*-coordinate shows out-of-plane lattice constant and the *y*-coordinate shows in-plane lattice constant in units of reciprocal lattice unit. The relaxation line shows that the films grown above are tensile strained and below are compressively strained. Presence of the $Ge_{0.94}Sn_{0.06}$ on the relaxation line shows that the film is strain relaxed. **(C)** Transmission electron microscopy images of $Ge_{0.94}Sn_{0.06}$ film shows epitaxial growth of Ge–Sn on a Si substrate. Arrows show misfit dislocations formed at the $Ge_{1-x}Sn_x$/Si interface. **(D)** The EDX spectrum of Si/$Ge_{0.94}Sn_{0.06}$ film shows the presence of Si (substrate), Ge and Sn (film), O (native oxide), and C (carbon contamination from the ambient). **(E)** The EDX surface maps of Ge and **(F)** Sn taken from scanning electron micrographs for $Ge_{0.94}Sn_{0.06}$ film shows uniform growth of $Ge_{1-x}Sn_x$ alloy.

Table 2 | Tin mole fraction calculation, lattice constant, and relaxation percentage of the grown samples.

Sample no.	Sn (%)	$a_{\parallel\Pi}$ (nm)	$a_{\perp}$ (nm)	a (nm)	Relaxation (%)	Thickness (nm)
1	1.2	5.666	5.671	5.668	98	615
2	2.1	5.673	5.679	5.676	98	423
3	2.9	5.678	5.687	5.682	97	295
4	4.2	5.689	5.695	5.692	98	207
5	5.8	5.699	5.712	5.706	97	108
6	7.0	5.715	5.719	5.717	99	532

$$2H_2 + SnCl_4 \rightarrow Sn + 4HCl \quad (2)$$

$$GeH_4 + SnCl_4 \rightarrow Ge + Sn + 4HCl \quad (3)$$

Higher temperature of the substrate results in higher density of depositing ad-atoms (Ge and Sn); however, it will result in production of HCl at a higher rate. In addition, higher flow rate of $SnCl_4$ increases the production rate of HCl as well. Controlling the temperature and flow rate of the gases could control the process so that growth is the dominant process in the chamber. The Ge/Sn film will be etched by HCl through the following reactions:

$$4HCl + Ge \rightarrow GeH_4 + 2Cl_2 \quad (4)$$

$$4HCl + Sn \rightarrow SnCl_4 + 2H_2 \quad (5)$$

Domination of etching over growth is the main mechanism that prevents direct growth of $Ge_{1-x}Sn_x$ on Si.

By controlling the flow through MFCs, we have grown $Ge_{1-x}Sn_x$ films on Si at different pressures with a fixed flow ratio of $GeH_4/SnCl_4 = 1.6$. Growth was observed at 13 Pa of deposition pressure and continued until the deposition pressure increased to 130 Pa. **Figure 3A** shows the thickness of $Ge_{1-x}Sn_x$ films versus deposition pressure of the chamber as well as Sn incorporation percentage. Incorporation of Sn in the Ge lattice is increased by raising the pressure due to the higher residence time of the precursors in the chamber. The residence time of the gases has increased from 2 s at 13 Pa to 19 s at 130 Pa. Meanwhile, HCl etched more of the $Ge_{1-x}Sn_x$ films after deposition at higher pressures. This trend has continued to 130 Pa and no growth has been observed at 200 and 265 Pa. The increase in Sn composition from 1 to 6%

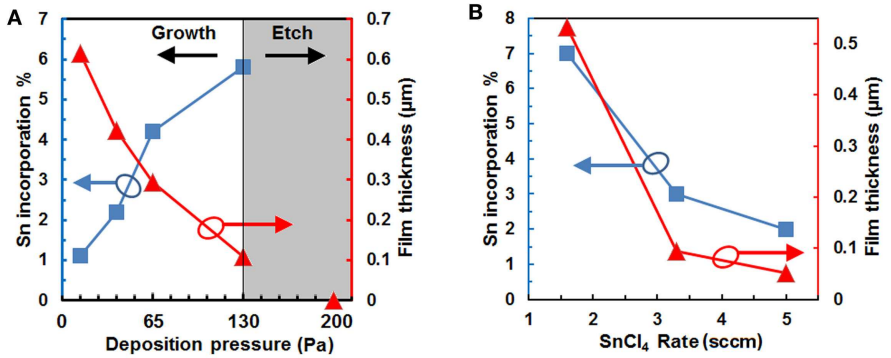

FIGURE 3 | (A) Variation of Sn incorporation percentage versus deposition pressure. Films were etched away for deposition pressures higher than 130 Pa. The secondary axis on the right shows the reduction of film thickness as a result of increase in the deposition pressure. **(B)** Tin incorporation and film thickness of the samples grown at 65 Pa growth pressure versus $GeH_4/SnCl_4$ flow ratios.

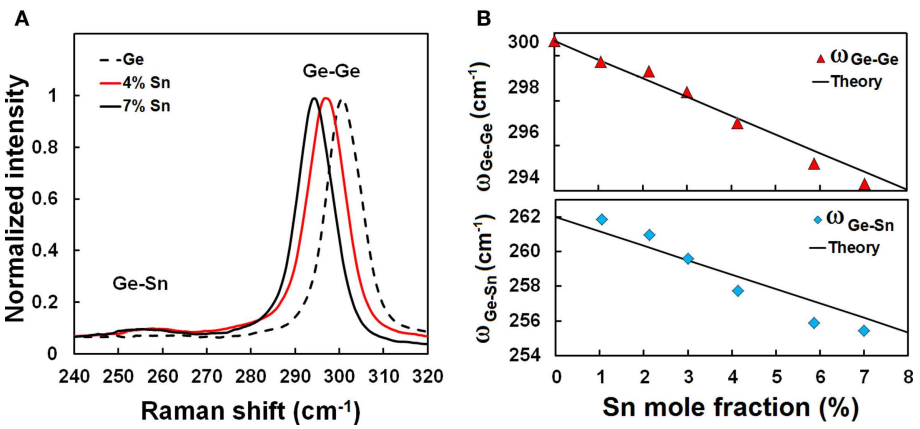

FIGURE 4 | (A) Raman spectra of the $Ge_{1-x}Sn_x$ film grown on a Si substrate. The shift in the Ge–Ge peak is due to the incorporation of Sn in Ge lattice. The shoulder on the left side of the Ge–Ge peak is due to the Ge–Sn peak at 285 cm^{-1}. The Ge–Sn peak is shown at lower wavenumber of 250–260 cm^{-1}. **(B)** Ge–Ge and Ge–Sn peak shifts versus Sn mole fraction. The solid symbols are experimental data and the curves are theoretical predictions for relaxed films. The Ge–Ge peak is expected to shift 0.8310 cm^{-1} for every 1% Sn incorporation in relaxed films. The expected shift (0.8311 cm^{-1}) for Ge–Sn peak is very close to that of Ge–Ge.

has been accompanied with reduction in the thickness from 615 to 108 nm. Films that were expected to have higher than 6% Sn content were totally etched off. Therefore, in order to grow higher Sn content films, growth mechanism under fixed pressure and changing the $SnCl_4$ flow was studied. Higher film thickness and higher Sn incorporation was achieved as a result of domination of growth over etching. **Figure 3B** shows Sn incorporation in $Ge_{1-x}Sn_x$ films versus $SnCl_4$ flow rate at 95 Pa deposition pressure. The secondary axis of **Figure 3B** shows film thicknesses of the samples. Due to the dominance of etching for higher $SnCl_4$ flow rate, the films were mostly etched and the film thickness was less than 100 nm.

Introduction of carrier gases has different effects on the growth of $Ge_{1-x}Sn_x$ films. Hydrogen changes the balance in the reaction to produce more HCl. Consequently, the $GeH_4/SnCl_4$ ratio at which the $Ge_{1-x}Sn_x$ films were depositing will not result in growth when hydrogen is introduced in the chamber. In addition, introduction of nitrogen and argon as carrier gases will reduce the activation energy of the growth (Wirths et al., 2013). Although reduction of activation energy enables easier breakdown of the molecules on the surface and enhances the growth quality and growth rate, it would prepare the conditions for easier etch due to the presence of an etchant agent. Therefore, the presence of carrier gases pushes the competition between growth and etching toward etching, resulting in film etching at even lower flow rates of carrier gases when the flow rate of $SnCl_4$ is of the same order of GeH_4.

OPTICAL CHARACTERIZATION

Raman spectroscopy

The $Ge_{1-x}Sn_x$ films were further investigated by Raman spectroscopy in order to analyze the crystal structure. Room temperature Raman spectra of the grown samples as well as a Ge reference sample are plotted in **Figure 4A**. The Ge–Ge longitudinal optical (LO) peak was observed at 300 cm^{-1} for the Ge reference sample while the Ge–Ge peak in the $Ge_{1-x}Sn_x$ films was shifted to lower

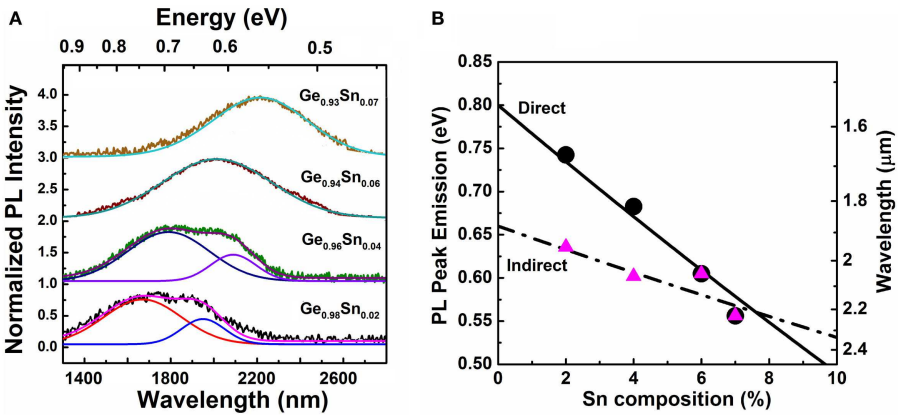

FIGURE 5 | (A) Photoluminescence spectra of the $Ge_{1-x}Sn_x$ films with 2, 4, 6, and 7% Sn mole fraction showing a red-shift in the band-gap of the films. Incorporation of Sn has shifted both direct band-gap and indirect band-gap toward lower energies. **(B)** The bowed Vegard's law interpolation for the direct (solid line) and indirect band-gap (dash line) of $Ge_{1-x}Sn_x$ alloy is plotted for different Sn compositions and is overlaid with experimental data (solid symbols).

wavenumbers due to the change in bonding energy of Ge–Ge by incorporation of Sn atoms. The intensity of the Ge–Ge LO peak at 300 cm^{-1} is normalized for all the samples for comparison of the peak positions. In addition to the main Ge–Ge peak, Raman spectra of $Ge_{1-x}Sn_x$ films show other peaks that are induced as a result of Sn incorporation. The Ge–Sn LO peaks for different Sn mole fractions were observed at 250–260 cm^{-1} in the films. A second peak of Ge–Sn is observed at 285 cm^{-1}, which can be seen as a shoulder of Ge–Ge main peak.

The peak positions are obtained by Lorentzian fitting to find the exact position for further analysis. The shift in the Ge–Ge LO peak depends on both strain and Sn composition of the films. Theoretical calculations for $\Delta\omega$ are different for strain-relaxed films and strained films for different Sn (x) content $[\Delta\omega_{Ge-Ge}(x) = bx\ cm^{-1}]$. The Ge–Ge peak is expected to shift by a factor of $b = -30.30$ for a strained alloy while this factor varies to $b = -83.10$ for a strain-relaxed film (Cheng et al., 2013). **Figure 4B** shows the experimental data obtained for Ge–Ge and Ge–Sn Raman shift from the sample compared with the theoretical calculations. The peak shifts match well with the theoretical calculations for strain-relaxed films.

Photoluminescence

Germanium has an indirect band-gap in the L valley with the energy of 0.644 eV and a direct band-gap at the γ point with 0.8 eV energy at room temperature. Incorporation of Sn in Ge lattice lowers the conduction band edge at the γ-point at a faster rate than that at the L-point. PL measurements on $Ge_{1-x}Sn_x$ samples allow determination of the band-gap edge for various Sn compositions.

Figure 5 depicts room temperature PL intensity spectra for as-grown $Ge_{1-x}Sn_x$ films with 2, 4, 6, and 7% Sn mole fractions. As indicated in **Figure 5A**, increase of the Sn mole fraction results in a band-gap reduction. Both direct and indirect PL peaks exhibit red-shift with Sn compositions increase from 2 to 7%. A Gaussian fitting function was employed to extract the PL peak positions of both direct and indirect transitions as described in Ghetmiri et al. (2014b). In $Ge_{0.94}Sn_{0.06}$ and $Ge_{0.93}Sn_{0.07}$ samples, the energies difference between direct and indirect transitions are very small, therefore the PL emissions from these indirect and direct transitions cannot be identified. A temperature-dependent study is needed to differentiate the direct and indirect peak positions which will be reported in the future. The PL peaks from the samples with 2, 4, 6, and 7% Sn compositions are shown in **Figure 5B** as solid symbols. The solid and the dashed lines show the direct and indirect band-gap energies based on bowed Vegard's law for the relaxed $Ge_{1-x}Sn_x$ alloy (Ghetmiri et al., 2014b), respectively. Since the $Ge_{1-x}Sn_x$ films are almost strain-free, as confirmed by XRD measurements, the experimental results closely follow the predicted values from Vegard's law.

CONCLUSION

Direct growth of $Ge_{1-x}Sn_x$ layers on Si substrates was achieved using a cold-wall UHV-CVD system. The films were grown by employing low-cost commercial available GeH_4 and $SnCl_4$ precursors without using any carrier gases and buffer layers. Characterizations of the samples with XRD showed successful incorporation of Sn up to 7%. The TEM images show fully epitaxial growth of the samples without any precipitation of Sn from the Ge lattice. The Raman results verified the Sn incorporation and PL measurements showed reduction of the band-gap to 0.55 eV for 7% Sn sample. The low-cost and CMOS compatible growth method and the performance of the samples indicate a promising future for $Ge_{1-x}Sn_x$ applications in Si photonics. Moreover, the samples were grown strain-relaxed enabling this material to be a universal compliant buffer layer which can be used in hybrid integration.

ACKNOWLEDGMENTS

The work at the UA was supported by NSF (EPS-1003970), the Arkansas Bioscience Institute, the Arktonics, LLC (Air Force SBIR, FA9550-14-C-0044, Dr. Gernot Pomrenke, Program Manager), and DARPA (W911NF-13-1-0196, Dr. Dev Palmer, Program Manager). Drs. RS and GS acknowledge support from AFOSR

(FA9550-14-1-0196, Dr. Gernot Pomrenke, Program Manager). JG acknowledges the support of NSF REU Program under Grant number EEC-1359306.

REFERENCES

Beeler, R. T., Grzybowski, G. J., Roucka, R., Jiang, L., Mathews, J., Smith, D. J., et al. (2011a). Synthesis and materials properties of Sn/P-doped Ge on Si (100): photoluminescence and prototype devices. *Chem. Mater.* 23, 4480–4486. doi:10.1021/cm201648x

Beeler, R., Roucka, R., Chizmeshya, A., Kouvetakis, J., and Menéndez, J. (2011b). Nonlinear structure-composition relationships in the $Ge_{1-y}Sn_ySi$ (100) ($y< 0.15$) system. *Phys. Rev. B* 84, 035204. doi:10.1103/PhysRevB.84.035204

Bhargava, N., Coppinger, M., Gupta, J. P., Wielunski, L., and Kolodzey, J. (2013). Lattice constant and substitutional composition of GeSn alloys grown by molecular beam epitaxy. *Appl. Phys. Lett.* 103, 041908. doi:10.1063/1.4816660

Bogumilowicz, Y., Hartmann, J. M., Truche, R., Campidelli, Y., Rolland, G., and Billon, T. (2005). Chemical vapour etching of Si, SiGe and Ge with HCl; applications to the formation of thin relaxed SiGe buffers and to the revelation of threading dislocations. *Semicond. Sci. Technol.* 20, 127. doi:10.1088/0268-1242/20/2/004

Chen, R., Huang, Y., Gupta, S., Lin, A. C., Sanchez, E., Kim, Y., et al. (2013). Material characterization of high Sn-content, compressively-strained GeSn epitaxial films after rapid thermal processing. *J. Cryst. Growth* 365, 29–34. doi:10.1016/j.jcrysgro.2012.12.014

Chen, R., Lin, H., Huo, Y., Hitzman, C., Kamins, T. I., and Harris, J. S. (2011). Increased photoluminescence of strain-reduced, high-Sn composition $Ge_{1-x}Sn_x$ alloys grown by molecular beam epitaxy. *Appl. Phys. Lett.* 99, 181125. doi:10.1063/1.3658632

Cheng, R., Wang, W., Gong, X., Sun, L., Guo, P., Hu, H., et al. (2013). Relaxed and strained patterned germanium-tin structures: a Raman scattering study. *ECS J. Solid State Sci. Technol.* 2, 138–145. doi:10.1149/2.013304jss

Conley, B. R., Mosleh, A., Ghetmiri, S. A., Du, W., Soref, R. A., Sun, G., et al. (2014a). Temperature dependent spectral response and detectivity of GeSn photoconductors on silicon for short wave infrared detection. *Opt. Express* 22, 15639–15652. doi:10.1364/OE.22.015639

Conley, B. R., Margetis, J., Du, W., Tran, H., Mosleh, A., Ghetmiri, S. A., et al. (2014b). Si based GeSn photoconductors with a 1.63 A/W peak responsivity and a 2.4 μm long-wavelength cutoff. *App. Phys. Lett.* 105, 221117. doi:10.1063/1.4903540

Du, W., Zhou, Y., Ghetmiri, S. A., Mosleh, A., Conley, B. R., Nazzal, A., et al. (2014a). Room-temperature electroluminescence from $Ge/Ge_{1-x}Sn_x/Ge$ diodes on Si substrates. *Appl. Phys. Lett.* 104, 241110. doi:10.1063/1.4884380

Du, W., Ghetmiri, S. A., Conley, B. R., Mosleh, A., Nazzal, A., Soref, R. A., et al. (2014b). Competition of optical transitions between direct and indirect bandgaps in $Ge_{1-x}Sn_x$. *Appl. Phys. Lett.* 105, 051104. doi:10.1063/1.4892302

Ghetmiri, S. A., Du, W., Margetis, J., Mosleh, A., Cousar, L., Conley, B. R., et al. (2014a). Direct-bandgap GeSn grown on Silicon with 2230 nm photoluminescence. *Appl. Phys. Lett.* 105, 151109. doi:10.1063/1.4898597

Ghetmiri, S. A., Du, W., Conley, B. R., Mosleh, A., Naseem, H. A., Yu, S., et al. (2014b). Shortwave-infrared photoluminescence from $Ge_{1-x}Sn_x$ thin films on silicon. *J. Vac. Sci. Technol. B* 32, 060601. doi:10.1116/1.4897917

Gurdal, O., Desjardins, P., Carlsson, J., Taylor, N., Radamson, H., Sundgren, J., et al. (1998). Low-temperature growth and critical epitaxial thicknesses of fully strained metastable $Ge_{1-x}Sn_x$ ($x \lesssim 0.26$) alloys on Ge (001) 2×1. *J. Appl. Phys.* 83, 162–170. doi:10.1063/1.366690

Kouvetakis, J., and Chizmeshya, A. V. G. (2007). New classes of Si-based photonic materials and device architectures via designer molecular routes. *J. Mater. Chem.* 17, 1649–1655. doi:10.1039/b618416b

Kouvetakis, J., Menendez, J., and Soref, R.A. *Strain-Engineered Direct-Gap Ge/SnxGe1-x Heterodiode and Multi-Quantum-Well Photodetectors, Laser, Emitters and Modulators Grown on SnySizGe1-y-z Buffered Silicon.* United States patent US 6897471 B1 (2005).

Li, H., Brouillet, J., Salas, A., Chaffin, I., Wang, X., and Liu, J. (2014). Low temperature geometrically confined growth of pseudo single crystalline GeSn on amorphous layers for advanced optoelectronics. *ECS Trans.* 64, 819–827. doi:10.1149/06406.0819ecst

Margetis, J., Ghetmiri, S. A., Du, W., Conley, B. R., Mosleh, A., Soref, R., et al. (2014). Growth and characterization of epitaxial $Ge_{1-X}Sn_x$ alloys and heterostructures using a commercial CVD system. *ECS Trans.* 64, 1830–1830. doi:10.1149/06406.0711ecst

Moontragoon, P., Soref, R., and Ikonic, Z. (2012). The direct and indirect bandgaps of unstrained $Si_x Ge_{1-xy}Sn_y$ and their photonic device applications. *J. Appl. Phys.* 112, 073106–073106–8. doi:10.1063/1.4757414

Mosleh, A., Benamara, M., Ghetmiri, S. A., Conley, B. R., Alher, M. A., Du, W., et al. (2014). Investigation on the formation and propagation of defects in GeSn thin films. *ECS Trans.* 64, 1845–1845. doi:10.1149/06406.0895ecst

Mosleh, A., Ghetmiri, S. A., Conley, B. R., Abu-Safe, H., Waqar, Z., Benamara, M., et al. (2013). "Nucleation-step study of silicon homoepitaxy for low-temperature fabrication of Si solar cells," in *Photovoltaic Specialists Conference (PVSC), IEEE 39th*. Tampa, FL.

Mosleh, A., Ghetmiri, S. A., Conley, B. R., Hawkridge, M., Benamara, M., Nazzal, A., et al. (2014a). Material characterization of $Ge_{1-x}Sn_x$ alloys grown by a commercial CVD system for optoelectronic device applications. *J. Electron. Mater.* 43, 938–946. doi:10.1007/s11664-014-3089-2

Mosleh, A., Ghetmiri, S. A., Conley, B. R., Abu-Safe, H. H., Benamara, M., Waqar, Z., et al. (2014b). Investigation of growth mechanism and role of H_2 in very low temperature Si epitaxy. *ECS Trans.* 64, 967–975. doi:10.1149/06406.0967ecst

Oehme, M., Buca, D., Kostecki, K., Wirths, S., Holländer, B., Kasper, E., et al. (2013). Epitaxial growth of highly compressively strained GeSn alloys up to 12.5% Sn. *J. Cryst. Growth* 384, 71–76. doi:10.1016/j.jcrysgro.2013.09.018

Stefanov, S., Conde, J., Benedetti, A., Serra, C., Werner, J., Oehme, M., et al. (2012). Laser synthesis of germanium tin alloys on virtual germanium. *Appl. Phys. Lett.* 100, 104101. doi:10.1063/1.3692175

Takeuchi, S., Sakai, A., Yamamoto, K., Nakatsuka, O., Ogawa, M., and Zaima, S. (2007). Growth and structure evaluation of strain-relaxed $Ge_{1-x}Sn$ buffer layers grown on various types of substrates. *Semicond. Sci. Technol.* 22, S231. doi:10.1088/0268-1242/22/1/S54

Vincent, B., Gencarelli, F., Bender, H., Merckling, C., Douhard, B., Petersen, D. H., et al. (2011). Undoped and in-situ B doped GeSn epitaxial growth on Ge by atmospheric pressure-chemical vapor deposition. *Appl. Phys. Lett.* 99, 152103–152103–3. doi:10.1063/1.3645620

Wang, L., Su, S., Wang, W., Gong, X., Yang, Y., Guo, P., et al. (2013). Strained germanium–tin (GeSn) p-channel metal-oxide-semiconductor field-effect-transistors (p-MOSFETs) with ammonium sulfide passivation. *Solid State Electron.* 83, 66–70. doi:10.1016/j.sse.2013.01.031

Werner, J., Oehme, M., Schmid, M., Kaschel, M., Schirmer, A., Kasper, E., et al. (2011). Germanium-tin pin photodetectors integrated on silicon grown by molecular beam epitaxy. *Appl. Phys. Lett.* 98, 061108–061108–3. doi:10.1063/1.3555439

Wirths, S., Buca, D., Mussler, G., Tiedemann, A., Holländer, B., Bernardy, P., et al. (2013). Reduced pressure CVD growth of Ge and $Ge_{1-x}Sn_x$ alloys. *ECS J. Solid State Sci. Technol.* 2, N99–N102. doi:10.1149/2.006305jss

Wirths, S., Geiger, R., Scherrer, P., Ikonic, Z., Tiedemann, A. T., Mussler, G., et al. (2014). "Epitaxy and photoluminescence studies of high quality GeSn heterostructures with Sn concentrations up to 13 at.%," in *11th International Conference on Group IV Photonics 27–29 August.* Paris.

Conflict of Interest Statement: The authors declare that the research was conducted in the absence of any commercial or financial relationships that could be construed as a potential conflict of interest.

*Received: 28 January 2015; accepted: 23 March 2015; published online: 27 April 2015. Citation: Mosleh A, Alher MA, Cousar LC, Du W, Ghetmiri SA, Pham T, Grant JM, Sun G, Soref RA, Li B, Naseem HA and Yu S-Q (2015) Direct growth of $Ge_{1-x}Sn_x$ films on Si using a cold-wall ultra-high vacuum chemical-vapor-deposition system. Front. Mater. **2**:30. doi: 10.3389/fmats.2015.00030*

This article was submitted to Optics and Photonics, a section of the journal Frontiers in Materials.

frontiers in
MATERIALS

ORIGINAL RESEARCH ARTICLE
published: 23 February 2015
doi: 10.3389/fmats.2015.00008

Room-temperature near-infrared electroluminescence from boron-diffused silicon pn-junction diodes

Si Li, Yuhan Gao, Ruixin Fan, Dongsheng Li and Deren Yang*

State Key Lab of Silicon Materials, Department of Materials Science and Engineering, Zhejiang University, Hangzhou, China

Edited by:
Dan-Xia Xu, National Research Council Canada, Canada

Reviewed by:
Jifeng Liu, Dartmouth College, USA
Tatiana S. Perova, The University of Dublin, Ireland

****Correspondence:***
Deren Yang, State Key Lab of Silicon Materials, Department of Materials Science and Engineering, Zhejiang University, Zheda Road 38, Hangzhou 310027, China
e-mail: mseyang@zju.edu.cn

Silicon pn-junction diodes with different doping concentrations were prepared by boron diffusion into Czochralski n-type silicon substrate. Their room-temperature near-infrared electroluminescence (EL) was measured. In the EL spectra of the heavily boron doped diode, a luminescence peak at ~1.6 μm (0.78 eV) was observed besides the band-to-band line (~1.1 eV) under the condition of high current injection, while in that of the lightly boron doped diode only the band-to-band line was observed. The intensity of peak at 0.78 eV increases exponentially with current injection with no observable saturation at room temperature. Furthermore, no dislocations were found in the cross-sectional transmission electron microscopy image, and no dislocation-related luminescence was observed in the low-temperature photoluminescence spectra. We deduce that the 0.78 eV emission originates from the irradiative recombination in the strain region of diodes caused by the diffusion of large number of the boron atoms into a silicon crystal lattice.

Keywords: boron diffusion, silicon pn-junction diode, near-infrared electroluminescence

INTRODUCTION

With the development of integrated circuits (ICs), the disadvantage of traditional metal interconnection structure, such as interlayer interference, energy dissipation, and signal delay, has become a bottleneck restricting the development of ultra-large-scale integration circuits (USLIs). Optical interconnection, which uses photons to transform information, will be an ultimate solution for future progress in USLIs. Because silicon is an indirect-band-gap semiconductor and fundamentally unable to emit light efficiently, achieving efficient silicon-based light sources compatible with current IC manufacturing technology has become the key issue of silicon optoelectronics. Many routes to fabricate efficient silicon light emitters have been proposed: porous silicon (Canham, 1990; Qin et al., 1996; Bisi et al., 2000; Zhao et al., 2005a,b), Si nanoprecipitates in SiO_2 (Pavesi et al., 2000; Wang et al., 2007), erbium-doped Si (Ennen et al., 1983; Zheng et al., 1994; Polman et al., 1995), Si/SiO_2 superlattice structures (Lu et al., 1995), and silicon pn-junction diodes (Sveinbjörnsson, 1996; Martin et al., 2001; Ng et al., 2001; Sun et al., 2004; Lourenco et al., 2005). Among these ways, silicon pn-junction diodes have attracted much attention. The most standout advantage of this kind of light-emitter is that the fabrication process is totally compatible with USLI technology. Both ion-implantation (Sveinbjörnsson, 1996; Martin et al., 2001; Ng et al., 2001; Sun et al., 2004; Lourenco et al., 2005; Sobolev, 2010) and thermal diffusion (Kveder et al., 2004; Hoang et al., 2006, 2007) have been used to manufacture silicon pn diodes. The past few years has seen great advances in the development of silicon pn-junction diodes. Electroluminescence (EL) efficiency of 0.1–1% has been achieved (Martin et al., 2001; Ng et al., 2001). In addition to the band-to-band emission around 1.1 μm, other near-infrared emissions have been found in boron-implanted and boron-diffused silicon pn diodes (Sveinbjörnsson, 1996; Sun et al., 2004). Sveinbjörnsson (1996) reported strong ~1.6 μm (0.78 eV) EL emission related to dislocation-related center D1 at room temperature from dislocation-rich silicon diodes. Sun et al. (2004) reported two luminescence bands around 1.05 and 0.95 eV related to doping spikes in boron-implanted silicon pn diodes. These emissions show great application potential in silicon optoelectronics. But the mechanism is still in dispute.

In this paper, we fabricated silicon pn-junction diodes with different boron doping concentrations. Their room-temperature EL was measured and their cross-sectional transmission electron microscopy (TEM) images were studied. The result shows that the heavily boron doped silicon pn-junction diode without dislocation loops can emit strong 0.78 eV luminescence under the condition of high current injection besides the band-to-band emission. It is considered that the 0.78 eV emission originates from the irradiative recombination in the strain regions caused by the diffusion of large number of boron atoms into silicon crystal lattice.

MATERIALS AND METHODS

Two kinds of boron diffusion sources were prepared by dissolving B_2O_3 into SiO_2 latex with B^{3+} concentration of 0.203 mol/L (marked as A) and 0.569 mol/L (marked as B), respectively. Boron sources were spin onto the surface of (100) oriented n-type Czochralski-grown Si substrates (2 ~ 10 Ω cm, 500 μm in thickness) after the substrate wafer was cut into 15 mm × 15 mm slices and carefully cleaned by standard RCA process. Rapid thermal treating method was used to form shallow pn junction by boron diffusion at 1100°C for 5 min in the flowing high-purity N_2 atmosphere. After a pn junction was formed, an indium tin oxide (ITO) electrode with a thickness of 100 nm was deposited on the p-layer side by magnetron sputtering, and an Al electrode with a thickness of 100 nm was evaporated on the n-layer side. Thus, a pn-junction diode was prepared.

The carrier concentration and the depth of pn junctions were studied by an SSM350 instrument of spreading resistance profile (SRP). The microstructure of pn junctions was measured by a transmission electron microscope (TEM, JEOL 2010). Photoluminescence (PL) and EL signals were recorded using an Edinburgh FLS920P Spectrometer with a nitrogen-cooled near-infrared photomultiplier tube. The low-temperature PL measurements were performed over the range of 20 ~ 300 K by using a helium flow cryostat.

RESULTS AND DISCUSSION

Figure 1 is the SRP results of pn junctions made from the two boron sources (A and B). It is clear from the figure that shallow pn junctions were formed. It can be seen that Sample B made from the B boron source has the higher carrier concentration than Sample A made from the A boron source. The surface carrier concentration of Sample B reaches 4.6×10^{17} cm^{-3}, while that of Sample A is 5×10^{16} cm^{-3}. It is necessary to notify that the SPR measures the activated dopant density only, which does not take into account the possible dopant clustering at the surface, so there can be a large amount of boron doping, which is inactive. The depth of Sample B pn junction is about 250 nm, a little deeper than that of Sample A, which is about 200 nm.

Figure 2 shows the *I–V* curves of the two pn diodes. As shown in the figure, both the pn diodes perform good rectifying properties. The forward current increases quickly with the voltage while the reverse current stays low. Under the same forward bias, the current of Sample B is greater than that of Sample A. This is because Sample B has the higher carrier concentration and less resistance. In addition, the turn-on voltage of Sample B is about 0.7 V, bigger than that of Sample A, which is about 0.6 V. The reason is that the pn-junction barrier of Sample B with higher doping concentration is larger, so that the forward voltage needed to overcome the barrier is larger.

The room-temperature EL spectra of Sample B and Sample A are different, as shown in **Figure 3**. In the room-temperature EL spectra of Sample A, only band-to-band emission is observed as the current increases. In contrast, Sample B emits 0.78 eV EL besides the band-to-band emission under the condition of high current injection (>705 mA) and its intensity increases greatly with the current. The band-to-band emission of both pn diodes demonstrates a small red shift with the increasing current; this is related to the device heating in response to the current injection.

Sveinbjörnsson (1996) and Xiang et al. (2012a,b) have reported strong emission of 0.78 eV EL at room temperature from silicon pn diodes containing dislocations. They have also found

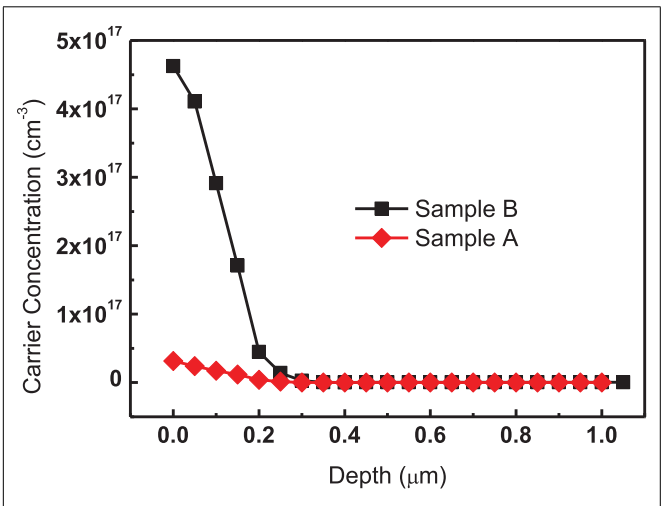

FIGURE 1 | Spreading resistance profile spectra of pn junctions made from Sample A and Sample B fabricated with two boron sources.

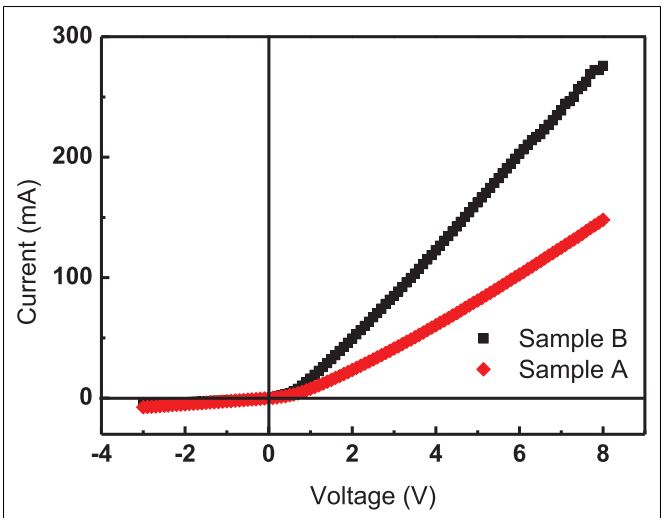

FIGURE 2 | *I–V* curves of the two pn diodes at room temperature.

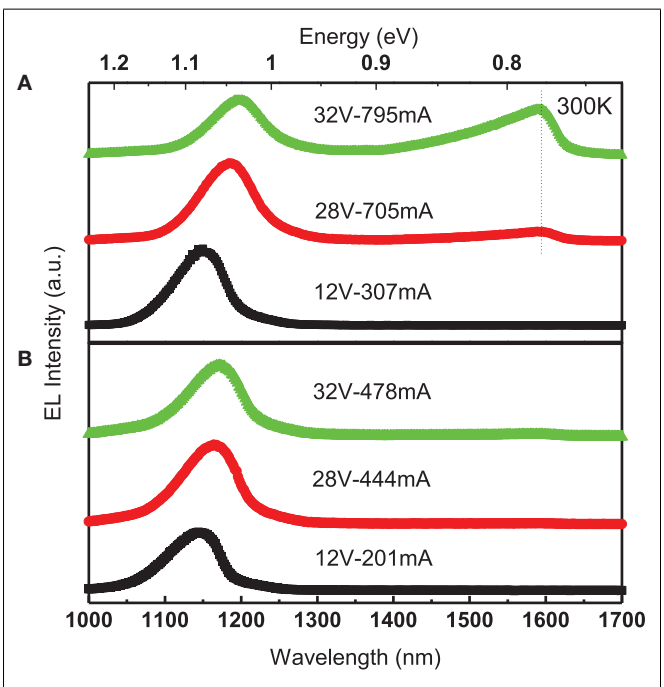

FIGURE 3 | Room-temperature EL spectra at different electrical currents of two pn diodes: (A) for sample B and (B) for sample A.

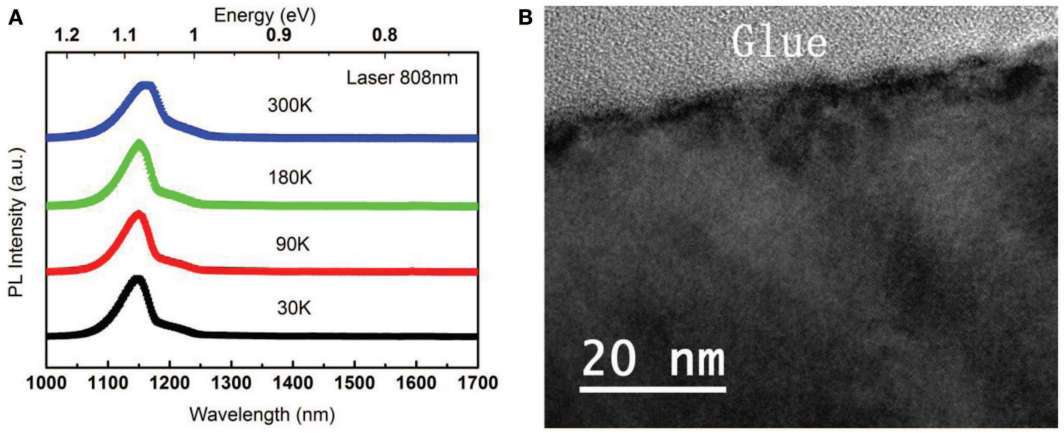

FIGURE 4 | (A) Photoluminescence spectra registered at different temperatures under laser excitation of 808 nm (500 mW) and **(B)** cross-sectional TEM image of sample B.

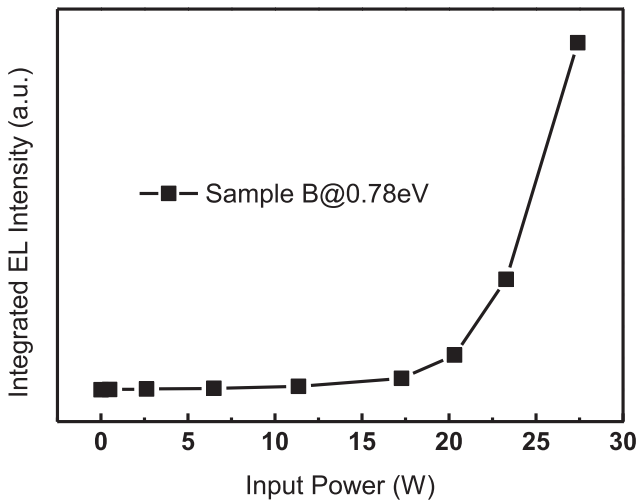

FIGURE 5 | The dependence of peak intensity of EL band at 0.78 eV on the input power of pn-junction diodes.

dislocation-related bands in the low-temperature PL spectra. They tended to regard the peak at 0.78 eV in PL spectrum at room temperature as a red-shifted luminescence band D1. However, for Sample B, no other luminescence band is found in the low-temperature PL spectrum (the pump power intensity is 0.22 W/cm^2) except the band-to-band emission and no dislocations are observed in the cross-sectional TEM image as shown in **Figure 4**. It can be seen from **Figure 4B** that Sample B is free from dislocations. Our work suggests that the 0.78 eV EL at room temperature has no direct connection with dislocations or dislocation-related luminescence bands. In fact, lots of lattice damage regions can be seen near the surface of Sample B in the TEM image. As mentioned before, although the measured dopant concentration by SPR is relatively low, a significant amount of inactive boron doping may exist, so we think that the observed lattice distortion is caused by large number of boron atoms diffusing into silicon lattice. Under the condition of high current injection, these regions can trap carriers and form effective irradiative recombination centers, which are related to the 0.78 eV luminescence.

Figure 5 shows the dependence of peak intensity of 0.78 eV on the input power. When the input power is low, there is no 0.78 eV EL emission. When the input power reaches ~15 W, Sample B starts to emit 0.78 eV luminescence and its intensity increases almost exponentially with the input power with no observable saturation. This means that if the turn-on power of the o.78 eV emission could be sufficiently decreased, a highly efficient light source would be achieved.

CONCLUSION

In this paper, two silicon pn diodes with different boron doping concentrations were fabricated by boron diffusion. We studied their room-temperature near-infrared EL. The results show that in the EL spectra of the heavily boron doped diode, a luminescence peak at ~1.6 μm (0.78 eV) was observed besides the band-to-band line (~1.1 eV) under the condition of high current injection, while in that of the lightly boron doped diode, only the band-to-band line was observed. In addition, no dislocations were found in the cross-sectional TEM image and no dislocation-related luminescence was observed in the low-temperature PL spectra. The 0.78 eV emission is proved to have no direct connection with dislocations or dislocation-related luminescence bands. In fact, lots of lattice damage regions can be seen near the surface of the highly doped diode in the TEM image. We deduce that the 0.78 eV emission may originate from the irradiative recombination in these regions. What is more, the intensity of 0.78 eV emission increases exponentially with the input power without observable saturation, which may be used as an efficient light source in future.

ACKNOWLEDGMENTS

This work is supported by the National Basic Research Program of China (973 Program) (No. 2013CB632102).

REFERENCES

Bisi, O., Ossicini, S., and Pavesi, L. (2000). *Surf. Sci. Rep.* 38, 1–126. doi:10.1016/S0167-5729(99)00012-6

Canham, L. T. (1990). Silicon quantum wire array fabrication by electrochemical and chemical dissolution of wafers. *Appl. Phys. Lett.* 57, 1046–1048. doi:10.1063/1.103561

Ennen, H., Schneider, J., Pomerenke, G., and Axmann, A. (1983). 1.54-μm Luminescence of erbium implanted III–V? semiconductors and silicon. *Appl. Phys. Lett.* 43, 943–945. doi:10.1063/1.94190

Hoang, T., Holleman, J., LeMinh, P., Schmitz, J., Mchedlidze, T., Arguirov, T., et al. (2007). Influence of dislocation loops on the near-infrared light emission from silicon diodes. *IEEE Trans. Electron Devices* 54, 1860–1866. doi:10.1109/TED.2007.901072

Hoang, T., LeMinh, P., Holleman, J., and Schmitz, J. (2006). Strong efficiency improvement of SOI-LEDs through carrier confinement. *IEEE Electron Device Lett.* 27, 383–385. doi:10.1109/LED.2007.895415

Kveder, V., Badylevich, M., Steinman, E., Lzotov, A., Seibt, M., and Schroter, W. (2004). Room-temperature silicon light-emitting diodes based on dislocation luminescence. *Appl. Phys. Lett.* 84, 2106–2108. doi:10.1063/1.1689402

Lourenco, M. A., Milosavljevic, M., Galata, S., Siddiqui, M. S. A., Shao, G., Gwilliam, R. M., et al. (2005). Silicon-based light-emitting devices. *Vacuum* 78, 551–556. doi:10.1016/j.vacuum.2005.01.085

Lu, Z. H., Lockwood, D. J., and Baribeau, J. M. (1995). Quantum confinement and light emission in SiO_2/Si superlattices. *Nature* 378, 258–260. doi:10.1038/378258a0

Martin, A. G., Zhao, J., Wang, A., Peter, J. R., and Michal, G. (2001). Efficient silicon light-emitting diodes. *Nature* 412, 805–808. doi:10.1038/35090539

Ng, W. L., Lourenco, M. A., Gwilliam, R. M., Ledain, S., Shao, G., and Hoomwood, K. P. (2001). An efficient room-temperature silicon-based light-emitting diode. *Nature* 410, 192–194. doi:10.1038/35069092

Pavesi, L., Dal, N. L., Mazzoleni, C., Franzo, G., and Priolo, F. (2000). Optical gain in silicon nanocrystals. *Nature* 408, 440–444. doi:10.1038/35044012

Polman, A., Van, D., Hoven, G. N., Custer, J. S., Shin, J. H., and Sema, R. (1995). Erbium in crystal silicon: optical activation, excitation, and concentration limits. *J. Appl. Phys.* 77, 1256–1262. doi:10.1063/1.358927

Qin, G. G., Song, H. Z., Zhang, B. R., Lin, J., Duan, J. Q., and Yao, G. Q. (1996). Experimental evidence for luminescence from silicon oxide layers in oxidized porous silicon. *Phys. Rev. B* 54, 2548–2555. doi:10.1103/PhysRevB.54.2548

Sobolev, N. A. (2010). Defect engineering in implantation technology of silicon light-emitting structures with dislocation-related luminescence. *Semiconductors* 44, 1–23. doi:10.1134/S106378261001001X

Sun, J. M., Dekorsy, T., Skorupa, W., Schmdt, B., Mucklich, A., and Helm, M. (2004). Below-band-gap electroluminescence related to doping spikes in boron-implanted silicon pn diodes. *Phys. Rev. B* 70, 1–11. doi:10.1103/PhysRevB.70.155316

Sveinbjörnsson, E. Ö, and Weber, J. (1996). Room temperature electroluminescence from dislocation-rich silicon. *Appl. Phys. Lett.* 69, 2686–2688. doi:10.1063/1.117678

Wang, M., Li, D., Yuan, Z., Yang, D., and Que, D. (2007). Photoluminescence of Si-rich silicon nitride: defect-related states and silicon nanoclusters. *Appl. Phys. Lett.* 90, 1–3. doi:10.1063/1.2717014

Xiang, L., Li, D., Jin, L., and Yang, D. (2012a). Dislocation-related electroluminescence of silicon after electron irradiation. *Solid State Commun.* 152, 1956–1959. doi:10.1016/j.ssc.2012.08.011

Xiang, L., Li, D., Jin, L., Pivac, B., and Yang, D. (2012b). The origin of 0.78eV line of the dislocation related luminescence in silicon. *J. Appl. Phys.* 112, 1–4. doi:10.1063/1.4754825

Zhao, Y., Yang, D., Li, D., and Jiang, M. (2005a). Annealing and amorphous silicon passivation of porous silicon with the blue light emission. *Appl. Surf. Sci.* 252, 1065–1069. doi:10.1016/j.apsusc.2005.01.176

Zhao, Y., Yang, D., Li, D., and Jiang, M. (2005b). Photoluminescence of oxidized porous silicon under UV-light illumination. *Mater. Sci. Eng. B* 116, 95–98. doi:10.1016/j.mseb.2004.08.014

Zheng, B., Michel, J., Ren, F. G., Kimerling, L. C., Jacobson, D. C., and Poate, J. M. (1994). Room-temperature sharp line electroluminescence at 1.54 μm from an erbium-doped silicon light-emitting diode. *Appl. Phys. Lett.* 64, 2842–2844. doi:10.1063/1.111977

Conflict of Interest Statement: The authors declare that the research was conducted in the absence of any commercial or financial relationships that could be construed as a potential conflict of interest.

Received: 17 August 2014; accepted: 20 January 2015; published online: 23 February 2015.

Citation: Li S, Gao Y, Fan R, Li D and Yang D (2015) Room-temperature near-infrared electroluminescence from boron-diffused silicon pn-junction diodes. Front. Mater. ***2****:8. doi: 10.3389/fmats.2015.00008*

This article was submitted to Optics and Photonics, a section of the journal Frontiers in Materials.

ADVANTAGES OF PUBLISHING IN FRONTIERS

FAST PUBLICATION

Average 90 days from submission to publication

COLLABORATIVE PEER-REVIEW

Designed to be rigorous – yet also collaborative, fair and constructive

RESEARCH NETWORK

Our network increases readership for your article

OPEN ACCESS

Articles are free to read, for greatest visibility

TRANSPARENT

Editors and reviewers acknowledged by name on published articles

GLOBAL SPREAD

Six million monthly page views worldwide

COPYRIGHT TO AUTHORS

No limit to article distribution and re-use

IMPACT METRICS

Advanced metrics track your article's impact

SUPPORT

By our Swiss-based editorial team

frontiers

EPFL Innovation Park · Building I · 1015 Lausanne · Switzerland
T +41 21 510 17 00 · info@frontiersin.org · frontiersin.org